
COUPLED NUCLEAR AND ELECTRON DYNAMICS IN MOLECULES: FROM SEMICLASSICAL TO FULL-QUANTUM

Thomas Benedikt Schnappinger

München 2021

Dissertation zur Erlangung des Doktorgrades
der Fakultät für Chemie und Pharmazie
der Ludwig-Maximilians-Universität München

**Coupled Nuclear and Electron Dynamics in Molecules:
From Semiclassical to Full-Quantum**

Thomas Benedikt Schnappinger
aus
Mühldorf am Inn, Deutschland

Erklärung

Diese Dissertation wurde im Sinne von § 7 der Promotionsordnung vom 28. November 2011 von Frau Prof. Dr. Regina de Vivie-Riedle betreut.

Eidesstattliche Versicherung

Diese Dissertation wurde eigenständig und ohne unerlaubte Hilfe erarbeitet.

München, 31.05.2021
Thomas Schnappinger

Dissertation eingereicht am:

31.05.2021

1. Gutachterin:

Prof. Dr. Regina de Vivie-Riedle

2. Gutachter:

Prof. Dr. Matthias Kling

Mündliche Prüfung am:

19.07.2021

CONTENTS

Abstract	v
List of publications	vii
Introduction	1
1 Dynamics of Thiophene and its Oligomers	5
1.1 Quantum Chemistry of Thiophene and Oligothiophenes	6
1.2 A Short Introduction to the SHARC Approach	7
1.3 Molecular Dynamics of Thiophene	10
1.4 Molecular Dynamics of Oligothiophenes	20
2 Control of Molecular Dynamics	33
2.1 A Short Introduction to Grid-based Nuclear Quantum Dynamics	34
2.2 Control of Molecular Dynamics Close to a Conical Intersection	36
3 Coupled Nuclear and Electron Dynamics: The NEMol ansatz	53
3.1 NEMol and its Extensions for Higher Dimensional Systems	54
3.2 Photoinduced Nuclear and Electron Dynamic in Uracil	59
3.3 Coupled Nuclear and Electron Dynamics in NO ₂	73
4 Summary and Outlook	93
Bibliography	97
List of abbreviations	115
Danksagung	117

ABSTRACT

The interaction of light with a molecular system is the fundamental step of various chemical, physical and biological phenomena. Investigating the nuclear and electron dynamics initiated by light-matter interaction is important to understand, optimize and control the underlying processes. In this thesis two theoretical methods describing the coupled nuclear and electron dynamics in molecular systems are addressed. In the presented studies the coupled dynamics induced by photoexcitation, the subsequent relaxation processes and the possibility to control the dynamics in the vicinity of conical intersections (CoIns) are investigated for different molecular systems.

In the first part of this work the photorelaxation pathways of a group of molecules commonly used in organic-based optoelectronic devices are characterized with the help of semiclassical *ab initio* molecular dynamics simulations. The relaxation pathways starting from the first excited singlet state of thiophene and of small oligothiophenes containing up to three rings is characterized by the interplay of internal conversion (IC) and intersystem crossing (ISC). Especially the ISC is mediated by ring-opening via a carbon-sulfur bond cleavage. The resulting entropically favored open-ring structures trap the molecules in a complex equilibrium between singlet and triplet states and a fast ring closure in the ground state is hindered. The extension of the π -system going from the monomer to the trimer weakens and slows down the ring opening process. Consequently the ISC is reduced for longer thiophene chains.

The following two chapters are centered around the topics of controlling the molecular dynamics near a CoIn and monitoring the coherent electron dynamics induced by CoIns and laser interactions in the nucleobase uracil and the symmetric molecule NO_2 . In order to investigate the coherent electron dynamics, the ansatz used in this work allows a full-quantum description of the electron and nuclear motion and is called nuclear and electron dynamics in molecular systems (NEMol). As part of this work NEMol was extended to capture the coupled dynamics in complex high dimensional molecular systems. The observed electron dynamics both in NO_2 and uracil reflects coherence, decoherence and reappearance which are all determined by the associated nuclear dynamics. The control of the molecular dynamics at a CoIn is realized with the help of a few-cycle infrared (IR) pulse. The applied control schema utilizes the carrier-envelope phase (CEP) of the pulse and allows to control the population distribution after the CoIn, the nuclear dynamics as well as the coherent electron dynamics. Depending on the chosen laser parameters and the molecular properties around the CoIn given by nature, two different mechanisms enable the control of the system. Both depend on the CEP but one is based on interference, which is generated by the interaction with the CoIn, and the other one is solely due to the few-cycle waveform of the pulse. As demonstrated for NO_2 and uracil, the CEP control scheme even works for quite challenging boundary conditions. Therefore, it seems to be a general concept which can be used also in different molecules.

LIST OF PUBLICATIONS

This thesis is based on the following five publications listed in chronological order. They are reprinted in the chapters 1 (**1-2**), 2 (**3**) and 3 (**4-5**).

- 1** **T. Schnappinger**, P. Kölle, M. Marazzi, A. Monari, L. González, and R. de Vivie-Riedle
Ab Initio Molecular Dynamics of Thiophene: The Interplay of Internal Conversion and Intersystem Crossing
Physical Chemistry Chemical Physics **19** (2017), 25662-25670.
- 2** **T. Schnappinger**, M. Marazzi, S. Mai, A. Monari, L. González, and R. de Vivie-Riedle
Intersystem Crossing as a Key Component of the Non-Adiabatic Relaxation Dynamics of Bithiophene and Terthiophene
Journal of Chemical Theory and Computation **14** (2018), 4530-4540.
- 3** F. Schüppel, **T. Schnappinger**, L. Bäuml and R. de Vivie-Riedle
Waveform Control of Molecular Dynamics Close to a Conical Intersection
Journal of Chemical Physics **153** (2020), 224307.
- 4** **T. Schnappinger** and R. de Vivie-Riedle
Coupled Nuclear and Electron Dynamics in the Vicinity of a Conical Intersection
Journal of Chemical Physics **154** (2021), 134306.
- 5** L. Bäuml, **T. Schnappinger**, M. F. Kling and R. de Vivie-Riedle
Photo-Induced Coupled Nuclear and Electron Dynamics in the Nucleobase Uracil
Frontiers in Physics **9** (2021), 246.

Additional publications listed in chronological order:

- 6 P. Kölle, **T. Schnappinger**, and R. de Vivie-Riedle
Deactivation Pathways of Thiophene and Oligothiophenes: Internal Conversion Versus Intersystem Crossing
Physical Chemistry Chemical Physics **18** (2016), 7903-7915.
 - 7 P. Liebhäuser, K. Keisers, A. Hoffmann, **T. Schnappinger**, I. Sommer, A. Thoma, C. Wilfer, R. Schoch, K. Stührenberg, M. Bauer, M. Dürr, I. Ivanović-Burmazović, and S. Herres-Pawlis
Record Broken: A Copper Peroxide Complex with Enhanced Stability and Faster Hydroxylation Catalysis
Chemistry A European Journal **23** (2017), 12171.
 - 8 C. Burger, A. Atia-Tul-Noor, **T. Schnappinger**, H. Xu, P. Rosenberger, N. Haram, S. Beaulieu, F. Légaré, A. S. Alnaser, R. Moshhammer, R. T. Sang, B. Bergues, M. S. Schuurman, R. de Vivie-Riedle, I. V. Litvinyuk, and M. F. Kling
Time-Resolved Nuclear Dynamics in Bound and Dissociating Acetylene
Structural Dynamics **5** (2018), 044302.
 - 9 **T. Schnappinger**, C. Burger, A. Atia-Tul-Noor, H. Xu, P. Rosenberger, N. Harem, R. Moshhammer, R. T. Sang, B. Bergues, M. S. Schuurman, I. Litvinyuk, M. F. Kling, and R. de Vivie-Riedle
Simulation of Time-Dependent Ionization Processes in Acetylene
International Conference on Ultrafast Phenomena XXI. EPJ Web Conf. **205** (2019), 09023.
 - 10 M. Lucchini, M. Murari, G. D. Lucarelli, F. Frassetto, L. Poletto, **T. Schnappinger**, R. de Vivie-Riedle and M. Nisoli.
Observation of Ultrafast Dynamics in CO₂ Highly Excited States
2019 Conference on Lasers and Electro-Optics Europe & European Quantum Electronics Conference (CLEO/Europe-EQEC) (2019), 1-1.
 - 11 S. Reiter, **T. Schnappinger** and R. de Vivie-Riedle
Using an Autoencoder for Dimensionality Reduction in Quantum Dynamics
Artificial Neural Networks and Machine Learning - ICANN 2019: Workshop and Special Sessions. Lecture Notes in Computer Science **11731** (2019), 783-787.
 - 12 S. Felicetti, J. Fregoni, **T. Schnappinger**, S. Reiter, R. de Vivie-Riedle, and J. Feist
Photoprotecting Uracil by Coupling with Lossy Nanocavities
Journal of Physical Chemistry Letters **11** (2020), 8810-8818.
 - 13 D. Keefer, **T. Schnappinger**, R. de Vivie-Riedle, and S. Mukamel
Visualizing Conical Intersection Passages via Vibronic Coherence Maps Generated by Stimulated Ultrafast X-Ray Raman Signals
Proceedings of the National Academy of Sciences of the United States of America **117** (2020), 24069-24075.
 - 14 F. Rott, M. Reduzzi, **T. Schnappinger**, Y. Kobayashi, K. F. Chang, H. Timmers, R. de Vivie-Riedle, and S. R. Leone
Ultrafast Dissociation of Vinyl Bromide: An Attosecond Transient Absorption Spectroscopy and Non-Adiabatic Molecular Dynamics Study
Structural Dynamics (2021), *accepted*.
-

The road goes ever on and on
Down from the door where it began.
Now far ahead the road has gone,
And I must follow, if I can,
Pursuing it with eager feet,
Until it joins some larger way
Where many paths and errands meet.
And whither then? I cannot say

The Lord of the Rings:
The Fellowship of the Ring
J.R.R. Tolkien,

INTRODUCTION

The initial step of numerous chemical, physical and biological processes is the interaction of light with a molecular system. This is a fundamental process in nature and can be found in photosynthesis [1–4], the process of vision [5–7], during vitamin D synthesis [8–11] and is one reason for formation of photolesions in the genetic code [12–19]. Beside these biological processes there are also artificial systems like inorganic and organic photovoltaics [20–24], photocatalysts [25, 26], molecular photoswitches [27–29] and molecular motors [30–33] based on light-matter interaction. In all these examples the involved molecule absorbs energy which leads to an increase of the electron and nuclear dynamics. In this very broad field of research, this work is focused on the situation where the molecule absorbs enough energy to promote a valence electron from the molecular ground state to higher electronic states.

This excited molecule undergoes different decay processes some of which are able to induce photochemical reactions. Consequently, it is desirable to understand how these decay mechanisms work on a molecular level and to predict which products emerge from such a photochemical reaction. In the simplest case of a single molecule in the gas phase, which is still very challenging, there are two basic ways for the system to return to the ground state after photoexcitation. The molecule can undergo fluorescence or phosphorescence, which means it returns to the ground state by emitting a photon. This statistical process happens with a certain lifetime depending on the two states involved. In the other case the electronic energy of the excited molecule dissipates by radiationless transitions between electronic states until the ground state is reached. If the spin state does not change by the transition from one state to another it is called internal conversion (IC) and the process is mediated by non-adiabatic coupling (NAC) elements. For the case in which the spin state changes one speaks of intersystem crossing (ISC) and the transition is induced by spin-orbit couplings (SOCs). In the case of IC the transition happens mainly in the vicinity of conical intersections (CoIns). These CoIns are extraordinary points, seams or even higher dimensional crossing spaces where two adiabatic states, solutions to the electronic Schrödinger equation, degenerate [34–37]. They allow an ultrafast and very efficient transition between the electronic states. In order to gain a complete picture of the relaxation process after photoexcitation it is necessary to simulate these complex processes where both nuclear and electronic motion and their interaction play a key role. The theoretical and experimental investigation of these fundamental processes offers a pathway to improve for example the performance of photovoltaics or even allow the design of artificial photosynthetic systems [38].

Beside the initiation of these ultrafast processes, the interaction of light with molecules also provides a possibility to study and analyze this dynamics via numerous spectroscopic techniques. The continuous development of new laser sources today allows to generate highly tunable pulses that cover a wide area of time scales from almost single cycle attosecond pulses to microsecond pulses and an energy range from the infrared via the ultraviolet up to the X-ray regime [39–52]. This makes it possible to monitor nuclear dynamics [53–56] and even electronic motion [57–59] of photoinitiated processes in atoms, molecules and solids. Especially in the attosecond domain, broad-band pulses are used to generate electron wavepackets in highly excited states of molecules, leading to the discovery of effects such as electron localization in diatomic molecules [60, 61] and purely electronic charge migration in biological relevant molecules [57, 62, 63]. The possibility to tune the phase, the frequency and the intensity of a laser pulse with high accuracy allows to design pulses which can guide the underlying molecular dynamics [64–66].

This brings us one step closer to control the outcome of photoinduced processes - one of the major goals in photochemistry. Again the simulation of the coupled electron and nuclear dynamics is necessary to explain and interpret the observations of these experiments but also to develop and expand new control schemes [67–70] and spectroscopic techniques [71, 72].

This work features three major topics around the coupled nuclear and electron dynamics in photoexcited molecules. In the first chapter the focus is on the photorelaxation of thiophene and its smaller oligomers. This class of organic heterocyclic molecules is widely used in photoelectronic applications [73–78]. Especially poly(3-hexylthiophene) (P3HT), is one of the most used donor materials in polymer based solar cells [79–81]. The beginning of the chapter gives a short recapitulation of the previously published results [82] on the deactivation pathways of photoexcited thiophene and of small oligothiophenes up to four rings. These results were obtained by state-of-the-art quantum chemical methods and provide a static picture of the possible relaxation pathways in this type of molecules. Within this work dynamics simulations of the photorelaxation of thiophene, 2,2'-bithiophene and 2,2':5',2''-terthiophene are performed. The used semiclassical methodology allows to treat all nuclear degrees of freedom simultaneously. The contribution of singlet and triplet states to the overall process are taken into account by applying the surface hopping including arbitrary couplings (SHARC) approach [83–86]. This ansatz is a generalization of Tully's fewest switches algorithm of surface hopping (SH) [87] and an introduction for both methods is given in section 1.2. The analysis of the dynamics simulations presented in the sections 1.3 and 1.4 reveal a complex interplay of multiple electronic states with different spin symmetry. For the first time a complete picture of the relaxation pathways of these three molecules is obtained and based on these results it is possible to make predictions about the behavior of longer oligothiophenes after photoexcitation.

The other two topics, namely the coherent electron dynamics induced by CoIns and the control of the nuclear and electron dynamics near a CoIn, are discussed in the second and third chapter. As introduced above, CoIns enable a radiationless transition between electronic states but more than that, in their vicinity they create an extraordinary situation. The adiabatic separation [88] between the nuclear and electronic motion breaks down and the time scales of their dynamics equalizes [34–37]. The molecular wave packet approaching a CoIn gains a non-trivial geometric phase (GP) also called Pancharatnam–Berry phase [34, 35, 89, 90], which can promote self-interference [91–94]. In summary CoIns are not a simple funnel but they create a coherent superposition of electronic states whose composition is determined by the shape and size of the NACs and the associated GP. The coherence lifetime of the superposition depends strongly on the nuclear dynamics [95–99] which is directly influenced by the shape of the CoIn. Comparable superpositions can also be achieved by the coupling of electronic states with the help of laser pulses. In such a case the composition is adjustable via the shape and the properties of the pulse, but again nuclear motion leads to decoherence of the superposition [95–99]. The control scheme studied in this work makes use of these two types of superpositions. Applying a few-cycle laser pulse before the nuclear wave packet reaches the CoIn creates a tunable superposition between the two states forming the CoIn. This superposition experiences the NACs and the associated GP when passing through the CoIn region, leading to constructive or destructive interference. This interference process can be controlled and influences the population transfer, the movement of the nuclei and also the coherent electron dynamics induced by the CoIn. The control scheme presented in chapter 2 relies on the manipulation of the phase of the molecular wave packet which makes the semiclassical methodology used in the first chapter not suitable anymore. Therefore, the nuclear motion is simulated with the help of a grid-based nuclear quantum dynamics method which is described in the section 2.1. The scheme to control the molecular dynamics near a CoIn is introduced in detail in section 2.2. Both its physical boundary conditions and its practicability are investigated on an analytic model system and the photactive molecule uracil. The influence of the control scheme on the electron dynamics in NO₂ is discussed in section 3.3.

Since the goal is to control the strongly coupled dynamics of electrons and nuclei in the vicinity of CoIns, a sophisticated approach is needed which is able to capture the electron motion in a dynamic molecular system. One possibility to do so is the coupled nuclear and electron dynamics in molecular systems (NEMol) ansatz [60, 100–103]. Its extension and further development is the main topic of the third

chapter and is presented in section 3.1. Introducing the NEMol-grid extension and the one-electron-two-orbital (1e-2o) approximation, the ansatz can now be applied to simulate coupled nuclear and electron dynamics in high dimensional complex molecular systems. This new implementation is tested by monitoring the coherent electron dynamics induced by laser pulse interaction and CoIns in the nucleobase uracil (section 3.2) and the small symmetric molecule NO_2 (section 3.3). In the NO_2 test case also the attempt to control the electron dynamics is investigated.

DYNAMICS OF THIOPHENE AND ITS OLIGOMERS

Thiophene and its derivatives are important organic heterocyclic compounds that, among others, are widely used as building blocks in pharmaceuticals [104–107] and organic materials for technological applications [74, 75]. Regarding the second topic the remarkable intrinsic properties of thiophene derivatives are of special interest. They undergo rapid ISC [108–110] leading to extremely high triplet quantum yields [111]. This is a rare behavior of organic molecules [76] which normally exhibit only IC. This property is important for charge separation and transport in conductive organic materials. In combination with their efficient light harvesting and structural versatility they have attracted much attention as building blocks for photoactive polymers and molecular aggregates. They are used as semiconductors [78], light emitting diodes [73, 78, 112–115] and solar cells [77, 79, 116–122]. The thiophene derivative poly(3-hexylthiophene) (P3HT) is an integral part of the P3HT/PCBM device [79–81] one of the most famous examples of an organic solar cell. Beside these technical applications thiophene and its derivatives are used as photoswitches [123] and biological labels [124–127]. It is also possible to enhance two-photon absorption cross sections with the help of polythiophene bridges [128–131].

In order to improve the performance of devices containing oligothiophene components, a detailed understanding of the photoinduced mechanism is necessary to go beyond trial and error. A first step in this direction is the investigation of the radiative and non-radiative process of isolated thiophene and its smaller oligomers. That alone is already a challenging task due to the involvement of multiple electronic states with different spin symmetry and the coupling of nuclear and electronic motion. In our previous publication [82], the possible deactivation processes from the first excited singlet state (S_1) of thiophene and of small oligothiophenes up to four rings are investigated by state-of-the-art quantum chemical methods. The key findings of this work are summarized in section 1.1. Based on these results the next step is to go beyond the static quantum chemical picture. Semiclassical on-the-fly dynamics offers the only achievable way to treat molecular systems of this size full-dimensional. For this purpose the SHARC approach [83–86] a generalization of Tully’s fewest switches algorithm of SH [87] is used which enables the treatment of IC and ISC on the same footing. In section 1.2 Tully’s fewest switches algorithm and the SHARC approach are introduced. The main results of this chapter are the *ab initio* molecular dy-

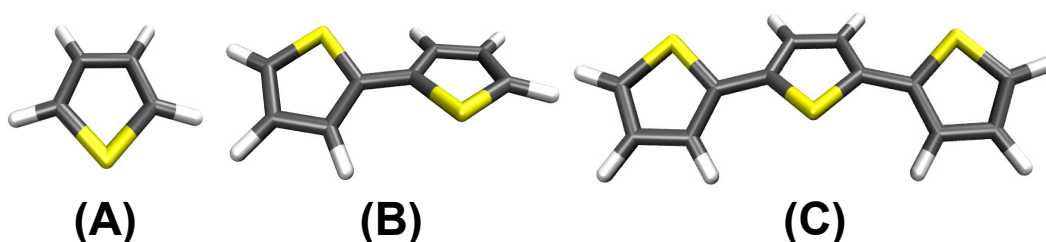


Figure 1.1: Ground state structure of thiophene (A), 2,2'-bithiophene (B) and 2,2':5',2''-terthiophene (C).

namcis simulations for thiophene, 2,2'-bithiophene and 2,2':5',2''-terthiophene which are presented in section 1.3 and section 1.4. The ground state structures of these molecules are shown in figure 1.1. The dynamic treatment including singlet and triplet states offers the possibility to extract time scales for the relaxation process and to assign corresponding pathways. Since the thiophene chain is extended step by step from monomer to trimer, these studies also allow to make predictions about the behavior of longer oligothiophenes.

1.1 Quantum Chemistry of Thiophene and Oligothiophenes

In the article "Deactivation Pathways of Thiophene and Oligothiophenes: Internal Conversion versus Intersystem Crossing" [82] the relaxation pathways after excitation of the bright S_1 state were studied in great detail for thiophene, 2,2'-bithiophene, 2,2':5',2''-terthiophene and the corresponding tetramer. In contrast to other studies [132–137] this was the first time that these four molecules were investigated comprehensively in context of photorelaxation including also the triplet states. The details are elucidated by means of static quantum chemical calculations of the low-lying excited states and of the SOC of the S_1 state and the triplet states. The quantum chemical results for the monomer, dimer and trimer are obtained using the state-average complete active space self-consistent field (CASSCF) method and the complete active space perturbation theory to the second order (CASPT2).

For the monomer thiophene the relevant geometries were optimized both on CASSCF and CASPT2 level of theory. The results obtained using both methods are in good agreement regarding geometries, energies and the state ordering of the singlet and triplet states. However, CASSCF overestimates the excitation energies by approximately 0.5 eV. Starting from the planar Franck-Condon (FC) point the molecule can reach a local S_1 minimum with $\pi\pi^*$ character and a closed-ring non-planar structure. Between this local S_1 minimum and the global minimum of the S_1 state is a small barrier (0.06 eV), which arises as a consequence of an avoided crossing [137]. The global S_1 minimum structure is characterized by the cleavage of one carbon-sulfur bond. In the vicinity of this open-ring minimum a low lying and thus very efficient S_1/S_0 CoIn seam along the $SCCC$ dihedral angle enables transfer in the ground state. Along the ring-opening coordinate and for the open-ring structures, the first two triplet states (T_1 and T_2) and the first two singlet states (S_0 and S_1) are approaching each other in energy. The SOC values increase with carbon-sulfur bond elongation and ISC becomes more likely. A subsequent ring-closure brings the system back to the closed-ring ground state.

Going to the dimer and trimer, CASSCF was used to optimize the relevant molecular structures. Although the obtained structures are in good agreement with the literature [132–135], CASSCF fails drastically to describe excitation energies and thus the state ordering. Therefore, CASPT2 is necessary to correct the energies for bithiophene and terthiophene. Both molecules are not planar in the electronic ground state but the degree of planarity increases with increasing chain length [138]. For both dimer and trimer triplet states are close to the S_1 state already at the FC point and the subsequent relaxation pathways are quite similar. A S_1 minimum is reached via planarization and along this coordinate the S_1 state intersects with a triplet state. This degeneracy can compensate the moderate spin-orbit interaction of the involved states and enables an effective ISC-pathway. A second, less effective ISC channel occurs around the S_1 minimum and is induced by thermal torsional fluctuations. Rotation around the inter-ring carbon-carbon bonds enables the relaxation into the lowest triplet state T_1 . Finally the ground state can be reached via phosphorescence or by T_1/S_0 crossings which are characterized by the cleavage of one carbon-sulfur bond. The direct ring-opening pathway of the monomer can also be found in bithiophene and terthiophene. For both systems not all carbon-sulfur bonds are equivalent and depending on the location of the bond, the opening can be more or less favorable. Even following the most favorable pathway, there is a higher barrier towards the corresponding open-ring S_1 minimum and the S_1/S_0 CoIn seam compared to the monomer. With increasing chain length this barrier height becomes even larger, which can be rationalized by the fact that the initial excitation is delocalized over a larger number of bonds, so each individual bond is weakened to a lesser extent.

In summary, the relaxation pathway in thiophene is characterized by ring-opening mediated by the cleavage of one carbon-sulfur bond. In the smaller oligothiophenes, a second pathway via inter-ring torsion and low-lying triplet states is present due to the extension of the π -system.

1.2 A Short Introduction to the SHARC Approach

Predicting the initial processes after photoexcitation and the subsequent relaxation mechanisms is challenging and it is not sufficient to just investigate the critical points (minima, transition states and CoIns) using a static picture. On an ultrafast time scale, the direction [139, 140] and the momentum [141, 142] of the wave packet have to be taken into account to understand the overall process. The most intuitive way to do so is to simulate the whole dynamics of the system. But with the growing size of the molecular system an exact description of the coupled motion of nuclei and electrons becomes increasingly challenging if not impossible. Nevertheless, in order to investigate complex molecules like thiophene and its oligomers a mixed semiclassical ansatz is the only way to simulate the photoinduced dynamics. Within this semiclassical description only the electrons are treated quantum mechanically, while the nuclei are treated as classical particles. To include more than one electronic state in a semiclassical simulation the most prominent method is Tully’s fewest switches algorithm of SH [87]. A generalization of Tully’s SH algorithm is the SHARC approach [83–86]. The SHARC approach allows to treat couplings like those induced by an electric field or SOC, which enable ISC and therefore are relevant for thiophene derivatives. In the following, a short introduction to Tully’s fewest switches algorithm of SH and the SHARC approach is given.

In a semiclassical SH algorithm the electrons are treated quantum mechanically and represented by a time-dependent electronic wave function $\Phi_{el}(r, t; R(t))$, written as a linear combination of the adiabatic electronic states of the system.

$$\Phi_{el}(r, t; R(t)) = \sum_{\alpha} c_{\alpha}(t) \varphi_{\alpha}(r; R(t)). \quad (1.1)$$

The index α runs over all electronic states, $c_{\alpha}(t)$ are the time-dependent coefficients, and $\varphi_{\alpha}(r; R(t))$ are the wave functions of the individual electronic states. The temporal evolution of $\Phi_{el}(r, t; R(t))$ is determined by the time-dependent Schrödinger equation (TDSE) of the electrons. All quantities are given in atomic units.

$$\hat{H}_{el} \Phi_{el}(r, t; R(t)) = i \frac{\partial}{\partial t} \Phi_{el}(r, t; R(t)). \quad (1.2)$$

The electronic Hamiltonian \hat{H}_{el} in most quantum chemistry calculations is the molecular Coulomb Hamiltonian (MCH), which describes beside the kinetic energy of the electrons only Coulomb interactions.

$$\hat{H}_{MCH} = -\frac{1}{2} \sum_i \nabla_i^2 - \sum_A \sum_i \frac{Z_A}{|\mathbf{R}_A - \mathbf{r}_i|} + \sum_i \sum_{j>i} \frac{1}{|\mathbf{r}_i - \mathbf{r}_j|} + \sum_A \sum_{B>A} \frac{1}{|\mathbf{R}_A - \mathbf{R}_B|}. \quad (1.3)$$

The electronic wave function $\Phi_{el}(r, t; R(t))$ is connected to the nuclear coordinates $R(t)$ through the parametric dependence of the electronic Hamiltonian on the vector $\mathbf{R}(t)$. Each nucleus A is treated as classical particle and obeys the classical equation of motion.

$$M_A \frac{\partial^2 \mathbf{R}_A}{\partial t^2} = - \frac{\partial E_{el}^{\alpha}(t)}{\partial \mathbf{R}_A}. \quad (1.4)$$

The classical force on nucleus A is the negative gradient of the electronic energy of the active state α . In this way, the nuclei follow classical trajectories (defined by the time-dependent positions \mathbf{R} of all nuclei), which are influenced by the quantum mechanically treated electrons. In contrast to a wave packet, the classical nuclei can only follow one particular force in each instant of time, and in SH this force is given by the gradient of the active electronic state α .

In order to determine the active state and to enable the change of the active state the population $|c_{\alpha}(t)|^2$ of each electronic state is used in the fewest switches SH ansatz [87, 143]. For this purpose the temporal

evolution of the coefficients $c_\beta(t)$ are calculated by left-multiplying the electronic TDSE (equation 1.2) with $\varphi_\beta(r; R(t))$.

$$\frac{\partial c_\beta(t)}{\partial t} = - \sum_\alpha \left[i \langle \varphi_\beta(r; R(t)) | \hat{H}_{MCH} | \varphi_\alpha(r; R(t)) \rangle + \langle \varphi_\beta(r; R(t)) | \frac{\partial}{\partial t} | \varphi_\alpha(r; R(t)) \rangle \right] c_\alpha(t). \quad (1.5)$$

The time-derivative coupling $\langle \varphi_\beta(r; R(t)) | \partial/\partial t | \varphi_\alpha(r; R(t)) \rangle$ between the two states α and β does not depend on the whole NAC vector $\mathbf{K}_{\beta\alpha} = \langle \varphi_\beta(r; R(t)) | \partial/\partial \mathbf{R} | \varphi_\alpha(r; R(t)) \rangle$, but only on its product with the classical nuclear velocities $\mathbf{v} = \partial \mathbf{R} / \partial t$:

$$\langle \varphi_\beta(r; R(t)) | \frac{\partial}{\partial t} | \varphi_\alpha(r; R(t)) \rangle = \mathbf{v} \cdot \langle \varphi_\beta(r; R(t)) | \frac{\partial}{\partial \mathbf{R}} | \varphi_\alpha(r; R(t)) \rangle = \mathbf{v} \cdot \mathbf{K}_{\beta\alpha}. \quad (1.6)$$

With the help of equation 1.5 a propagator matrix $\mathbf{B}^{MCH}(t + \Delta t, t)$ can be defined to propagate the coefficient vector \mathbf{c} from one time step t to the next $t + \Delta t$ step. After each time step, the coefficients $c_\alpha(t)$ have to be corrected for decoherence effects [144–146]. The coefficients are used to calculate the hopping probability $P_{\alpha \rightarrow \beta}(t)$ [85, 87, 147] at every time step. If $P_{\alpha \rightarrow \beta}(t)$ is negative, it is set equal to zero.

$$P_{\alpha \rightarrow \beta}(t) = \frac{2\Delta t \text{Im}\{c_\alpha^* c_\beta\}}{|c_\alpha|^2} \langle \varphi_\beta(r; R(t)) | \hat{H}_{MCH} | \varphi_\alpha(r; R(t)) \rangle - \frac{2\Delta t \text{Re}\{c_\alpha^* c_\beta\}}{|c_\alpha|^2} \mathbf{v} \cdot \mathbf{K}_{\beta\alpha}. \quad (1.7)$$

The value of $P_{\alpha \rightarrow \beta}(t)$ defines the probability that the active state of the trajectory changes from state α to state β . This change is called hopping event or surface hop. Based on all probabilities $P_{\alpha \rightarrow \beta}$, a stochastic algorithm chooses if a surface hop occurs and defines the new active state. For a successful hopping event two conditions have to be simultaneously fulfilled. For the first condition a uniformly selected random number ζ in the interval $[0, 1]$ has to satisfy the following inequality [147], with N being the number of electronic states.

$$\sum_{k=1}^{N-1} P_{\alpha \rightarrow k}(t) < \zeta \leq \sum_{k=1}^{N-1} P_{\alpha \rightarrow k}(t) + P_{\alpha \rightarrow \beta}(t). \quad (1.8)$$

The second condition ensures that conservation of total energy after hopping can be achieved by adding a momentum equivalent to $E_{el}^\beta(t) - E_{el}^\alpha(t)$ in the direction of the NAC vector [147, 148].

$$E_{el}^\beta(t) - E_{el}^\alpha(t) \leq \frac{\mathbf{M} \cdot (\mathbf{v} \cdot \mathbf{K}_{\beta\alpha})^2}{2K_{\beta\alpha}^2}. \quad (1.9)$$

If both conditions are fulfilled a surface hop is performed and the trajectory continues on the new active state. Situations where only equation 1.8 is satisfied are called frustrated hopping events [149] and the trajectory remains in the old active state. Since the non-adiabatic transitions are based on a stochastic algorithm, an ensemble of trajectories is needed to properly reflect the fundamental quantum mechanical process [87, 147, 150]. The ensemble should reflect the initial distribution of the phase space, each initial phase space point should give rise to multiple trajectories and if necessary initial conditions should also be distributed over multiple electronic states.

Up to this point \hat{H}_{MCH} is used for the electronic part of the dynamics but this Hamiltonian neither can describe interaction with an external field nor SOC. In order to incorporate these arbitrary couplings the electronic Hamiltonian \hat{H}_{el} has to be extended.

$$\hat{H}_{el} = \hat{H}_{MCH} + \hat{H}_{ad}. \quad (1.10)$$

The additional coupling term \hat{H}_{ad} can contain the field dipole moment couplings which are necessary to describe light-matter interactions, e.g. excitation or the Stark effect [151, 152]. To include ISC, the necessary SOC elements can be described by the Breit–Pauli Hamiltonian [153, 154] or different mean-field approximations [154–156].

As discussed in great detail in the literature [83, 85, 87, 146, 157, 158], SH works best when the hopping events only occur in small regions of configuration space with large couplings or in other words if the state-to-state couplings are very localized. This situation is true for non-adiabatic transitions in the adiabatic picture defined by the eigenstates of the MCH Hamiltonian. In contrast to other representation like the diabatic one SH in the adiabatic picture reproduces very well the results of the exact factorization formalism [159, 160]. The degree of localization of the couplings directly influences the number of hops in the SH [157, 158] and thus the stability of the stochastic hopping algorithm. Simply including SOC in the SH leads to a problem since couplings between states of different spin-symmetry are usually very extended in space, see for example reference [161].

Beside this rather fundamental problem there exists also a more practical problem. Standard quantum chemistry programs do not deliver the eigenstates or all other related quantities of the electronic Hamiltonian defined in equation 1.10. The SHARC approach [83–85] offers a solution for both problems. First of all, approximate eigenstates of \hat{H}_{el} can be found using quasi-degenerate perturbation theory [162–164]. In this approach the eigenfunctions $\varphi_\alpha(r; R(t))$ of the MCH Hamiltonian are combined with the full electronic Hamiltonian to calculate the non-diagonal Hamilton matrix \mathbf{H}_{MCH} . The diagonalization of \mathbf{H}_{MCH} gives rise to approximate eigenenergies (the diagonal elements of \mathbf{H}_{diag}) of the total electronic Hamiltonian \hat{H}_{el} .

$$\mathbf{H}_{diag} = \mathbf{U}^\dagger \mathbf{H}_{MCH} \mathbf{U}. \quad (1.11)$$

In addition, also the corresponding approximate eigenstates $\varphi_\beta^{diag}(r; R(t))$ are obtained.

$$\varphi_\beta^{diag}(r; R(t)) = \sum_\alpha \varphi_\alpha(r; R(t)) U_{\alpha\beta}. \quad (1.12)$$

The main advantages of this diagonal representation is that all couplings are localized [83–85] so that independent of the spin symmetry, no state crossing occurs and if the states touch a CoIn is formed. In addition, all multiplet components are split up. The main idea of the SHARC approach is to perform fewest switches SH on these diagonal states. Therefore, several aspects of the basic SH algorithm have to be adjusted to make it numerically stable and accurate. The temporal evolution of the electronic wave function in the diagonal representation more precisely, those of the coefficients c_{diag} is determined with a three-step propagator [84].

$$c_{diag}(t + \Delta t) = \mathbf{U}^\dagger(t + \Delta t) \mathbf{B}^{MCH}(t + \Delta t, t) \mathbf{U}(t) c_{diag}(t). \quad (1.13)$$

First the $c_{diag}(t)$ are transformed into the MCH representation followed by a propagation from $c_{MCH}(t)$ to $c_{MCH}(t + \Delta t)$ with the help of the propagator matrix $\mathbf{B}^{MCH}(t + \Delta t, t)$ defined according to equation 1.5. For this electronic propagation only MCH quantities are used, which are accessible by standard quantum chemistry programs. In the last step the coefficients $c_{MCH}(t + \Delta t)$ are transformed to $c_{diag}(t + \Delta t)$. The diagonal coefficients are used to determine the probability $P_{\alpha \rightarrow \beta}(t)$ of a hopping event according to equation 1.14 [84, 85].

$$P_{\alpha \rightarrow \beta}(t) = \left(1 - \frac{|c_\alpha^{diag}(t + \Delta t)|^2}{|c_\alpha^{diag}(t)|^2} \right) \frac{\text{Re} \left\{ c_\beta^{diag}(t + \Delta t) (B_{\beta\alpha}^{diag})^* (c_\alpha^{diag}(t))^* \right\}}{|c_\alpha^{diag}(t)|^2 - \text{Re} \left\{ c_\alpha^{diag}(t + \Delta t) (B_{\alpha\alpha}^{diag})^* (c_\alpha^{diag}(t))^* \right\}}. \quad (1.14)$$

Here $B_{\alpha\beta}^{diag}$ and $B_{\beta\beta}^{diag}$ are the elements of the propagator matrix in the diagonal representation.

$$\mathbf{B}^{diag}(t + \Delta t, t) = \mathbf{U}^\dagger(t + \Delta t) \mathbf{B}^{MCH}(t + \Delta t, t) \mathbf{U}(t). \quad (1.15)$$

To propagate the classic nuclei within the diagonal representation the MCH gradients have to be transformed into the diagonal ones. The gradients of the diagonal states can be written as a linear combination of several MCH gradients plus a contribution of the energy-difference-scaled NAC vector. For further technical details please refer to the review [85] and the SHARC manual [86].

1.3 Molecular Dynamics of Thiophene

The quantum chemical results for the relaxation processes of thiophene are briefly summarized in section 1.1. Based on these results *ab initio* molecular dynamics simulations were performed using the SHARC approach to include both singlet and triplet states. The underlying electronic structure calculations were done on the CASSCF level of theory. Ideally one would use CASPT2 as for the static quantum chemical study [82] but the usage of CASPT2 was not feasible at the time the dynamics simulations were performed. Even though there are several studies [165–168] performing dynamics simulations on thiophene some open questions remain. First of all, nothing is known about the relaxation dynamics after the ring-opening, since only time scales in the range of 100 fs to 400 fs were studied. Secondly, for most of these simulations no triplet states were taken into account. But as soon as the carbon-sulfur bond is elongated, the SOC become large and the singlet–triplet energy gaps become small.

In the article "*Ab Initio* Molecular Dynamics of Thiophene: The Interplay of Internal Conversion and Intersystem Crossing" published by Physical Chemistry Chemical Physics [169] the first dynamical study of thiophene on a picosecond time scale including also triplet states is presented. The key findings of the article are:

- The initial vibrational dynamics in the S_1 state as well as the subsequent carbon-sulfur bond cleavage occur on a time scale of about 100 fs. This timing is in good agreement with the fast time constants observed in the experiment [170] and in the other theoretical studies [165–167]. During the ring-opening processes ISC is already partly active.
- In the literature [137, 167] a second relaxation pathway via ring-puckering is reported mediated by two closed-ring CoIns. In contrast to the reported dynamics of Prlj, Curchod and Corminboeuf [167] these two relaxation pathways (ring-opening and ring-puckering) are not clearly distinguishable but rather occur together.
- In the previous studies [165–167] a fast relaxation process leading back to the closed-ring ground state was proposed after the carbon-sulfur bond cleavage. In principle, there is a S_0/S_1 CoIn seam near the open-ring S_1 minimum and one could assume that the system directly returns to the closed-ring ground state. However, this process is very unlikely since it would require nearly momentum inversion. Due to the long simulation time and the right description of the open-ring structures using a multi-reference method this fast relaxation path is not observed in the present work.
- Preserving the momentum of the ring-opening process leads to flat potential, where the SOC get large and the singlet–triplet energy gaps nearly vanish. In general, the corresponding open-ring structures are mostly non-planar and very flexible leading to the situation that the system is trapped in this area of the configuration space. The dynamics of the open-ring system is characterized by the interplay of IC (S_0/S_1) and ISC (S_0/T_1 and T_1/S_1). The resulting long-lived entropically favored open-ring structures in the singlet as well as in the triplet states agree with the long, constant signal observed in the experiment [170] and for the first time provide an explanation for this signal.

On the following pages the article "*Ab Initio* Molecular Dynamics of Thiophene: The Interplay of Internal Conversion and Intersystem Crossing" published by Physical Chemistry Chemical Physics is reprinted from *Physical Chemistry Chemical Physics* **19** (2017), 25662–25670 with permission from the PCCP Owner societies. The supporting information of this article is available under <https://doi.org/10.1039/C7CP05061E>.



PCCP

PAPER

View Article Online
View Journal | View IssueCite this: *Phys. Chem. Chem. Phys.*,
2017, 19, 25662

***Ab initio* molecular dynamics of thiophene: the interplay of internal conversion and intersystem crossing†**

Thomas Schnappinger,^a Patrick Kölle,^a Marco Marazzi,^{bc} Antonio Monari,^{bc}
Leticia González^d and Regina de Vivie-Riedle^{da}

The fast and slow components of the relaxation of photoexcited thiophene have been investigated by means of SHARC (surface hopping including arbitrary couplings) molecular dynamics based on multiconfiguration electronic structure calculations. Triplet states are included to ascertain their role in the relaxation process. After thiophene is excited to the S_1 state, ultrafast dynamics ($\tau_{\text{fast}} = 96$ fs) initiates a ring opening due to cleavage of a carbon sulfur bond and simultaneous ring puckering. This time constant is in agreement with previous experimental and theoretical studies. The subsequent dynamics of the open-ring structures is characterized by the interplay of internal conversion and intersystem crossing. For the opening structures, the S_0 , S_1 , T_1 and T_2 states are nearly degenerate and the spin-orbit couplings are large. The underlying potential energy surface is flat and long-lived open-ring structures in the singlet as well as in the triplet states are formed. Both the participation of triplet states and the shape of the energy surface explain the experimentally observed slow ring closure in the ground state.

Received 26th July 2017,
Accepted 30th August 2017

DOI: 10.1039/c7cp05061e

rsc.li/pccp

1 Introduction

Thiophene derivatives in the form of oligomers, polymers or molecular aggregates have been shown to be one of the most promising candidates of organic materials for technological applications.^{1,2} In particular, owing to their efficient light harvesting, structural versatility and intrinsic charge transport behavior, thiophene based π -conjugated systems have attracted much attention as solar cells,^{3–6} light emitting diodes,^{7,8} photo-switches⁹ and as biological labels.^{10–12} In addition polythiophene bridges are also used to enhance two-photon absorption cross sections.^{13–15} As poly(3-hexylthiophene) (P3HT) they form in combination with phenyl-C61-butyric acid methyl ester (PCBM) the famous P3HT/PCBM solar cell. This material combination is still one of the most general and popular ones for fundamental and conceptual studies.^{6,16} Detailed knowledge of the initial processes after photoexcitation and the subsequent

radiative and nonradiative relaxation mechanisms of oligothiophenes should be advantageous to improve the performance of thiophene-based applications. Furthermore, thiophene and its oligomers exhibit remarkable intrinsic properties. For example, small oligothiophenes show extremely high triplet quantum yields.¹⁷ This property deviates strongly from the common behavior found in most organic molecules where the ratio of intersystem crossing (ISC) to internal conversion (IC) and fluorescence is rather small.¹⁸

In contrast to the oligothiophenes no triplet quantum yield was detected for the monomer, but weak phosphorescence with a suggested lifetime of about 1 μ s was reported.^{17,19,20} Using fs pump-probe experiments Weinkauff *et al.*²¹ determined three time constants ($\tau_1 = 80$ fs, $\tau_2 = 25$ fs and $\tau_3 > 50$ ps) for the relaxation path of thiophene after excitation to the S_1 singlet state. The time constant τ_1 is associated with a vibrational dynamics in the excited S_1 state. The ultrafast time constant τ_2 is assigned to the ring opening due to cleavage of a carbon sulfur (C–S) bond. The third time constant is an indication that in the gas phase the ring-closure is slower than 50 ps. Based on static quantum chemical calculations^{22–24} and dynamics simulations,^{25–27} the deactivation processes from the S_1 state of thiophene up to the conical intersections with the ground state are discussed exclusively *via* its singlet states with minor or no involvement of triplet states. The main deactivation pathway is characterized through a low-lying conical intersection seam arising from the ring opening. This seam is associated with

^a Department of Chemistry, Ludwig-Maximilians-Universität München, Butenandtstraße 5-13, 81377 Munich, Germany.

E-mail: Regina.de_Vivie@cup.uni-muenchen.de

^b Université de Lorraine-Nancy, TMS, SRSMC, Boulevard des Aiguillettes, 54506 Vandoeuvre-Lès-Nancy, France

^c CNRS, TMS, SRSMC, Boulevard des Aiguillettes, 54506 Vandoeuvre-Lès-Nancy, France

^d Institute of Theoretical Chemistry, Faculty of Chemistry, University of Vienna, Währinger Straße 17, 1090 Vienna, Austria

† Electronic supplementary information (ESI) available. See DOI: 10.1039/c7cp05061e

a very small barrier with respect to the Franck–Condon (FC) region, which allows a fast internal conversion.²⁴ It was suggested that ISC cannot compete with this fast internal conversion process.^{22,24} Beside the ring opening a second relaxation channel was reported *via* ring puckering.^{23,27}

The previous dynamics simulations explored the initial steps of the relaxation mechanism and enabled a better understanding of the photochemical properties of thiophene. However, two critical points were not taken into account due to the methods employed^{26,27} or the focus chosen.²⁵ Neither the time-dependent density functional theory (TDDFT)²⁶ nor the algebraic diagrammatic construction to the second order method (ADC(2))²⁷ allow, in combination with trajectory surface hopping, us to describe the relaxation dynamics after the ring opening or the ring puckering. As a consequence, only timescales in the range of 100–400 fs were studied. Secondly, for these simulations no triplet states were taken into account. But as soon as the carbon sulfur bond is elongated, the spin orbit couplings (SOC) become large and the singlet–triplet energy gaps become small.^{22,24}

This work presents the first dynamical study of thiophene on a picosecond timescale including also triplet states. It was possible to give an explanation for the third time constant τ_3 and to figure out the role of triplet states. For this study we have used the surface hopping including arbitrary couplings (SHARC) software package,^{28–31} which has already been successfully applied to an important number of molecular systems.^{32–36}

2 Computational details

The electronic states of thiophene were computed using the state-averaged complete active space self-consistent field method³⁷ including two singlet and three triplet states in the stage-averaging procedure (SA(2S+3T)-CASSCF). The SA(2S+3T)-CASSCF wave function was used as reference for the complete active space second-order perturbation theory method (CASPT2).³⁸ Minima (Min), transition states (TS), conical intersections (CoIn) and singlet–triplet minimum-energy crossings (STC) were optimized using the SA(2S+3T)-CASSCF method and for a few important stationary points also CASPT2 optimizations were performed. All optimized geometries are given in the ESI.† The MOLPRO 2012 program^{39,40} was used for all CAS calculations. The molecular dynamics of thiophene was simulated using the SHARC *ab initio* dynamics package version 1.01.^{28–31} The necessary energies, gradients, non-adiabatic couplings and spin–orbit couplings were calculated on-the-fly at the SA(2S+3T)-CASSCF level of theory.

2.1 *Ab initio* level of theory

The SA(2S+3T)-CASSCF and CASPT2 calculations were carried out using the 6-31G* basis set.^{41–43} This basis set proved to be suitable to describe the excited states and the molecular dynamics of thiophene properly as shown by Fazzi *et al.*²⁶ The CASPT2 calculations were performed using a level shift of 0.1 a.u. The IPEA shift was set to zero as suggested by Zobel *et al.*⁴⁴ In our previous work²⁴ the critical points along the

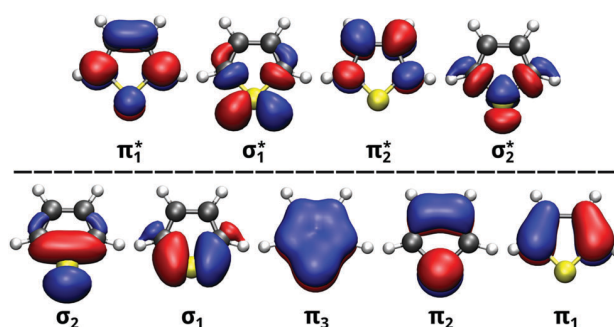


Fig. 1 State-averaged CASSCF molecular orbitals included in the active space CAS(10/9) of thiophene, obtained using the 6-31G* basis set at the SA(2S+3T)-CASSCF optimized ground state equilibrium geometry.

reaction pathway of thiophene were explored on the CASPT2(8/7)/6-31G* level of theory and the results were benchmarked against various quantum chemical methods. The active space included all π -orbitals of thiophene and one pair of σ -orbitals (σ/σ^*) allowing us to describe the bond cleavage of one of the two C–S bonds (see Fig. S1 in the ESI†) and is sufficient for static calculations. However, for dynamics simulations both indistinguishable carbon sulfur bonds must be described equivalently in the active space. Hence, an active space CAS(10/9) (Fig. 1) was employed in this work including all π -orbitals of thiophene and the two pairs of σ -orbitals (σ/σ^*) for both C–S bonds.

The spin–orbit coupling can be considered as the length of the spin–orbit-coupling vector.^{24,45} Its components correspond to the spin–orbit coupling matrix elements calculated by an efficient method using the Breit–Pauli–spin–orbit operator.⁴⁶

2.2 Dynamics

Dynamics simulations were performed using the active space CAS(10/9) with and without consideration of the spin–orbit couplings in order to determine the influence of triplet states on the relaxation mechanism after photoexcitation up to ring closure. The initial conditions were generated based on a Wigner distribution computed from harmonic vibrational frequencies in the optimized ground state equilibrium geometry. For the CAS(10/9) singlet and triplet dynamics (CAS(10/9)-ST), 200 starting geometries and velocities in the energy window 5.0–10.0 eV were stochastically chosen. Analogously, 100 trajectories were generated for the singlet only dynamics simulation (CAS(10/9)-S). All trajectories started in the S_1 state. The SHARC *ab initio* surface-hopping algorithm uses a fully diagonal, spin-mixed electronic basis, resulting from the diagonalization of the Hamiltonian containing non-adiabatic and spin–orbit couplings.^{30,31} The integration of the nuclear motion is done using the Velocity-Verlet algorithm with a maximal time of 5 ps using a time step of 0.5 fs. The coefficients of the electronic wavefunction are propagated on interpolated intermediates with a time step of 0.02 fs. Decoherence correction was taken into account using the energy-based method of Granucci and Persico with a parameter of $\alpha = 0.1$ a.u.⁴⁷ For the sake of completeness the dynamics simulations were also performed

Table 1 Calculated vertical singlet and triplet excitation energies (eV) for the low-lying excited states at the optimized ground-state minimum of thiophene compared to experimental data. Energies were calculated using CASSCF(10/9)/6-31G* and CASPT2(10/9)/6-31G*

State	Char.	CASSCF	CASPT2	Exp.
S ₁	$\pi_2 \rightarrow \pi_1^*$	6.18	5.52	5.26 ^a
T ₁	$\pi_1 \rightarrow \pi_1^*$	3.78	3.74	3.74 ^b
T ₂	$\pi_2 \rightarrow \pi_1^*$	5.06	4.72	4.50 ^b
T ₃	$\pi_2 \rightarrow \sigma_1^*$	6.25	6.08	—

^a Magnetic circular dichroism.⁴⁸ ^b Electron energy loss spectroscopy.⁴⁹

using the small active space CAS(8/7). These results are summarized in the ESI.†

3 Results and discussion

3.1 Validation of the level of theory

First, it was checked if the static SA(2S+3T)-CASSCF(10/9) results are in qualitative agreement with the CASPT2 and the experimental data. Therefore, the excitation energies of the critical points along the relaxation path were benchmarked against data from previous theoretical^{23,24} and experimental^{48,49} studies. The excitation energies were also calculated at the CASPT2(10/9)/6-31G* level of theory in order to check whether the previous CASPT2(8/7) results²⁴ are reproduced. Besides the S₁ also the S₂ state of thiophene has an oscillator strength different from zero.^{24,27} Prlj *et al.*²⁷ showed that the S₂ state is already depopulated within 10 fs by the S₁ state. Therefore, the overall deactivation pathway is not strongly dependent on the initial state (S₁ or S₂) and we can restrict our simulations to start in the S₁ state. The excitation energies at the optimized ground-state minimum are shown in Table 1.

The calculated S₁ excitation energies are larger than the experimental value of 5.26 eV, whereby the CASSCF result differs strongly. Regarding the triplet excitation energies, the CASSCF results are in good agreement with the CASPT2 values. In particular, the experimental excitation energy of the T₁($\pi_1\pi_1^*$) state is reproduced very well. The excitation energy of the T₂($\pi_2\pi_1^*$) state is slightly higher. The order and the character of the four states are the same as in the previous studies.^{22,24,27}

The photochemistry of thiophene is characterized by two deactivation pathways: ring opening due to the C–S bond cleavage and ring puckering arising from the out-of-plane

mode. Accordingly, the S₁/S₀-CoIns of both relaxation pathways were optimized besides the FC region and the stationary points of the S₁ potential energy surface. For all these structures the excitation energies of the four low-lying excited states were determined and compared to the data from previous CASPT2 calculations^{23,24} in Table 2. Additional optimizations were performed for the T₁ and T₂ states and the T₁/S₀- and the T₂/S₁-STC. These results can be found in the ESI† (Tables S1 and S2). All data show similar reaction profiles starting from the FC region of the S₁ state. First the local S₁-Min-a is passed, then a small barrier (S₁-TS) has to be overcome to reach the global minimum of the S₁ state (S₁-Min-b). This relaxation is characterized by a ring opening *via* C–S bond cleavage. In the vicinity of the S₁-Min-b the lowest CoIns with the ground state is located (S₁/S₀-CoIn-a). A further pathway *via* ring puckering was also reported,^{23,27} leading to two conical intersections S₁/S₀-CoIn-b and S₁/S₀-CoIn-c. Stenrup²³ distinguished two types of puckering, one mainly on the sulfur atom (S₁/S₀-CoIn-b) and another on one of the alpha carbons (S₁/S₀-CoIn-c). At all levels of theory the different CoIns are energetically reachable, but the two puckering CoIns lie well above S₁/S₀-CoIn-a. The energetic position of the triplet states with respect to the S₁ singlet state is similar for the CASSCF and CASPT2 calculations. Furthermore, the optimized triplet minima and singlet–triplet minimum-energy crossings (ESI†) are in agreement with previous theoretical results.²²

The main differences between the CASSCF and the CASPT2 results arise from the overestimation of the S₁ excitation energy (see Table 1) and a stronger stabilization of the S₁/S₀-CoIn-a at the CASSCF level (see Table 2). On a relative scale (Δ_{CASSCF} versus Δ_{CASPT2}) the S₁/S₀-CoIn-a is about 1.24 eV and the S₁-TS barrier is about 0.34 eV lower in energy with respect to the S₁ state at the FC point for the CASSCF results compared to the CASPT2 results. This will accelerate the relaxation dynamics towards S₁/S₀-CoIn-a and simultaneously reduce the possibility of choosing the puckering pathway in the CASSCF dynamics. In summary, the crucial area (S₁-Min-a and S₁-TS) where the pathways towards the CoIns are discriminated is described to be qualitatively correct using the chosen SA(2S+3T)-CASSCF(10/9) methodology compared to our CASPT2 results.²⁴ The energetic order of the triplet states compared to the S₁ state is correct. Thus, even though there are a few quantitative differences, we

Table 2 Calculated excitation energies (eV) for singlet and triplet states of thiophene at the most relevant geometries. Shown are the CASSCF and CASPT2 values of this work and the CASPT2 results from previous calculations (references).^{23,24} All energies are relative to the ground state minimum energy. The energies of the optimized states are given in bold

Structure	CASSCF(10/9)/6-31G*					CASPT2(10/9)/6-31G*					Ref.				
	S ₀	S ₁	T ₁	T ₂	T ₃	S ₀	S ₁	T ₁	T ₂	T ₃	S ₀	S ₁	T ₁	T ₂	T ₃
S ₀ -Min	0.00	6.18	3.78	5.06	6.25	0.00	5.52	3.74	4.72	6.08	0.00^b	5.58 ^b	3.76 ^b	4.75 ^b	6.11 ^b
S ₁ -Min-a	0.83	5.45	3.36	4.88	6.45	1.49	5.16	4.02	4.61	6.14	1.49 ^b	5.08^b	4.04 ^b	4.55 ^b	6.09 ^b
S ₁ -TS	1.02	5.56	3.65	5.03	5.80	1.09	5.24	3.73	4.81	5.30	1.64 ^b	5.15^b	3.81 ^b	4.65 ^b	5.47 ^b
S ₁ -Min-b	3.29	3.44	3.17	3.66	5.52	3.58	4.04	3.70	4.30	5.72	3.55 ^b	4.00^b	3.64 ^b	4.29 ^b	5.69 ^b
S ₁ /S ₀ -CoIn-a	3.46	3.46	3.19	3.70	5.58	4.03 ^a	4.04 ^a	3.85 ^a	4.31 ^a	5.95 ^a	4.03^b	4.08^b	3.80 ^b	4.31 ^b	5.94 ^b
S ₁ /S ₀ -CoIn-b	4.93	4.93	4.86	6.38	7.20	4.69 ^a	4.71 ^a	4.86 ^a	6.14 ^a	6.87 ^a	4.61^c	4.61^c	—	—	—
S ₁ /S ₀ -CoIn-c	5.51	5.51	5.44	7.38	7.89	5.20 ^a	5.21 ^a	5.23 ^a	7.12 ^a	7.62 ^a	4.97^c	4.97^c	—	—	—

^a Single point calculation using the CASSCF optimized structure. ^b CASPT2(8/7)/6-31G*. ^c CASPT2(10/8)/6-311G*.²³

are convinced that the chosen methodology is adequate to describe the dynamics of thiophene.

3.2 Excited state dynamics of thiophene

The thiophene dynamics is started in the S_1 state and could be followed through the conical intersections until ring closure in the ground state. These non-adiabatic pathways were thought to be the dominant relaxation pathways. To find out whether triplet states are also involved we performed trajectory calculations with (CAS(10/9)-ST) and without (CAS(10/9)-S) triplet states.

For the stochastic analysis the number of aborted trajectories has to be considered. Some trajectories experienced convergence problems and therefore terminated before reaching 5 ps. Fig. 2 presents how many CAS(10/9)-ST and CAS(10/9)-S trajectories reached a given simulation time. In order to find a good compromise between the simulation time considered and the number of trajectories inspected, we restrict our analysis to trajectories with at least 100 fs of simulation time. Trajectories that terminate within the first 100 fs explore high energy regions unimportant for the relaxation and are discarded. Accordingly, 198 trajectories for CAS(10/9)-ST and 95 trajectories for CAS(10/9)-S have been analyzed. In general the CAS(10/9)-S trajectories are more stable than the CAS(10/9)-ST trajectories and the average simulation time of CAS(10/9)-S (1821.1 fs) is larger than the CAS(10/9)-ST average time (902.0 fs).

All the trajectories were analyzed according to the following aspects: the observed type of dynamics *i.e.* non-adiabatic relaxation *versus* S_1 vibrational dynamics, the final populated state and the final molecular geometry. The results are summarized in Table 3. For both simulation sets few trajectories, approximately 20%, show exclusively vibrational dynamics in the S_1 state before termination in a time span between 200 fs and 4 ps. All other trajectories relax either to the ground state or to the triplet states T_1 and to a small amount to T_2 . The final distribution between the singlet and the triplet states is nearly one-to-one. Within the singlet moiety the relative distribution $S_1:S_0$ is about 22:32. This changes when only singlets are

Table 3 Distribution of the CAS(10/9)-ST and CAS(10/9)-S trajectories according to the observed type of dynamics, the final populated state as well as the final geometry. All percentages are given with respect to the total number of analyzed trajectories. Trajectories that only show vibrational dynamics in the S_1 state without any participation of other states are counted as vibrational dynamics

	(10/9)-ST	(10/9)-S
Non-adiabatic dynamics	83.3	83.2
Vibrational dynamics	16.7	16.8
Final state		
S_0	31.8	75.8
S_1	22.2	24.2
T_1	43.9	—
T_2	2.0	—
T_3	0.0	—
Final geometry		
Thiophene	41.4	54.7
Open-ring	53.5	25.3
Cyclopropene	5.1	16.8
Cyclobutene	0.0	3.2

included (CAS(10/9)-S) to a ratio of 24:76 indicating that the triplet states offer an additional effective relaxation channel.

Approximately half of the trajectories in both sets terminate in thiophene-like closed-ring geometries. For the open-ring structures we often observe premature termination. In these cases we find high kinetic energy in the system, which makes

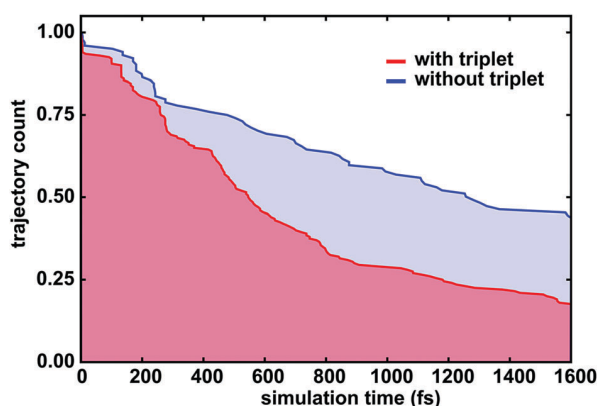


Fig. 2 Percentage of trajectories which have reached at least a given simulation time. The 200 CAS(10/9)-ST trajectories are represented in red, while the 100 CAS(10/9)-S trajectories are shown in blue.

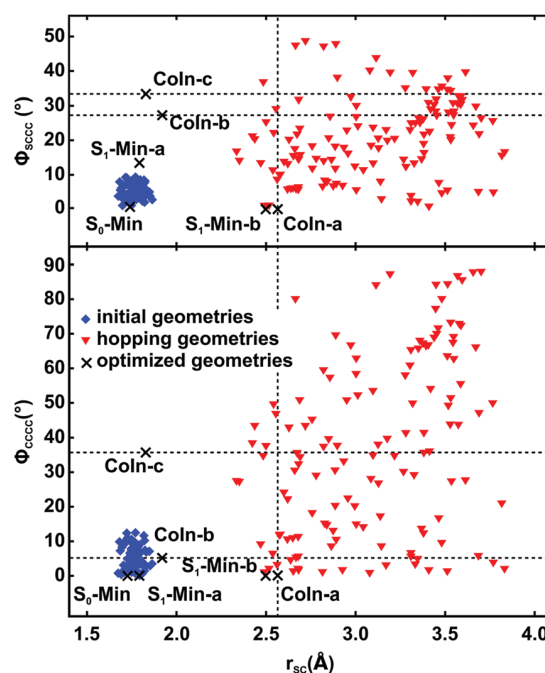


Fig. 3 Locations of the initial geometries and the geometries where surface hops from the S_1 state to the S_0 state occurred depending on the averaged C–S distance r_{CS} and dihedral angles ϕ_{SCCC} (top) and ϕ_{CCCC} (bottom). Only trajectories from the CAS(10/9)-ST dynamics simulation set are shown. The initial geometries are represented in blue, while the S_1/S_0 hopping geometries are marked in red. Both dihedral angles were redefined in the range between 0° and 90° . Additionally important CASSCF(10/9)/6-31G* optimized geometries are represented in black.

recombination to the thiophene ring within the total propagation time of 5 ps highly unlikely. These trajectories are thus counted as final open-ring geometries. For longer time scales, not simulated, we expect that all open-ring structures are going to form thiophene like closed-ring geometries. In the presence of triplet states the ratio between open- and closed ring geometries is 50 : 50. Without triplet states only 30% terminate in open-ring structures, the remaining 20% form cyclopropene or cyclobutene derivatives. These cyclopropene and cyclobutene derivatives are S_0 minimum structures (see the ESI†).

Prlj *et al.*²⁷ reported that both possible relaxation mechanisms (ring opening and puckering) are active and clearly distinguishable. To figure out which relaxation pathway is followed by our CASSCF trajectories, we defined three collective variables associated to the encountered three CoIns and analyzed the geometries at the hopping events from the S_1 to the S_0 state. S_1/S_0 -CoIn-a describing the ring opening is characterized by the averaged C–S distance r_{CS} . The dihedral angles Φ_{SCCC} (averaged over both possibilities) and Φ_{CCCC} (for the definition of the angles see the ESI†) were used to distinguish both puckering mechanisms. Fig. 3 shows the initial geometries (blue diamonds) and the geometries where surface hops to the S_0 state occurred (red triangles) depending on the

three collective variables, the distance r_{CS} and the dihedral angles Φ_{SCCC} (top) and Φ_{CCCC} (bottom). The results are shown for the CAS(10/9)-ST dynamics simulation, analogous figures for the CAS(10/9)-S and the CAS(8/7)-ST dynamics can be found in the ESI† (Fig. S4 and S5).

We observe no S_1/S_0 hopping event in the proximity of the puckering CoIns (CoIn-b and CoIn-c). All S_1/S_0 hopping geometries show a C–S distance r_{CS} larger than 2.2 Å. The values of Φ_{CCCC} vary between 0° and 90° and for Φ_{SCCC} between 0° and 50°. Thus the deactivation mechanism involves mainly simultaneous ring opening and ring puckering. Only for the CAS(8/7)-ST dynamics, for which the ring opening is less probable due to the choice of the active space (see Section 2.1), relaxation *via* exclusive ring puckering was detected up to 11%. Our CAS(10/9) results are in agreement with the dynamics simulations of Fazzi *et al.*,²⁶ but in contrast to the ADC(2) dynamics simulation of Prlj *et al.*²⁷ where ring puckering plays a significant role. This difference may lie in the CASSCF description slightly favoring the open-ring S_1/S_0 -CoIn-a (see Section 3.1) as well as in the ADC(2) description, which is, as pointed out by the authors, not accurate for distorted geometries close to the conical intersections with the ground state.²⁷

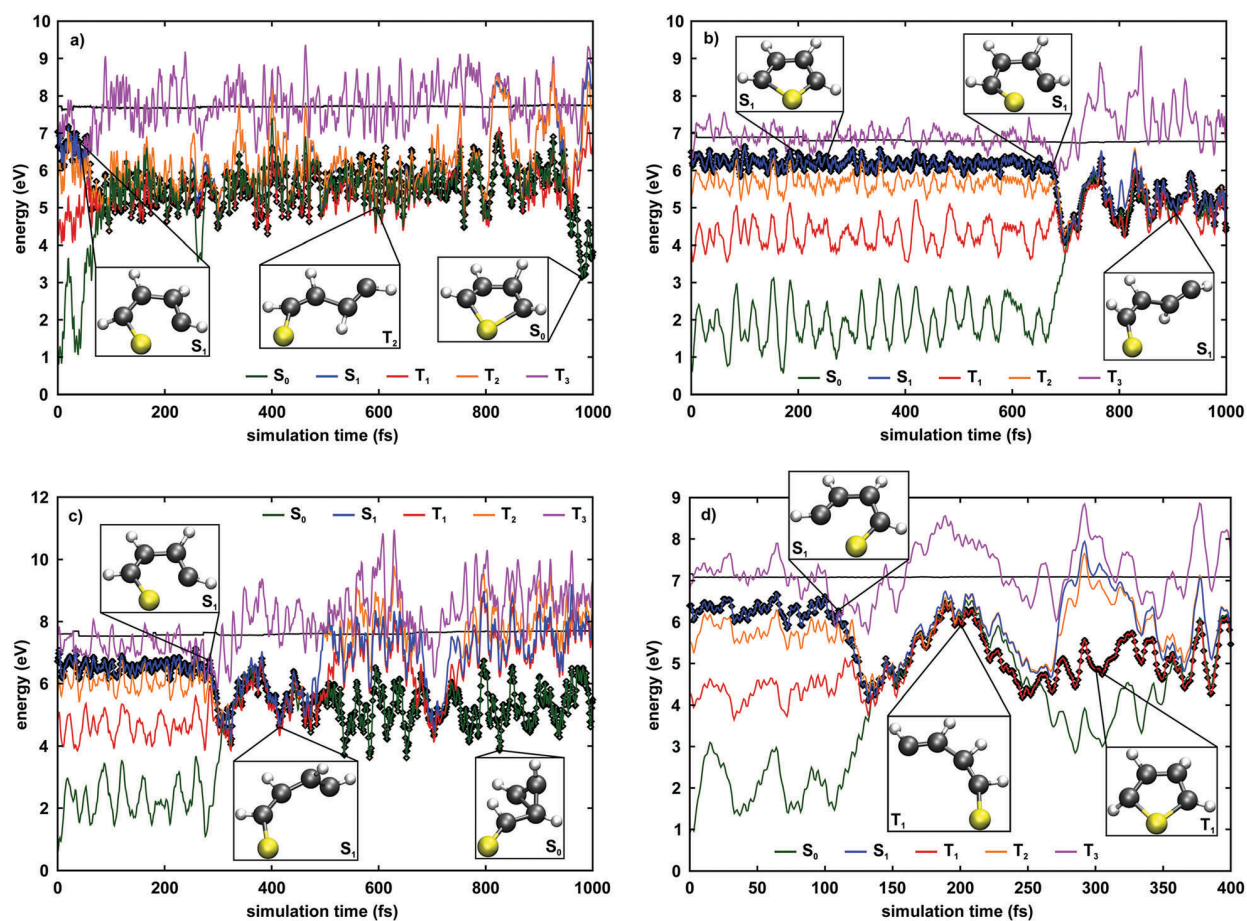


Fig. 4 Energy profiles of four representative trajectories following the ring opening mechanism. All trajectories were initiated on the S_1 potential energy surface. The time evolution of the ground and the four lowest excited states are displayed in color, whereas the running state is indicated in black. The energies are plotted relative to the ground state minimum. Example geometries are given for each trajectory.

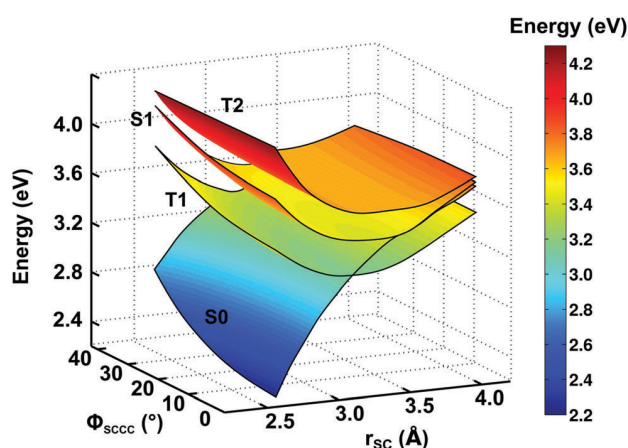


Fig. 5 Two-dimensional potential energy surface of the S_0 , S_1 , T_1 and T_2 states as a function of the C–S distance r_{CS} and dihedral angle ϕ_{SCCC} . The surfaces were obtained through a two-dimensional relaxed potential energy surface scan of the S_1 state along the two reactive coordinates using the SA(2S+3T)-CASSCF(10/9)/6-31G* level of theory. The C–S distance was scanned between 2.6 and 4.0 Å and the dihedral angle ϕ_{SCCC} between 0° and 40°.

The energy profiles of four illustrative trajectories of the CAS(10/9)-ST simulation are shown in Fig. 4.

All four trajectories are characterized by the ring opening mechanism but differ in time when this event happens. After ring opening the four states, S_0 , S_1 , T_1 and T_2 , are nearly degenerate and the corresponding potential energy surface is flat. A two-dimensional cut along the C–S bond r_{CS} and the dihedral angle ϕ_{SCCC} for all four states illustrate this scenario in Fig. 5.

Several hops between these states occur since here the SOC values are large and the energy gaps are small (ESI† Table S4). We were able to optimize several singlet–triplet minimum-energy crossings with an open-ring structure (see the ESI†). The dynamics simulation suggests that in general the open-ring structures are mostly non-planar and very flexible. Nevertheless, it was not possible to optimize an open-ring S_0 minimum.

In Fig. 4(a) the C–S bond is broken after approximately 50 fs. The resulting open-ring structure exists for about 900 fs

allowing many hops between the four degenerate states. At about 1 ps the ring closes in the S_0 state forming the thiophene ring again. The second trajectory in Fig. 4(b) shows vibrational dynamics in the S_1 state for about 700 fs before the C–S bond opens and the four states become degenerate. The subsequent ring-closure does not take place within the presented 1 ps. The last two trajectories are examples for different pathways that can occur on the way to ring-closure. In Fig. 4(c) a cyclopropene derivative is formed in the S_0 state; Fig. 4(d) shows the participation of triplet states whereby a five membered thiophene ring is formed intermediately in the T_1 state leading to a minimum geometry.

The populations of the individual excited states as a function of time are shown in Fig. 6 for the CASSCF(10/9)-ST (left) and the CASSCF(10/9)-S (right) dynamics simulations.

After a short latency time between 10 fs and 20 fs the S_1 population decreases and the S_0 population increases. This latency time was also observed on the same time scale by Prlj *et al.*²⁷ and can be attributed to pure vibrational dynamics in the S_1 state. During the first 200 fs the triplet states T_2 and T_1 do participate to a small extent; however, the evolution of the S_1 and the S_0 population is still comparable for the CAS(10/9)-ST and CAS(10/9)-S dynamics. After this first period most of the trajectories show open-ring structures allowing IC into the S_0 state and enhancing the possibility of ISC significantly. The population of the T_1 state increases further and after 600 fs the S_0 and the T_1 populations are almost equal. Simultaneously, the depopulation of the S_1 state slows down. The T_2 population remains constant and the T_3 state is nearly inactive within the simulation time of 1 ps. The ratio between S_0 , S_1 and T_1 after 1 ps simulation time is approx. 40:20:40. The evolution of the singlet state population of the CAS(10/9)-S dynamics significantly differs from the CAS(10/9)-ST dynamics and leads to a S_0/S_1 ratio of 70:30. The presence of triplet states opens up a further decay channel leading to the T_1 population. The ratio of S_0 , S_1 and T_1 is an indication that both channels are more or less equally effective. In addition, due to the energetic position of the three involved states, a continuous exchange is possible.

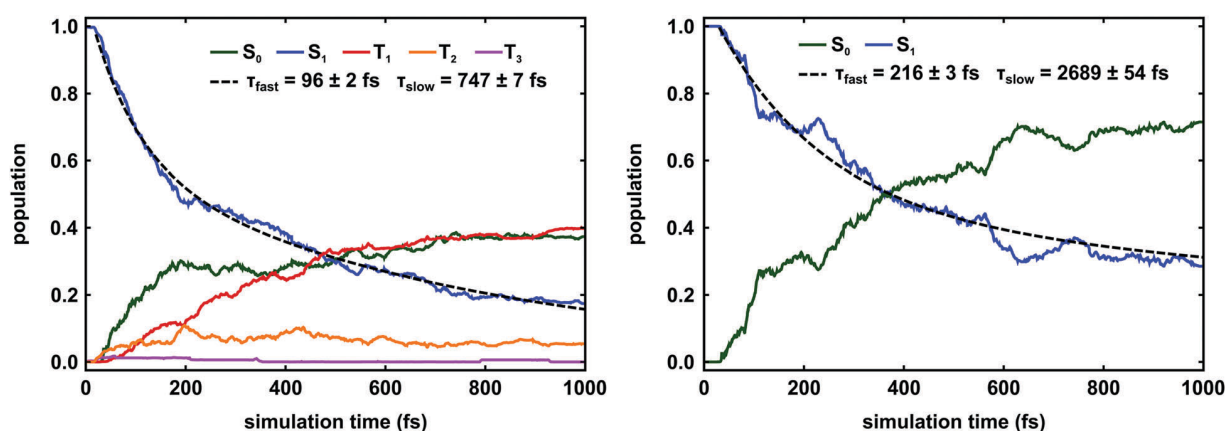


Fig. 6 Time evolution of the average populations of the considered excited states for the CAS(10/9)-ST (left) and the CAS(10/9)-S trajectories (right). The ground and the four lowest excited states are displayed in color. The fitting function used is $a \exp(-t/\tau_{fast}) + b \exp(-t/\tau_{slow})$.

Table 4 The parameters of the biexponential decay of the S_1 state for the CAS(10/9)-ST and CAS(10/9)-S dynamics simulations. The fitting function used is $a \exp(-t/\tau_{\text{fast}}) + b \exp(-t/\tau_{\text{slow}})$. Additionally the experimental time constants are also shown²¹

	(10/9)-ST	(10/9)-S	Exp.
a	0.495 ± 0.004	0.643 ± 0.004	—
b	0.599 ± 0.005	0.443 ± 0.005	—
τ_{fast} (fs)	96 ± 2	216 ± 3	105 ± 10
τ_{slow} (fs)	747 ± 7	2686 ± 54	$> 50\,000$

Also in the singlet only case a continuous exchange, now between the two singlet states, is observed in this region.

In both cases the overall evolution of the S_1 state is more complex than a single exponential decay. Hence, we decided to fit the S_1 decay with a biexponential function of the form $f(t) = a \exp(-t/\tau_{\text{fast}}) + b \exp(-t/\tau_{\text{slow}})$. The time constant τ_{fast} describes the fast component of the depopulation and can be assigned to the sum of the two fast time constants extracted from the fs two-color pump-probe photoelectron spectrum²¹ $\tau_1 = 80 \pm 10$ fs and $\tau_2 = 25 \pm 10$ fs. The second time constant τ_{slow} can be associated with the long experimental time $\tau_3 > 50$ ps,²¹ although due to the limited simulation time quantitative agreement cannot be expected. The fitting parameters for the CAS(10/9)-ST and CAS(10/9)-S dynamics simulations are summarized in Table 4. The time constant τ_{fast} is twice the experimental value when only singlet states are considered. Previous simulations^{26,27} which also considered only singlet states, reported fast relaxation times in the 100 fs regime, which are closer to the experimental value, but relied on a different evaluation strategy. The trajectories were stopped the first time the S_1 and S_0 states were nearly degenerate. In contrast, in our longer simulations forth and back transfer between both singlet states occurs and prolongs the decay time. When the triplet states were included, both decay times decreased as now the two additional decay channels T_1 and T_2 are opened. This is clear evidence that triplet states play a role in the relaxation dynamics. After the initial ultrafast dynamics (100–200 fs) leading to the ring-opening path especially the triplet T_1 becomes important. Now intersystem crossing can compete with fast internal conversion since the SOC values are large and the singlet-triplet energy gaps are small (ESI† Table S4). The potential energy surface for the open-ring structures is rather flat and the four states S_0 , S_1 , T_1 , and T_2 are nearly degenerate (see Fig. 5). This situation leads to long-living open-ring structures in the singlet as well as in the triplet states. The ring closure of these entropically favored structures happens on a long time scale and is maybe mediated *via* collisions with the environment. Our decay time τ_{slow} and the experimental time constant τ_3 , respectively, can be attributed to these long-lived open-ring structures as already proposed by Weinkauff *et al.*²¹ As shown in Fig. 4(d) closed-ring structures occurring in the T_1 state can exist for several 100 fs. These intermediate structures may be the origin of the observed weak phosphorescence.^{17,19,20} However, the reported emission band at 2.88 eV¹⁷ rather lies between the calculated vertical excitation energies of the closed-ring triplet T_1 and T_2 minima (ESI† Table S2). Overall, our

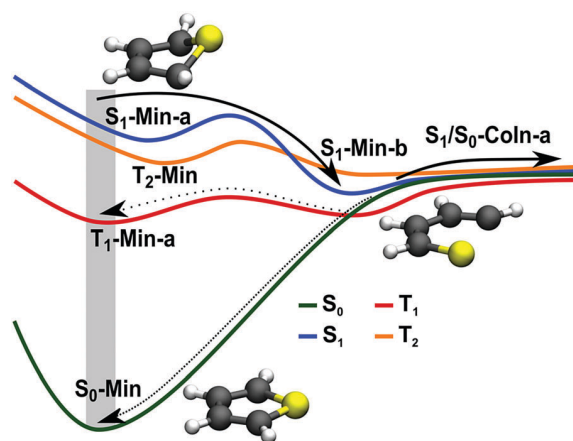


Fig. 7 Schematic overview of our proposed relaxation pathway of photo-excited thiophene. The ground and the three lowest excited states are displayed in color. The gray bar indicates the vertical absorption region.

dynamics simulations complement the picture of the relaxation mechanisms of thiophene after excitation to the first excited singlet state.

4 Conclusions

The relaxation mechanisms of thiophene after photoexcitation have been investigated using *ab initio* dynamics simulations including both singlet and triplet states. The simulations were carried out at the SA(2S+3T)-CASSCF(10/9) electronic structure level using the on-the-fly surface hopping program SHARC.^{28,29,31} The electronic structure method was carefully benchmarked against experimental and theoretical data.

We were able to analyze the relaxation process of thiophene up to 1.6 ps after photoexcitation to the S_1 state. Our proposed relaxation pathway is summarized in Fig. 7.

The observed initial vibrational dynamics in the S_1 state and the subsequent ring opening *via* C–S bond cleavage occur with a fast time constant τ_{fast} of about 100 fs, which is in good agreement with experimental results²¹ and previous simulations.^{25–27} In this fast relaxation period the system reaches the open-ring S_1 minimum (S_1 -Min-b) and intersystem crossing is already partly active. When reaching the region of the ring-opening CoIn in principle two pathways open. One directly returns the system to the closed-ring ground state, but requires nearly momentum inversion. The second, more probable one, preserves the momentum and leads to a flat potential. Along this flat potential the spin-orbit couplings get large and the singlet-triplet energy gaps nearly vanish. The system is trapped in open-ring structures and the dynamics of the system is characterized by the interplay of internal conversion (S_0/S_1) and intersystem crossing (S_0/T_1 and S_1/T_1). The resulting long-lived entropically favored open-ring structures in the singlet as well as in the triplet states agree with the long constant signal observed in the experiment²¹ and provide for the first time an explanation for this signal. In contrast to previous theoretical simulations,^{25–27} our results demonstrate that in thiophene no fast relaxation process leads back to the closed-ring ground state.

Upon irradiation the thiophene polymers can in principle form entropically favored open-ring structures. Even if only a small fraction undergoes ring opening, this indicates a possible drawback for thiophene-based devices. In the monomer case the triplets lead to elongation of the excited state lifetime. Their role is expected to become even more important and diversified in the longer oligothiophenes and polythiophenes.

Conflicts of interest

There are no conflicts of interest to declare.

Acknowledgements

Financial support of this work from Deutsche Forschungsgemeinschaft through the SFB749 and the excellence cluster 'Munich-Centre for Advanced Photonics' (MAP) is gratefully acknowledged.

References

- 1 *Handb. Conduct. Polym.*, ed. T. A. Skotheim and J. R. Reynolds, CRC Press, Boca Raton, FL, 3rd edn, 2007.
- 2 *Handbook of Thiophene-Based Materials: Applications in Organic Electronics and Photonics*, ed. I. F. Perepichka and D. F. Perepichka, John Wiley & Sons Ltd, Chichester, UK, 2007.
- 3 B. L. Rupert, W. J. Mitchell, A. J. Ferguson, M. E. Köse, W. L. Rance, G. Rumbles, D. S. Ginley, S. E. Shaheen and N. Kopidakis, *J. Mater. Chem.*, 2009, **19**, 5311–5324.
- 4 F. Zhang, D. Wu, Y. Xu and X. Feng, *J. Mater. Chem.*, 2011, **21**, 17590–17600.
- 5 P. M. Beaujuge and J. M. J. Fréchet, *J. Am. Chem. Soc.*, 2011, **133**, 20009–20029.
- 6 D. Chi, S. Qu, Z. Wang and J. Wang, *J. Mater. Chem. C*, 2014, **2**, 4383.
- 7 G. Gigli, O. Inganäs, M. Anni, M. De Vittorio, R. Cingolani, G. Barbarella and L. Favaretto, *Appl. Phys. Lett.*, 2001, **78**, 1493–1495.
- 8 M. Mazzeo, D. Pisignano, L. Favaretto, G. Barbarella, R. Cingolani and G. Gigli, *Synth. Met.*, 2003, **139**, 671–673.
- 9 M. Irie, T. Fukaminato, K. Matsuda and S. Kobatake, *Chem. Rev.*, 2014, **114**, 12174–12277.
- 10 G. Barbarella, M. Zambianchi, A. Ventola, E. Fabiano, F. Della Sala, G. Gigli, M. Anni, A. Bolognesi, L. Polito, M. Naldi and M. Capobianco, *Bioconjugate Chem.*, 2006, **17**, 58–67.
- 11 H.-A. Ho, A. Najari and M. Leclerc, *Acc. Chem. Res.*, 2008, **41**, 168–178.
- 12 M. Zambianchi, F. D. Maria, A. Cazzato, G. Gigli, M. Piacenza, F. D. Sala and G. Barbarella, *J. Am. Chem. Soc.*, 2009, **131**, 10892–10900.
- 13 A. Bhaskar, G. Ramakrishna, K. Hagedorn, O. Varnavski, E. Mena-Osteritz, P. Bäuerle and T. Goodson, *J. Phys. Chem. B*, 2007, **111**, 946–954.
- 14 H. Zhou, F. Zhou, S. Tang, P. Wu, Y. Chen, Y. Tu, J. Wu and Y. Tian, *Dyes Pigm.*, 2012, **92**, 633–641.
- 15 H. T. Turan, Y. Eken, M. Marazzi, M. Pastore, V. Aviyente and A. Monari, *J. Phys. Chem. C*, 2016, **120**, 17916–17926.
- 16 M. Huix-Rotllant, H. Tamura and I. Burghardt, *J. Phys. Chem. Lett.*, 2015, **6**, 1702–1708.
- 17 R. S. Becker, J. Seixas de Melo, A. L. Maçanita and F. Elisei, *J. Phys. Chem.*, 1996, **100**, 18683–18695.
- 18 *Modern Molecular Photochemistry*, ed. N. J. Turro, V. Ramamurthy and J. Scaiano, University Science Books, Mill Valley, CA, 1st edn, 2010.
- 19 S. Rentsch, J. P. Yang, W. Paa, E. Birckner, J. Schiedt and R. Weinkauff, *Phys. Chem. Chem. Phys.*, 1999, **1**, 1707–1714.
- 20 J. Yang, W. Paa and S. Rentsch, *Synth. Met.*, 1999, **101**, 624–625.
- 21 R. Weinkauff, L. Lehr, E. W. Schlag, S. Salzmann and C. M. Marian, *Phys. Chem. Chem. Phys.*, 2008, **10**, 393–404.
- 22 S. Salzmann, M. Kleinschmidt, J. Tatchen, R. Weinkauff and C. M. Marian, *Phys. Chem. Chem. Phys.*, 2008, **10**, 380–392.
- 23 M. Stenrup, *Chem. Phys.*, 2012, **397**, 18–25.
- 24 P. Kölle, T. Schnappinger and R. de Vivie-Riedle, *Phys. Chem. Chem. Phys.*, 2016, **18**, 7903–7915.
- 25 G. Cui and W. Fang, *J. Phys. Chem. A*, 2011, **115**, 11544–11550.
- 26 D. Fazzi, M. Barbatti and W. Thiel, *Phys. Chem. Chem. Phys.*, 2015, **17**, 7787–7799.
- 27 A. Prlj, B. F. E. Curchod and C. Corminboeuf, *Phys. Chem. Chem. Phys.*, 2015, **17**, 14719–14730.
- 28 M. Richter, P. Marquetand, J. González-Vázquez, I. Sola and L. González, *J. Chem. Theory Comput.*, 2011, **7**, 1253–1258.
- 29 S. Mai, M. Richter, M. Ruckebauer, M. Oppel, P. Marquetand and L. González, *SHARC: Surface Hopping Including Arbitrary Couplings – Program Package for Non-Adiabatic Dynamics*, sharc-md.org, 2014.
- 30 S. Mai, P. Marquetand, M. Richter, J. González-Vázquez and L. González, *ChemPhysChem*, 2013, **14**, 2920–2931.
- 31 S. Mai, P. Marquetand and L. González, *Int. J. Quantum Chem.*, 2015, **115**, 1215–1231.
- 32 M. Richter, S. Mai, P. Marquetand and L. González, *Phys. Chem. Chem. Phys.*, 2014, **16**, 24423–24436.
- 33 J. Cao, Z.-Z. Xie and X. Yu, *Chem. Phys.*, 2016, **474**, 25–35.
- 34 M. Marazzi, S. Mai, D. Roca-Sanjuán, M. G. Delcey, R. Lindh, L. González and A. Monari, *J. Phys. Chem. Lett.*, 2016, **7**, 622–626.
- 35 S. Mai, M. Pollum, L. Martínez-Fernández, N. Dunn, P. Marquetand, I. Corral, C. E. Crespo-Hernández and L. González, *Nat. Commun.*, 2016, **7**, 13077.
- 36 S. Mai, P. Marquetand and L. González, *J. Phys. Chem. Lett.*, 2016, **7**, 1978–1983.
- 37 B. O. Roos, P. R. Taylor and P. E. Siegbahn, *Chem. Phys.*, 1980, **48**, 157–173.
- 38 P. Celani and H.-J. Werner, *J. Chem. Phys.*, 2000, **112**, 5546–5557.
- 39 H.-J. Werner, P. J. Knowles, G. Knizia, F. R. Manby and M. Schütz, *Wiley Interdiscip. Rev.: Comput. Mol. Sci.*, 2012, **2**, 242–253.

- 40 H.-J. Werner, P. J. Knowles, G. Knizia, F. R. Manby, M. Schütz, P. Celani, T. Korona, R. Lindh, A. Mitrushenkov, G. Rauhut, K. R. Shamasundar, T. B. Adler, R. D. Amos, A. Bernhardsson, A. Berning, D. L. Cooper, M. J. O. Deegan, A. J. Dobbyn, F. Eckert, E. Goll, C. Hampel, A. Hesselmann, G. Hetzer, T. Hrenar, G. Jansen, C. Köppl, Y. Liu, A. W. Lloyd, R. A. Mata, A. J. May, S. J. McNicholas, W. Meyer, M. E. Mura, A. Nicklass, D. P. O'Neill, P. Palmieri, D. Peng, K. Pflüger, R. Pitzer, M. Reiher, T. Shiozaki, H. Stoll, A. J. Stone, R. Tarroni, T. Thorsteinsson and M. Wang, *MOLPRO, version 2012.1, a package of ab initio programs*, 2012, see <http://www.molpro.net/>.
- 41 W. J. Hehre, R. Ditchfield and J. A. Pople, *J. Chem. Phys.*, 1972, **56**, 2257–2261.
- 42 P. Hariharan and J. Pople, *Theor. Chem. Acc.*, 1973, **28**, 213–222.
- 43 M. M. Francl, W. J. Pietro, W. J. Hehre, J. S. Binkley, M. S. Gordon, D. J. DeFrees and J. A. Pople, *J. Chem. Phys.*, 1982, **77**, 3654–3665.
- 44 J. P. Zobel, J. J. Nogueira and L. González, *Chem. Sci.*, 2017, **8**, 1482–1499.
- 45 M. Merchán, L. Serrano-Andrés, M. A. Robb and L. Blancafort, *J. Am. Chem. Soc.*, 2005, **127**, 1820–1825.
- 46 A. Berning, M. Schweizer, H.-J. Werner, P. J. Knowles and P. Palmieri, *Mol. Phys.*, 2000, **98**, 1823–1833.
- 47 G. Granucci and M. Persico, *J. Chem. Phys.*, 2007, **126**, 134114.
- 48 R. Håkansson, B. Nordén and E. W. Thulstrup, *Chem. Phys. Lett.*, 1977, **50**, 306–308.
- 49 H. Haberkern, K. R. Asmis, M. Allan and P. Swiderek, *Phys. Chem. Chem. Phys.*, 2003, **5**, 827–833.

1.4 Molecular Dynamics of Oligothiophenes

Following the analysis of the photoinduced dynamics of the monomer thiophene, this section focuses on the relaxation dynamics of 2,2'-bithiophene and 2,2':5',2''-terthiophene. Again, the SHARC approach is used to simulate the *ab initio* molecular dynamics of both molecules. As mentioned in section 1.1, a meaningful description of the excited states of bithiophene and terthiophene is not possible using the CASSCF method. The excitation energies on CASSCF level as well as the state ordering are wrong and the use of the CASPT2 methodology to include the necessary dynamic electron correlation would be desirable for the dynamics but is, even today, computationally unfeasible. In the end the used electronic structure method is linear-response time-dependent density functional theory (LR-TDDFT) within the Tamm-Dancoff approximation. Since LR-TDDFT is known to suffer from problems recovering CoIns between excited states and the ground state [171, 172] this level of theory has been carefully benchmarked against high level theoretical as well as experimental data, assuring a qualitatively correct and almost quantitative description of all states involved in bithiophene and terthiophene.

Although there are other studies [166, 167] available, modeling the relaxation dynamics in oligothiophenes, the paper "Intersystem Crossing as a Key Component of the Non-Adiabatic Relaxation Dynamics of Bithiophene and Terthiophene" published by the Journal of Chemical Theory and Computation [173] is the first dynamical study of these two molecules covering a picosecond time scale and explicitly including SOC and triplet states. The key statements of the article are:

- As expected from the previous quantum chemical calculations [82] the population transfer to the triplet states via ISC plays a major role in the relaxation process of bithiophene and terthiophene. Compared to the monomer, the initial vibrational dynamics in the S_1 state is significantly longer.
- After the vibrational dynamics in the S_1 state, the relaxation process for the majority of the trajectories is described by ring-opening and inter-ring rotation. Similar to the monomer case this ring-opening channels lead to an extended region of quasidegeneracy between the triplet and singlet potential energy surfaces. The dynamics in this region is characterized by the interplay of IC and ISC between the different states involved. The high flexibility of the open-ring structures even allows *trans-cis* isomerization.
- On longer time scales ring closure can take place either on the S_0 or the T_1 state. The formation of these closed-ring structures in the T_1 state of the dimer and trimer can be an explanation of the experimentally observed phosphorescence [174] for longer thiophene chains.
- The observed relaxation process is modified with increasing length of the thiophene chain. The ISC channel induced by the carbon-sulfur bond cleavage is getting more and more hindered. For the trimer the overall process is qualitatively similar to the dimer, but the initial period of vibrational dynamics in the S_1 is longer and the ring-opening is less pronounced. This trend should continue for the tetramer and even longer oligothiophenes.

Hereafter, the article "Intersystem Crossing as a Key Component of the Non-Adiabatic Relaxation Dynamics of Bithiophene and Terthiophene" published by the Journal of Chemical Theory and Computation is reprinted with permission from *Journal of Chemical Theory and Computation* **14** (2018), 4530-4540. Copyright 2018 American Chemical Society. The Supporting Information for this article is available under <https://doi.org/10.1021/acs.jctc.8b00492>.

Intersystem Crossing as a Key Component of the Nonadiabatic Relaxation Dynamics of Bithiophene and Terthiophene

Thomas Schnappinger,[†] Marco Marazzi,^{‡,¶} Sebastian Mai,[§] Antonio Monari,[¶] Leticia González,^{§,ID} and Regina de Vivie-Riedle^{*,†,¶,ID}

[†]Department of Chemistry, Ludwig-Maximilians-Universität München, D-81377 München, Germany

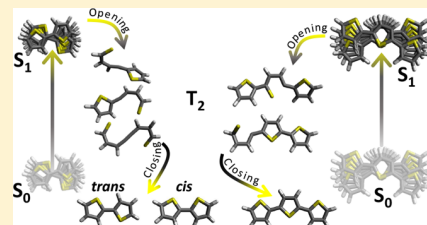
[‡]Departamento de Química, Centro de Investigación en Síntesis Química (CISQ), Universidad de La Rioja, 26006 Logroño, Spain

[¶]Université de Lorraine and CNRS, LPCT UMR 7019, F-54000 Nancy, France

[§]Institute of Theoretical Chemistry, Faculty of Chemistry, University of Vienna, 1090 Vienna, Austria

Supporting Information

ABSTRACT: We present a nonadiabatic dynamics study concerning the subpicosecond relaxation of excited states in dimeric and trimeric thiophene chains. The influence of the triplet states in the overall process is, for the first time, taken into account by explicitly including spin–orbit couplings and hence allowing intersystem crossing phenomena. We observe the fundamental role of the triplet state manifold in driving the full relaxation process. In particular we evidence the effect of both, inter-ring rotation and ring-opening, in the process, as compared to the monomer, where the ring-opening process appears as the dominant one. In addition, the evolution of the open structures allows for *trans* to *cis* isomerization in the dimer and trimer. The overall relaxation process slows down with chain elongation. The complex decay mechanism characterized by the presence of different competing channels, due to the presence of a quasi degenerate manifold, is explained allowing the rationalization of oligothiophenes photophysics.



INTRODUCTION

Due to their remarkable intrinsic properties thiophene derivatives and their oligomers are promising candidates to be employed in organic materials for technological applications.^{1,2} They undergo rapid intersystem crossing (ISC)^{3–5} leading to extremely high triplet quantum yields.⁶ This property deviates strongly from the common behavior found in most organic molecules where the ratio of ISC to internal conversion (IC) and fluorescence is rather small.⁷ Also, it is important for charge separation and transport in conductive organic materials. In combination with their efficient light harvesting and structural versatility they have attracted much attention as building blocks for photoactive polymers and molecular aggregates. Examples are solar cells,^{8–12} light emitting diodes,^{13,14} photoswitches,¹⁵ and biological labels.^{16–18} In addition, polythiophene bridges are also used to enhance two-photon absorption cross sections.^{19–21} As poly(3-hexylthiophene) (P3HT) they form in combination with phenyl-C61-butyric acid methyl ester (PCBM) the famous P3HT/PCBM solar cell.^{11,22}

A deeper understanding of the initial processes after photoexcitation and the subsequent relaxation mechanisms of oligothiophenes is essential to improve the performance of thiophene-based applications. In our previous works^{23,24} we were able to explain the relaxation processes for the monomer thiophene with the aid of static quantum chemical calculations and nonadiabatic molecular dynamics simulations: after photoexcitation, fast ring-opening (approximately 100 fs)

leads to a degeneracy of singlet and triplet states. This degeneracy and the corresponding flat potential energy surface traps the system in entropically favored open-ring structures in the singlet as well as in the triplet states (up to 50 ps).²⁵

The structures of the most stable conformer are shown in Figure 1 for the dimer TP2 (2,2'-bithiophene) and the trimer TP3 (2,2':5',2''-terthiophene). For both TP2 and TP3 experimental results^{6,26–28} indicate that ultrafast ISC takes place from the first excited singlet state. Moreover experimental and theoretical studies suggested two ISC channels for both systems with time scales ranging from 1 ps up to 140 ps.^{26,27} Based on static quantum chemical calculations^{23,29–32} and dynamics simulations (excluding triplet states)^{33,34} the relaxation processes after photoexcitation for TP2 and TP3 are mainly ascribed to the torsional motion around the quite flexible inter-ring bonds,³⁵ whereas ring-opening via CS-bond cleavage should only play a minor role in the initial relaxation processes of both systems. However, for the previous dynamics simulations^{33,34} only short simulation times (300–500 fs) were studied, and important ISC processes were excluded.

This work presents the first nonadiabatic dynamical study of the dimer TP2 and the trimer TP3 at picosecond time scale explicitly including spin–orbit couplings and triplet states. For this study we have used the surface hopping including arbitrary

Received: May 22, 2018

Published: August 9, 2018

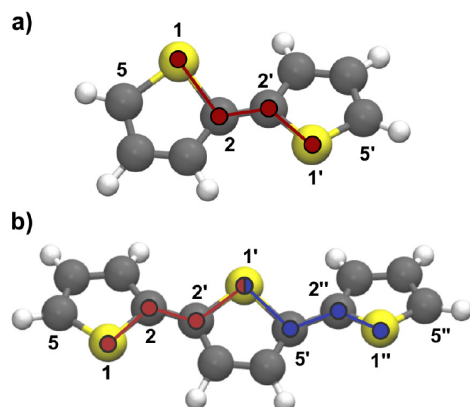


Figure 1. Structure of 2,2'-bithiophene (TP2) in the *trans* conformation a) and of 2,2':5',2''-terthiophene (TP3) in the *eclipsed-anti-anti* (eAA) conformation b). All relevant atoms are labeled, as well as the inter-ring dihedral angles: Φ_{SCCS} (red) in TP2 and Φ_{SCCS}^1 (red) and Φ_{SCCS}^2 (blue) in TP3, respectively. The nomenclature is explained in more detail in the [Supporting Information](#) (SI).

couplings (SHARC) software package,^{36–39} which has already been successfully applied to an important number of molecular systems.^{24,40–44}

COMPUTATIONAL METHODS

Ab Initio Level of Theory. The electronic states of TP2 and TP3 were computed using the density functional theory (DFT) and linear response time dependent DFT (LR-TDDFT). All LR-TDDFT calculations have been performed within the so-called Tamm-Dancoff approximation (TDA).⁴⁵ The DFT and TDA calculations were carried out with the ADF program package (version 2017),^{46,47} using the B3LYP^{48–50} exchange-correlation functional with the D3 dispersion correction by Grimme and co-workers.⁵¹ Minima (Min), transition states (TS), conical intersections (CoIn), and singlet–triplet minimum-energy crossings (STC) were opti-

mized with the ORCA code (version 3.0.3)⁵² as an external optimizer. All optimized geometries are given in the [Supporting Information](#) (SI). The DFT and TDA calculations were carried out with the double- ζ polarized basis set (DZP)⁵³ and a Becke^{54,55} and Zlmfit⁵⁶ grid of good quality. For benchmarking purposes, some calculations were performed with the triple- ζ polarized basis set (TZP)⁵³ in combination with the same grid quality. In all optimization calculations symmetry was not used. Scalar relativistic effects were included with the zeroth-order regular approximation (ZORA),^{57–61} and the spin–orbit couplings (SOC) were calculated using a perturbative method, as developed and implemented by Wang and Ziegler.⁶²

Dynamics. The molecular dynamics of TP2 and TP3 were simulated using the SHARC *ab initio* dynamics package version 2.0.^{36–39} The necessary energies, gradients, nonadiabatic couplings, and spin–orbit couplings were calculated on-the-fly at the TDA/B3LYP level of theory.

The initial conditions for the dynamics simulations were generated based on a Wigner distribution computed from harmonic vibrational frequencies in the optimized ground state equilibrium geometry. The underlying frequency calculations were performed at B3LYP/DZP level of theory. For TP2 only the *trans* conformer was studied, since it has been shown to be the ground state global minimum.^{23,63} Time-resolved spectroscopic studies on the dimer^{26,27} used an excitation energy of 4.02 eV to reach the rising edge of the first absorption peak. Corresponding to these experiments we have centered the spectral window (3.0–4.0 eV) at the rising edge of the first absorption peak (see the simulated absorption spectrum in the [SI](#)). 84 starting geometries and velocities were stochastically chosen.

For TP3, among the total number of ten ground state minima,^{31,64–66} two nearly isoenergetic minima exist.²³ The *eclipsed-anti-anti* (eAA) conformer is the global minimum, and the *gauche-anti-anti* (gAA) conformer is only 0.02 eV (ΔG)²³ above. Since these conformers can easily interconvert, as will be shown below, we restrict our initial condition generation to

Table 1. Calculated Vertical Singlet and Triplet Excitation Energies (eV) for the Low-Lying Excited States at the Optimized Ground-State Minimum of TP2 and TP3 Compared to Experimental and Theoretical Data^a

state	char.	B3LYP/DZP	B3LYP/TZP	CASSCF ^a	CASPT2 ^b	exp.
2,2'-bithiophene (TP2)						
S ₁	$\pi_1 \rightarrow \pi_1^*$	4.50 (0.54)	4.24 (0.48)	6.44 (0.45)	4.51 (0.45)	4.29 ^c
S ₂	$\pi_1 \rightarrow \pi_2^*$	5.07 (0.01)	4.94 (0.00)	5.87 (0.01)	4.85 (0.01)	5.08 ^c
T ₁	$\pi_1 \rightarrow \pi_1^*$	3.01	2.76	2.94	2.86	2.32 ^d
T ₂	$\pi_1 \rightarrow \pi_2^*$	4.00	3.95	3.94	3.82	
T ₃	$\pi_2 \rightarrow \pi_1^*$	4.28	4.11	5.08	4.41	
T ₄	$\pi_3 \rightarrow \pi_1^*$	4.32	4.22	4.91	4.48	
state	char.	B3LYP/DZP	B3LYP/TZP	CASSCF ^e	CASPT2 ^f	exp.
2,2':5',2''-terthiophene (TP3)						
S ₁	$\pi_1 \rightarrow \pi_1^*$	3.81 (0.52)	3.46 (0.49)	5.84 (0.55)	4.03 (0.55)	3.50 ^g
S ₂	$\pi_2 \rightarrow \pi_1^*$	4.37 (0.00)	4.10 (0.00)	4.77 (0.00)	4.42 (0.00)	
T ₁	$\pi_1 \rightarrow \pi_1^*$	2.59	2.21	2.51	2.40	1.90 ^d
T ₂	$\pi_1 \rightarrow \pi_2^*$	3.40	3.15	3.34	3.19	2.99 ^d
T ₃	$\pi_1 \rightarrow \pi_3^*$	4.00	3.81	4.05	3.85	
T ₄	$\pi_3 \rightarrow \pi_1^*$	4.08	4.00	4.81	4.30	

^aCASSCF(12/11)/6-31G* underlying results from ref 23. ^bCASPT2(12/11)/6-31G*. ^cGas-phase absorption spectrum at room temperature.⁷¹

^dPhotodetachment photoelectron spectrum in the gas phase.³² ^eCASSCF(18/15)/6-31G*²³ underlying results from ref 23. ^fCASPT2(18/15)/6-31G*. ^gAbsorption spectrum in solution at room temperature.^{6,72,73} ^hOscillator strength values are given in parentheses. Energies were calculated using B3LYP/DZP and B3LYP/TZP.

the ϵ AA conformer. For the dynamics simulations of TP3, 36 starting geometries and velocities in the energy window 3.0–4.0 eV were stochastically chosen from a Wigner distribution (see the simulated absorption spectrum in the SI). For both systems, in accord with the chosen excitation window, all trajectories started in the S_1 state.

The SHARC *ab initio* surface-hopping algorithm uses a fully diagonal, spin-mixed electronic basis, resulting from the diagonalization of the Hamiltonian containing spin–orbit couplings.^{37,67} The integration of the nuclear motion is done with the Velocity-Verlet algorithm with a maximal time of 1 ps using a time step of 0.5 fs. In each time step, gradients were computed for all states which are closer than 0.2 eV to the active state; this is required in order to construct the gradient of the spin-mixed active state. The coefficients of the electronic wave function are propagated on interpolated intermediates with a time step of 0.02 fs applying a local diabaticization technique⁶⁸ in combination with the WFOverlaps code⁶⁹ to compute the wave function overlaps. Decoherence correction was taken into account using the energy-based method of Granucci and Persico with the parameter $\alpha = 0.1$ au.⁷⁰

For the statistical analysis of the results stemming from the nonadiabatic dynamics, the number of aborted trajectories has to be considered. Some trajectories experienced convergence problems and therefore terminated before reaching 1 ps. Beside the convergence, also problems arising from the DFT/TDA methodology (e.g., the multiconfigurational character of the ground state) have to be taken into account since they may lead to unphysical behavior of the energy and the gradients. In order to find a good compromise between the simulation time considered and the number of trajectories inspected, we restrict our analysis to trajectories with at least 400 fs of simulation time, a maximum change in the total energy of 0.2 eV, a maximum change in the total energy per step of 0.2 eV, and a maximal interstate hop energy of 1.0 eV.

RESULTS AND DISCUSSION

Validation of the Level of Theory. First, it was checked whether the static B3LYP/DZP and B3LYP/TZP results for both systems are in qualitative agreement with previous CASPT2 results²³ and the experimental data.^{6,32,71–73} Therefore, the excitation energies of the optimized ground-state minima (*trans* for TP2 and ϵ AA for TP3) were benchmarked (see Table 1).

The calculated S_1 and S_2 excitation energies for TP2 are in between the CASPT2 and the experimental results. For the first four triplet states the B3LYP energies are in good agreement with the CASPT2 values. The energetic order and the electronic character of all tested states are the same as in previous studies.^{23,29,30,32} Moreover, the B3LYP functional reproduces the CASPT2 excitation energies for the first six states of TP3 quite well. The character of the states is also the same as in previous studies,^{23,31,32} except for a slight difference in the state ordering. Using TDA the third triplet state T_3 lies above the S_1 independently of the chosen basis set. For both systems the TZP basis set gives better agreement with experiment than the smaller basis set DZP. In order to save time for the dynamics simulations we decided to use the small DZP basis set, as it is sufficient to well describe the low-lying excited states of TP2 and TP3 in the Franck–Condon region. In contrast to the CASPT2 methodology the excitation energies at the CASSCF level as well as the state ordering is

wrong for TP2 and TP3. Hence, a meaningful description of TP2 and TP3 is not possible using CASSCF.

Based on static quantum chemical calculations^{23,29–32} two possible deactivation pathways for TP2 and also TP3 were discussed: the first pathway is described by the rotation around the inter-ring bonds. This rotation leads to a near-degeneracy region of triplet states and the S_1 state. In combination with the moderate spin–orbit couplings this degeneracy should allow ISC; subsequent internal conversion steps lead the system in the T_1 state. The relaxation back to the ground state can take place through either phosphorescence or nonradiative processes like cleavage of a C–S bond. The second pathway is similar to the relaxation mechanism in the thiophene monomer:²⁴ the C–S bond cleavage leads to open-ring structures where the S_0 , T_1 , S_1 , and T_2 states are nearly degenerate and the SOC increases significantly. Via these open-ring structures, closed-ring conformers can be formed in the ground state. In principle for TP2 as well as for TP3 many open-ring structures are possible. As shown in our previous work,²³ structures with only one broken C–S bond are energetically favored. In TP2 the four C–S bonds can be distinguished into two groups: the *inner* bonds (1,2 and 1',2', see Figure 1) and the *outer* bonds (1,5 and 1',5'). The cleavage of the *inner* bonds is energetically favored. The C–S bonds of TP3 can be distinguished analogously in three groups: for both terminal rings the C–S bonds can be divided into *inner* and *outer* ones. The C–S bonds of the central thiophene ring form the third group, the *central* bonds. The cleavage of one of the *inner* or *central* bonds leads again, compared to *outer* bonds, to more stable structures. In the following the discussion is restricted to open-ring structures with a single broken *inner* or *central* C–S bond.

All critical points of TP2 and TP3 along both relaxation pathways were optimized using the small basis set DZP. The excitation energies of the six low-lying excited states were determined and compared with previous CASPT2 calculations.²³ These results are collected in the SI. For all closed-ring structures the B3LYP/DZP results are in sufficient agreement with the CASPT2 values with slightly higher deviations for open-ring structures. We are aware of the inherent problems of the TD-DFT methodology to describe the multiconfigurational character in the ground state and conical intersection between S_1/S_0 . However, in previous studies on oligothiophenes,^{23,32–34} the relaxation pathway can be split into two parts. In the first part describing the path from the Franck–Condon region to the open-ring structures, the triplet states lie energetically close to the S_1 state, and the spin–orbit coupling is large. We are very confident that this first part of the relaxation is fully described by TD-DFT. The second part is the dynamic of the open-ring structures and the relaxation back to the ground-state. Here the conical intersection between S_1/S_0 is very important but not described well using TD-DFT. This may be biasing the simulation toward the triplet state population. On the other hand, the relaxation into triplet states is also present in thiophene where we could perform the dynamics simulation at the CASSCF level.²⁴ Nevertheless, the overall shape of the potential energy surfaces along the pathways is qualitatively well reproduced using the B3LYP/DZP methodology. Therefore, we are convinced that the chosen methodology is adequate to describe the dynamics of TP2 and TP3.

Excited State Dynamics of 2,2'-Bithiophene (TP2). Using our selection criteria, 53 trajectories out of 84 trajectories were taken into account to analyze the excited

state dynamics of TP2. These 53 trajectories were first analyzed according to the final populated state and the final molecular geometry. A geometry is characterized as open-ring structure if one of the C–S bonds is larger than 2.4 Å. The results are summarized in Table 2.

Table 2. Distribution (%) of the TP2 B3LYP/DZP Trajectories According to the Final Populated State as Well as the Final Geometry^a

final state	final geometry			Σ
	open	cis	trans	
S_0	16	12	6	34
S_1	4	0	0	4
T_1	24	4	10	38
T_2	24	0	0	24
Σ	68	16	16	100

^aAll percentages are given with respect to the total number of analyzed trajectories. The shown numbers are statistically not fully converged. The maximum statistical error is 13%.⁷⁴

After excitation to the S_1 state, all analyzed trajectories show nonadiabatic relaxation within the first picosecond. The final distribution between the singlet and the triplet states is nearly 2:3. Within the triplet manifold the relative distribution $T_1:T_2$ is about 3:2; within the singlet moiety $S_0:S_1$ is 8.5:1. Most final geometries are open-ring structures (68%), where one *inner* bond is broken. Closed-ring conformations (*trans* or *cis*) are only found for the S_0 and the T_1 state. Note that in the monomer almost no triplet closed-ring structures were found.²⁴ Although all trajectories have been propagated from an initial *trans* conformation, a one-to-one mixture of *trans* and *cis* conformers is observed after relaxation.

The overall change in population of the ground state and the individual excited states for the first picosecond is shown in Figure 2 for the TP2 dynamics.

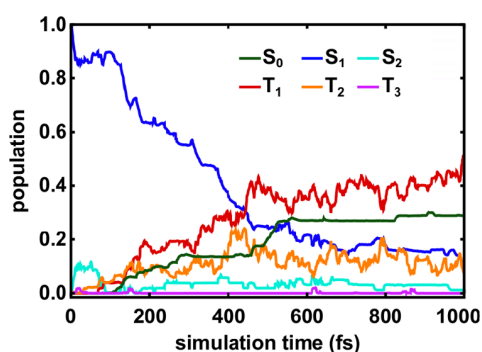


Figure 2. Time evolution of the average populations along the TP2 trajectories. The ground and the five lowest excited states are displayed.

The populations dynamics of TP2 is more complex than for the thiophene monomer²⁴ and far from exponential behavior. It is characterized by a fast decay of the S_1 state population. In the first 3 to 5 fs there is an ultrafast exchange of some population between S_1 and S_2 states, probably attributable to the initial conditions. Nevertheless, during the whole process the S_2 state plays no role. Indeed, after this initial exchange, the S_1 state population stays constant for about 100 fs. Thereafter the first two triplet states, T_2 and T_1 , start to participate via

ISC. The S_1 state is mainly depopulated via the T_2 . Subsequently the T_1 state is populated via IC. This cascade $S_1 \rightarrow T_2 \rightarrow T_1$ finally enables the population transfer back in the ground state S_0 . The T_3 state is nearly not populated. The ratio between S_0 , S_1 , T_1 , and T_2 after 1 ps simulation time is approximately 30:10:50:10. Compared to the monomer dynamics, the relaxation from S_1 state is significantly slower in the first 200 fs.

Next we analyze which relaxation pathway leads to the final structures. The two most relevant internal coordinates, previously introduced, are the rotation around the inter-ring bond (i.e., the dihedral angle Φ_{SCCS}) and the C–S bond cleavage described as the averaged C–S distance r_{CS} of both *inner* C–S bonds. In Figure 3 the time evolution (color coded) of the trajectories is shown for the first 200 fs.

Starting from the Wigner distribution (dark blue dots) the dihedral angle Φ_{SCCS} varies between 130° and 160° (S_0 -minimum at 143.0°), and an averaged *inner* C–S distance r_{CS} is found between 1.7 and 1.9 Å (S_0 -minimum value 1.75 Å). Within the first 100 fs a small part of the trajectories leads to planarization, while the majority undergoes ring-opening reaching an average bond distance of up to 2.6 Å. Thereafter further bond elongation is accompanied by significant planarization reaching 180°. The dynamics simulation shows that both reaction coordinates (ring-opening and planarization) are active on the same time scale. The energetic barrier for the ring-opening in TP2 is estimated to be 0.2 eV (B3LYP/DZP). The maximal barrier at the CCSD/6-31G* level of theory was found to be 0.4 eV.²³ Both values are higher than for the barrier in the monomer²⁴ found at 0.1 eV. Our dynamics simulations confirm that due to the excess kinetic energy deposited in the photon absorption process this barrier can still be overcome, but it explains the slower decay of the S_1 population (see Figure 2). The complete temporal evolution up to 1 ps for Φ_{SCCS} and r_{CS} can be found in the SI.

The geometrical deformations observed in the first 200 fs lead to many intersystem crossing events from the S_1 state into the triplet states (see Figure 4). Mostly transitions into the T_2 and T_3 state are observed, which is in agreement with previous results.^{23,34} In principal these hopping events can be distinguished geometrically and temporally. Hops between the S_1 state and the T_3 state only occur for closed-ring and nonplanar geometries, hence very early. They are mainly forward and backward hops with no net populations exchange. This explains the plateau in the S_1 state population observed in Figure 2 in the range from 3 up to 100 fs. Hops to the T_2 state are observed around two different r_{CS} values. For the slightly elongated C–S bonds (2.0–2.2 Å) the SOC values increase and the two states T_2 and S_1 cross. This initiates the decay of the S_1 state after 100 fs in Figure 2. Further elongation of r_{CS} (up to 2.5–2.6 Å) leads to a further increase in the SOC and to a near degeneracy of the T_2 and S_1 state, giving rise to a second enhancement of hops shown in Figure 4. A complete analysis of all hopping events for the whole simulation time can be found in the SI. The open-ring dynamics leads, as in the case of the thiophene monomer,²⁴ to a dynamical equilibrium between singlet and triplet states. All states involved, S_0 , S_1 , T_1 , and T_2 , come close in energy accompanied by rather large effective spin–orbit couplings (SI). Although the degeneracy is not as complete among all states as in case of the monomer, many back and forward hops between S_1 , T_1 , and T_2 establish the dynamical equilibrium. Due to the chosen methodology, i.e. TDDFT, hops back into the ground state are only possible

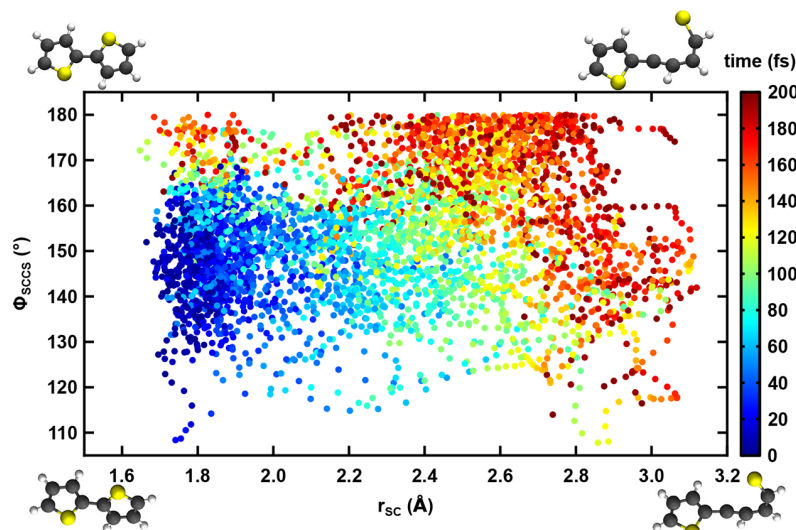


Figure 3. Analysis of the nonadiabatic dynamics of TP2 within the first 200 fs. Time evolution (see color code) of the trajectories in the subspace spanned by the averaged 'inner' C–S distance r_{CS} and the dihedral angle Φ_{SCCS} .

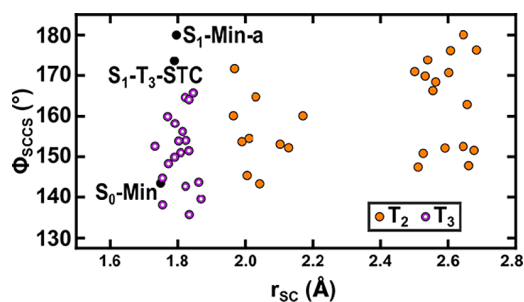


Figure 4. Locations of the geometries where the first surface hops from the S_1 state to triplet states (T_2 and T_3) occurred depending on r_{CS} and Φ_{SCCS} in TP2 within the first 200 fs. The hopping geometries are displayed in different colors according to the target state of the hopping event. Additionally, relevant B3LYP/DZP optimized geometries are represented in black, including minima (Min) and singlet-to-triplet crossings (STC).

via the T_1 and T_2 state because of a poor description of the open-ring S_1/S_0 conical intersection. This might explain why the final population in S_0 is lower than in T_1 , while for the monomer, calculated at the CASSCF level, both states were equally populated.²⁴

The energy profiles of four illustrative trajectories are shown in Figure 5. The individual states are color coded, and the populated state is marked with black diamonds.

All four trajectories undergo ring-opening with the cleavage of one of the *inner* C–S bonds after the first 100 fs. In Figure 5a),b) we focus on the first 400 fs. In the open-ring structure, the system switches mostly between the quasi-degenerate S_1 and the T_2 state. In contrast to the monomer case, the ground state S_0 and the first triplet state T_1 show much less participation to the process. Two different reaction pathways leading to closed-ring structures are shown in Figure 5c),d). In example c) one C–S bond is broken after approximately 90 fs. The T_1 state is reached via S_1 and T_2 20 fs later. Although the T_1 state and the ground state are nearly degenerate, no hops occur for the next 100 fs, and the ring-closure takes place in the triplet state forming a nearly planar *trans* conformer. In contrast, Figure 5d) reports an example of relaxation to a

closed ring *trans* conformer in the S_0 state, reached from the S_1 state via the T_2 and the T_1 state. Note that although we presented trajectories leading to *trans* products, the open ring structures can rotate almost freely around the inter-ring bond and hence can easily undergo isomerization into the *cis* conformer. This is reflected in the ratio between *trans* and *cis* products shown in Table 2. The amount of closed-ring conformers found for the T_1 state explains the experimentally observed phosphorescence⁷⁵ which might occur from these stable geometries.

Excited State Dynamics of 2,2':5',2''-Terthiophene (TP3). For TP3, 34 out of 36 trajectories were taken into account for discussion of the excited state dynamics. These 34 trajectories were first analyzed according to the final populated state and the final molecular geometry. Just as for the TP2 analysis a geometry is characterized as open-ring structure if one of the C–S bonds is larger than 2.4 Å. The results are summarized in Table 3.

Overall 62% of the trajectories terminate in the singlet manifold from which only 8.8% reach the S_0 state. The triplet states are significantly less populated compared to the dimer. The relative distribution of the T_1 and the T_2 state is 8:5, while the T_3 and S_2 states play no role. This is a first hint for an enhanced lifetime of the S_1 state. For all excited states the open-ring structures are again dominant (53%). No significant preference toward the cleavage of the *inner* or the *central* C–S bonds is observed. The sum of the closed-ring structures in the T_1 and S_0 states amounts to 35%, with an excess of the *eAA* conformer. In contrast to the TP2 dynamics, nearly 29% of the analyzed trajectories stay near the FC-region in the S_1 state, thereof 12% show only vibrational dynamics.

The time evolution of the populations of the ground state and the individual excited states is shown in Figure 6 for the TP3.

The relaxation process of the S_1 state is significantly slower than in TP2 and again nonexponential. In the first 400 fs the S_1 population stays nearly constant. The time needed for geometrical rearrangement is thus four times longer than for the dimer. After this period, the first two triplet states (T_2 and T_1) can participate in the dynamics and start the nonadiabatic decays. A cascade $S_1 \rightarrow T_2 \rightarrow T_1$ enables the population

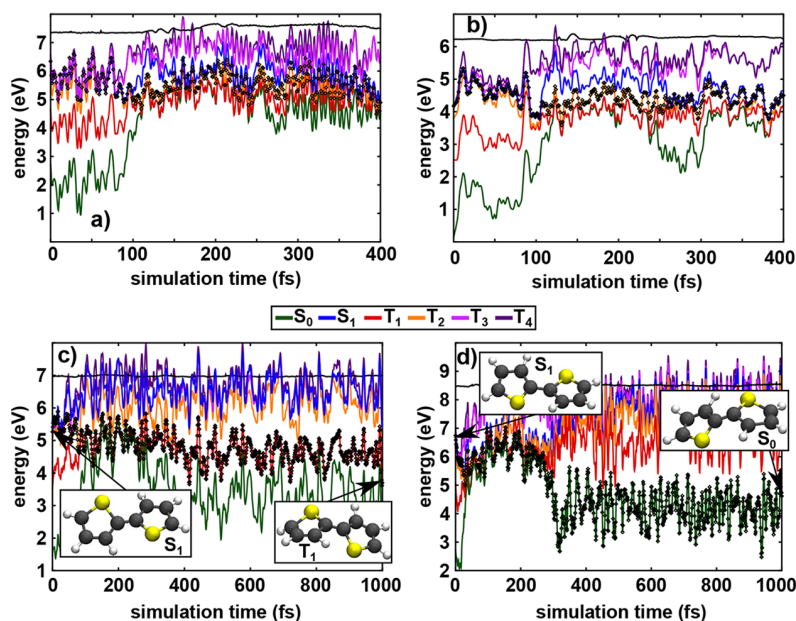


Figure 5. Energy profiles of four representative TP2 trajectories following the ring-opening mechanism. All trajectories were initiated on the S_1 potential energy surface. The time evolution of the ground and the six lowest excited states is displayed in color, whereas the running state is indicated with black diamonds. The energies are plotted relative to the ground state minimum. Initial and final structures are given for the last two trajectories.

Table 3. Distribution (Absolute Numbers) of the TP3 B3LYP/DZP Trajectories According to the Final Populated State as Well as the Final Geometry^c

final state	final geometry								Σ
	inner	central	vib only ^a	e-AA ^b	e-SS ^b	g-AA ^b	g-SA ^b	g-SS ^b	
S_0	0	0	0	0	1	1	1	0	3
S_1	5	4	4	2	0	1	0	0	16
S_2	1	1	0	0	0	0	0	0	2
T_1	2	1	0	4	0	0	1	1	9
T_2	1	3	0	0	0	0	0	0	4
Σ	9	9	4	6	1	2	2	1	34

^aOnly vibrational dynamics observed. ^bThe nomenclature is explained in the SI. ^cThe shown numbers are statistically not fully converged. The maximum statistical error is 17%.⁷⁴

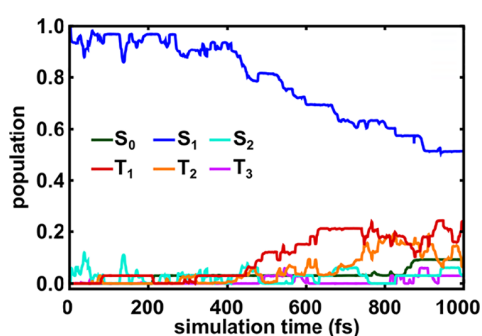


Figure 6. Time evolution of the average populations of the participating excited states for the TP3 trajectories. The ground and the five lowest excited states are displayed.

transfer back to the ground state S_0 , comparable to the relaxation dynamics in TP2. Again S_2 and T_3 do not participate. The ratio between S_0 , S_1 , T_1 , and T_2 after 1 ps simulation time is approximately 15:50:25:10.

The geometrical relaxation process is analyzed with the help of four collective variables associated with ring-opening and

the rotation around the inter-ring bonds. The inter-ring rotation is characterized by the two dihedral angles, Φ_{SCCS}^1 and Φ_{SCCS}^2 (see Figure 1b)). The ring-opening is characterized by the averaged CS distance of both *inner* bonds (r_{CS}^{inner}) and of both *central* bonds ($r_{CS}^{central}$). The time evolution of these variables is shown in Figure 7.

The bond coordinates show a similar behavior as well as the dihedral angles, with no clear preferences. In the first 200 fs only a small part of the trajectories undergoes ring-opening and therefore the planarization of TP3 may be considered as the dominant geometrical deformation. After this first period more trajectories show open-ring structures, still accompanied by the out-of-plane vibrational motion around the complete planar structure. Overall, the bond elongation as well as the inter-ring rotation is less pronounced in the trimer. The *inner* C–S bonds open slightly further than the *central* ones, finally leading to longer time scales for *inner* bonds elongation.

The position of the first hopping events from the S_1 state into the triplet manifold was also analyzed. In Figure 8 the position of these hopping events is shown depending on the two averaged C–S bonds r_{CS} and both dihedral angles Φ_{SCCS} (see Figure 1b)).

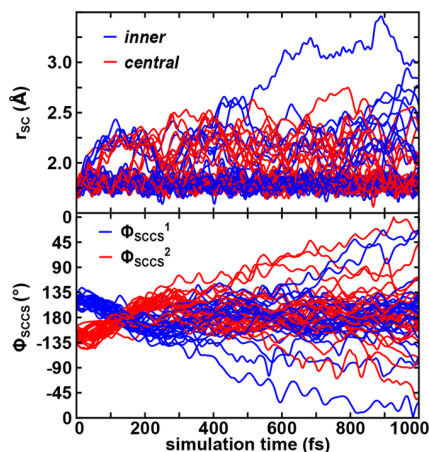


Figure 7. Temporal evolution of the two averaged C–S bonds r_{cs} and both dihedral angles Φ_{SCCS} of TP3, up to 1 ps.

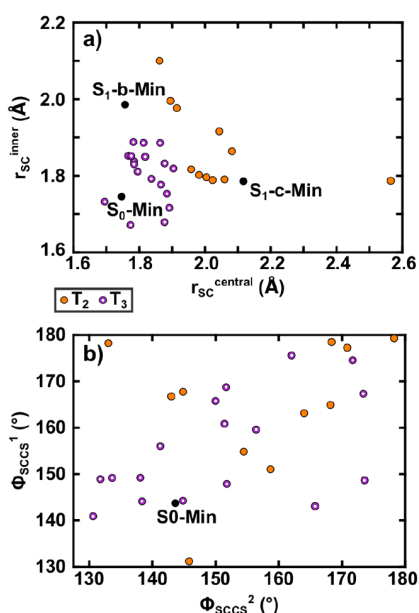


Figure 8. Locations of the TP3 geometries where the first surface hops from the S_1 state to triplet states (T_2 and T_3) occurred depending on both r_{cs} distances (a) and both Φ_{SCCS} dihedral angles (b) for definition see Figure 1b). The hopping geometries are displayed in different colors according to the target state of the hopping event. Additionally, relevant B3LYP/DZP optimized geometries are represented in black.

Only intersystem crossing events from the S_1 state into the T_2 and T_3 state are observed. Near the Franck–Condon region, for averaged r_{cs} values between 1.7 and 1.9 Å, hops to the T_3 state occur. As in the dimer these hops are only intermediate and thus ineffective. Effective hops to the T_2 state are again observed for slightly elongated C–S bonds (1.9–2.2 Å). More hops into the T_2 are observed for *central* bonds longer than 1.9 Å than for *inner* bonds. For both Φ_{SCCS} dihedral angles (Figure 8b) no clear trend is observed. T_2 -hops occur for dihedral angles in the range 130°–180°. Thus, also for TP3 bond elongation is the key process. It enables the intersystem crossing into the triplet states as well as the internal conversion back to the ground state. The energy profiles of four illustrative trajectories are shown in Figure 9.

The trajectory of Figure 9a) only shows vibrational dynamics in the S_1 state and presents no nonadiabatic phenomenon. The other trajectories (Figure 9b), c), and d)) are characterized by intermediate ring-opening events. They can be distinguished either geometrically or regarding their time evolution. In b) and c) one of the *central* C–S bonds is elongated/broken after 600 fs. The resulting open-ring structures survive 10 to 100 fs and form closed-ring structures, respectively, in the T_1 state (b) or the ground state S_0 (c). In the last example d) one of the two *inner* C–S bonds is broken after approximately 100 fs. The resulting open-ring structure persists for about 700 fs allowing hops between the S_1 , T_1 , and T_2 state. This is in good agreement with the observed slight preference for *inner* bond elongation (compare with Figure 7 top). The excited state lifetime is globally longer compared to dimer and monomer. This is due to (i) a decrease in spin–orbit couplings as the average C–S bond elongation is smaller and (ii) an increase in the barrier toward bond elongation. Like the dimer, closed-ring structures are formed in the T_1 state opening the path to phosphorescence.

CONCLUSIONS

The relaxation mechanisms of gas-phase irradiated oligothiophene have been unraveled and critically characterized by means of nonadiabatic surface-hopping dynamics. The TDDFT level of theory has been employed to calculate the energies and gradients as well as nonadiabatic and spin–orbit couplings on-the-fly along the trajectories. This level of theory has been carefully benchmarked against high level theoretical as well as experimental data, assuring a qualitatively correct and almost quantitative description of all states involved. In our interpretation we took into account possible limitations of the method in describing the IC back to the ground state. In partial contrast with previous studies performed without the explicit inclusion of the spin–orbit coupling elements, the simulation presents a quite complex scenario in which different competitive pathways are active. Moreover, the influence of the triplet state manifold appears crucial in driving the process. Indeed, in the case of TP2 more than 60% of the trajectories end in the triplet manifold after 1 ps.

The strong influence of the triplet states was also observed for the case of the thiophene monomer,²⁴ where it was connected to the carbon sulfur bond cleavage, leading to ring-opening and to a region of singlet triplet quasi-degeneracy and increased spin–orbit couplings. As schematically reported in Figure 10, a similar picture holds also in the case of oligothiophene, even though the complexity is strongly increased.

After excitation to the S_1 state, the relaxation process for the majority of the trajectories is described by ring-opening and inter-ring rotation, leading to an extended region of quasi-degeneracy between the triplet and singlet potential energy surfaces. Hence, in this region a complex equilibrium between the different states involved is established, characterized by frequent back and forward nonadiabatic events. Eventually the system can further evolve to the ring closure that can take place either on the S_0 or the T_1 state. In addition, the ring-opening and subsequent closure are accompanied by a high flexibility of the intermediate molecular systems, and indeed *trans-cis* isomerization is observed. The conclusions for the TP3 are qualitatively similar, even if in this case the ring-opening is less pronounced and one should speak of a carbon–sulfur bond elongation rather than of bond cleavage. With increasing chain

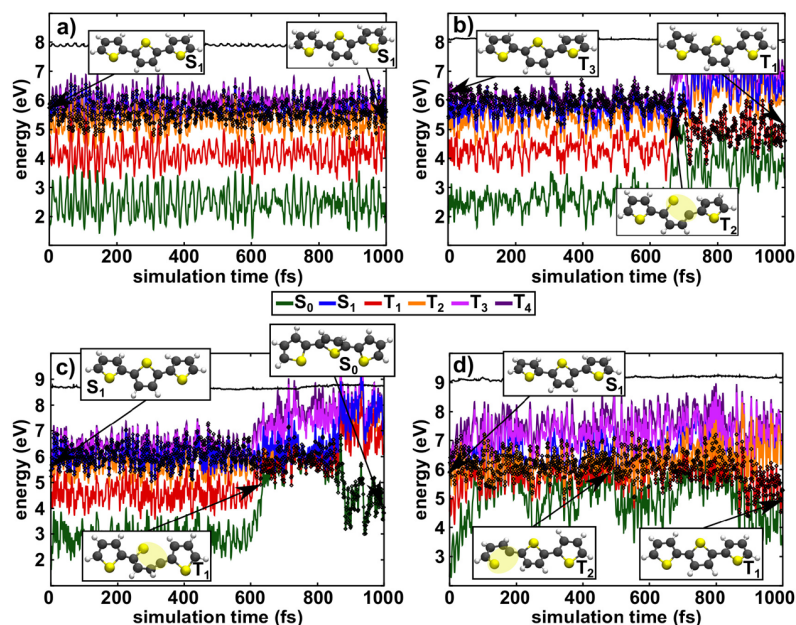


Figure 9. Energy profiles of four representative TP3 trajectories following the ring-opening mechanism. All trajectories were initiated on the S_1 potential energy surface. The time evolution of the ground and the six lowest excited states is displayed in color, whereas the running state is indicated with black diamonds. The energies are plotted relative to the ground state minimum. Example geometries are given for each trajectory, with the broken carbon sulfur bond highlighted in yellow.

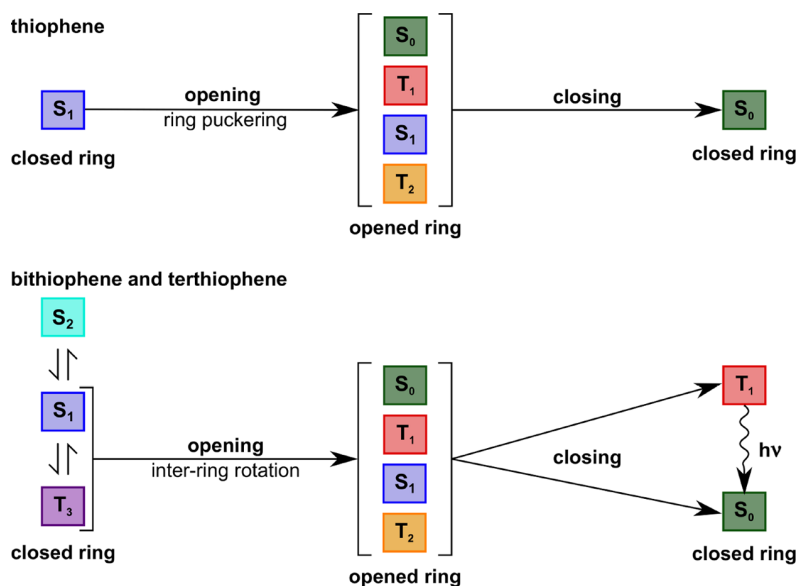


Figure 10. Schematic representation of the pathways active in the excited state relaxation of thiophene monomer compared with bithiophene (TP2) and terthiophene (TP3), as rationalized from nonadiabatic dynamics.

length the excitation is delocalized over a larger number of bonds, so each individual bond is weakened less.

Our results clearly identify the bond cleavage (or elongation) as the key coordinate driving the relaxation, also via the population of the triplet manifold. This process involves rather large rearrangements of the molecular geometries all along the 1 ps trajectory, even leading to a certain amount of *trans-cis* isomerization. The formation of closed-ring structures in the T_1 state of the dimer and trimer is a prominent difference from the thiophene monomer, and we believe it is the reason why phosphorescence is experimentally observable for longer thiophene chains. The efficiency of the ISC is

reduced for longer thiophene chains as the driving coordinate, the carbon sulfur bond cleavage, is hindered. Hence, we have provided a consistent description of the photophysics of oligomeric thiophene, taking into account the coupling between intersystem crossing and the geometrical reorganization. However, it has to be underlined that our simulations have been performed in gas phase. The influence of a viscous environment, such as polymeric matrices, can be quite important since the geometric reorganization may be hampered. In the near future we plan to tackle this problem by performing QM/MM nonadiabatic dynamics in thiophene oligomers embedded in rigid polymeric matrices.

■ ASSOCIATED CONTENT

■ Supporting Information

The Supporting Information is available free of charge on the ACS Publications website at DOI: 10.1021/acs.jctc.8b00492.

Validation of the static quantum chemical calculations and comparison with the reference values, time series of some relevant geometrical coordinates up to the ps time scale and distribution of the hops between the states, coordinates of the optimized geometries of the relevant critical points, evolution of the average population of the states and of the hops between states obtained from the full set of trajectories (PDF)

■ AUTHOR INFORMATION

Corresponding Author

*E-mail: Regina.de_Vivie@cup.uni-muenchen.de.

ORCID

Leticia González: 0000-0001-5112-794X

Regina de Vivie-Riedle: 0000-0002-7877-5979

Funding

Financial support of this work from Deutsche Forschungsgemeinschaft through the SFB749 and the excellence cluster 'Munich-Centre for Advanced Photonics' (MAP) is gratefully acknowledged. The computational results presented have been partially achieved using the Vienna Scientific Cluster (VSC). M.M. is grateful to the Universidad de La Rioja (UR) for a postdoctoral grant. A.M. also acknowledges French CNRS and Université de Lorraine for support. S.M. and L.G. acknowledge funding from the Austrian Science Fund (FWF) within project I2883 (DeNeTheor) and the University of Vienna.

Notes

The authors declare no competing financial interest.

■ REFERENCES

- (1) *Handbook of Conducting Polymers*, 3rd ed.; Skotheim, T. A., Reynolds, J. R., Eds.; CRC Press: Boca Raton, FL, 2007.
- (2) *Handbook of Thiophene-Based Materials: Applications in Organic Electronics and Photonics*; Perepichka, I. F., Perepichka, D. F., Eds.; John Wiley & Sons Ltd.: Chichester, UK, 2007.
- (3) Yu, W.; Donohoo-Vallett, P. J.; Zhou, J.; Bragg, A. E. Ultrafast photo-induced nuclear relaxation of a conformationally disordered conjugated polymer probed with transient absorption and femtosecond stimulated Raman spectroscopies. *J. Chem. Phys.* **2014**, *141*, 044201.
- (4) Wang, C.; Angelella, M.; Doyle, S. J.; Lytwak, L. A.; Rossky, P. J.; Holliday, B. J.; Tauber, M. J. Resonance Raman Spectroscopy of the T₁ Triplet Excited State of Oligothiophenes. *J. Phys. Chem. Lett.* **2015**, *6*, 3521–3527.
- (5) Thomas, A. K.; Brown, H. A.; Datko, B. D.; Garcia-Galvez, J. A.; Grey, J. K. Interchain Charge-Transfer States Mediate Triplet Formation in Purified Conjugated Polymer Aggregates. *J. Phys. Chem. C* **2016**, *120*, 23230–23238.
- (6) Becker, R. S.; Seixas de Melo, J.; Maçanita, A. L.; Elisei, F. Comprehensive Evaluation of the Absorption, Photophysical, Energy Transfer, Structural, and Theoretical Properties of α -Oligothiophenes with One to Seven Rings. *J. Phys. Chem.* **1996**, *100*, 18683–18695.
- (7) *Modern Molecular Photochemistry*, 1st ed.; Turro, N. J., Ramamurthy, V., Scaiano, J., Eds.; University Science Books: Mill Valley, CA, 2010.
- (8) Rupert, B. L.; Mitchell, W. J.; Ferguson, A. J.; Köse, M. E.; Rance, W. L.; Rumbles, G.; Ginley, D. S.; Shaheen, S. E.; Kopidakis, N. Low-bandgap thiophene dendrimers for improved light harvesting. *J. Mater. Chem.* **2009**, *19*, 5311–5324.
- (9) Zhang, F.; Wu, D.; Xu, Y.; Feng, X. Thiophene-based conjugated oligomers for organic solar cells. *J. Mater. Chem.* **2011**, *21*, 17590–17600.
- (10) Beaujuge, P. M.; Fréchet, J. M. J. Molecular Design and Ordering Effects in π -Functional Materials for Transistor and Solar Cell Applications. *J. Am. Chem. Soc.* **2011**, *133*, 20009–20029.
- (11) Chi, D.; Qu, S.; Wang, Z.; Wang, J. High efficiency P3HT:PCBM solar cells with an inserted PCBM layer. *J. Mater. Chem. C* **2014**, *2*, 4383.
- (12) Hu, H.; Jiang, K.; Yang, G.; Liu, J.; Li, Z.; Lin, H.; Liu, Y.; Zhao, J.; Zhang, J.; Huang, F.; Qu, Y.; Ma, W.; Yan, H. Terthiophene-Based D-A Polymer with an Asymmetric Arrangement of Alkyl Chains That Enables Efficient Polymer Solar Cells. *J. Am. Chem. Soc.* **2015**, *137*, 14149–14157.
- (13) Gigli, G.; Ingañäs, O.; Anni, M.; De Vittorio, M.; Cingolani, R.; Barbarella, G.; Favaretto, L. Multicolor oligothiophene-based light-emitting diodes. *Appl. Phys. Lett.* **2001**, *78*, 1493–1495.
- (14) Mazzeo, M.; Pisignano, D.; Favaretto, L.; Barbarella, G.; Cingolani, R.; Gigli, G. Bright oligothiophene-based light emitting diodes. *Synth. Met.* **2003**, *139*, 671–673.
- (15) Irie, M.; Fukaminato, T.; Matsuda, K.; Kobatake, S. Photochromism of Diarylethene Molecules and Crystals: Memories, Switches, and Actuators. *Chem. Rev.* **2014**, *114*, 12174–12277.
- (16) Barbarella, G.; Zambianchi, M.; Ventola, A.; Fabiano, E.; Della Sala, F.; Gigli, G.; Anni, M.; Bolognesi, A.; Polito, L.; Naldi, M.; Capobianco, M. Bright Oligothiophene N-Succinimidyl Esters for Efficient Fluorescent Labeling of Proteins and Oligonucleotides. *Bioconjugate Chem.* **2006**, *17*, 58–67.
- (17) Ho, H.-A.; Najari, A.; Leclerc, M. Optical Detection of DNA and Proteins with Cationic Polythiophenes. *Acc. Chem. Res.* **2008**, *41*, 168–178.
- (18) Zambianchi, M.; Maria, F. D.; Cazzato, A.; Gigli, G.; Piacenza, M.; Sala, F. D.; Barbarella, G. Microwave-Assisted Synthesis of Thiophene Fluorophores, Labeling and Multilabeling of Monoclonal Antibodies, and Long Lasting Staining of Fixed Cells. *J. Am. Chem. Soc.* **2009**, *131*, 10892–10900.
- (19) Bhaskar, A.; Ramakrishna, G.; Hagedorn, K.; Varnavski, O.; Mena-Osteritz, E.; Bäuerle, P.; Goodson, T. Enhancement of Two-Photon Absorption Cross-Section in Macrocyclic Thiophenes with Cavities in the Nanometer Regime. *J. Phys. Chem. B* **2007**, *111*, 946–954.
- (20) Zhou, H.; Zhou, F.; Tang, S.; Wu, P.; Chen, Y.; Tu, Y.; Wu, J.; Tian, Y. Two-photon absorption dyes with thiophene as π -electron bridge: Synthesis, photophysical properties and optical data storage. *Dyes Pigm.* **2012**, *92*, 633–641.
- (21) Turan, H. T.; Eken, Y.; Marazzi, M.; Pastore, M.; Aviyente, V.; Monari, A. Assessing One- and Two-Photon Optical Properties of Boron Containing Arenes. *J. Phys. Chem. C* **2016**, *120*, 17916–17926.
- (22) Huix-Rotllant, M.; Tamura, H.; Burghardt, I. Concurrent Effects of Delocalization and Internal Conversion Tune Charge Separation at Regioregular Polythiophene-Fullerene Heterojunctions. *J. Phys. Chem. Lett.* **2015**, *6*, 1702–1708.
- (23) Kölle, P.; Schnappinger, T.; de Vivie-Riedle, R. Deactivation pathways of thiophene and oligothiophenes: internal conversion versus intersystem crossing. *Phys. Chem. Chem. Phys.* **2016**, *18*, 7903–7915.
- (24) Schnappinger, T.; Kölle, P.; Marazzi, M.; Monari, A.; González, L.; de Vivie-Riedle, R. Ab initio molecular dynamics of thiophene: the interplay of internal conversion and intersystem crossing. *Phys. Chem. Chem. Phys.* **2017**, *19*, 25662–25670.
- (25) Weinkauff, R.; Lehr, L.; Schlag, E. W.; Salzmann, S.; Marian, C. M. Ultrafast dynamics in thiophene investigated by femtosecond pump probe photoelectron spectroscopy and theory. *Phys. Chem. Chem. Phys.* **2008**, *10*, 393–404.
- (26) Lap, D. V.; Grebner, D.; Rentsch, S. Femtosecond Time-Resolved Spectroscopic Studies on Thiophene Oligomers. *J. Phys. Chem. A* **1997**, *101*, 107–112.

- (27) Paa, W.; Yang, J.-P.; Rentsch, S. Intersystem crossing in oligothiophenes studied by fs time-resolved spectroscopy. *Appl. Phys. B: Lasers Opt.* **2000**, *71*, 443–449.
- (28) Barclay, M. S.; Quincy, T. J.; Williams-Young, D. B.; Caricato, M.; Elles, C. G. Accurate Assignments of Excited-State Resonance Raman Spectra: A Benchmark Study Combining Experiment and Theory. *J. Phys. Chem. A* **2017**, *121*, 7937–7946.
- (29) Rubio, M.; Merchán, M.; Ortí, E.; Roos, B. O. A theoretical study of the electronic spectrum of bithiophene. *J. Chem. Phys.* **1995**, *102*, 3580.
- (30) Rubio, M.; Merchán, M.; Pou-AméRigo, R.; Ortí, E. The Low-Lying Excited States of 2,2'-Bithiophene: A Theoretical Analysis. *ChemPhysChem* **2003**, *4*, 1308–1315.
- (31) Rubio, M.; Merchán, M.; Ortí, E. A. Theoretical Study on the Low-Lying Excited States of 2,2':5',2''-Terthiophene and 2,2':5',2'':5'',2'''-Quaterthiophene. *ChemPhysChem* **2005**, *6*, 1357–1368.
- (32) Siegert, S.; Vogeler, F.; Marian, C. M.; Weinkauff, R. Throwing light on dark states of α -oligothiophenes of chain lengths 2 to 6: radical anion photoelectron spectroscopy and excited-state theory. *Phys. Chem. Chem. Phys.* **2011**, *13*, 10350–10363.
- (33) Fazzi, D.; Barbatti, M.; Thiel, W. Modeling ultrafast exciton deactivation in oligothiophenes via nonadiabatic dynamics. *Phys. Chem. Chem. Phys.* **2015**, *17*, 7787–7799.
- (34) Prlj, A.; Curchod, B. F. E.; Corminboeuf, C. Excited state dynamics of thiophene and bithiophene: new insights into theoretically challenging systems. *Phys. Chem. Chem. Phys.* **2015**, *17*, 14719–14730.
- (35) Lin, J. B.; Jin, Y.; Lopez, S. A.; Druckerman, N.; Wheeler, S. E.; Houk, K. N. Torsional Barriers to Rotation and Planarization in Heterocyclic Oligomers of Value in Organic Electronics. *J. Chem. Theory Comput.* **2017**, *13*, 5624–5638.
- (36) Richter, M.; Marquetand, P.; González-Vázquez, J.; Sola, I.; González, L. SHARC: ab initio Molecular Dynamics with Surface Hopping in the Adiabatic Representation Including Arbitrary Couplings. *J. Chem. Theory Comput.* **2011**, *7*, 1253–1258.
- (37) Mai, S.; Marquetand, P.; González, L. A General Method to Describe Intersystem Crossing Dynamics in Trajectory Surface Hopping. *Int. J. Quantum Chem.* **2015**, *115*, 1215–1231.
- (38) Mai, S.; Marquetand, P.; González, L. Nonadiabatic dynamics: The SHARC approach. *Wiley Interdiscip. Rev.: Comput. Mol. Sci.* **2018**, *0*, e1370.
- (39) Mai, S.; Richter, M.; Heindl, M.; Menger, M. F. S. J.; Atkins, A.; Ruckebauer, M.; Plasser, F.; Oppel, M.; Marquetand, P.; González, L. SHARC2.0: Surface Hopping Including Arbitrary Couplings - Program Package for Non-Adiabatic Dynamics; 2018. <https://sharc-md.org> (accessed Aug 16, 2018).
- (40) Richter, M.; Mai, S.; Marquetand, P.; González, L. Ultrafast intersystem crossing dynamics in uracil unravelled by ab initio molecular dynamics. *Phys. Chem. Chem. Phys.* **2014**, *16*, 24423–24436.
- (41) Cao, J.; Xie, Z.-Z.; Yu, X. Excited-state dynamics of oxazole: A combined electronic structure calculations and dynamic simulations study. *Chem. Phys.* **2016**, *474*, 25–35.
- (42) Marazzi, M.; Mai, S.; Roca-Sanjuán, D.; Delcey, M. G.; Lindh, R.; González, L.; Monari, A. Benzophenone Ultrafast Triplet Population: Revisiting the Kinetic Model by Surface-Hopping Dynamics. *J. Phys. Chem. Lett.* **2016**, *7*, 622–626.
- (43) Mai, S.; Pllum, M.; Martínez-Fernández, L.; Dunn, N.; Marquetand, P.; Corral, I.; Crespo-Hernández, C. E.; González, L. The origin of efficient triplet state population in sulfur-substituted nucleobases. *Nat. Commun.* **2016**, *7*, 13077.
- (44) Mai, S.; Marquetand, P.; González, L. Intersystem Crossing Pathways in the Noncanonical Nucleobase 2-Thiouracil: A Time-Dependent Picture. *J. Phys. Chem. Lett.* **2016**, *7*, 1978–1983.
- (45) Hirata, S.; Head-Gordon, M. Time-dependent density functional theory within the Tamm-Dancoff approximation. *Chem. Phys. Lett.* **1999**, *314*, 291–299.
- (46) Baerends, E. J. et al. ADF2017, SCM, Theoretical Chemistry; Vrije Universiteit, Amsterdam, The Netherlands. <https://www.scm.com> (accessed Aug 16, 2018).
- (47) te Velde, G.; Bickelhaupt, F. M.; Baerends, E. J.; Fonseca Guerra, C.; van Gisbergen, S. J. A.; Snijders, J. G.; Ziegler, T. Chemistry with ADF. *J. Comput. Chem.* **2001**, *22*, 931–967.
- (48) Lee, C.; Yang, W.; Parr, R. G. Development of the Colle-Salvetti correlation-energy formula into a functional of the electron density. *Phys. Rev. B: Condens. Matter Mater. Phys.* **1988**, *37*, 785–789.
- (49) Becke, A. D. Density-functional thermochemistry. III. The role of exact exchange. *J. Chem. Phys.* **1993**, *98*, 5648–5652.
- (50) Stephens, P. J.; Devlin, F. J.; Chabalowski, C. F.; Frisch, M. J. Ab Initio Calculation of Vibrational Absorption and Circular Dichroism Spectra Using Density Functional Force Fields. *J. Phys. Chem.* **1994**, *98*, 11623–11627.
- (51) Grimme, S.; Antony, J.; Ehrlich, S.; Krieg, H. A consistent and accurate ab initio parametrization of density functional dispersion correction (DFT-D) for the 94 elements H-Pu. *J. Chem. Phys.* **2010**, *132*, 154104.
- (52) Neese, F. The ORCA program system. *Wiley Interdiscip. Rev.: Comput. Mol. Sci.* **2012**, *2*, 73–78.
- (53) Van Lenthe, E.; Baerends, E. J. Optimized Slater-type basis sets for the elements 1–118. *J. Comput. Chem.* **2003**, *24*, 1142–1156.
- (54) Becke, A. D. A multicenter numerical integration scheme for polyatomic molecules. *J. Chem. Phys.* **1988**, *88*, 2547–2553.
- (55) Franchini, M.; Philipsen, P. H. T.; Visscher, L. The Becke Fuzzy Cells Integration Scheme in the Amsterdam Density Functional Program Suite. *J. Comput. Chem.* **2013**, *34*, 1819–1827.
- (56) Franchini, M.; Philipsen, P. H. T.; van Lenthe, E.; Visscher, L. Accurate Coulomb Potentials for Periodic and Molecular Systems through Density Fitting. *J. Chem. Theory Comput.* **2014**, *10*, 1994–2004.
- (57) van Lenthe, E.; Baerends, E. J.; Snijders, J. G. Relativistic regular two-component Hamiltonians. *J. Chem. Phys.* **1993**, *99*, 4597–4610.
- (58) van Lenthe, E.; Baerends, E. J.; Snijders, J. G. Relativistic total energy using regular approximations. *J. Chem. Phys.* **1994**, *101*, 9783–9792.
- (59) van Lenthe, E.; Snijders, J. G.; Baerends, E. J. The zero-order regular approximation for relativistic effects: The effect of spin-orbit coupling in closed shell molecules. *J. Chem. Phys.* **1996**, *105*, 6505–6516.
- (60) van Lenthe, E.; van Leeuwen, R.; Baerends, E. J.; Snijders, J. G. Relativistic regular two-component Hamiltonians. *Int. J. Quantum Chem.* **1996**, *57*, 281–293.
- (61) van Lenthe, E.; Ehlers, A.; Baerends, E.-J. Geometry optimizations in the zero order regular approximation for relativistic effects. *J. Chem. Phys.* **1999**, *110*, 8943–8953.
- (62) Wang, F.; Ziegler, T. A simplified relativistic time-dependent density-functional theory formalism for the calculations of excitation energies including spin-orbit coupling effect. *J. Chem. Phys.* **2005**, *123*, 154102.
- (63) Duarte, H. A.; Dos Santos, H. F.; Rocha, W. R.; De Almeida, W. B. Improved quantum mechanical study of the potential energy surface for the bithiophene molecule. *J. Chem. Phys.* **2000**, *113*, 4206–4215.
- (64) Ciofalo, M.; Manna, G. L. Ab initio conformational study of 2,2':5',2''-terthiophene. *Chem. Phys. Lett.* **1996**, *263*, 73–78.
- (65) Millefiori, S.; Alparone, A.; Millefiori, A. Conformational properties of thiophene oligomers. *J. Heterocycl. Chem.* **2000**, *37*, 847–853.
- (66) Liu, F.; Zuo, P.; Meng, L.; Zheng, S. J. On the optical properties of thiophene oligomers: configuration interaction study on their ground (S_0) and first singlet excited (S_1) states. *J. Mol. Struct.: THEOCHEM* **2005**, *726*, 161–169.
- (67) Mai, S.; Marquetand, P.; Richter, M.; González-Vázquez, J.; González, L. Singlet and Triplet Excited-State Dynamics Study of the Keto and Enol Tautomers of Cytosine. *ChemPhysChem* **2013**, *14*, 2920–2931.

- (68) Granucci, G.; Persico, M.; Toniolo, A. Direct semiclassical simulation of photochemical processes with semiempirical wave functions. *J. Chem. Phys.* **2001**, *114*, 10608–10615.
- (69) Plasser, F.; Ruckebauer, M.; Mai, S.; Oppel, M.; Marquetand, P.; González, L. Efficient and Flexible Computation of Many-Electron Wave Function Overlaps. *J. Chem. Theory Comput.* **2016**, *12*, 1207–1219.
- (70) Granucci, G.; Persico, M. Critical appraisal of the fewest switches algorithm for surface hopping. *J. Chem. Phys.* **2007**, *126*, 134114.
- (71) Belletête, M.; Leclerc, M.; Durocher, G. Potentialities of Semiempirical Calculations (AMPAC and INDO/S) in Determining the Conformation and Electronic Properties of 2,2'-Bithiophene: A New Joint Experimental and Theoretical Approach. *J. Phys. Chem.* **1994**, *98*, 9450–9456.
- (72) Grebner, D.; Helbig, M.; Rentsch, S. Size-Dependent Properties of Oligothiophenes by Picosecond Time-Resolved Spectroscopy. *J. Phys. Chem.* **1995**, *99*, 16991–16998.
- (73) DiCésare, N.; Belletête, M.; Marrano, C.; Leclerc, M.; Durocher, G. Intermolecular Interactions in Conjugated Oligothiophenes. 1. Optical Spectra of Terthiophene and Substituted Terthiophenes Recorded in Various Environments. *J. Phys. Chem. A* **1999**, *103*, 795–802.
- (74) Crespo-Otero, R.; Barbatti, M. Recent Advances and Perspectives on Nonadiabatic Mixed Quantum-Classical Dynamics. *Chem. Rev.* **2018**, *118*, 7026–7068.
- (75) Rentsch, S.; Yang, J. P.; Paa, W.; Birckner, E.; Schiedt, J.; Weinkauff, R. Size dependence of triplet and singlet states of α -oligothiophenes. *Phys. Chem. Chem. Phys.* **1999**, *1*, 1707–1714.

CONTROL OF MOLECULAR DYNAMICS

The main subject of the previous chapter was the investigation of molecular relaxation after photoexcitation. To simulate the relaxation pathways a semiclassical description of the molecules is used and the resulting dynamics is characterized by the evolution of the populations and the classic nuclear geometries. The semiclassical approach allows to treat large systems including all nuclear degrees of freedom and can be easily parallelized, since each individual trajectory propagates without knowledge of the other ones. These advantages are bought by neglecting the quantum nature of the nuclei. However, there are situations where these quantum properties play a non-negligible role. The non-adiabatic transitions between two electronic states near CoIns are one of the most prominent examples. The electron dynamics slows down and approaches the time scale of the nuclear motion leading to a situation where both are strongly influencing each other [34, 35]. In the vicinity of CoIns a non-trivial GP also called Pancharatnam–Berry phase is introduced [34, 35, 89, 90], which can promote self-interference of the molecular wave packet [91–94]. Also the bifurcation [175, 176] of the wave packet is not well described if the nuclei are treated classically. Another critical aspect is the lack of decoherence in many semiclassical approaches like Tully’s SH algorithm [87]. Coherence and decoherence can influence the appearance and the shape of spectroscopic signals [95–99], which are the final observables to compare with experiment. In order to describe all these phenomena correctly, a quantum description of the nuclei is necessary, since it allows a proper description of non-adiabatic transitions and also the interaction of a molecule with a short laser pulse.

In section 2.1 of this chapter a short introduction to the grid-based nuclear quantum dynamics method used in this work is given. Based on the simulation of nuclear quantum dynamics, the idea of controlling the molecular dynamics near CoIns is discussed in detail in this chapter. One of the major goals of laser chemistry is the control of reactions with tailored light fields [64–66, 177]. Here the usage of laser pulses goes beyond a simple excitation process. The aim is to monitor nuclear dynamics [53–56] and even electron motion [57–59] induced by light-matter interaction on ultrashort time scales and to control chemical reactions by modifying specific reaction pathways. In the latter cases the laser field takes over the role of a reactive ingredient. The main parameters of the laser pulse that can be manipulated, are the shape, the relative phase, the absolute phase, the intensity and to a lesser extent the frequency [151, 178–180]. The control of the nuclear and electron dynamics with a laser field, is a rich and active field of research and there are a variety of control schemes present in literature. One of the most advanced schemes, both in experiment and theory, is the optimal control theory (OCT) [69, 142, 181–188]. By using feedback-driven setups, laser pulses are optimized to prepare specific molecular wave packets. This concept is used in multiple areas ranging from reaction control over quantum information to the control of electronic motion. In order to gain control over the outcome of a photochemical reaction also a sequence of laser pulses [67, 68, 189–191] can be applied for example in a pump-dump scheme. Another possibility is to modify the potential energy surfaces (PESs) itself via the Stark effect [151, 192]. Closely related is the idea of placing the molecules in nanocavities forming hybrid light-matter states, termed as polaritons or dressed states. By tuning the properties of the cavity new light-induced CoIns can be formed and

new reaction pathways can be opened [193–198]. The control scheme on which this work is focused relies on the absolute phase, also called carrier-envelope phase (CEP) of a few-cycle infrared (IR) pulse. In section 2.2 the idea of applying the CEP control scheme in the vicinity of a CoIn is introduced. Its potential is investigated using an analytic model system and the practicability is tested on a real molecular system, namely the nucleobase uracil. Due to the short pulse duration and the proximity to a CoIn the used CEP pulse not only effects the nuclear motion but also influences the electron dynamics. This aspect will be discussed in section 3.3 of the third chapter for the molecule NO_2 .

2.1 A Short Introduction to Grid-based Nuclear Quantum Dynamics

The grid-based methodology [176] to simulate the nuclear quantum dynamics works in the adiabatic picture. The adiabatic picture is based on the Born-Oppenheimer (BO) separation [88] of electronic and nuclear variables which leads to the introduction of electronic wave functions which are parametrically dependent on the nuclear coordinates. This separation is also the basis for the semiclassical dynamics used in chapter 1 and the foundation of its derivation in section 1.2. The use of the BO separation allows to describe the nuclear motion as the propagation of a nuclear wave packet on a single uncoupled PES. Within the adiabatic picture there are regions in the nuclear coordinate space where the PESs can either come close or even touch each other forming a CoIn. By incorporating all electronic states whose PESs are energetically close and including the relevant NAC terms the nuclear wave packet can now evolve on coupled PESs. In addition, the coupling between different PESs can also be introduced by the interaction with the electric field of a laser-pulse. In this section a brief outline is given, how such a propagation of a nuclear wave packet on multiple coupled PESs can be realized.

In the BO separation the total molecular wave function $\Psi_{tot}(r, R, t)$ is formulated as a sum of the nuclear wave functions $\chi_i(R, t)$ and the electronic wave functions $\varphi_i(r; R)$.

$$\Psi_{tot}(r, R, t) = \sum_i \chi_i(R, t) \varphi_i(r; R) \quad (2.1)$$

The nuclear wave functions $\chi(R, t)$ are propagated on the individual PESs formed by the corresponding electronic states and can be written as a multi-dimensional vector $\chi(R, t)$.

$$\chi(R, t) = \begin{pmatrix} \chi_1(R, t) \\ \chi_2(R, t) \\ \vdots \\ \chi_n(R, t) \end{pmatrix}. \quad (2.2)$$

The time-independent electronic wave functions $\varphi(r; R)$ are parametrically dependent on R and the orthonormal electronic eigenfunctions $\varphi_\alpha(r; R)$ of the time-independent MCH Hamiltonian. The definition of \hat{H}_{MCH} is given in equation 1.3. To obtain the PES $V_\alpha(R)$ of a specific electronic state α , the time-independent Schrödinger equation (TISE) of the electrons is solved for different nuclear geometries R .

$$V_\alpha(R) = E_{el}^\alpha(R) = \langle \varphi_\alpha(r; R) | \hat{H}_{MCH} | \varphi_\alpha(r; R) \rangle_r \quad (2.3)$$

The temporal evolution of $\chi(R, t)$ is determined by the TDSE of the nuclei.

$$i \frac{\partial}{\partial t} \chi(R, t) = [\hat{T}_{nuc} + \mathbf{V}(R, t)] \chi(R, t). \quad (2.4)$$

Here \hat{T}_{nuc} is the operator of the kinetic energy of the nuclei. The matrix $\mathbf{V}(R, t)$, shown in equation 2.5, includes all relevant PESs $V_\alpha(R)$ and all couplings which allow the population transfer between the corresponding electronic states.

$$\mathbf{V}(R, t) = \begin{pmatrix} V_1(R) - \mu_{11}(R)\epsilon(t) & \tau_{12}(R) - \mu_{12}(R)\epsilon(t) & \cdots & \tau_{1n}(R) - \mu_{1n}(R)\epsilon(t) \\ \tau_{21}(R) - \mu_{21}(R)\epsilon(t) & V_2(R) - \mu_{22}(R)\epsilon(t) & \cdots & \tau_{2n}(R) - \mu_{2n}(R)\epsilon(t) \\ \vdots & \vdots & \ddots & \vdots \\ \tau_{n1}(R) - \mu_{n1}(R)\epsilon(t) & \tau_{n2}(R) - \mu_{n2}(R)\epsilon(t) & \cdots & V_n(R) - \mu_{nn}(R)\epsilon(t) \end{pmatrix}. \quad (2.5)$$

Within this setup two kinds of couplings are taken into account. First the time-independent ones which are mediated by the position-dependent NAC terms $\tau_{\alpha\beta}(R)$. The complete NACs are defined as follows.

$$\tau_{\alpha\beta}(R) = \langle \varphi_\alpha(r; R) | \nabla_R | \varphi_\beta(r; R) \rangle_r \nabla_R + 0.5 \langle \varphi_\alpha(r; R) | \nabla_R^2 | \varphi_\beta(r; R) \rangle_r. \quad (2.6)$$

Since the ∇^2 term, which contains the second derivatives, is much smaller than the ∇ term, it can be neglected in a first approximation. However, this would lead to a non-Hermitian Hamiltonian operator. To avoid this, the non-Hermitian behavior can be compensated for by using the partition equation 2.7 [176, 199, 200]. Here the term $\langle \nabla_R \varphi_\alpha(r; R) | \nabla_R \varphi_\beta(r; R) \rangle_r$ can be neglected without losing the hermiticity.

$$\langle \varphi_\alpha(r; R) | \nabla_R^2 | \varphi_\beta(r; R) \rangle_r = \nabla_R \langle \varphi_\alpha(r; R) | \nabla_R | \varphi_\beta(r; R) \rangle_r - \langle \nabla_R \varphi_\alpha(r; R) | \nabla_R \varphi_\beta(r; R) \rangle_r. \quad (2.7)$$

Thus the only term used to describe the coupling is the NAC vector $\mathbf{K}_{\alpha\beta} = \langle \varphi_\alpha(r; R) | \nabla_R | \varphi_\beta(r; R) \rangle_r$, which is accessible by standard quantum chemistry programs. The second coupling considered in $\mathbf{V}(R, t)$ is the time-dependent interaction with a laser pulse. This light-matter interaction is treated in the dipole approximation as the product of the state specific dipole moment $\mu_{\alpha\alpha}(R)$, or respectively the transition dipole moment $\mu_{\alpha\beta}(R)$, with the time-dependent electrical field $\epsilon(t)$ of the laser pulse. Here the transition between the electronic states is mediated via the transition dipole moment. The dipole moment is calculated as follows.

$$\mu_{\alpha\beta}(R) = \langle \varphi_\alpha(r; R) | \hat{\mu} | \varphi_\beta(r; R) \rangle_r. \quad (2.8)$$

This section concludes with two rather technical aspects. First, the method used in this work to solve equation 2.4 and simulate the nuclear quantum dynamics is the dynamic Fourier method (DFM) [201–203], which uses a discretized spatial representation of nuclear wave packet on *ab initio* PESs. The numerical propagation is performed by integration of the TDSE (see equation 2.4) according to

$$\chi(t + dt) = e^{-i[\hat{T}_{nuc} + \mathbf{V}(R, t)]dt} \chi(t) = \hat{U} \chi(t). \quad (2.9)$$

The evolution operator \hat{U} is expanded in a Chebyshev series [202]. The advantage of this propagation scheme is that in principle arbitrarily large time steps can be chosen, limited only by the amount of Chebyshev polynomials which must be employed to support it [202]. The second aspect directly connected with the DFM is the problem of the so called *curse of dimensionality*. Simulations within the DFM are only feasible in few dimensions due to the number of grid points scaling exponentially with additional degrees of freedom. This means that a full-dimensional quantum mechanical representation of the internal motion of a small organic molecule is not feasible in terms of computational effort. Therefore only a low-dimensional subspace of internal coordinates can be used. In order to select a proper subspace for given molecular process *a priori* knowledge of the molecular system is necessary. The simplest way to construct such a subspace is the manual selection of either pure normal modes or linear combinations thereof. But there are also attempts to automate the coordinate reduction and selection process [204–206]. Once a suitable subspace is found, the expressions including the derivatives with respect to the nuclear coordinates \mathbf{R} must be transformed. For the transformation of \hat{T}_{nuc} the G-matrix formalism is used [207–210] and for coupling vectors $\mathbf{K}_{\alpha\beta}$ an analog transformation is applied [176, 199].

A more detailed introduction to the topic of grid-based nuclear quantum dynamics can be found in the references [199, 211]. Beyond this grid based approach, there are methods that allow to include more degrees of freedom in the nuclear quantum dynamics simulation. A commonly used example are the different formulations of the multi-configuration time-dependent Hartree (MCTDH) ansatz [212, 213], enabling the inclusion of few dozens of degrees of freedom. It works well in cases where the system's Hamiltonian is expandable in a normal mode fashion [214–216], but is less applicable if the PES can be described only poorly with the help of this harmonic approximation, or if there is strong correlation between the degrees of freedom [217].

2.2 Control of Molecular Dynamics Close to a Conical Intersection

There are a lot of different schemes and methods discussed in the literature on how to influence and to control the dynamics of a molecular system with the help of a laser pulse. Using a few-cycle pulse with a well-defined waveform, it is possible to directly manipulate the dynamics of the molecule [65, 218]. The electric field of such a few-cycle laser pulse with a Gaussian shape in the time domain can be written as follows.

$$E(t) = E_{max} \cdot e^{-2\left(\frac{t-t_0}{\sigma}\right)^2} \cdot \cos(\omega_0(t-t_0) + \phi),$$

$$\text{with } \sigma = \frac{\text{FWHM}}{\sqrt{2 \log(2)}}.$$
(2.10)

The product in front of the cosine defines the envelope of the pulse, which is influenced by the maximum electric field strength E_{max} and the full width half maximum FWHM. The remaining pulse parameters are the central frequency ω_0 , the time zero t_0 defining the temporal position of the pulse with respect to the global simulation time and the phase ϕ between the central frequency and the envelope, also called the CEP. For all simulations in this work an optimal alignment of the transition dipole moment and the electric component of the pulse is assumed. Figure 2.1 depicts the electric field of three laser pulses which only differ in the chosen CEP. For $\phi = 0.0\pi$ (orange line) the maximum of the electric field coincides with the maximum of the envelope, i.e. the maximal electric field strength E_{max} (black line) at the time $t_0 = 0.0$ fs. By changing the CEP (purple and green line) the maximum shifts along the envelope in time. Therefore, each of the three pulses has a different intensity distribution and a different maximum of the electric field depending on the CEP. With an increasing number of optical cycles the difference in the intensity distribution becomes smaller and the influence of the CEP vanishes.

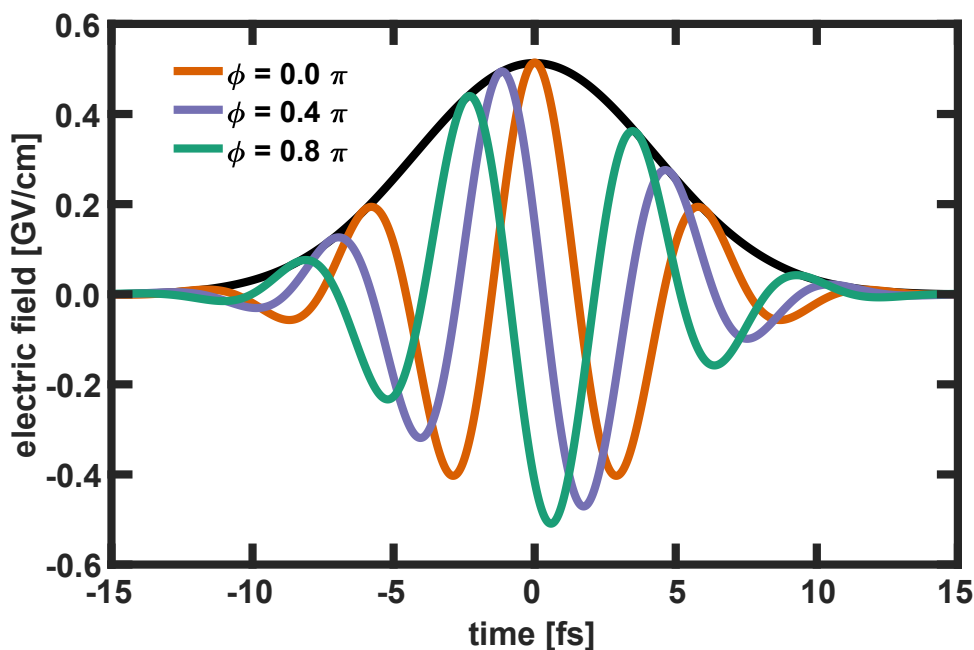


Figure 2.1: Three laser pulses with varying CEP ϕ (color-coded) but the same envelope (black), showing the difference in the intensity distribution caused by the absolute phase of the laser pulses.

There are multiple examples [65, 219–224] how the dynamics of a molecule is controlled by varying the CEP of a few-cycle laser pulse. If the chosen electric field strength is large enough to modify the PESs itself via the Stark effect, the shape of the intersection region in the vicinity of the CoIn can be controlled by the variation of the CEP [223–226]. Another example of a CEP based control is the creation of a superposition of vibrational states which can be adjusted by variation of the CEP. This was demonstrated both in experiment and theory [219, 227] for the controlled deprotonation and bond rearrangement of small hydrocarbons after ionization with a few-cycle laser pulse. The control scheme which is discussed

in this section follows the idea of creating an adjustable superposition of electronic states in the vicinity of CoIn. This idea was formulated for the first time in the references [99, 228, 229] and tested for an analytic model system. The NACs of a CoIn induce a population transfer between the two involved electronic states leading to a coherent superposition between these two states. The phase relationship of this superposition is determined by the from an shape of the NAC elements and the associated GP. This phase in combination with the strength of the coupling defines the distribution of the population of the involved states after the CoIn. The goal is now to create a second coherent superposition between the two electronic states before the CoIn is reached by applying a few-cycle laser pulse. The phase relationship of the laser pulse induced superposition can be varied via the CEP of the pulse. The interplay of the laser induced superposition and the one created by the CoIn leads to constructive or destructive interference, when passing the CoIn region. This interference influences the distribution of the population after the CoIn and can be controlled by varying the CEP.

The main focus of the article "Waveform Control of Molecular Dynamics Close to a Conical Intersection" published by the Journal of Chemical Physics [230] is to explore the physical boundaries of the CEP control near a CoIn. In a first step, a two-dimensional analytic model system is used to elucidate the necessary molecular properties and to optimize the remaining parameters of the laser pulse. To extend the study the CEP control scheme is applied to the CoIn mediated relaxation of the nucleobase uracil after photoexcitation. The key findings of the article are summarized as follows:

- In order to quantify the degree of controllability which can be achieved by this CEP control scheme the CEP efficiency $\Gamma(t)$ is introduced. It is calculated as the difference of the maximum and the minimum population $A_{jj}(t, \phi)$ of a given target state j for each time step.

$$\Gamma(t) = \max(A_{jj}(t, \phi)) - \min(A_{jj}(t, \phi')), \quad (2.11)$$

with $A_{jj}(t, \phi) = \langle \chi_j(R, t, \phi) | \chi_j(R, t, \phi) \rangle_R$.

For its maximum value the population of the state j shows the highest CEP dependence and consequently the highest degree of controllability. In this work the value of $\Gamma(t)$ is maximized by varying all laser parameters except of ϕ . In combination with the population of the target state itself $\Gamma(t)$ offers a great tool to characterize the CEP control scheme.

- By optimization of the laser parameters, it was possible to identify two different processes, which both enable a control over the population transfer and depend on the CEP. The first one is the process described above, based on interference. The second process occurs due to the few-cycle waveform of the laser pulse and shows no dependence on the shape and size of the NACs. This process is refereed to as field-only mechanism, because it occurs even if no NACs between the evolved states are considered at all and it strongly depends on the field strength of the laser pulse. The periodicity of the CEP dependence of the population can be used to distinguish between the two mechanisms.
- Depending on the molecular system and the chosen laser parameters, both processes can be active, vary in their strength, and even obstruct each other. Assuming ideal conditions for the transition dipole moment and NACs in the analytic model system, it is possible to optimize a laser pulse that leads to a CEP efficiency of 40 %, which is almost entirely based on the interference process.
- The interplay of the transition dipole moment and the NACs is essential to obtain CEP control over the population transfer. The shape of the NACs and the transition dipole moment along the direction of the wave packet motion enable the interference process or rather prevent it. In principle it should be possible to achieve a high degree of CEP control assuming that there is a non-zero transition dipole moment if the wave packet moves along a suitable pathway toward the CoIn. Some molecular systems may provide these pathways naturally. For others molecules, it should be possible to control the nuclear wave packet motion using OCT to open up the desired pathway. Therefore, specially optimized and shaped laser pulses are used for the excitation process [142, 231].
- The CEP control scheme also works in the challenging boundary conditions of the nucleobase uracil. In uracil the S_2 - S_1 -relaxation is mediated by a seam of CoIns and the wave packet is crossing

this coupling region multiple times. By using two different starting conditions, two different types of wave packets were studied. For the first one, the excited state wave packet oscillates around the S_2 minimum before parts of it are able to cross the barrier and reach the CoIn. In the second case, the wave packet directly approaches the barrier and, thereafter, the CoIn in a more localized form. The starting conditions determine the CEP efficiency $\Gamma(t)$ and also the mechanism.

- The control of the branching ratio induced by a CoIn via a CEP pulse is a general concept. The control is most effective for a system where a localized wave packet crosses the CoIn only once and the transition dipole moment is extended in this area. Interestingly the CEP efficiency is long-lived, which should be favorable for experimental detection.

On the next pages the article "Waveform Control of Molecular Dynamics Close to a Conical Intersection" published by the Journal of Chemical Physics is reprinted from *Journal of Chemical Physics* **153** (2020), 224307 with permission from AIP Publishing. The supporting information of this article is available under <https://aip.scitation.org/doi/full/10.1063/5.0031398>.

Waveform control of molecular dynamics close to a conical intersection

Cite as: J. Chem. Phys. 153, 224307 (2020); doi: 10.1063/5.0031398

Submitted: 30 September 2020 • Accepted: 24 November 2020 •

Published Online: 14 December 2020



Franziska Schüppel, Thomas Schnappinger,  Lena Bäuml, and Regina de Vivie-Riedle^{a)} 

AFFILIATIONS

Department of Chemistry, LMU Munich, D-81377 Munich, Germany

^{a)}Author to whom correspondence should be addressed: Regina.de_Vivie@cup.uni-muenchen.de

ABSTRACT

Conical intersections are ubiquitous in chemical systems but, nevertheless, extraordinary points on the molecular potential energy landscape. They provide ultra-fast radiationless relaxation channels, their topography influences the product branching, and they equalize the timescales of the electron and nuclear dynamics. These properties reveal optical control possibilities in the few femtosecond regime. In this theoretical study, we aim to explore control options that rely on the carrier envelope phase of a few-cycle IR pulse. The laser interaction creates an electronic superposition just before the wave packet reaches the conical intersection. The imprinted phase information is varied by the carrier envelope phase to influence the branching ratio after the conical intersection. We test and analyze this scenario in detail for a model system and show to what extent it is possible to transfer this type of control to a realistic system like uracil.

Published under license by AIP Publishing. <https://doi.org/10.1063/5.0031398>

I. INTRODUCTION

Non-adiabatic effects are well-known to influence the dynamics of the photo-relaxation and photo-reaction of molecular systems. These effects are especially pronounced in the vicinity of a conical intersection (CoIn), where the adiabatic separation between nuclear and electronic motion breaks down^{1–3} and the electronic states involved become degenerate. CoIn's open up funnels for radiationless electronic transitions, whose efficiency and branching relation is determined by the shape and size of the non-adiabatic coupling elements (NACs) and the topography in the vicinity. They play a central role in many chemical and biological processes, such as retinal isomerization in vision,^{4,5} DNA photo-protection mechanisms,^{6–9} molecular photo-switches,^{10–12} and molecular motors.^{13–15} As in the entire field of chemistry, the major goal in photo-chemistry is to control the outcome of a reaction. Classical control agents used in chemical synthesis are temperature, solvents, catalysts, pressure, or concentration. Another avenue to obtain control in photo-chemical reactions is to guide the underlying molecular dynamics with specifically designed laser pulses.^{16–18} For this purpose, laser parameters such as the frequency, the phase, and polarization can be optimized. In addition, the waveform of a carrier envelope phase (CEP) stabilized few-cycle laser pulse can be used as a control

parameter. These few-cycle laser pulses can be described via an envelope function $E_0(t)$, the central carrier frequency ω_0 , and a carrier envelope phase ϕ (CEP). This CEP offers the possibility to steer electrons and nuclei.^{19–23} The steering relies on a superposition of two or more electronic or vibrational states with a well-defined phase relationship.

In our theoretical study, we take advantage of the fact that the electron dynamics slows down in the vicinity of CoIn's and approaches the timescale of the nuclear dynamics. For control, we apply a few-cycle IR laser pulse when the system's dynamics approaches a CoIn. The CEP pulse builds up a superposition of the electronic states forming the CoIn, with its phase relationship depending on the CEP. Since this occurs near a CoIn, also a non-trivial phase (called the geometric or Pancharatnam–Berry phase) is introduced.^{1,2,24,25} These two phase terms now lead to an interference process when the CoIn is passed. The interference (constructive or destructive) can be changed by varying the CEP. This process modulates the population transfer via the CoIn toward competing channels. The control of the coupled electron–nuclear dynamics at a CoIn with a laser field is a rich and active field of research, and there are a variety of laser control schemes present in the literature. Both in the experiment and theory, optimal control theory^{26–29} was applied to guide the dynamics of a molecular system via a CoIn toward a

desired target state with shaped laser pulses. Another possibility to obtain control is to modify the potential energy surfaces (PESs) and, thus, the CoIn itself via the Stark shift.^{30,31} The high pulse intensities used in this methodology can create new light-induced CoIn's.^{32–34} The main difference of our applied CEP-control-scheme^{17,35,36} compared to the two mentioned methods is that the control laser is very short and only interacts with the molecular system shortly before the CoIn is reached. The goal is not to control or change the pathway toward the CoIn but to manipulate the phase relationship in the system^{17,35,36} during the transfer.

After introducing the realization of the CEP-control-scheme in our simulations, we want to ascertain to what extent this IR control scheme is possible and determine its boundary conditions. For this, we consider a two-dimensional analytical model system, which is composed of three states. Two of them are connected via a CoIn in a dissociation process. The CEP-control-scheme is applied to modify the ratio between the two competing channels. Since we work with a model, it is possible to change the size and shape of the NACs and the transition dipole moment (TDM) and, thus, to evaluate the necessary molecular conditions for a CEP control. Besides the molecular properties, also the parameters of the few-cycle laser pulse (such as the frequency, the timing, and the strength of the electric field) influence the efficiency of the CEP-control-scheme and have to be optimized. Through a detailed analysis of the CEP dependent population, it is possible to distinguish between the interference process and a process solely due to the component light. Besides the analytic model system, we apply the CEP-control-scheme to a photo-physical active molecule. As an example, we have chosen the nucleobase uracil, where a CoIn enables an ultra-fast few hundred femtosecond relaxation mechanism that prevents harmful chemical modification.^{37,38} In previous studies,^{8,9} we demonstrated that the S_2 – S_1 relaxation dynamics can be accelerated and decelerated by light control. Here, we focus on the control possibilities at the CoIn. The relaxation process occurs step-wise including forth and back crossing through the CoIn, which results in a quite complex situation regarding the geometric phase. Besides this, the TDM between the relevant states is rather weak and localized. Therefore, uracil is a quite challenging system for the CEP-control-scheme.

II. LIGHT-MATTER INTERACTION AND THE CEP EFFICIENCY

Our goal is to influence the population transfer through a CoIn with the waveform of a CEP stabilized few-cycle pulse in the IR and to quantify the controllability. The dynamics of the model system and uracil is simulated on coupled adiabatic PESs (V_{S1} and V_{S2}) by solving the time-dependent Schrödinger equation

$$i\hbar \frac{\partial}{\partial t} \Psi = \hat{H} \Psi, \quad (1)$$

with

$$\hat{H} \Psi = \begin{pmatrix} \hat{T} + V_{S1} & \tau_{12} - \mu_{12} \varepsilon(t) \\ \tau_{12} - \mu_{12} \varepsilon(t) & \hat{T} + V_{S2} \end{pmatrix} \begin{pmatrix} \Psi_1 \\ \Psi_2 \end{pmatrix}. \quad (2)$$

The used Hamiltonian includes the NACs τ_{12} and the transition dipole moments μ_{12} between the first two excited states. This means the light–matter interaction is treated within the dipole approximation and effects such as the Stark shift are taken into account in the dipole-limit.³⁰ For more details, see Sec. I of the [supplementary material](#). The few-cycle pulse has a Gaussian shape and is defined as

$$E(t) = E_{\max} \cdot e^{-2\left(\frac{t-t_0}{\sigma}\right)^2} \cdot \cos(\omega_0(t-t_0) + \phi), \quad (3)$$

with $\sigma = \frac{\text{FWHM}}{\sqrt{2\log(2)}}$.

We assume an optimal alignment of the transition dipole moment and the electric component of the pulse. There are methods described in the literature,^{39–41} which would, in principle, allow for such an alignment of the molecular system. With the assumed optimal alignment, the maximal possible effect of the CEP-control-scheme for a given laser pulse is determined. Except for the orientation of the electric field, all other laser pulse parameters remain open for optimization to realize a CEP control. Besides the CEP ϕ itself, these are the electric field strength E_{\max} , the central frequency ω_0 , the full width half maximum (FWHM), and the timing of the few-cycle pulse. Time zero t_0 of the pulse, defining the position of the maximum, is selected to match the time when the wave packet approaches the vicinity of the CoIn. The frequency and the time are related to the topography of the CoIn, and the electric field interacts with the TDM of the system. Beyond these parameters, the direct influence of the NACs and the TDM as well as their interplay can be tested in the model system, whereas, for uracil, these values are fixed quantities. The main observable is the time-dependent and phase-dependent population $a(t, \phi)$ of a given target state. As a figure of merit of how efficient the CEP control is, we define the quantity $\Gamma(t)$. The CEP efficiency $\Gamma(t)$ is calculated as the difference of the maximum and the minimum population $a(t, \phi)$ for each time step,

$$\Gamma(t) = \max(a(t, \phi)) - \min(a(t, \phi')). \quad (4)$$

For its maximum value, the population of the target state shows the highest CEP dependence and, consequently, the highest degree of controllability. In a sense, $\Gamma(t)$ is comparable to the asymmetry parameter used in electron recollision and attosecond photoionization experiments.^{23,42–45} Since our model system describes a dissociation process, the wave packet reaches the CoIn region only once and $\Gamma(t)$ remains constant after this event. In this case, we can take this constant value to quantify the controllability of the system for a given laser pulse. It is maximized by varying the parameters relevant to the light–molecule interaction. In cases of non-radiative relaxation without dissociation, the wave packet may cross the CoIn multiple times and $\Gamma(t)$ will not become constant as long as there is an exchange of population between the states. This situation will be discussed for our second example, the nucleobase uracil. In these cases, we aim for a maximum value of $\Gamma(t)$ after the laser pulse.

III. MODEL SYSTEM

The two-dimensional analytical model system is selected as an ideal test system for CEP control at a CoIn. It describes a dissociation process after photo-excitation with two competing pathways. The basic model⁴⁶ is introduced in the diabatic representation and consists of three diabatic electronic states and the corresponding coupling element. Their analytic form can be found in the [supplementary material](#) [Eq. (S3)] together with the relevant parameters in Table S1]. The interference process of the CEP-control-scheme depends on the fact that the wave packet acquires a nontrivial geometric phase when approaching a CoIn. To ensure the correct description, we work in the adiabatic representation. Therefore, we transform from the diabatic to the adiabatic picture. The resulting adiabatic potential energy surfaces (PESs) are shown as a one-dimensional cut along the dissociation coordinate (x -coordinate) together with the CoIn in Fig. 1(a). The transformation depends

on the adiabatic–diabatic transformation angle,^{1,2,47} which is characterized by a phase jump. Either the signed or the absolute value of the transformation angle is taken into account leading to two different pairs of NACs. The two pairs are shown in Fig. 1(b). Details of these two transformations can be found in the [Appendix](#). Using the absolute value leads to model A and the signed value to model B. The differences in the NACs emerge in the number of nodes in the x -element and y -element. The two coordinates x, y are chosen in such a way that the two-dimensional space is identical to the branching space of the CoIn. For the simulations, the first eigenfunction of the S_0 potential is set to the S_2 potential assuming a delta pulse excitation to create a localized wave packet on the excited state surface. In a previous study¹⁷ on the model system, the excitation pulse was explicitly included in the simulation leading to a localized wave packet. With a subsequent applied laser pulse, it was possible to control the population transfer by varying the CEP of the pulse. In this work, we want to focus solely on the effect of the CEP-control-scheme and leave the excitation process out of discussion. For more information regarding the quantum dynamics simulation setup and the free evolution of the population for both models, see Secs. I and II of the [supplementary material](#). The transition dipole moment is chosen arbitrarily with a maximum value of $\sqrt{4.5}$ a.u. Its specific form is discussed later in Sec. III A, and the analytic expressions can be found in the [supplementary material](#) (Table S2).

A. Influence of the TDM and the NACs

Models A and B are combined with TDMs of different shape, as listed in Fig. 2. In this way, we want to find out whether and how the form of the NACs and the TDM as well as their interplay is associated with a possible CEP control. As mentioned, both model systems just differ in the form of the NACs, especially in their nodal structure. Since the x -coordinate is the main direction of motion, the NAC- x elements are decisive for the non-adiabatic coupling efficiency. The origin of the nodal planes in the TDMs is set to the intersection point. More details about the TDMs can be found in the [supplementary material](#) (Table S2). In this simulation series, the following laser pulse parameters are used: $E_{\max} = 0.0082$ GV cm⁻¹, $t_0 = 39$ fs, FWHM = 10 fs, and $\omega_0 = 0.33$ eV (3760 nm). The results are summarized in Fig. 2.

Essential for the control is the interplay of the coupling via the NACs and via the TDM along the direction of the wave packet's motion. In case of model A, the NAC- x element has no nodal structure and CEP control is achieved for a TDM without nodes (case 1). It is also achieved in case 2 although now the TDM has a nodal plane perpendicular to the direction of motion. However, this nodal structure makes no impact as the few-cycle pulse interacts with the wave packet before it has reached the CoIn and, thus, the nodal plane of the TDM is not active. In case 3, the nodal structure of the TDM is in the direction of motion and the interplay with the NAC- x element leads to a cancellation of the CEP-control contributions. In case 4, the nodal structure is the same as in case 3 but without a change in sign. The individual contributions interfere constructively and eventuate in CEP control. In case of model B, the NAC- x element has a nodal plane parallel to the direction of motion and constructive interference in the interplay is only realized when the TDM has the same nodal structure. Thus, for both

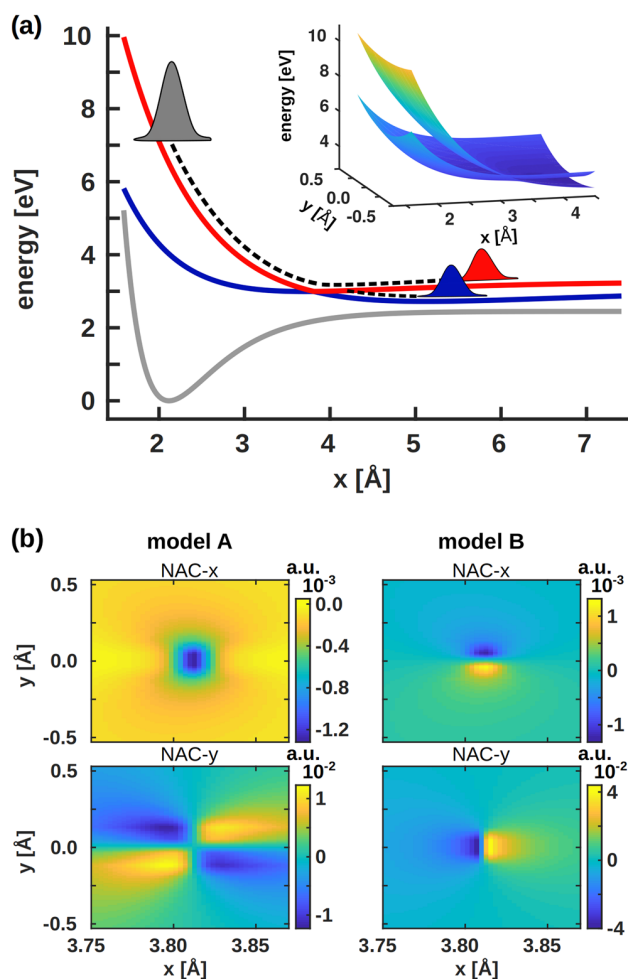


FIG. 1. (a) One-dimensional cut at $y = 0.0$ Å of the 2D adiabatic PES. Gray: S_0 ; blue: S_1 ; red: S_2 . The area of the CoIn is enlarged and shown as an inset. (b) Non-adiabatic coupling elements of model A and model B.

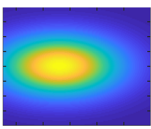
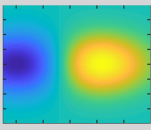
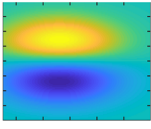
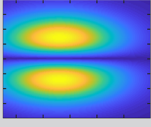
Transition dipole moment		model A	model B
1		CEP	no CEP
2		CEP	no CEP
3		no CEP	CEP
4		CEP	no CEP

FIG. 2. CEP-control possibility depending on the form of the NACs and the TDM. TDM-1 and TDM-3 take values from 0 to $\sqrt{4.5}$ a.u. TDM-2 and TDM-4 take values from $-\sqrt{4.5}$ to $\sqrt{4.5}$ a.u. More information of the TDMs can be found in the [supplementary material](#) (Fig. S1 and Table S2).

model systems, a combination with TDMs exists that allows for a CEP control. For the following simulations, we select model **B** because there the full mixing angle is used to calculate the NACs and, therefore, the complete phase relationship is preserved. It was combined with the TDM in case 3, which is showing the same sign change.

B. Correlation of time zero t_0 and central frequency ω_0 of the few-cycle pulse

The optimal control window is determined by the time when the wave packet is at or in the vicinity of the CoIn. This window can be scanned by variation of the pulse parameters, time zero t_0 and the central frequency ω_0 of the few-cycle IR pulse. The variations are performed for model **B**. Ideally, t_0 matches the time window when the wave packet is located at the CoIn [Fig. 3(b), gray area]. For this time, the frequency (ω_0) has to be resonant with the actual energy gap ΔE . The ΔE value is always taken at the maximum of the wave packet [Fig. 3(b), blue line]. Figure 3(a) shows the final CEP efficiency Γ of the target state S_1 in dependence of both variables. One pronounced maximum is found between 30 fs and 45 fs and between 0.2 eV and 0.28 eV. The CEP efficiency is best when t_0 coincides with the arrival time of the wave packet at the CoIn. For comparison,

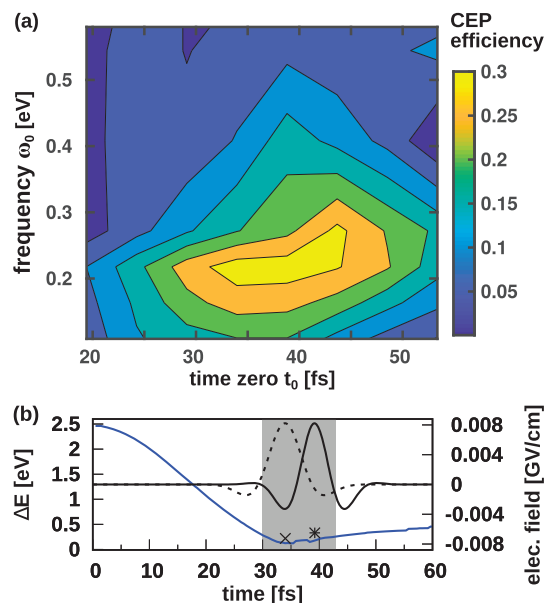


FIG. 3. (a) Two-dimensional CEP-control scheme of model **B** with the laser pulse parameters t_0 and ω_0 . (b) ΔE between S_1 and S_2 at the maximum location of the wave packet (blue), applied laser pulses with a phase shift of $\phi = 0.0\pi$ for the maximum (dashed line), and the time window of the wave packet at the CoIn (gray bar). The cross marks the parameters of the optimal pulse. The subsequently used laser pulse is shown as a solid line, and its parameters are marked with an asterisk.

the free population dynamics without the CEP pulse is shown in Sec. II of the [supplementary material](#). While the central frequency has to match the small energy gap, the CEP efficiency is less sensitive to the timing. The resulting laser pulse is almost a one-cycle pulse and is shown in Fig. 3(b) as a dashed line. Its pulse parameters, $t_0 = 34$ fs and $\omega_0 = 0.22$ eV, are marked with a cross. About 30% CEP efficiency is obtained with that laser pulse. For the following simulations, the parameters $t_0 = 39$ fs and $\omega_0 = 0.33$ eV are used (marked with an asterisk). With 20%, the CEP efficiency is still good and the laser pulse has almost two cycles [Fig. 3(b)].

C. Interference vs field-only mechanism

CEP control based on the cooperative interaction of a few-cycle IR pulse with a CoIn relies on the generation of an electronic superposition with a well-defined phase-relation. The IR pulse induced electronic wave packet interferes with the electronic superposition generated by the non-adiabatic coupling at the CoIn. Their mutual phase relation gives rise to constructive or destructive interference, which can be controlled by varying the CEP. Control via the electron dynamics is possible because here the electron and nuclear dynamics are on the same timescale. The interference pattern modifies the population-transfer through the CoIn and, thus, the branching ratio. This interaction is called the interference mechanism from now on. The degree of modification can solely be controlled by the laser pulse

induced superposition, as the one induced by the CoIn is a given molecular property.

The optimal CEP pulse is just a few-cycle IR pulse, and its shape becomes asymmetric while varying the CEP. Due to this asymmetry, the interaction with the electric field alone, i.e., without contributions from NACs, already creates a CEP dependence of the population. This interaction is called the field-only mechanism from now on. The CEP dependence of both mechanisms enters in the control quantity $\Gamma(t)$. To evaluate their individual contributions, the simulations are done twice once with and once without the NACs included. In this way, it is possible to determine the CEP efficiency $\Gamma(t)$ of the field-only mechanism and compare it with the combined impact. For a detailed understanding of both processes, we varied the parameters of the dipole-laser interaction, i.e., the electric field strength E_{\max} and the size of the TDM. All other laser parameters are kept constant ($t_0 = 39$ fs, FWHM = 10 fs, and $\omega_0 = 0.33$ eV). The variation of the TDM is performed for $E_{\max} = 0.0082$ GV cm $^{-1}$. In the field-free simulation, we observe a population of 67% in the S_1 state after the wave packet passed the CoIn (Fig. S2). Thus, the pure CoIn induced transfer from the S_2 to the S_1 state itself is quite effective. In the following, we discuss the effects of the CEP-control-scheme on the basis of the transferred population to S_1 . The results of the first simulation set are visualized in Fig. 4. For low electric field strengths ($E_{\max} < 0.01$ GV cm $^{-1}$), no CEP efficiency due to the field-only process is observed [orange line, Fig. 4(a)]. Its efficiency increases steadily with field strength even surpassing the combined efficiency (blue line). For the simulations including the NACs, $\Gamma(t)$ is already larger than 0.1 for low field strengths. It reaches a maximum of 0.41 at $E_{\max} = 0.04$ GV cm $^{-1}$ and decreases afterward. At the maximum of the combined efficiency, the field-only contributions are minor with about 5%. This is a clear indication that the interference process dominates for lower field strengths, whereas, for higher field strengths, contributions from the field-only process become important. Both mechanisms may influence the CEP dependent variation of the population. In Fig. 4(b), this variation is shown for different field strengths. The solid lines refer to the simulations including the NACs and the dashed lines to the ones with the laser interaction only. The simulations with low field strength v1 (green lines, $E_{\max} = 0.0041$ GV cm $^{-1}$) and v2 (orange lines, $E_{\max} = 0.0082$ GV cm $^{-1}$) have a mean population transfer of 67% and 65% (averaged over all CEPs), respectively. These transfer rates are almost identical to the field-free case [Fig. 4(b), black dotted line] because the contribution of the field-only process is minimal. The variation of the CEP leads to a change in the mean value by +6% and -7% for v1 and by +11% and -12% for v2. If these values are related to the field-free case, the population can be varied in the range of 13% and 23%, respectively. The CEP dependent population shows a clear sinusoidal behavior with a periodicity of 2π if the NACs are included. This periodicity is typical for an interference process. Without NACs, no CEP dependence is present and the transferred population is constant around zero. In the simulation v3 (violet lines, $E_{\max} = 0.0411$ GV cm $^{-1}$) with maximal $\Gamma(t)$, a mean population transfer of around 51% is observed, which means, in average, the laser pulse is weakening the population transfer via the CoIn. However, at the same time, the CEP-schema modifies the population transfer by +4% and -38% in relation to the field-free case. This is a quite remarkable effect because here it is possible to invert the field-free product distribution by adjusting the CEP. With a larger field strength, simulation v4

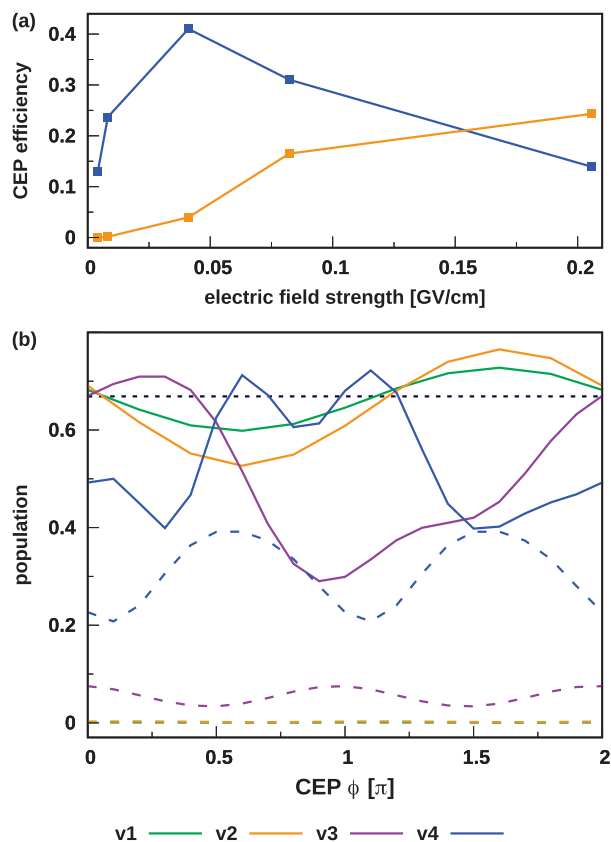


FIG. 4. (a) CEP efficiency with (blue) and without (orange) NACs included for increasing electric field strengths. (b) CEP dependence of the population in the state S_1 at the end of the simulation for selected electric field strengths. In (b), calculations with NACs are shown by solid lines and those without NACs by dashed lines. The field strengths are color coded starting from low (v1) to large (v4) values. The black dotted line shows the population after the CoIn in the S_1 state (67%) of the field-free simulation for comparison.

(blue lines, $E_{\max} = 0.0823$ GV cm $^{-1}$), the variation of the population transfer gets smaller (+5% and -27% in reference to the field-free case). In both simulations (v3 and v4), the transferred population under field-only conditions shows a clear sinusoidal dependence with a periodicity of π . This periodicity reflects the asymmetry in the electric field. Correspondingly, the CEP dependent population with NACs is of a complex sinusoidal form. For v3, the 2π periodicity is still recognizable, whereas v4 already tends more toward the π periodicity. This is an indication that with the increasing field strength, the field-only mechanism gains more and more influence on the overall process. The periodicity of π vs 2π can be used as an indicator whether the interference or field-only mechanism is present and which one is dominating. Our results show that a complex interplay between both mechanisms determines the combined CEP efficiency. It can be increased by increasing the field strength up to a certain limit. Beyond this limit, higher electric field strengths do not improve the combined CEP efficiency [blue line in Fig. 4(a)].

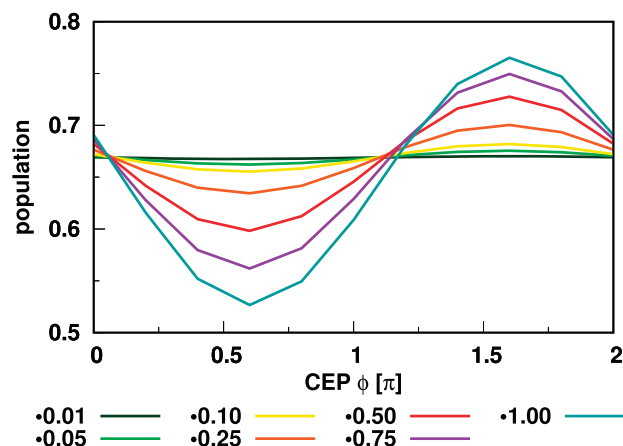


FIG. 5. CEP dependence of the population with different sized TDMs. The maximal TDM value is set to $n\sqrt{4.5}$ a.u., meaning the maximum of the dark green curve is set to $0.01\sqrt{4.5}$ a.u.

For the higher field strengths, we observe an increasing influence of the laser pulse on the field-only simulation, which can be attributed to the temporal asymmetry of the pulse. However, the overall CEP efficiency decreases, see Fig. 4(a). The used field strengths are of a magnitude that is sufficient to shift the PESs via the Stark effect.^{30–34} This can lead to the deformation of the CoIn, which occurs only for a very short timescale due to the duration of the laser pulse (FWHM = 10 fs). So, the expected influence on the population dynamics may not dominate but can partially explain the decreasing CEP efficiency.

In the second set of simulations, we vary the TDM. The maximum of the TDM is set to $n\sqrt{4.5}$ a.u., with $n = 0.01, 0.05, 0.10, 0.25, 0.50, 0.75, 1.00$. The CEP dependent population is shown in Fig. 5.

For a small TDM of around 0.02 a.u., the population shows no CEP dependence (dark green curve). For higher values between 0.11 a.u. and 1.59 a.u., the population shows a clear sinusoidal behavior with a 2π periodicity and an increasing CEP efficiency. The higher TDM enables a better population transfer between the electronic states in the CEP-pulse induced superposition. If their ratio matches the one induced at the CoIn, the best possible CEP control is achieved and the interference process is most efficient. For even larger TDMs, the sinusoidal curves become asymmetric in the height of the amplitudes while the CEP efficiency is still increasing. The periodicity of 2π is conserved, and thus, the mechanism does not change. In molecular systems, the TDM is a fixed quantity and at least a value 0.10 a.u. is required to allow for CEP control. From our results, we can deduce that large TDMs at the CoIn are favorable for the CEP control. Together with the finding in Sec. III A, it becomes clear that both the shape and the size of the TDM are essential quantities for the CEP control.

D. Tolerance on the pulse width

The last tested laser pulse parameter is the pulse width FWHM. The main request is how broad the laser pulse can be to still observe a CEP control. Figure 6 summarizes two simulation series for

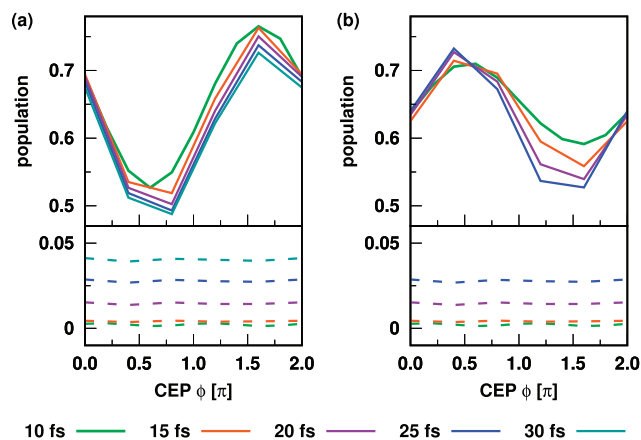


FIG. 6. CEP dependence of the population with pulse widths in the range from 10 fs to 30 fs (color coded). In (a), the laser pulse is applied at $t_0 = 39$ fs and in (b) at $t_0 = 31$ fs. Calculations with NACs are shown by solid lines and those without NACs by dashed lines.

different time zeros where the pulse widths are varied from 10 fs to 30 fs. The solid lines refer to the simulations including the NACs (top), and the dashed lines represent the field-only situation (bottom). The time zero for (a) is $t_0 = 39$ fs, and that for (b) is $t_0 = 31$ fs. The further laser parameters are $E_{\text{max}} = 0.0082$ GV cm⁻¹, for which only the interference process is active, and $\omega_0 = 0.33$ eV.

In the field-only case, the population transfer is constant with the CEP but slightly increases with the pulse length, see Fig. 6 (bottom). With NACs included, the population in the target state follows the sinusoidal form with a periodicity of 2π . We find that a CEP control is possible for laser pulses with a FWHM up to 30 fs, a tolerance that was already indicated in Fig. 3(a) showing the CEP efficiency with respect to the central frequency ω_0 and time zero t_0 . The tolerance in the FWHM of the CEP pulse facilitates experimental realization.

IV. URACIL

Besides the analytic model system, we want to extend our investigations to a more realistic system. We selected the nucleobase uracil, which has an experimentally well studied ultra-fast photo-relaxation channel starting in S_2 and mediated by conical intersections. In previous studies,^{8,9} we demonstrated that the S_2 - S_1 relaxation dynamics can be well described on two-dimensional potential surfaces and offers opportunities for laser control. Here, we focus on the control possibilities at the CoIn. The geometry of uracil is shown as an inset in Fig. 7(a). A seam of CoIn's [Fig. 7(a), black line] enables the ultrafast relaxation mechanism of a few hundred femtoseconds. For the dynamics simulation, we adopted the PES reported by Keefer *et al.*⁸ The system is described fully coherently as no coupling to an external bath is considered. On the timescales relevant to the relaxation process studied, this should be of no major consequence for the reported message. The PESs are spanned by a two-dimensional coordinate space, which properly samples the relaxation pathway in the bright S_2 state [PES shown in Fig. 7(a)]. The S_2 potential energy

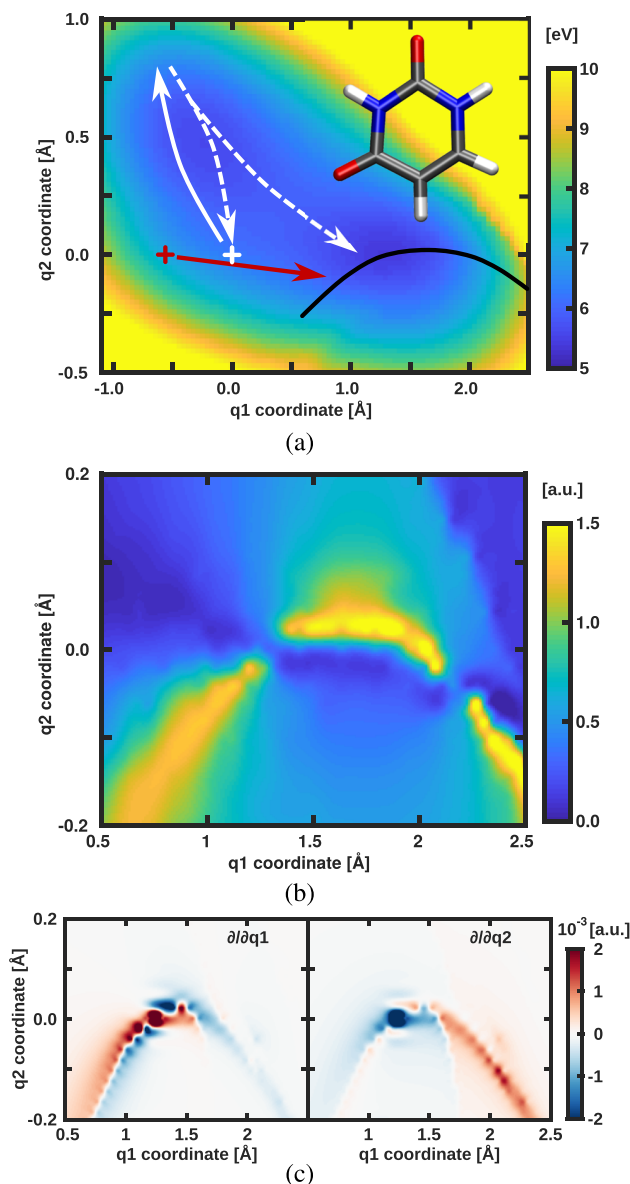


FIG. 7. (a) Potential energy surface of the bright S_2 state of uracil. The conical intersection seam is marked in black, and the evolution of the *uracil A* and the *uracil B* wave packet is sketched in white and red, respectively. The structure of uracil at the Franck-Condon point is shown as an inset. (b) Absolute value of the S_2 – S_1 transition dipole moment at the Coln. (c) Non-adiabatic coupling elements between S_2 and S_1 at the Coln, q_1 —element left and q_2 —element right.

surface exhibits a double-well structure with a barrier in between. The left well includes the S_2 minimum, and the right one coincides with the minimum energy Coln. The absolute value of the TDM between S_2 and S_1 and the non-adiabatic-couplings (NACs) are displayed in Figs. 7(b) and 7(c). Further information about the simulation setup can be found in Sec. I of the [supplementary material](#).

Uracil introduces new aspects compared to the model. Primarily, its dynamics takes place on coupled bound states and is not dissociative, and thus, the wave packet will pass the coupling area several times. In addition, the shape and size of the NACs and the TDM differ from those of the idealized model system. For uracil, not only a single Coln but parts of the Coln seam are included, and thus, coupling can occur all along the seam and the behavior of the geometric phase becomes more complex. The absolute value of the TDM is strongly structured and very localized along the seam, but with regard to Sec. III C, in principle, it is large enough to allow for a CEP control. On the other hand, there are regions along the seam where the values of the TDM drop to almost zero. The combination of NACs and TDM in uracil leads to a situation where the control is sensitive to the direction the wave packet hits the seam. Two different starting conditions for the simulations are investigated. For the first, *uracil A*, the dynamics starts on the S_2 state at the Franck-Condon point, assuming a delta pulse excitation. The wave packet motion is indicated in white in Fig. 7(a), its initial oscillation by a solid line, and the subsequent splitting by dashed lines. After the first oscillation period (about 80 fs), the barrier is reached. The parts of the wave packet passing the barrier successively reach the Coln seam. In the *uracil B* case, a Gaussian shaped wave packet is placed at a position shifted to negative q_1 values with respect to the Franck-Condon point and is marked by the red cross. From here, most of the wave packet directly reaches the Coln seam in a quite localized way. This relaxation pathway is shown in red in Fig. 7(a). The evolution of the population for both starting conditions can be found in Sec. II of the [supplementary material](#).

A. Optimization of the CEP pulse parameters

First, the optimal control window is determined as in the model system by varying the central frequency ω_0 and the time zero t_0 of the laser pulse. The pulse width is set to 10 fs FWHM for all following studies. The wave packet crosses the seam multiple times so that the CEP efficiency $\Gamma(t)$ will not converge to a constant value. Instead, the end of the laser interaction $t_0 + \text{FWHM}$ is used to record $\Gamma(t)$. As the target state, we refer to the S_2 state. Electric field strengths of 0.15 GV cm^{-1} for *uracil A* and 0.10 GV cm^{-1} for *uracil B* are used. In Fig. 8, the resulting two-dimensional optimization landscapes are shown for *uracil A* (top) and *uracil B* (bottom).

Both landscapes are more complex compared to the model system (Fig. 3). The CEP efficiency of *uracil A*, shown in Fig. 8(a), has four maxima. The largest value of 5% is found for a frequency of 0.2 eV and a t_0 value of 90 fs. Another maximum is located 10 fs earlier for the same frequency. In this time period (80 fs to 90 fs), the first part of the wave packet reaches the vicinity of the Coln seam. The maxima for later times (100 fs to 110 fs) are shifted toward higher (0.3 eV) and lower (0.1 eV) frequencies and correspond to the subsequent parts of the wave packet. In the following, we will focus on the largest maximum at 0.2 eV and 90 fs. For *uracil B*, shown in Fig. 8(b), only two significant maxima are found. The largest CEP efficiencies form an extended plateau located in the range from 30 fs to 35 fs and from 0.05 eV to 0.20 eV with a global maximum of 30% CEP efficiency at 30 fs and 0.2 eV. A further local maximum is located at a t_0 value of 30 fs and a frequency of 0.3 eV. Again, the time window reflects the time period in which the wave packet reaches the

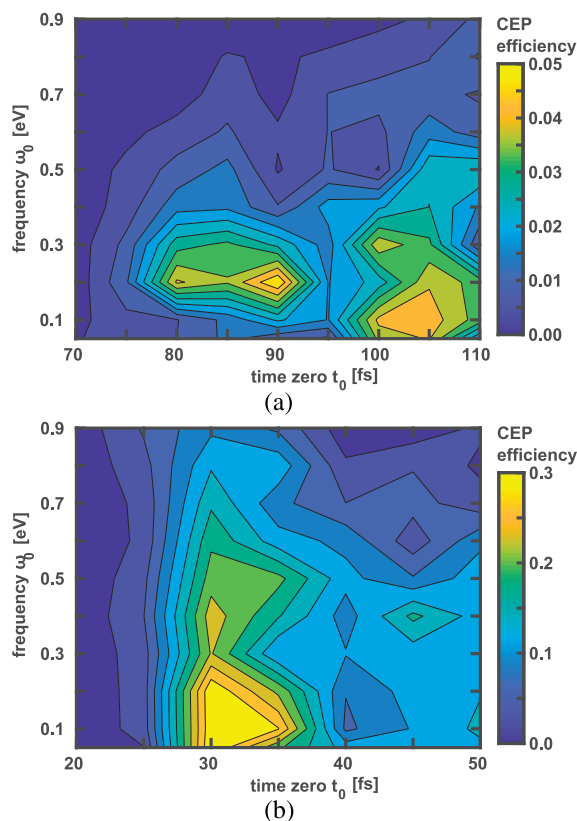


FIG. 8. Two-dimensional optimization landscapes of the CEP efficiency for *uracil A* (a) and *uracil B* (b) determined by varying the central frequency ω_0 of the pulse and its timing classified by the value of its time zero t_0 related to the propagation time of the wave packet.

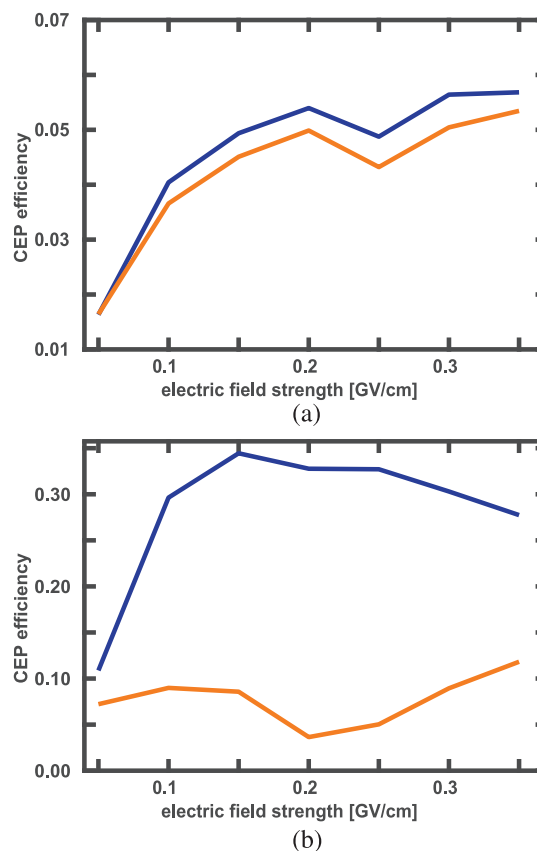


FIG. 9. CEP efficiency determined for increasing electric field strengths with (blue) and without (orange) NACs included for *uracil A* (a) and *uracil B* (b).

vicinity of the CoIn seam for the first time. For this first event, more than 50% of the population is transferred. The maximum efficiency for *uracil B* is nearly six times larger and concentrated on two main peaks, defining an extended time and frequency window. The differences between A and B are due to the fact that the wave packets approach the CoIn seam along different pathways and thereby experience the NACs and the TDM differently. The A-pathway [white lines in Fig. 7(a)] lies between cases 4A and 4B of the model system (Fig. 2) but with a much more localized TDM. This explains the low CEP efficiency confined to small areas. For case *uracil B*, the experienced parts of the NACs and the TDM are similar to those in model case 1A and the TDM near the seam is more extended compared to that in *uracil A*.

The next optimized parameter is the electric field strength. As shown in Sec. III C, this parameter has a strong influence on the CEP induced processes. The CEP efficiency is determined for both starting conditions using the previous optimized values for ω_0 and t_0 in combination with a FWHM of 10 fs. The results of these calculations are visualized in Fig. 9.

For *uracil A* [see Fig. 9(a)], the CEP efficiency with (blue line) and without (orange line) NACs included shows a very similar

response. After an initial increase, the CEP efficiency converges to a value of about 5.5% with a small dip at 0.25 GV cm⁻¹. Overall, the efficiency obtained with NACs is slightly larger. The CEP efficiency of *uracil B*, shown in Fig. 9(b), behaves completely different. When NACs (blue line) are included, the efficiency rises rapidly, reaches a maximum for 0.15 GV cm⁻¹, and decreases slowly afterward. Without NACs (orange line), the efficiency stays on a significant lower level around an average value of 0.1. Obviously, the underlying process leading to the CEP efficiency is different for both cases. For *uracil A*, the simulations with and without NACs show qualitatively and quantitatively a similar behavior, which is an indication that the field-only process dominates. The CEP efficiency of *uracil B* differs strongly whether or not NACs are taken into account. This suggests that now also the interference process is responsible for the CEP efficiency. Just like for the model system, the higher field strengths used are sufficient to shift the PESs and deform the CoIn for a short timescale.

B. Optimal CEP pulses

So far, we restricted our analysis to the CEP efficiency at $t_0 + \text{FWHM}$, shortly after the laser pulse. However, the uracil wave

packet crosses the CoIn seam multiple times, which influences the long-term evolution of the CEP efficiency. We characterize the underlying mechanism following the CEP dependence of the population in time. For *uracil A*, the optimal laser parameters were determined to be $t_0 = 90$ fs, $E_{\max} = 0.2$ GV cm $^{-1}$, and $\omega_0 = 0.2$ eV. The width of the pulse was set to 10 fs. The temporal evolution of the CEP efficiency after t_0 and the CEP dependent population of the target state S_2 at three selected times are shown in Fig. 10.

The CEP efficiency decreases fast already after the maximal field strength of the laser pulse at 90 fs. When the laser pulse is no longer present at approximately 100 fs, the efficiency decreases more slowly. A second large step is observed at 170 fs. A final value of about 3.0% is reached at 200 fs. The field-only CEP efficiency is constant after the laser pulse; its value is plotted as a dashed black line. From 120 fs on, it is higher than the combined effect (blue line). Interestingly, the CEP efficiency survives for the complete simulation

time, although several crossings of the CoIn seam occurred modifying the phase information of the wave packet. In order to analyze the CEP dependence of the population [see Fig. 10(b)], its mean difference is recorded for three selected times marked as vertical lines in Fig. 10(a). The mean difference of the population is chosen for better visualization. The first line at $t_0 + \text{FWHM}$ (100 fs, green) corresponds to the time when the laser pulse is over. The second point (red line) is taken at 150 fs and the third one (yellow line) at the end of the simulation time (197 fs). For all three times, the CEP dependent population shows a sinusoidal oscillation with a periodicity of approximately π , which indicates that, for *uracil A*, the field-only mechanism is the dominating process in the complete simulation time.

The optimal laser parameters for *uracil B* are $t_0 = 30$ fs, $E_{\max} = 0.15$ GV cm $^{-1}$, and $\omega_0 = 0.2$ eV. The temporal evolution of the CEP efficiency starting at t_0 and the CEP dependent population at

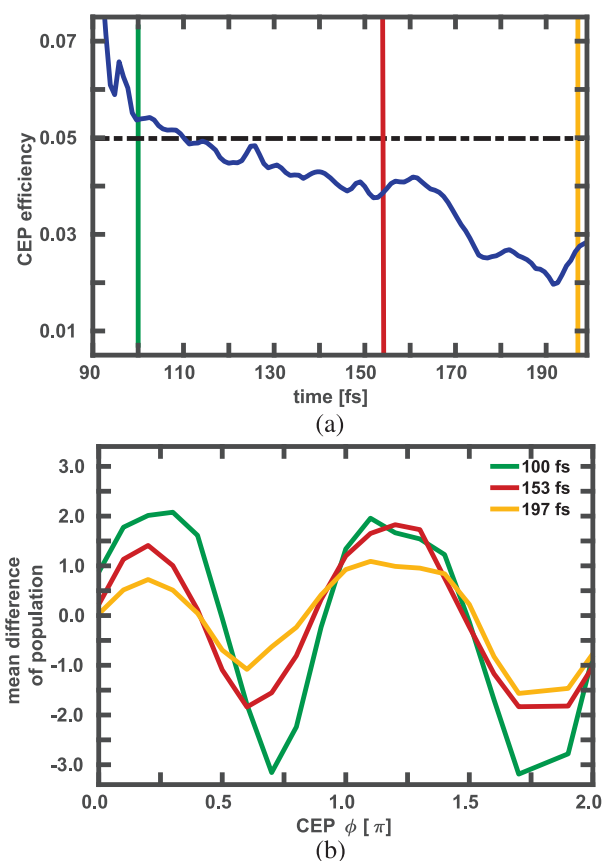


FIG. 10. (a) Temporal evolution of the CEP efficiency for *uracil A* after t_0 using a laser pulse with optimized parameters and a field strength of 0.2 GV cm $^{-1}$. The black dotted line represents the obtained efficiency without NACs included. The blue line denotes the efficiency obtained with the coupling elements included. The vertical colored lines indicate the points in time that are examined more closely. (b) Mean difference of the phase-dependent populations for different points in times obtained including the NACs.

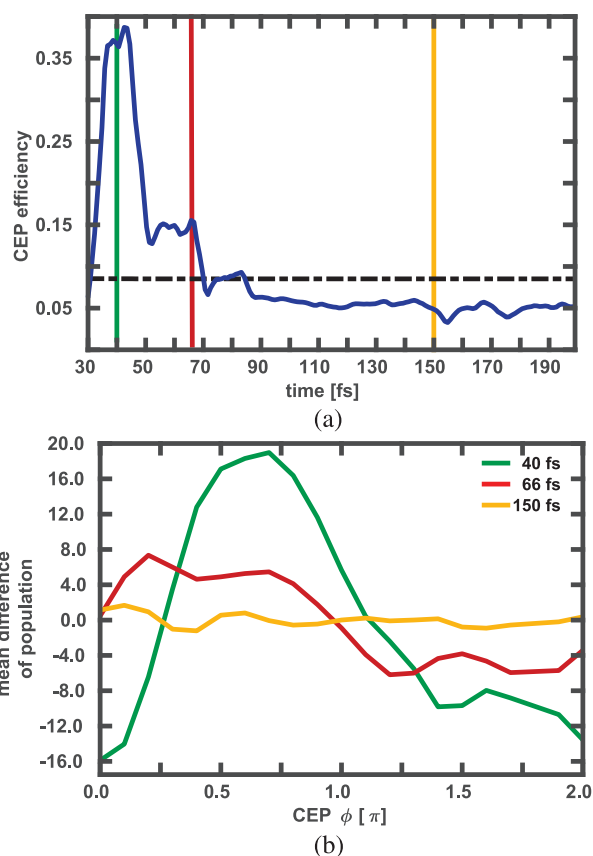


FIG. 11. (a) Temporal evolution of the CEP efficiency for *uracil B* after t_0 using a laser pulse with optimized parameters and a field strength of 0.15 GV cm $^{-1}$. The black dotted line represents the obtained efficiency without NACs included. The blue line denotes the efficiency obtained with the coupling elements included. The vertical colored lines indicate the points in time that are examined more closely. (b) Mean difference of the CEP dependent population for different points in times obtained including the NACs.

three selected times are shown in Fig. 11. Again, the mean difference of the population is plotted.

The higher CEP efficiency for *uracil B* persists for the complete simulation time [Fig. 11(a)]. The main peak occurs between 40 fs and 45 fs, which is 10 fs–15 fs after the field maximum. Thereafter, the efficiency drops in two smaller steps to a value of 6% at 90 fs reflecting the back and forth crossing of the CoIn seam of a still localized wave packet. For the remaining simulation time, the CEP efficiency stays almost constant. The field-only efficiency (black dotted line) is smaller up to 90 fs. Again, the CEP dependence persists for the complete simulation time. The analysis of the CEP dependent population [see Fig. 11(b)] is performed at three points in time, marked as colored lines. Again, the first time at $t_0 + \text{FWHM}$ (40 fs) is taken in the maximum of the efficiency. The second point at 66 fs is at the edge of the second step. The third point is taken at 150 fs in an area where the efficiency stays constant. For the first time (green curve), the CEP dependent population shows a strongly deformed

sinusoidal dependence with no clear periodicity. For the second time (red curve), still some kind of sinusoidal behavior is observed, which is washed out for the third time (yellow curve). This ambiguous periodicity and form are indicators (see Sec. III C) for strong interaction between the interference and the field-only mechanism. To weaken the field-only process, we lower the field strengths to 0.05 GV cm^{-1} (see Fig. S4 in the supplementary material) and 0.025 GV cm^{-1} (see Fig. 12).

In both cases, the achieved CEP efficiency is lower, but its temporal evolution stays qualitatively the same. The CEP dependent population at the same selected points in time now shows a clear sinusoidal form with a periodicity of 2π . This is most distinct for the lowest field strength. These findings confirm our conclusions from the model system (Sec. III C): For low electric field strengths, the dominating mechanism is the interference process that can be identified by the 2π periodicity. Overall, for both starting conditions, the CEP efficiency is surprisingly long-lived and not impaired by the nuclear wave packet motion. Differences are found in magnitude and for the temporal evolution. These are also reflected in the CEP dependent population. Their periodicity classifies the mechanism. In the *uracil A* case, the field-only process dominates, and in *uracil B*, the interference process becomes important. For low field conditions, the 2π periodicity is clearly seen, whereas higher field strengths induce both processes. In general, the field-only process becomes dominant for high field strengths or when the interplay of the NACs and TDM as in *uracil A* does not lead to constructive interference.

V. CONCLUSION

Conical intersections are known to be crucial branching points for excited state reactions. To control the dynamics at these sensitive points, we examined the controllability using the waveform of a CEP stabilized few-cycle pulse in the IR. Performing quantum dynamical simulations on coupled potential energy surfaces, the necessary boundary conditions were defined and appropriate laser pulses were optimized. In the first part, we focused on an analytical model system, describing a dissociation process with two competing pathways connected via a CoIn. Within the model system, we were able to study the mutual influence of the decisive molecular properties, the non-adiabatic coupling elements, and the transition dipole moment. CEP control is only possible if the interplay of these two fundamental quantities allows for constructive interference. For this, their shape along the direction of the wave packet motion is most important. Via optimization of the laser parameters, we could identify two different processes, which both contribute to the overall CEP efficiency. The optimal few-cycle CEP pulse creates a superposition with a well-defined phase-relation just before the CoIn is reached. Together with the geometric phase, this creates an interference when the superposition passes through the CoIn. This interference process modifies the branching ratio after the CoIn. The second process, the field-only mechanism, occurs due to the few-cycle waveform of the IR pulse and is not affected by the NACs. Depending on the molecular system and the chosen laser parameters, both processes can be active, vary in their strength, and even obstruct each other. Assuming ideal conditions for the NACs and TDM, we were able to optimize a laser pulse that leads to a CEP efficiency of 40%, which is almost entirely based on the interference process. This large efficiency is favored by the dissociative character of the model, which leads to a situation where

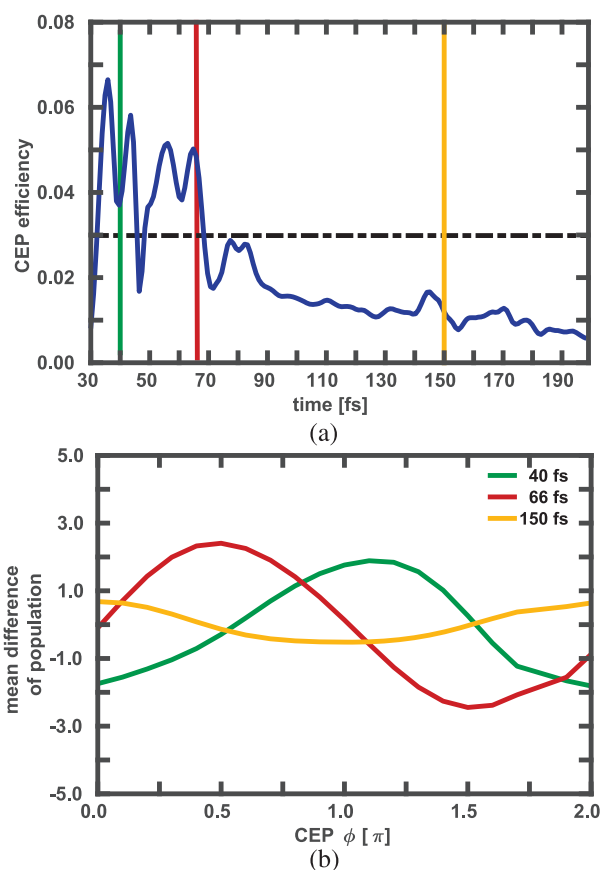


FIG. 12. (a) Temporal evolution of the CEP efficiency for *uracil B* after t_0 using a laser pulse with optimized parameters and a field strength of 0.025 GV cm^{-1} . The black dotted line represents the obtained efficiency without NACs included. The blue line denotes the efficiency obtained with the coupling elements included. The vertical colored lines indicate the points in time that are examined more closely. (b) Mean difference of the CEP dependent population for different points in times obtained including the NACs.

a very localized wave packet passes the CoIn only once. In the second part, we focus on a more realistic molecular system, the nucleobase uracil, whose CoIn's ensure its photostability. We applied the CEP-control scheme to the population dynamics between the S_2 and the S_1 state. As both states are strongly bound, multiple crossings of the CoIn's occur. These molecular boundary conditions are quite challenging for CEP control. Nevertheless, we were able to achieve a short time CEP efficiency between 6% and 37% depending on the two starting conditions. For the first, the excited state wave packet oscillates around the S_2 minimum before parts of it are able to cross the barrier and reach the CoIn. In the second case, the wave packet directly approaches the barrier and, thereafter, the CoIn in a localized form. Besides the overall CEP efficiency, the starting conditions determine also the mechanism. The active parts of the NACs and the TDM for both pathways vary between situations, which enable the interference process or rather prevent it. This finding shows that if a wave packet moves along a suitable pathway toward a CoIn, it is possible to achieve a high degree of CEP control. Some molecular systems may provide these pathways naturally, and for others, such a pathway can be opened by the use of specially shaped laser pulses in the excitation process.⁸ We demonstrated that the control of the branching ratio induced by a CoIn via a CEP pulse is a general concept. The control is most effective for a system where a localized wave packet crosses the CoIn only once and the TDM is extended in this area, but even for a more complex chemical system as uracil situations can be found where a CEP control is realizable. The CEP efficiency is long-lived, which should be favorable for experimental detection. In addition, we showed for the model system that the CEP control tolerates pulse widths up to 30 fs for the IR pulse.

SUPPLEMENTARY MATERIAL

See the [supplementary material](#) for the details of the wave packet simulation setup and the population dynamics without any CEP laser pulse for both the model system and uracil. In addition, the temporal evolution of the CEP efficiency and the CEP dependent population for *uracil B* obtained with the optimized laser parameters and a field strength of 0.05 GV cm^{-1} are shown.

AUTHORS' CONTRIBUTIONS

F.S. and T.S. contributed equally to this work. T.S. and R.d.V.R. initiated the project. F.S. performed the calculations on the model system, and L.B. and T.S. did the simulations for uracil. F.S., T.S., and R.D.V.R. analyzed and interpreted the results. All authors contributed to the final version of the manuscript.

ACKNOWLEDGMENTS

The authors gratefully acknowledge the DFG Normalverfahren and the Munich Center of Advanced Photonics (MAP).

APPENDIX: ADIABATIZATION OF THE MODEL SYSTEM

In this section, the transformation of the diabatic Hamiltonian matrix [Eq. (A1)] of the model system to the adiabatic picture

is described in detail. The model system consists of the three diabatic electronic states V_0 , V_1 , and V_2 and the diabatic coupling element D_{12} ,

$$\hat{H}_{dia} = \begin{pmatrix} \hat{T} + V_0 & 0 & 0 \\ 0 & \hat{T} + V_1 & D_{12} \\ 0 & D_{12} & \hat{T} + V_2 \end{pmatrix}. \quad (\text{A1})$$

The diagonalization^{1,2,48} is done using a unitary transformation matrix U [Eq. (A2)],

$$U = \begin{pmatrix} 1 & 0 & 0 \\ 0 & \cos(\theta) & +\sin(\theta) \\ 0 & -\sin(\theta) & \cos(\theta) \end{pmatrix}. \quad (\text{A2})$$

Here, the angle θ is the adiabatic–diabatic transformation angle (or shortened the mixing angle)^{1,2,47} between the coupled diabatic states V_1 and V_2 . Based on Eq. (A3), this angle θ is defined in a range of $[-0.5\pi, +0.5\pi]$,

$$\theta = \frac{1}{2} \arctan\left(\frac{2D_{12}}{V_2 + V_1}\right). \quad (\text{A3})$$

Following θ along a closed path of nuclear configurations encircling the CoIn, a phase shift of π is observed. This phase shift is called the geometric phase or Pancharatnam–Berry phase^{24,25} and leads to a sign change of adiabatic electronic wavefunctions, if a closed path around the CoIn is followed. Within our two-dimensional model, we can observe the full phase shift of π since we describe the full branching space. For higher dimensional systems, where the chosen sub-space is not identical to the branching space, no clear statement can be made about the phase behavior.⁴⁹ Using the transformation matrix (A2), the adiabatic eigenfunctions can be expressed as a linear combination of the diabatic ones,

$$|\Psi_0^{adi}\rangle = |\Phi_0^{dia}\rangle, \quad (\text{A4})$$

$$|\Psi_1^{adi}\rangle = +\cos(\theta)|\Phi_1^{dia}\rangle + \sin(\theta)|\Phi_2^{dia}\rangle, \quad (\text{A5})$$

$$|\Psi_2^{adi}\rangle = -\sin(\theta)|\Phi_1^{dia}\rangle + \cos(\theta)|\Phi_2^{dia}\rangle. \quad (\text{A6})$$

The corresponding adiabatic states can be calculated from the diabatic states,

$$S_0 = V_0, \quad (\text{A7})$$

$$S_1 = \frac{V_2 + V_1}{2} - \sqrt{\left(\frac{V_2 - V_1}{2}\right)^2 + D_{12}^2}, \quad (\text{A8})$$

$$S_2 = \frac{V_2 + V_1}{2} + \sqrt{\left(\frac{V_2 - V_1}{2}\right)^2 + D_{12}^2}. \quad (\text{A9})$$

The non-adiabatic coupling elements τ_{12} required for the dynamics can be determined as derivatives of the mixing angle θ (A3),^{1,2,50,51}

$$\begin{aligned}\tau_{12} &= \langle \Psi_1^{adi} | \nabla | \Psi_2^{adi} \rangle + \frac{1}{2} \langle \Psi_1^{adi} | \nabla^2 | \Psi_2^{adi} \rangle \\ &= \nabla \theta + \frac{1}{2} \nabla^2 \theta.\end{aligned}\quad (\text{A10})$$

Since the $\nabla^2 \theta$ term, which contains the second derivatives, is much smaller than the $\nabla \theta$ term, it can be neglected in first approximation. However, this would lead to a non-Hermitian Hamiltonian operator. To avoid this, the non-Hermitian behavior can be compensated for by using the partition equation (A11).^{49,52} Here, the term $\langle \nabla \Psi_1^{adi} | \nabla \Psi_2^{adi} \rangle$ can be neglected without losing the hermiticity,

$$\langle \Psi_1^{adi} | \nabla^2 | \Psi_2^{adi} \rangle = \nabla \langle \Psi_1^{adi} | \nabla | \Psi_2^{adi} \rangle - \langle \nabla \Psi_1^{adi} | \nabla \Psi_2^{adi} \rangle. \quad (\text{A11})$$

There are two possible ways to handle the phase shift in θ ,^{50,51} using the absolute value of θ (model A) or using the full value (model B) of it. In both cases, there is a discontinuous point along the closed cycle around the CoIn, but it appears that, at different positions and for model A, the phase shift is neglected. This results in two different coupling pairs with a different number of nodal planes in the resulting elements.

DATA AVAILABILITY

The data that support the findings of this study are available from the corresponding author upon reasonable request.

REFERENCES

- D. R. Yarkony, "Diaboloical conical intersections," *Rev. Mod. Phys.* **68**, 985–1013 (1996).
- M. Baer, "Introduction to the theory of electronic non-adiabatic coupling terms in molecular systems," *Phys. Rep.* **358**, 75–142 (2002).
- M. S. Schuurman and A. Stolow, "Dynamics at conical intersections," *Annu. Rev. Phys. Chem.* **69**, 427–450 (2018).
- R. Send and D. Sundholm, "Stairway to the conical intersection: A computational study of the retinal isomerization," *J. Phys. Chem. A* **111**, 8766–8773 (2007).
- D. Polli, P. Altoè, O. Weingart, K. M. Spillane, C. Manzoni, D. Brida, G. Tomasello, G. Orlandi, P. Kukura, R. A. Mathies, M. Garavelli, and G. Cerullo, "Conical intersection dynamics of the primary photoisomerization event in vision," *Nature* **467**, 440–443 (2010).
- L. Serrano-Andrés and M. Merchán, "Are the five natural DNA/RNA base monomers a good choice from natural selection? A photochemical perspective," *J. Photochem. Photobiol., C* **10**, 21–32 (2009).
- L. Blancafort, "Photochemistry and photophysics at extended seams of conical intersection," *ChemPhysChem* **15**, 3166–3181 (2014).
- D. Keefer, S. Thallmair, S. Matsika, and R. de Vivie-Riedle, "Controlling photorelaxation in uracil with shaped laser pulses: A theoretical assessment," *J. Am. Chem. Soc.* **139**, 5061–5066 (2017).
- S. Reiter, D. Keefer, and R. de Vivie-Riedle, "RNA environment is responsible for decreased photostability of uracil," *J. Am. Chem. Soc.* **140**, 8714–8720 (2018).
- B. L. Feringa, R. A. van Delden, N. Koumura, and E. M. Geertsema, "Chiroptical molecular switches," *Chem. Rev.* **100**, 1789–1816 (2000).
- A. Nenov, T. Cordes, T. T. Herzog, W. Zinth, and R. de Vivie-Riedle, "Molecular driving forces for z/e isomerization mediated by heteroatoms: The example hemithioindigo," *J. Phys. Chem. A* **114**, 13016–13030 (2010).
- B. Maerz, S. Wiedbrauk, S. Oesterling, E. Samoylova, A. Nenov, P. Mayer, R. de Vivie-Riedle, W. Zinth, and H. Dube, "Making fast photoswitches faster—using Hammett analysis to understand the limit of donor–acceptor approaches for faster hemithioindigo photoswitches," *Chem. -Eur. J.* **20**, 13984–13992 (2014).
- S. Kassem, T. van Leeuwen, A. S. Lubbe, M. R. Wilson, B. L. Feringa, and D. A. Leigh, "Artificial molecular motors," *Chem. Soc. Rev.* **46**, 2592–2621 (2017).
- F. F. Graupner, T. T. Herzog, F. Rott, S. Oesterling, R. de Vivie-Riedle, T. Cordes, and W. Zinth, "Photoisomerization of hemithioindigo compounds: Combining solvent- and substituent- effects into an advanced reaction model," *Chem. Phys.* **515**, 614–621 (2018).
- R. Wilcken, M. Schildhauer, F. Rott, L. A. Huber, M. Guentner, S. Thumser, K. Hoffmann, S. Oesterling, R. de Vivie-Riedle, E. Riedle, and H. Dube, "Complete mechanism of hemithioindigo motor rotation," *J. Am. Chem. Soc.* **140**, 5311–5318 (2018).
- T. Brixner and G. Gerber, "Quantum control of gas-phase and liquid-phase femtochemistry," *ChemPhysChem* **4**, 418–438 (2003).
- M. F. Kling, P. von den Hoff, I. Znakovskaya, and R. de Vivie-Riedle, "(Sub-)femtosecond control of molecular reactions via tailoring the electric field of light," *Phys. Chem. Chem. Phys.* **15**, 9448–9467 (2013).
- S. Thallmair, D. Keefer, F. Rott, and R. de Vivie-Riedle, "Simulating the control of molecular reactions via modulated light fields: From gas phase to solution," *J. Phys. B: At., Mol. Opt. Phys.* **50**, 082001 (2017).
- K.-M. Weitzel, "Controlling the electrons provides means for controlling chemistry," *ChemPhysChem* **8**, 213–215 (2007).
- M. F. Kling and M. J. J. Vrakking, "Attosecond electron dynamics," *Annu. Rev. Phys. Chem.* **59**, 463–492 (2008).
- I. Znakovskaya, P. von den Hoff, N. Schirmel, G. Urbasch, S. Zhrebtsov, B. Bergues, R. de Vivie-Riedle, K.-M. Weitzel, and M. F. Kling, "Waveform control of orientation-dependent ionization of DCL in few-cycle laser fields," *Phys. Chem. Chem. Phys.* **13**, 8653–8658 (2011).
- I. Znakovskaya, P. von den Hoff, G. Marcus, S. Zhrebtsov, B. Bergues, X. Gu, Y. Deng, M. J. J. Vrakking, R. Kienberger, F. Krausz, R. de Vivie-Riedle, and M. F. Kling, "Subcycle controlled charge-directed reactivity with few-cycle midinfrared pulses," *Phys. Rev. Lett.* **108**, 063002 (2012).
- A. Alnaser, M. Kübel, R. Siemering, B. Bergues, N. G. Kling, K. Betsch, Y. Deng, J. Schmidt, Z. Alahmed, A. Azzeer, J. Ullrich, I. Ben-Itzhak, R. Moshhammer, U. Kleineberg, F. Krausz, R. de Vivie-Riedle, and M. Kling, "Subfemtosecond steering of hydrocarbon deprotonation through superposition of vibrational modes," *Nat. Commun.* **5**, 3800 (2014).
- H. C. Longuet-Higgins, U. Öpik, M. H. L. Pryce, and R. A. Sack, "Studies of the Jahn-Teller effect. II. The dynamical problem," *Proc. R. Soc. London, Ser. A* **244**, 1–16 (1958).
- M. V. Berry, "Quantal phase factors accompanying adiabatic changes," *Proc. R. Soc. London, Ser. A* **392**, 45–57 (1984).
- J. L. Herek, W. Wohlleben, R. J. Cogdell, D. Zeidler, and M. Motzkus, "Quantum control of energy flow in light harvesting," *Nature* **417**, 533–535 (2002).
- R. Mitrić, M. Hartmann, J. Pittner, and V. Bonačić-Koutecký, "New strategy for optimal control of femtosecond pump-dump processes," *J. Phys. Chem. A* **106**, 10477–10481 (2002).
- D. Geppert, A. Hofmann, and R. de Vivie-Riedle, "Control of a collision complex via a conical intersection," *J. Chem. Phys.* **119**, 5901–5906 (2003).
- M. Abe, Y. Ohtsuki, Y. Fujimura, and W. Domcke, "Optimal control of ultrafast cis-trans photoisomerization of retinal in rhodopsin via a conical intersection," *J. Chem. Phys.* **123**, 144508 (2005).
- D. Townsend, B. J. Sussman, and A. Stolow, "A Stark future for quantum control," *J. Phys. Chem. A* **115**, 357–373 (2011).
- B. Wolter, M. G. Pullen, A.-T. Le, M. Baudisch, K. Doblhoff-Dier, A. Senftleben, M. Hemmer, C. D. Schröter, J. Ullrich, T. Pfeifer, R. Moshhammer, S. Gräfe, O. Vendrell, C. D. Lin, and J. Biegert, "Ultrafast electron diffraction imaging of bond breaking in di-ionized acetylene," *Science* **354**, 308–312 (2016).

- ³²N. Moiseyev, M. Šindelka, and L. S. Cederbaum, "Laser-induced conical intersections in molecular optical lattices," *J. Phys. B: At., Mol. Opt. Phys.* **41**, 221001 (2008).
- ³³G. J. Halász, M. Šindelka, N. Moiseyev, L. S. Cederbaum, and Á. Vibók, "Light-induced conical intersections: Topological phase, wave packet dynamics, and molecular alignment," *J. Phys. Chem. A* **116**, 2636–2643 (2012).
- ³⁴A. Natan, M. R. Ware, V. S. Prabhudesai, U. Lev, B. D. Bruner, O. Heber, and P. H. Bucksbaum, "Observation of quantum interferences via light-induced conical intersections in diatomic molecules," *Phys. Rev. Lett.* **116**, 143004 (2016).
- ³⁵C. Liekhuis-Schmaltz, G. A. McCracken, A. Kaldun, J. P. Cryan, and P. H. Bucksbaum, "Coherent control using kinetic energy and the geometric phase of a conical intersection," *J. Chem. Phys.* **145**, 144304 (2016).
- ³⁶C. Arnold, O. Vendrell, R. Welsch, and R. Santra, "Control of nuclear dynamics through conical intersections and electronic coherences," *Phys. Rev. Lett.* **120**, 123001 (2018).
- ³⁷S. Tommasi, M. F. Denissenko, and G. P. Pfeifer, "Sunlight induces pyrimidine dimers preferentially at 5-methylcytosine bases," *Cancer Research* **57**, 4727–4730 (1997).
- ³⁸L. Esposito, A. Banyasz, T. Douki, M. Perron, D. Markovitsi, and R. Improta, "Effect of C5-methylation of cytosine on the photoreactivity of DNA: A joint experimental and computational study of TCG trinucleotides," *J. Am. Chem. Soc.* **136**, 10838–10841 (2014).
- ³⁹L. Holmegaard, J. H. Nielsen, I. Nevo, H. Stapelfeldt, F. Filsinger, J. Küpper, and G. Meijer, "Laser-induced alignment and orientation of quantum-state-selected large molecules," *Phys. Rev. Lett.* **102**, 023001 (2009).
- ⁴⁰J. L. Hansen, H. Stapelfeldt, D. Dimitrovski, M. Abu-samha, C. P. J. Martiny, and L. B. Madsen, "Time-resolved photoelectron angular distributions from strong-field ionization of rotating naphthalene molecules," *Phys. Rev. Lett.* **106**, 073001 (2011).
- ⁴¹J. L. Hansen, L. Holmegaard, J. H. Nielsen, H. Stapelfeldt, D. Dimitrovski, and L. B. Madsen, "Orientation-dependent ionization yields from strong-field ionization of fixed-in-space linear and asymmetric top molecules," *J. Phys. B: At., Mol. Opt. Phys.* **45**, 015101 (2011).
- ⁴²H. Niikura, F. Légaré, R. Hasbani, M. Y. Ivanov, D. M. Villeneuve, and P. B. Corkum, "Probing molecular dynamics with attosecond resolution using correlated wave packet pairs," *Nature* **421**, 826–829 (2003).
- ⁴³M. F. Kling, J. Rauschenberger, A. J. Verhoef, E. Hasović, T. Uphues, D. B. Milošević, H. G. Müller, and M. J. J. Vrakking, "Imaging of carrier-envelope phase effects in above-threshold ionization with intense few-cycle laser fields," *New J. Phys.* **10**, 025024 (2008).
- ⁴⁴G. Sansone, F. Kelkensberg, J. F. Pérez-Torres, F. Morales, M. F. Kling, W. Siu, O. Ghafur, P. Johnsson, M. Swoboda, E. Benedetti, F. Ferrari, F. Lépine, J. L. Sanz-Vicario, S. Zharebtsov, I. Znakovskaya, A. L'Huillier, M. Y. Ivanov, M. Nisoli, F. Martin, and M. J. J. Vrakking, "Electron localization following attosecond molecular photoionization," *Nature* **465**, 763–766 (2010).
- ⁴⁵S. Kangaparambil, V. Hanus, M. Dörner-Kirchner, P. He, S. Larimian, G. Paulus, A. Baltuška, X. Xie, K. Yamanouchi, F. He, E. Lötstedt, and M. Kitzler-Zeiler, "Generalized phase sensitivity of directional bond breaking in the laser-molecule interaction," *Phys. Rev. Lett.* **125**, 023202 (2020).
- ⁴⁶P. Cattaneo and M. Persico, "Wave packet dynamics in the presence of a conical intersection," *J. Phys. Chem. A* **101**, 3454–3460 (1997).
- ⁴⁷S. Matsika and P. Krause, "Nonadiabatic events and conical intersections," *Annu. Rev. Phys. Chem.* **62**, 621–643 (2011).
- ⁴⁸D. Simah, B. Hartke, and H.-J. Werner, "Photodissociation dynamics of H₂S on new coupled *ab initio* potential energy surfaces," *J. Chem. Phys.* **111**, 4523–4534 (1999).
- ⁴⁹A. Hofmann and R. de Vivie-Riedle, "Adiabatic approach for ultrafast quantum dynamics mediated by simultaneously active conical intersections," *Chem. Phys. Lett.* **346**, 299–304 (2001).
- ⁵⁰A. F. Izmaylov, J. Li, and L. Joubert-Doriol, "Diabatic definition of geometric phase effects," *J. Chem. Theory Comput.* **12**, 5278–5283 (2016).
- ⁵¹I. G. Ryabinkin, L. Joubert-Doriol, and A. F. Izmaylov, "Geometric phase effects in nonadiabatic dynamics near conical intersections," *Acc. Chem. Res.* **50**, 1785–1793 (2017).
- ⁵²W. Domcke and G. Stock, "Theory of ultrafast nonadiabatic excited-state processes and their spectroscopic detection in real time," in *Advances in Chemical Physics* (John Wiley & Sons, 2007), pp. 1–169.

COUPLED NUCLEAR AND ELECTRON DYNAMICS: THE NEMOL ANSATZ

This chapter is directly connected to the idea of controlling the nuclear and electron dynamics in molecular systems. An accurate description of the effect of an ultrashort laser pulse on a molecular system requires a sophisticated approach, which is able to capture both the electron motion and the nuclear motion. Many methods in the literature, which are able to describe the electron dynamics, are often modified versions of their well-known quantum chemical counter parts, like time-dependent Hartree-Fock [232], time-dependent density-functional theory [233], time-dependent configuration-interaction [234, 235] and time-dependent coupled-cluster [236, 237]. The main drawback of these theories is the focus on the evolution of the electronic subsystem and the negligence of the nuclear motion. However nuclear motion in general causes decoherence in molecules leading to the situation, where electronic wave packets are strongly influenced by the nuclear dynamics and exist only for short time scales [60, 95–99, 229]. The technique used most to include nuclear motion in the simulation of electron dynamics is the semiclassical Ehrenfest ansatz [238–247]. Here the classical nuclei propagate on a mean potential surface corresponding to an electronic superposition state, while the electron dynamics is treated quantum mechanically. Beside the problems [248] arising from this mean-field approach, this method does not reflect the quantum nature of the nuclei, which becomes important for treating excitation by ultrashort laser pulses and non-adiabatic transitions. It should be mentioned that there are approaches like multiconfigurational Ehrenfest [249, 250], which also describe the nuclei quantum mechanically. A direct full-quantum mechanical treatment of the coupled electron and nuclear dynamics is only possible for three particle problems like H_2^+ or D_2^+ [251]. Larger systems require computationally very demanding methods based on a multi-configurational ansatz [252] or on the coupled description of nuclear and electronic flux [253, 254]. The most prominent method that allows to describe the coupled nuclear and electron dynamics on a quantum level is the exact factorization approach [255–259]. In this technique the time-dependent molecular Schrödinger equation is formulated as two coupled equations, one for the nuclear wave function and one for the conditional electronic wave function. Both wave functions are propagated on a single time-dependent potential energy surface.

Another approach that has similarities to the exact factorization formalism is the NEMol ansatz [60, 100–103]. Its further development is a central part of this chapter and the main focus of section 3.1. With the NEMol ansatz it is possible to calculate the temporal evolution of the electronic density coupled to a nuclear quantum dynamics calculation. In its original formulation it is based on a single centroid approach and was used for one-dimensional problems [60, 100–103]. Based on this formulation, the NEMol ansatz is now extended beyond this single geometry approximation to describe the coupled nuclear and electron dynamics beyond diatomics. A brief derivation of the old formulation and the key modifications of the new NEMol ansatz are given in the section 3.1. The new implementation is used to study the coupled nuclear and electron dynamics of the nucleobase uracil (section 3.2) and the small symmetric molecule NO_2 (section 3.3). For uracil the excitation with a short laser pulse is simulated explicitly and the coupled

dynamics during the photoexcitation and its modification by the relaxation via a CoIn seam is studied. In the NO₂ example the coupled dynamics is monitored and its temporal evolution is characterized by the coherent electron dynamics induced by a CoIn. Due to the decent structure of the coupling region in the NO₂ case the coherent dynamics is modulated with the help of the CEP control scheme. The resulting control of nuclear and electronic motion is discussed in section 3.3.

3.1 NEMol and its Extensions for Higher Dimensional Systems

The NEMol ansatz was developed and first published in 2008 [100] as an approach to describe the dynamics of electrons in molecules which exploits quantum dynamics and quantum chemistry "in a new way". In this purely quantum mechanical ansatz the quantum dynamical description of the nuclear motion is combined with the propagation of the electronic wavefunctions in the eigenstate basis. It was used to study the electron dynamics induced by ultrashort laser pulses in various diatomic species like CO [60, 101] or K₂ [102, 103]. With the help of NEMol, effects like electron localization [60, 100, 101] and electronic charge oscillations [102, 103] could be explained.

The starting point for NEMol is the total molecular wave function $\Psi_{tot}(r, R, t)$ which is setup as the sum over the electronic states with $\chi(R, t)$ the nuclear wave functions, $\varphi(r, t; R)$ the electronic wave functions, the nuclear and electronic coordinates R and r and the time t . In this ansatz both the electronic and the nuclear wave functions are explicitly time-dependent.

$$\Psi_{tot}(r, R, t) = \sum_i \chi_i(R, t) \cdot \varphi_i(r, t; R). \quad (3.1)$$

The electronic wave functions φ_i (hereafter referred to as uncoupled) depend parametrically on the nuclear coordinates R and define a multi-dimensional vector comprising the electronic states involved. Analogously, the total nuclear wave function χ_{tot} is given by a multi-dimensional vector composed of the nuclear wave function χ_i residing in the i -th PES. The propagation of the nuclear wave functions on the coupled PESs is done as described in section 2.1. It should be noted that in principle also other quantum dynamics methods like MCTDH could be used for the description of the nuclear dynamics. Multiplying $\Psi_{tot}(r, R, t)$ from the left with χ_{tot} and the subsequent integration over the nuclear coordinates R results in an expression of the coupled total electronic wave function $\Phi_{tot}(r, t; \langle R \rangle(t))$ [60, 100, 101].

$$\Phi_{tot}(r, t; \langle R \rangle(t)) = \int \chi_{tot}^*(R, t) \cdot \Psi_{tot}(r, R, t) dR = \begin{pmatrix} \Phi_1(r, t; \langle R \rangle(t)) \\ \Phi_2(r, t; \langle R \rangle(t)) \\ \vdots \\ \Phi_j(r, t; \langle R \rangle(t)) \end{pmatrix}, \quad (3.2)$$

$$\text{with } \langle R \rangle(t) = \sum_i \langle \chi_i(R, t) | R | \chi_i(R, t) \rangle_R. \quad (3.3)$$

The integration over R results in a parametrical dependence of the coupled total electronic wave function on the time-dependent expectation value of the position $\langle R \rangle(t)$ which is defined in equation 3.3. The nuclear geometry represented by $\langle R \rangle(t)$ changes with time and the $\Phi_{tot}(r, t; \langle R \rangle(t))$ is evaluated at this single position in the coordinate space. The individual components Φ_j of the total coupled electronic wave function are given by:

$$\Phi_j(r, t; \langle R \rangle(t)) = A_{jj}(t) \cdot \varphi_j(r, t; \langle R \rangle(t)) + \sum_{k \neq j} A_{jk}(t) \cdot \varphi_k(r, t; \langle R \rangle(t)), \quad (3.4)$$

$$\text{with } A_{jk}(t) = \langle \chi_j(R, t) | \chi_k(R, t) \rangle_R. \quad (3.5)$$

Each coupled electronic wave function Φ_j consists of two parts. The first one is defined by the uncoupled electronic wave function φ_j multiplied with the population $A_{jj}(t)$ of the respective state j . The second part is the sum over all other uncoupled electronic wave functions weighted with the nuclear overlap $A_{jk}(t)$ which specifies the degree of coherence induced between the two states j and k . Both the population and the nuclear overlap are time dependent reflecting, the transfer of population between states and

the motion of the nuclear wave packet encoded in the complex overlap terms. Both types of quantities are determined by the nuclear quantum dynamics simulation. If the coupling between the electronic states is weak, the nuclear wave functions propagate independently and the coherence term becomes zero. In this case, the coupled electronic wave functions Φ_j in equation 3.4 become equivalent to the uncoupled electronic wave function φ_j . As stated in the beginning the uncoupled electronic wave functions are explicitly time-dependent in the NEMol ansatz and after the integration over R also parametrically dependent on t . The parametrical dependence is due to the temporal evolution of $\langle R \rangle(t)$ leading to a deformation of the electronic structure induced by the nuclear motion. The explicit time-dependence corresponds to the propagation in the complex phase space within the eigenstate basis [60, 100, 101]. Starting at time zero of the simulation, the uncoupled electronic wave function is equal to the real-valued eigenfunctions $\varphi_j(r; \langle R \rangle(t))$ of the MCH Hamiltonian. As time progresses, $\varphi_j(r, t; \langle R \rangle(t))$ propagates in the complex plane which can be determined by multiplying the real-valued eigenfunctions with an exponential factor containing the electronic phase $\xi_j(t)$.

$$\varphi_j(r, t; \langle R \rangle(t)) = \varphi_j(r; \langle R \rangle(t)) \cdot e^{-i\xi_j(t)} \quad (3.6)$$

This electronic phase $\xi_j(t)$ is computed by numerical integration of the electronic eigenenergies $E_j(\langle R \rangle(t))$ over time.

$$\xi_j(t) = \int_0^t E_j(\langle R \rangle(t)) dt. \quad (3.7)$$

Since $\langle R \rangle(t)$ varies with time $\xi_j(t)$ has to be calculated recursively to retain the memory of the progressing electronic phase as illustrated in Figure 3.1.

$$\xi_j(t) = E_j(\langle R \rangle(t))\Delta t + \xi_j(t - \Delta t). \quad (3.8)$$

In order to obtain a smooth change of the phase in the complex plane with time while the nuclear wave packet propagates, a much smaller time step must be used for the calculation of the phase term $\xi_j(t)$ than for the nuclear dynamics.

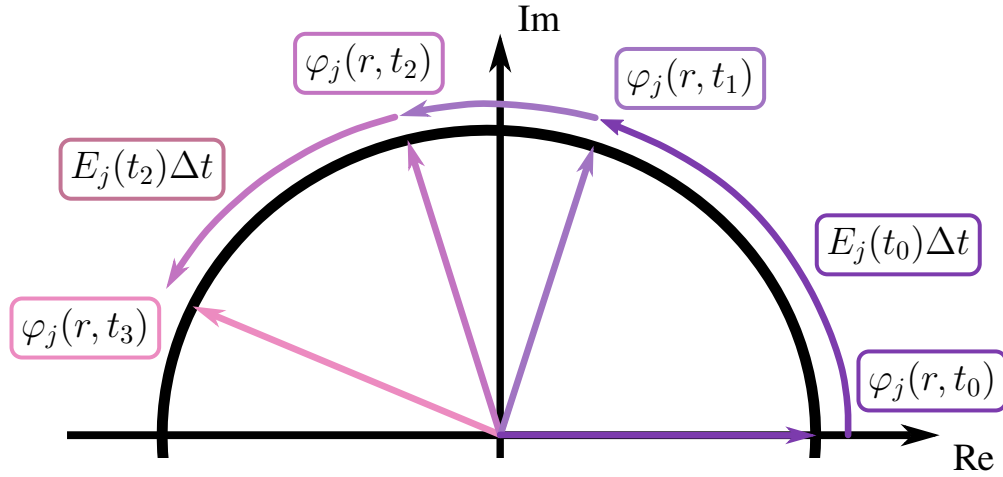


Figure 3.1: Time evolution of the electronic wave function φ_j in the complex plane. The new position in the complex plane is determined based on the previous time step. The change of the phase for each step depends on the eigenenergy E_j at a given point in time.

The total coupled electronic wave function is a high-dimensional, complex-valued quantity and difficult to handle and analyze. Therefore, the main quantity used in NEMol is the coupled one-electron density $\rho(r, t; \langle R \rangle(t))$ [60, 100, 101]. It is determined by multiplying $\Phi_{tot}(r, t; \langle R \rangle(t))$ from the left with φ_{tot} and the subsequent integration over $N - 1$ electronic coordinates (with N being the total number of electrons).

$$\rho(r, t; \langle R \rangle(t)) = \sum_j A_{jj}(t) \rho_{jj}(r; \langle R \rangle(t)) + \sum_{k>j} 2\text{Re}\{A_{jk}(t) \rho_{jk}(r; \langle R \rangle(t)) e^{-i\xi_{jk}(t)}\}, \quad (3.9)$$

$$\text{with } \xi_{jk}(t) = \Delta E_{jk}(\langle R \rangle(t))\Delta t + \xi_{jk}(t - \Delta t). \quad (3.10)$$

Analogously to the coupled electronic wave functions, the expression for $\rho(r, t; \langle R \rangle(t))$ can be decomposed into two parts. The first one is the summation of the state specific electronic density $\rho_{jj}(r, t; \langle R \rangle(t))$ weighted with the corresponding time-dependent population $A_{jj}(t)$. All terms of this summation are real-valued and their temporal evolution is completely determined by the nuclear dynamics, i.e. its expectation value of the position $\langle R \rangle(t)$. The second summation defines the coherent contribution to the coupled electron density. This coherent contribution consists of the real-valued one-electron transition density $\rho_{jk}(r, t; \langle R \rangle(t))$, the time-dependent nuclear overlap $A_{jk}(t)$ and an exponential factor containing the electronic phase $\xi_{jk}(t)$. The overall phase of the coherent contribution and thus the velocity of the electron dynamics is determined by two factors. The obvious one is the electronic phase $\xi_{jk}(t)$ defined by the energy difference ΔE_{jk} between the involved electronic states. If the states are close in energy difference ΔE_{jk} is small and the dynamics slows down. The second influence is the phase of the nuclear overlap $A_{jk}(t)$ which is connected to the difference in momentum of the nuclear wave functions involved.

In Figure 3.2 a schematic illustration of the original NEMol ansatz is given. A nuclear wave packet (indicated in black) propagating in a two dimensional coordinate space is shown for three points in time $t - \Delta t$, t and $t + \Delta t$. At each time the populations and the overlap terms are calculated for the complete coordinate space (indicated in green) and the expectation value of the position $\langle R \rangle(t)$ (red crosses) is determined. The temporal evolution of $\langle R \rangle(t)$ is depicted as a blue line. For the nuclear geometry defined by $\langle R \rangle(t)$ all necessary densities $\rho_{jj}(r; \langle R \rangle(t))$ and $\rho_{jk}(r; \langle R \rangle(t))$ are calculated and the energy gaps $\Delta E_{jk}(\langle R \rangle(t))$ are determined.

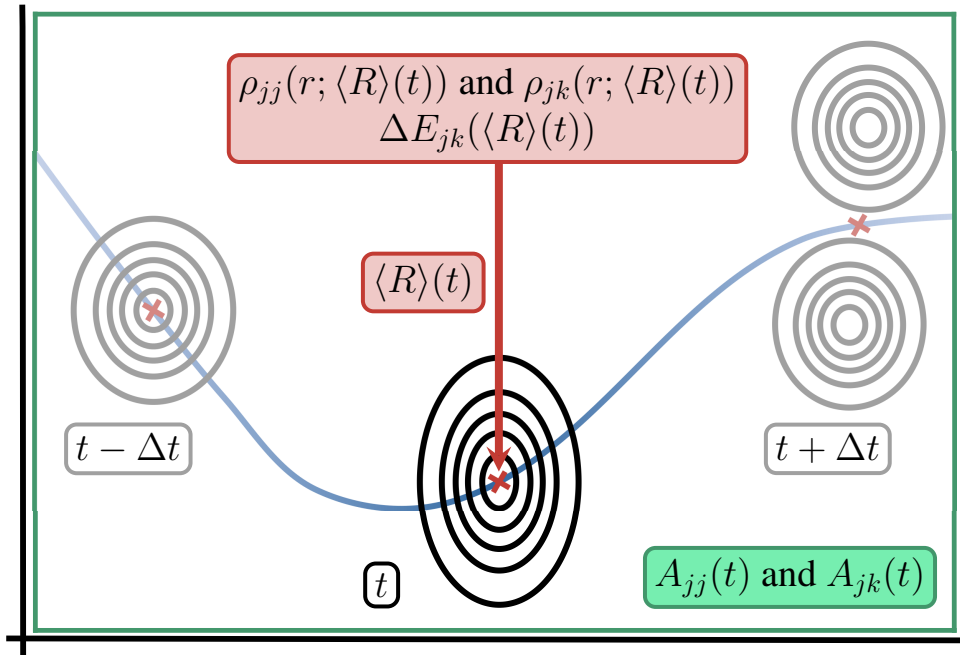


Figure 3.2: Schematic illustration of the original NEMol ansatz in a two dimensional coordinate space. The evolving wave packet is depicted in black and the expectation value of the position $\langle R \rangle$ for the three shown timesteps are marked with red crosses. All electronic properties calculated at this position are highlighted in red. Its temporal evolution is indicated with a blue line. The green box marks the full two-dimensional nuclear coordinate space over which the nuclear wave packet is integrated to obtain the nuclear overlaps $A_{jk}(t)$ and populations $A_{jj}(t)$.

Due to the integration over R , the electronic structure used to evaluate the couple density is only determined at one geometry per time step. For situations where the wave packet is fairly localized in space, $\langle R \rangle(t)$ describes the nuclear dynamics quite well, see the time steps $t - \Delta t$ and t in Figure 3.2. If the wave packet starts to delocalize $\langle R \rangle(t)$ gets progressively worse at describing the nuclear dynamics completely, as indicated for the time step $t + \Delta t$ in Figure 3.2. Beside this, the usage of $\langle R \rangle(t)$ leads to another problem. For a rather delocalized wave packet only parts of it are responsible for the occurrence of nuclear

overlap terms and these parts are not necessarily in an area near $\langle R \rangle(t)$. Therefore, the electronic structure at $\langle R \rangle(t)$ is not appropriate to capture the induced electronic coherence. As this is increasingly the case for two- and more-dimensional systems, it is necessary to generalize the NEMol ansatz.

In the following, two extensions for the original NEMol ansatz are introduced. The first one allows the simulation of the coupled dynamics in molecular systems beyond diatomics and in more than one dimension. This is done by modifying the integration over the full nuclear coordinate space. In the following the extension of the NEMol ansatz is described using an exemplary system with two nuclear coordinates c_1 and c_2 , but in principle also higher-dimensional coordinate spaces are possible. First, the full two-dimensional nuclear coordinate space is split up into $M \times L$ segments defined by their boundaries m_{min} , m_{max} and l_{min} , l_{max} . This segmentation defines the so called NEMol-grid. For each of the segments ml the population terms $\alpha_{jj}^{ml}(t)$ and the overlap terms $\alpha_{jk}^{ml}(t)$ are calculated.

$$\alpha_{jk}^{ml}(t) = \int_{m_{min}}^{m_{max}} \int_{l_{min}}^{l_{max}} \chi_j^*(R, t) \chi_k(R, t) dc_1 dc_2. \quad (3.11)$$

The sum over the $\alpha_{jj}^{ml}(t)$ and $\alpha_{jk}^{ml}(t)$ terms of the complete NEMol-grid results in the corresponding total population and overlap.

$$\sum_{m=1}^M \sum_{l=1}^L \alpha_{jk}^{ml}(t) = \langle \chi_j(R, t) | \chi_k(R, t) \rangle_R = A_{jk}(t). \quad (3.12)$$

At the center R_{ml} of each segment, the state specific electronic densities $\rho_{jj}(r; R_{ml})$, the one-electron transition densities $\rho_{jk}(r; R_{ml})$ and the energy difference between the states ΔE_{jk} are determined. These electronic quantities are combined with the population terms and the overlap terms to calculate the coupled one-electron density for each individual segment $\rho_{ml}(r, t; R_{ml})$.

$$\rho_{ml}(r, t; R_{ml}) = \sum_j \alpha_{jj}^{ml}(t) \rho_{jj}(r; R_{ml}) + \sum_{k \neq j} 2 \operatorname{Re} \{ \alpha_{jk}^{ml}(t) \rho_{jk}(r; R_{ml}) e^{-i \xi_{jk}^{ml}(t)} \}, \quad (3.13)$$

$$\text{with } \xi_{jk}^{ml}(t) = \Delta E_{jk}(R_{ml}) \Delta t + \xi_{jk}^{ml}(t - \Delta t). \quad (3.14)$$

The coupled density of each segment ml is parametrically dependent on its center R_{ml} . Since these centers are not changing with time $\rho_{jj}(r; R_{ml})$, $\rho_{jk}(r; R_{ml})$ and the energy difference ΔE_{jk} are no longer time-dependent. The electronic phase $\xi_{jk}^{ml}(t)$ of a single segment is determined by a constant ΔE value. To obtain the total coupled electron density the individual contributions of each segment are summed up.

$$\rho(r, t; R) = \sum_{m=1}^M \sum_{l=1}^L \rho_{ml}(r, t; R_{ml}). \quad (3.15)$$

The idea of the NEMol-grid extension is visualized in Figure 3.3 using the same wave packet as in Figure 3.2. The nuclear wave packet (black) is evolving in the two dimensional coordinate space which is partitioned in the segments of the NEMol-grid (green). At each time step the population terms $\alpha_{jj}^{ml}(t)$ and the overlap terms $\alpha_{jk}^{ml}(t)$ for each segment are determined. Whenever parts of the nuclear wave packet are located in a segment the corresponding coupled one-electron density $\rho_{ml}(r, t; R_{ml})$ for this individual segment is calculated (indicated with red crosses in Figure 3.3). At each time step all partial densities are summed up to obtain $\rho(r, t; R)$. This total coupled one-electron density contains the information of the electronic phase and densities at multiple grid points, which improves the spatial resolution of the electronic dynamics. The number of contribution to the total density can vary from step to step and thus it is possible to describe even very delocalized wave packets well. In the limit the NEMol-grid is equal to the grid representing the nuclear wave packet, but in the example shown in this work a coarser one is chosen.

The second extension for NEMol developed within the context of this work is the 1e-2o approximation which can be used to obtain a condensed and simple description of the coupled dynamics. The basic

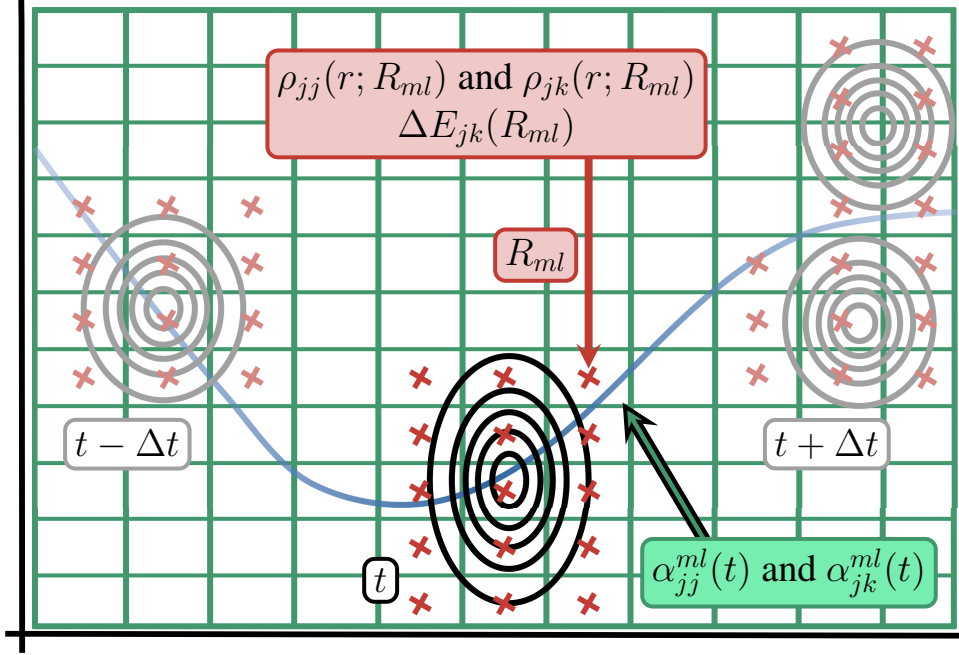


Figure 3.3: Schematic illustration of the NEMol-grid extension in a two dimensional coordinate space. The evolving wave packet is marked in black and the blue line shows the trajectory of the expectation value of the position $\langle R \rangle$. The positions for which electronic properties are calculated are highlight in red. The segments of the NEMol-grid are shown in green.

approximation for the 1e-2o picture is the idea that the entire dynamics or at least parts of it can be described by only two coupled states. For clarity reasons it is here formulated in terms of the original NEMol ansatz but it can also be applied in combination with the NEMol-grid. The electronic structure of this two states are approximately defined by two Slater determinants φ_1 and φ_2 , which only differ in the occupation of one spin orbital θ .

$$\begin{aligned}\varphi_1(r, t; \langle R \rangle(t)) &= |\theta_1 \theta_2 \dots \theta_{N-1} \theta_s\rangle, \\ \varphi_2(r, t; \langle R \rangle(t)) &= |\theta_1 \theta_2 \dots \theta_{N-1} \theta_t\rangle.\end{aligned}\tag{3.16}$$

Using these two Slater determinants, the coupled one-electron density can be expressed in terms of the spin orbitals.

$$\begin{aligned}\rho_{1e2o}(r, t; \langle R \rangle(t)) &= \sum_{j=1}^{N-1} |\theta_j(r; \langle R \rangle(t))|^2 + A_{11}(t) |\theta_s(r; \langle R \rangle(t))|^2 + A_{22}(t) |\theta_t(r; \langle R \rangle(t))|^2 \\ &\quad + 2Re\{A_{12}(t)\theta_s(r; \langle R \rangle(t))\theta_t(r; \langle R \rangle(t))e^{-i\xi_{12}(t)}\}.\end{aligned}\tag{3.17}$$

Here the first summation includes the densities of the $N-1$ equally occupied orbitals, which defines a background density evolving with the nuclear dynamics but does not include any coherent contribution. The next two terms are the densities of the two specific orbitals θ_t and θ_s weighted with the populations $A_{11}(t)$ and $A_{22}(t)$. The last part denotes the coherence between the states characterized by the product of the two orbitals, the nuclear overlap $A_{12}(t)$ and the electronic phase $\xi_{12}(t)$. Within this simplification it is now possible to neglect the contributions of the equally occupied orbitals in order to study the coupled electron dynamics in very condensed and clear way.

Both newly developed extensions to NEMol, the NEMol-grid and the 1e-2o approximation are used to study the coupled nuclear and electron dynamics of the nucleobase uracil (3.2) and the small symmetric molecule NO_2 (3.3).

3.2 Photoinduced Nuclear and Electron Dynamic in Uracil

The first example to test the NEMol-grid and the 1e-2o approximation is the photoinduced nuclear and electron dynamic in uracil, one of the four nucleobases in RNA. The photochemical properties of uracil as well as of the other nucleobases are investigated in great detail, both theoretically [142, 196, 260–265] and experimentally [15, 266–268] due to their biological relevance. After photoexcitation they can undergo harmful chemical modifications such as methylation or base alteration [12, 269, 270] leading to mutations, genomic instability and cancer [12, 13, 15]. The inherent photostability of the nucleobases is a key factor in assuring that the vast majority of photoexcitations do not lead to harmful modifications [15]. The photostability of all nucleobases is rooted in presence of fast relaxation mechanisms back to the ground state. In uracil the relaxation is mediated via CoIns between the first two excited states and the ground state. For the overall relaxation process two time constants are observed in pump-probe experiments in the gas phase [266, 267] and in solution [268, 271]. The fast one is around 100 fs and is associated with the initial relaxation from the bright S_2 state into the dark S_1 state. The slower one with up to 2.4 ps is explained by the subsequent population transfer back to the ground state. In this work the photoinduced dynamics in uracil starting with the explicit simulation of the excitation processes via a short laser pulse and the fast first relaxation step from the S_2 state into the S_1 state via a seam of CoIns is studied. As previously shown, both processes are well described using quantum dynamics on two-dimensional surfaces [142, 196, 264, 265].

The laser excitation as well as the relaxation via CoIns induce electronic coherence in a molecular system which is subsequently modulated by the nuclear motion. In the publication "Photo-Induced Coupled Nuclear and Electron Dynamics in the Nucleobase Uracil" published in *Frontiers in Physics* [272] NEMol is used to monitor the induced coherent electron dynamics. One practical aspect of using the NEMol approach for the simulation of the excitation processes should be mentioned. It is important to ensure that the phase information of the laser pulse is solely imprinted on the electronic wave function and not also on the nuclear wave functions. In previous works [102, 103], this was realized by calculating the dynamics in the rotating-wave-approximation to describe the laser-induced coupling between the molecular states. For the case of uracil the phase information of the laser pulse ΔE_{pulse} is removed from the nuclear wave functions according to the following equation.

$$\chi_{\alpha}^{cor}(R, t) = \chi_{\alpha}(R, t)e^{-i\Delta E_{pulse}t}. \quad (3.18)$$

The NEMol simulations demonstrate that the electron dynamics even in larger molecular systems reflect coherence, decoherence and reappearance due to nuclear motion. In previous work, the effect of decoherence has been discussed from the nuclear dynamics side [95–97], and the reappearance has been reported for small molecular systems [98, 99, 273]. The key findings of the article are:

- The NEMol-grid extension is able to describe the coupled nuclear and electron dynamics in a complex molecular system like uracil. It is suitable to capture the electronic coherence induced by laser pulse excitation and the relaxation via CoIns, although very delocalized wave packets are present in the second case. Another interesting aspect is that apart from small deviations, the results in the 1e-2o approximation are quite similar to those obtained from the total electron density. Therefore, the simplified 1e-2o picture can be sufficient to describe the coupled electron dynamics.
- Due to the short light pulse, the excitation process and the relaxation dynamics are temporally and spatially separated and are treated separately. In the coupled one-electron density the excitation of one electron from a bonding π orbital into an anti-bonding π^* orbital is clearly visible. During the excitation process the temporal evolution of the induced dipole moment shows fast oscillations with frequencies close to the central frequency of the excitation pulse. This dynamics can be directly attributed to the coherent electron dynamics induced by the laser pulse. The subsequent nuclear motion leads to decoherence. A partial reappearance is induced at the end of the laser pulse when the nuclear wave packet has reentered the FC area in the S_2 state.
- The electron dynamics induced by the CoIn seam is significantly more complex. When the nuclear wave packet approaches the CoIn seam the induced coherent electron dynamics slows down which

is clearly observable in the induced dipole moment. This is expected since CoIns equalize the time scales of the electron and nuclear dynamics [34, 35]. The more interesting observation is the longevity of the signal which can be attributed to the coherent electron dynamics. This is in good agreement with recently published simulations [265] of TRUECARS signals (transient redistribution of ultrafast electronic coherences in attosecond Raman signals) of the uracil S_2/S_1 relaxation.

- The longevity of the observed signal can be well explained by the delocalized character of the nuclear wave packet. Every time parts of the wave packet enter the coupling region, coherent electron dynamics is induced. The individual parts of the wave packet itself are only responsible for a short coherence and due to the nuclear motion the corresponding overlap disappears fast. In uracil, the relaxation process happens stepwise for a few hundreds of femtoseconds so there is an almost continuous flow of parts of the wave packet into the coupling region. Each of these parts induced electronic coherence and therefore the lifetime of the overall signal increases. In principle, this effect which is responsible for the long lived signal is a general mechanism and can probably occur also in other molecules as long as a rather delocalized wave packet progressively reaches a CoIn.

In the following the article "Photo-Induced Coupled Nuclear and Electron Dynamics in the Nucleobase Uracil" published by *Frontiers in Physics* under a Creative Commons Attribution 4.0 International License (CC BY 4.0, URL: <https://creativecommons.org/licenses/by/4.0>) is reprinted from *Frontiers in Physics* **9** (2021), 246. The supporting information of this article is available under <https://www.frontiersin.org/articles/10.3389/fphy.2021.674573>.



Photo-Induced Coupled Nuclear and Electron Dynamics in the Nucleobase Uracil

Lena Bäuml^{1†}, Thomas Schnappinger^{1†}, Matthias F. Kling^{2,3} and Regina de Vivie-Riedle^{1*}

¹ Department of Chemistry, Ludwig-Maximilians-University Munich, Munich, Germany, ² Max Planck Institute of Quantum Optics, Garching, Germany, ³ Department of Physics, Ludwig-Maximilians-University Munich, Garching, Germany

OPEN ACCESS

Edited by:

Tamar Seideman,
Northwestern University, United States

Reviewed by:

Burkhard Schmidt,
Freie Universität Berlin, Germany
Jiri Pittner,
J. Heyrovsky Institute of Physical
Chemistry (ASCR), Czechia

*Correspondence:

Regina de Vivie-Riedle
Regina.de_Vivie@cup
.uni-muenchen.de

[†] These authors have contributed
equally to this work and share first
authorship

Specialty section:

This article was submitted to
Physical Chemistry and Chemical
Physics,
a section of the journal
Frontiers in Physics

Received: 01 March 2021

Accepted: 19 April 2021

Published: 20 May 2021

Citation:

Bäuml L, Schnappinger T, Kling MF
and de Vivie-Riedle R (2021)
Photo-Induced Coupled Nuclear and
Electron Dynamics in the Nucleobase
Uracil. *Front. Phys.* 9:674573.
doi: 10.3389/fphy.2021.674573

Photo-initiated processes in molecules often involve complex situations where the induced dynamics is characterized by the interplay of nuclear and electronic degrees of freedom. The interaction of the molecule with an ultrashort laser pulse or the coupling at a conical intersection (CoIn) induces coherent electron dynamics which is subsequently modified by the nuclear motion. The nuclear dynamics typically leads to a fast electronic decoherence but also, depending on the system, enables the reappearance of the coherent electron dynamics. We study this situation for the photo-induced nuclear and electron dynamics in the nucleobase uracil. The simulations are performed with our ansatz for the coupled description of the nuclear and electron dynamics in molecular systems (NEMol). After photo-excitation uracil exhibits an ultrafast relaxation mechanism mediated by CoIn's. Both processes, the excitation by a laser pulse and the non-adiabatic relaxation, are explicitly simulated and the coherent electron dynamics is monitored using our quantum mechanical NEMol approach. The electronic coherence induced by the CoIn is observable for a long time scale due to the delocalized nature of the nuclear wavepacket.

Keywords: quantum dynamics, coupled nuclear and electron dynamics, electronic coherence, conical intersection, photo-excitation, uracil

1. INTRODUCTION

The interaction of molecular systems with light induces numerous chemical processes which can be natural, such as vision [1–3] and photosynthesis [4–7], or artificial like organic photovoltaics [8–12] and photocatalysis [13, 14]. In these processes a molecule often absorbs light with a wavelength in the visible or ultraviolet range where electrons are promoted from the molecular ground state to higher electronic states. The excited molecule can undergo radiative or non-radiative decay processes. Only the non-radiative processes can lead to photo-chemical reactions which are often mediated by non-adiabatic transitions [15]. The necessary non-adiabatic couplings (NACs) between the states involved are only present in the vicinity of a conical intersection (CoIn) [16–18] or an avoided crossing. Depending on the number of degrees of freedom these CoIn's are extraordinary points, seams or even higher dimensional crossing spaces. Besides the possibility of non-radiative relaxation they lead to the breakdown of the adiabatic separation between nuclear and electronic motion and equalize the time scales of their dynamics. Overall the excitation process and the non-adiabatic transitions are complex situation where both nuclear and electronic motion and their interaction play a key role. In order to simulate these situations a theoretical approach is needed that can describe the coupled nuclear and electron dynamics in a molecular system.

Most methods which can describe the electron dynamics are often modified versions of their well-known quantum-chemical counter parts and neglect the influence of the nuclear motion [19–23] or treat it classically [24–27]. One of the possibilities to treat both the nuclear and the electron dynamics in a molecular systems is the quantum-mechanical NEMol ansatz [28–32]. Within this ansatz the electronic wavefunctions are propagated in the eigenstate basis and coupled to the nuclear wavepacket propagated on coupled potential surfaces. Compared to similar but more expensive approaches based on the coupled propagation of the nuclear and electronic wavefunction on a single time-dependent potential energy surface [33–36], in NEMol the feedback of the electron motion to the nuclear dynamics is less directly included. In the beginning we give a brief introduction to the NEMol ansatz and how we determine the time-dependent electron density. This density is used to distinguish the Born-Oppenheimer part of the dynamics from the coherent electron dynamics. With the help of the NEMol ansatz the electron and nuclear dynamics along a photo-induced relaxation process in molecular systems can be simulated, including both interaction with a laser pulse and non-adiabatic events.

In the main part of this paper we apply NEMol to derive photo-induced dynamics in uracil which is one of the four nucleobases in RNA. Like all other nucleobases uracil absorbs mainly in the UV range due to an accessible $\pi \rightarrow \pi^*$ transition [37, 38]. After the excitation uracil can undergo harmful chemical modifications, such as methylation or base alteration [39–41]. The altered structures and the subsequent changed base pairings can lead to mutations, genomic instability and cancer [37, 40, 42]. To prevent potential mutations in advance, the inherent photostability of the nucleobases is a key factor, assuring that the vast majority of photoexcitations do not lead to harmful modifications [37]. The photostability of all nucleobases is due to the presence of fast relaxation mechanisms back to the ground state. Uracil exhibits an ultrafast relaxation mechanism with experimentally observed relaxation times between 50 fs and 2.4 ps [37, 43–46]. The relaxation is mediated via CoIn's between the first two excited states and has been well-studied using quantum-dynamics on two-dimensional surfaces [47, 48], as well as semi-classical approaches allowing for all degrees of freedom [38, 49–51]. As already demonstrated [52] the coherence induced by these CoIn's is long-lived since the non-adiabatic transition is rather a continuous process due to the delocalized nature of the nuclear wavepacket. We are following the photoinduced dynamics in uracil starting with the explicit simulation of the excitation processes via a laser pulse up to the relaxation via CoIn's. During the whole process NEMol is used to monitor the temporal evolution of the electron dynamics. The simulations demonstrate that the electron dynamics even in large molecular systems reflect coherence, decoherence, and reappearance due to nuclear motion. In previous work the effect of decoherence has been discussed from the nuclear dynamics side [53–55], and the reappearance has been reported for small molecular systems [56–58].

2. COUPLED NUCLEAR AND ELECTRON DYNAMICS IN MOLECULES (NEMol)

To describe the coupled nuclear and electron dynamics it is necessary to determine the temporal evolution of the total molecular wavefunction. This is realized with our NEMol ansatz [28–30]. In a system with multiple electronic states the total wavefunction $\Psi_{tot}(r, R, t)$ can be expressed as a sum over the products consisting of the electronic wavefunctions $\varphi(r, t; R)$ and the wavefunctions of the nuclei $\chi(R, t)$ (see Equation 1), with the nuclear and electronic coordinates R and r and the time t . In this ansatz both the electronic and the nuclear wavefunctions are explicitly time-dependent.

$$\Psi_{tot}(r, R, t) = \sum_i \chi_i(R, t) \cdot \varphi_i(r, t; R). \quad (1)$$

The electronic wavefunctions φ_i are parametrically depending on the nuclear coordinates R and define a multi-dimensional vector comprising the electronic states involved. Analogously, the total nuclear wavefunction χ_{tot} is given by a multi-dimensional vector composed of the nuclear wavefunctions χ_i residing in the i potential surfaces. Its temporal evolution is simulated on coupled potential energy surfaces (PES), for details see **Supplementary Section I**. Multiplying $\Psi_{tot}(r, R, t)$ from the left with χ_{tot} and the subsequent integration over the nuclear coordinates results in an expression of the coupled total electronic wavefunction [28–30].

$$\Phi_{tot}(r, t; \langle R \rangle(t)) = \int \chi_{tot}^*(R, t) \cdot \Psi_{tot}(r, R, t) dR \quad (2)$$

The individual components Φ_j of this vector are defined by the following equation:

$$\begin{aligned} \Phi_j(r, t; \langle R \rangle(t)) &= A_{jj}(t) \cdot \varphi_j(r, t; \langle R \rangle(t)) \\ &+ \sum_{k \neq j} A_{jk}(t) \cdot \varphi_k(r, t; \langle R \rangle(t)), \end{aligned} \quad (3)$$

$$\text{with } A_{jk}(t) = \langle \chi_j(R, t) | \chi_k(R, t) \rangle_R. \quad (4)$$

The time-dependent populations $A_{jj}(t)$ and the time-dependent nuclear overlap terms $A_{jk}(t)$ are determined by the nuclear quantum-dynamics simulation. The overlap terms specify the degree of coherence induced between two states j and k . If the coupling between the electronic states is weak, the nuclear wavefunctions propagate independently and the overlap term becomes zero. In this case, the coupled electronic wavefunctions Φ_j in Equation (3) become equivalent to the uncoupled electronic wavefunction φ_j . All electronic wavefunctions coupled and uncoupled are parametrically depending on the time-dependent expected value of the position $\langle R \rangle(t)$. This means that the coupled electronic wavefunctions are evaluated at one single nuclear geometry which changes with time. The time evolution of the $\varphi_j(r, t; \langle R \rangle(t))$ is determined by the deformation of the electronic structure induced by the nuclear motion and the propagation in the electronic phase space [28–30].

$$\varphi_j(r, t; \langle R \rangle(t)) = \varphi_j(r; \langle R \rangle(t)) \cdot e^{-i\mathbf{k}_j(t)} \quad (5)$$

Here the $\varphi_j(r; \langle R \rangle(t))$ are the real-valued electronic wavefunctions of the relevant electronic states and $\xi_j(t)$ is the electronic phase factor computed by numerical integration of the electronic eigenenergies $E_j(\langle R \rangle(t))$ over time.

$$\xi_j(t) = \int_0^t E_j(\langle R \rangle(t)) dt. \quad (6)$$

In practice the calculation of $\xi_j(t)$ has to be done recursively to retain the memory of the progressing electronic phase since $E_j(\langle R \rangle(t))$ changes with propagation time

$$\xi_j(t) = E_j(\langle R \rangle(t)) \Delta t + \xi_j(t - \Delta t). \quad (7)$$

Thereby the propagation velocity of the phase in the complex plane changes smoothly in time while the nuclear wavepacket propagates. Within the original NEMol a much smaller time step must be used for the calculation of the phase term $\xi_j(t)$. The coupled total electronic wavefunction is used to determine the coupled one-electron density $\rho(r, t; \langle R \rangle(t))$ [28–30].

$$\rho(r, t; \langle R \rangle(t)) = \sum_j A_{jj}(t) \rho_{jj}(r; \langle R \rangle(t)) + \sum_{k>j} 2\text{Re}\{A_{jk}(t) \rho_{jk}(r; \langle R \rangle(t)) e^{-i\xi_{jk}(t)}\}, \quad (8)$$

$$\text{with } \xi_{jk}(t) = \Delta E_{jk}(\langle R \rangle(t)) \Delta t + \xi_{jk}(t - \Delta t). \quad (9)$$

The first summation consists of the state specific electronic density $\rho_{jj}(r; \langle R \rangle(t))$ weighted with the corresponding time-dependent population $A_{jj}(t)$. The second summation defines the coherent contribution to the coupled electron density and consists of the time-dependent overlap $A_{jk}(t)$, the one-electron transition density $\rho_{jk}(r; \langle R \rangle(t))$ and its pure electronic phase $\xi_{jk}(t)$ defined by the energy difference ΔE_{jk} between the electronic states involved. This coherent part of the density can be induced by an interaction with a laser pulse or by non-adiabatic coupling events. For non-dissociative molecular dynamics like in uracil the time-dependent overlap determines the disappearance and especially the potential reappearance of the coherent electron dynamics.

To go beyond this single geometry approximation we introduced the NEMol-grid [32] where the full nuclear coordinate space is split up into segments for which partial densities are calculated. In the limit the NEMol-grid is equal to the grid for the nuclear wavepacket propagation, but in practice we choose a coarser one. The partial densities $\rho_{ml}(r, t; R_{ml})$ are defined by:

$$\rho_{ml}(r, t; R_{ml}) = \sum_j \alpha_{jj}^{ml}(t) \rho_{jj}(r; R_{ml}) + \sum_{k>j} 2\text{Re}\{\alpha_{jk}^{ml}(t) \rho_{jk}(r; R_{ml}) e^{-i\xi_{jk}^{ml}(t)}\}, \quad (10)$$

$$\text{with } \xi_{jk}^{ml}(t) = \Delta E_{jk}(R_{ml}) \Delta t + \xi_{jk}^{ml}(t - \Delta t). \quad (11)$$

The population terms $\alpha_{jj}^{ml}(t)$ and the overlap terms $\alpha_{jk}^{ml}(t)$ are calculated by integration over the wavepackets within the

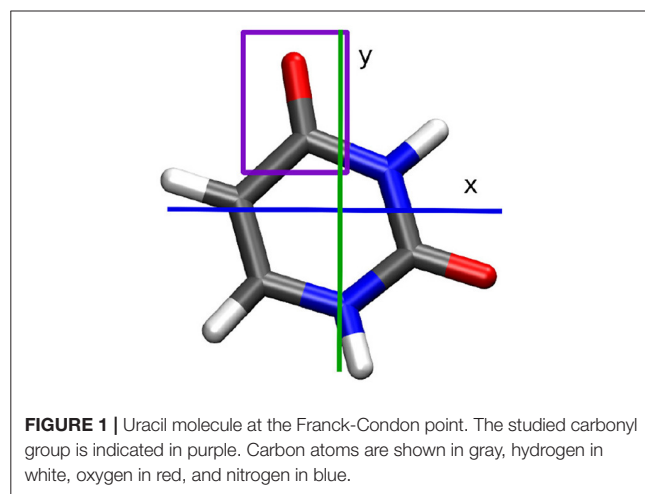
boundaries of the segments. At the center R_{ml} of each segment the state specific electronic densities $\rho_{jj}(r; R_{ml})$, the one-electron transition densities $\rho_{jk}(r; R_{ml})$, and the pure electronic phase $\xi_{jk}^{ml}(t)$ are determined. Since the positions R_{ml} do not vary with time the time step for the calculation of the phase term can be chosen larger than for the original NEMol. In this work a time step of 1 a.u. is used. To obtain the total coupled electron density the individual contributions for each segment are summed up.

$$\rho(r, t; R) = \sum_{m=1}^M \sum_{l=1}^L \rho_{ml}(r, t; R_{ml}). \quad (12)$$

This total coupled one-electron density $\rho(r, t; R)$ (also called full electron density in the following) contains the information of all partial densities determined at multiple grid points weighted with the corresponding population and overlap terms. This is a significant difference from the original NEMol where the electronic structure was only considered at one geometry. To visualize the coupled one-electron density the weighted average R of all R_{ml} is formed. The NEMol-grid extension is used to sample the nuclear wavefunction to improve the resolution of the spatial dependence of the electronic phase term. This is crucial for situations where the nuclear wavepacket is delocalized and only parts of the wavepacket induce coherence in the system. As this is increasingly the case for two and more dimensional systems, the expected value of the position $\langle R \rangle(t)$ is no longer appropriate to capture the electron dynamics. Since uracil is such case we apply the NEMol-grid for all calculations in this work. To study the electron dynamics the induced dipole moment vector $\vec{\mu}$ is calculated using the coupled one-electron density:

$$\vec{\mu}(t) = \int d\vec{r} \rho(r, t; R) \cdot \vec{r}. \quad (13)$$

If the entire dynamics or at least parts of it can be described by two coupled states, it is possible to obtain a simplified description of the electron density in the one-electron-two-orbital (1e-2o)



picture, which was derived and successfully applied in reference [32]. Based on the assumption that the two states are described by two Slater determinants, which only differ in the occupation of one spin orbital θ , it is possible to condense the coupled dynamics in a simple 1e-2o-density. The following Equation (14) is based on the original NEMol ansatz (see Equation 8), but the 1e-2o-density can also be determined in combination with the NEMol-grid.

$$\rho_{1e2o}(r, t; \langle R \rangle(t)) = A_{11}(t)|\theta_1(r; \langle R \rangle(t))|^2 + A_{22}(t)|\theta_2(r; \langle R \rangle(t))|^2 + 2\text{Re}\{A_{12}(t)\theta_1(r; \langle R \rangle(t))\theta_2(r; \langle R \rangle(t))e^{-i\xi_{12}(t)}\}. \quad (14)$$

Neglecting the contributions of the equally occupied orbitals, the first two terms represent the remaining two orbitals weighted with their respective population $A_{jj}(t)$. The third term denotes the coherence between the states characterized by the product of the two orbitals.

3. PHOTO-INDUCED DYNAMICS OF URACIL

In this work we investigate the photo-induced nuclear and electron dynamics of the nucleobase uracil with NEMol. The geometry of uracil at the Franck-Condon (FC) point is depicted in **Figure 1**. Uracil is characterized by an ultrafast photo-relaxation channel starting in the second excited state (S_2) which is mediated by CoIn's. As shown in previous studies [47, 48], the photo-excitation and the initial steps of the subsequent relaxation can be well-described on two-dimensional PES. We adopt these adiabatic PES, which were first reported by Keefer et al. [47] and later modified [52, 59]. The underlying two-dimensional coordinate space spanned by the vectors q_1 and q_2 includes all relevant structures, the FC point, the S_2 minimum, the optimized

S_2/S_1 CoIn and also parts of the associated CoIn seam. Both vectors are depicted on the right side of **Figure 2**. The resulting PES for the bright S_2 state is shown on the left of **Figure 2**. The potential surface exhibits a double-well structure with a small barrier separating the S_2 minimum on the top left from the CoIn seam on the bottom right (black). Further information about the simulations can be found in the **Supplementary Section I**. The molecular orientation within the laboratory frame is chosen in such a way that the molecular plane is equal to the xy -plane at the FC point and the center of mass defines the origin of the laboratory frame (see **Figure 1**). To initiate the dynamics and promote the system from the electronic ground state to the S_2 state we use a Gaussian shaped pulse. Its parameters were adapted from a previous work [47]. The pulse has a central frequency ω_0 of 6.12 eV, a full width at half maximum (FWHM) of 30 fs and a maximum field strength of 0.036 GV cm⁻¹. This maximum is reached after 40 fs simulation time. The light-matter interaction is treated within the dipole approximation. We assume that the electric component of the pulse is optimally aligned with the transition dipole moment whose absolute value is used. The complete temporal evolution of the population of all three states is shown in **Figure 3**. The excitation pulse is active in the time period between 10 and 75 fs and leads to an S_2 population yield close to 90%. The motion of the wavepacket in the S_2 state is indicated in white in **Figure 2**. The wavepacket evolves from the FC point toward the S_2 minimum and oscillates back near the FC region. After this first oscillation period (about 80 fs) a part of the wavepacket splits and travels toward the CoIn seam. At around 100 fs the population of the S_2 state starts to decay. During the following oscillations this behavior continues leading to a rather continuous flow of population into the S_1 state.

The NEMol simulations are used to monitor the coupled nuclear and electron dynamics of uracil during the first 200 fs. We assume that the coherent part of the electron dynamics

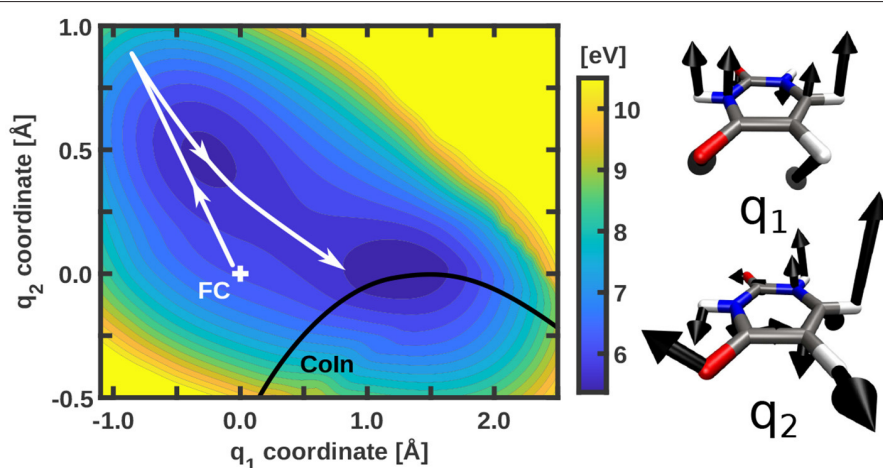
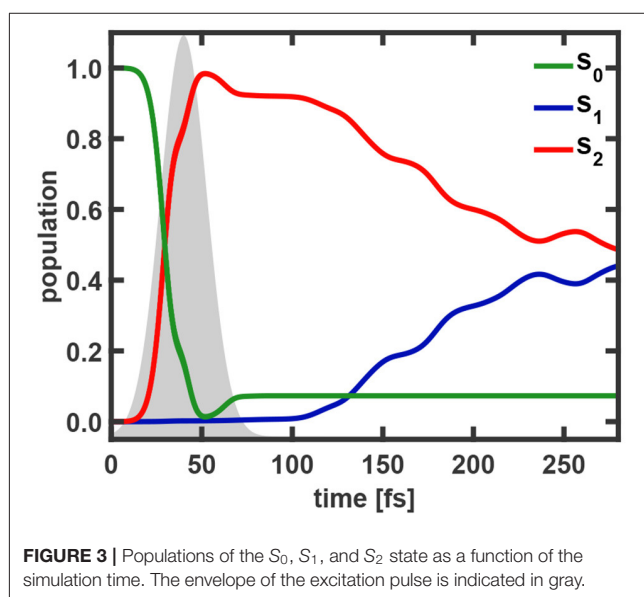
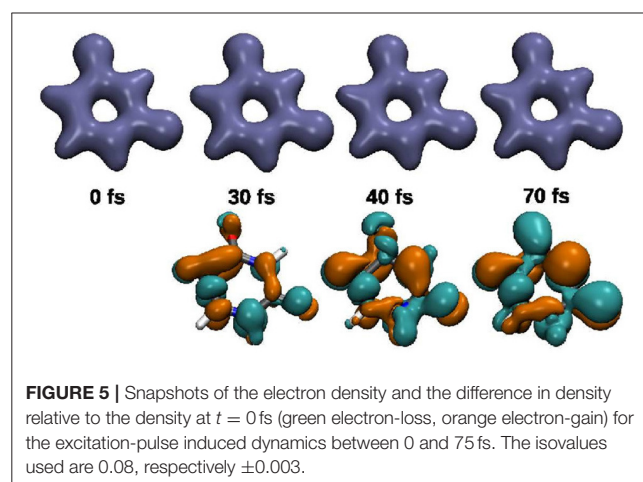
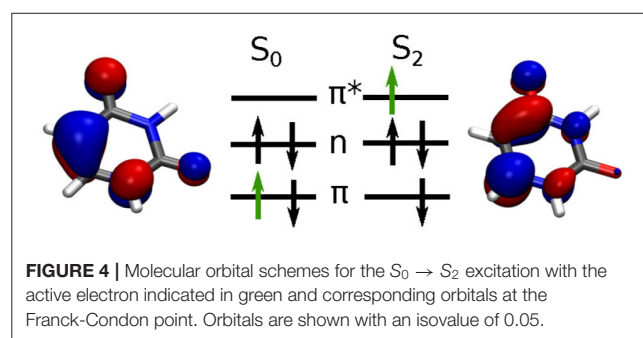


FIGURE 2 | Potential energy surface of the bright S_2 state of uracil with indicated CoIn seam (black) and a schematic representation of the path of the wavepacket (white). The energy scale is given with respect to the global minimum of the S_0 potential energy surface. The two coordinate vectors defining the two-dimensional coordinate space are shown on the right. Only contributions larger than 0.3 Å are depicted.



is only active during the laser pulse excitation and when the wavepacket is interacting with the CoIn seam. Since these two events are spatially and temporally separated from each other we split our simulation into two parts. Within the interval of the excitation process (0–75 fs) we calculate the coupled electron density including only the properties (densities, population and overlap) of the S_0 and S_2 states. In the second part (75–200 fs), characterized by the relaxation via the CoIn seam, we include only the properties of the S_1 and S_2 states. For both cases we use a NEMol-grid of 14×10 segments equally distributed between -0.37 and 1.57 Å in the q_1 coordinate and from -0.57 to 0.86 Å in the q_2 coordinate, shown in **Supplementary Figure 1**. For each of these segments the population terms and the overlap terms of the involved states were determined. The population outside the NEMol-grid was added to the nearest segment on the edge of the grid. For the detailed analysis of the electron dynamics we focus on two quantities, the induced dipole moment and the temporal evolution of the local density at the upper carbonyl group (marked in purple in **Figure 1**). Both are observables, e.g., the fluctuations in the local density could be probed by transient X-ray absorption spectroscopy [60, 61]. Both observables show qualitatively very similar features. The results for the induced dipole moment are presented and discussed in the manuscript, while the ones for the local density are shown in the **Supplementary Material**. We should note that for the excitation dynamics it is important to ensure that the phase information of the laser pulse is solely imprinted on the electronic wavefunction and not also on the nuclear wavefunctions. In our previous work [62, 63], this was realized by calculating the dynamics in the rotating-wave-approximation to describe the laser-induced coupling between the molecular states. In this work we have chosen to remove the phase information of the laser pulse from the nuclear overlap terms.

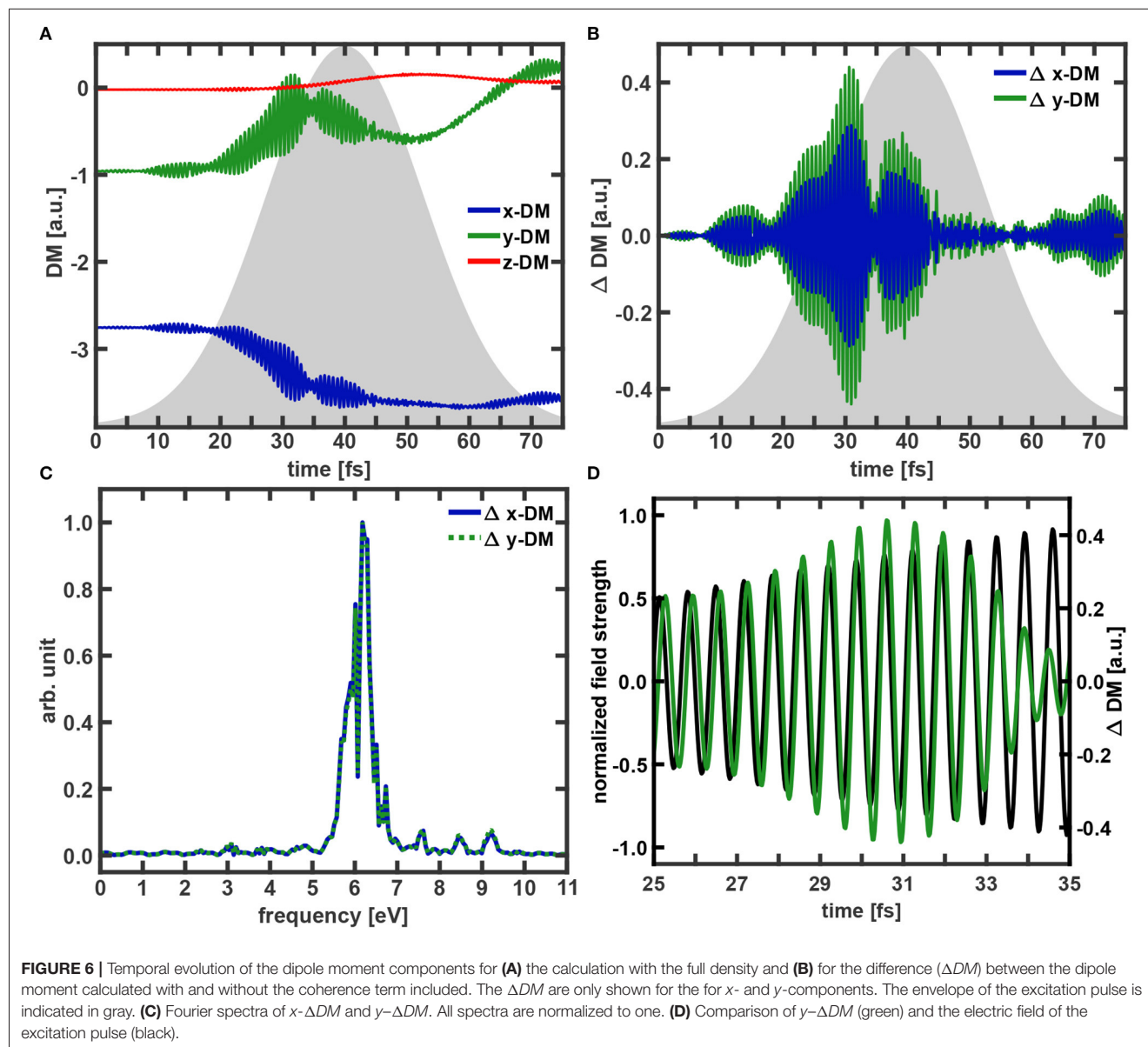


3.1. Excitation-Pulse Induced Dynamics

The dynamics induced by the laser pulse excitation is basically characterized by the excitation of one electron from a bonding π orbital into an anti-bonding π^* orbital. This process is illustrated in **Figure 4**. For the following analysis we calculate the full coupled electron density according to Equation (12).

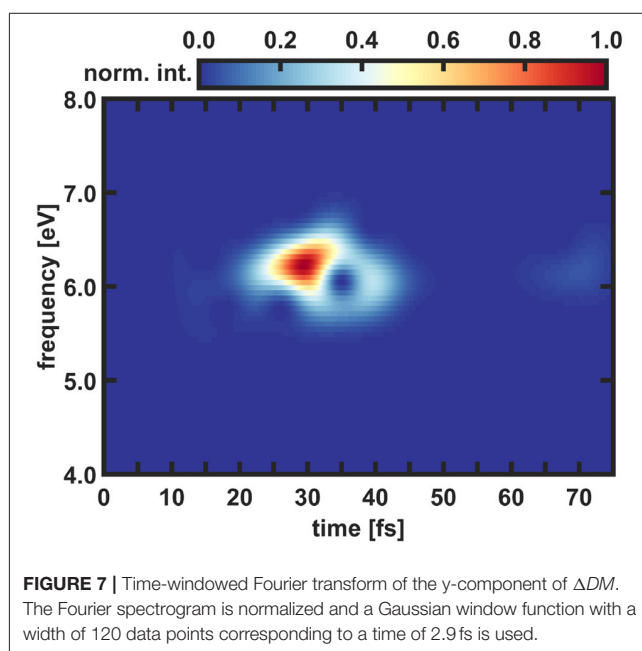
Snapshots of the full coupled electron density are depicted in **Figure 5**. The excitation process follows with slight delay the profile of the resonant light pulse (**Figure 3**). Close to its maximum we observe a slight backtransfer from S_2 to S_0 . Thereafter the S_2 population smoothly further increases up to nearly 100% reached at 52 fs. Toward the end of the pulse (at 60–70 fs) about 5% of the population is transferred back to the ground state. In total, 92% of the population was promoted into the S_2 state. With the naked eye nearly no variation is visible in the temporal evolution of the full electron density (top row **Figure 5**). However, studying the difference in density (bottom row) recorded with respect to the one at $t = 0$ fs the change in the bonding/anti-bonding pattern of the π -system becomes observable. In addition the deplanarization of the molecule leads to changes in the σ -system. The corresponding snapshots of the 1e-2o-density can be found in **Supplementary Figure 4**.

The temporal evolution of the induced dipole moment (DM) is determined with and without the coherent part of the coupled electron density included. The difference ΔDM is used to monitor the part of the dipole moment which is induced by the



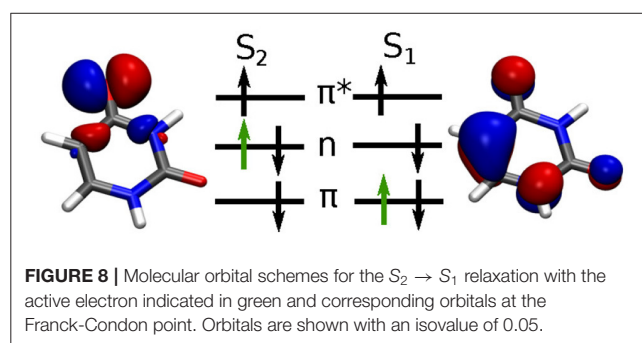
coherent electron dynamics. The DM components, the ΔDM along the x - and y -coordinate and their Fourier transforms are shown in **Figure 6**. In addition also the comparison of the y - ΔDM signal and the laser field is depicted. In the beginning of the excitation process the wavepacket mostly remains near the FC point and the molecular geometry stays planar in the xy -plane. Therefore, up to 30 fs the z -component of the induced dipole moment stays zero. After this period the wavepacket movement toward the S_2 minimum breaks up the planar structure and small modulations of the z -component are observed. Compared to the other two components it does not change significantly and is neglected for the further analysis. Regarding the x - and y -components of the DM, two main features are apparent. There is an overall increase (y -component), respectively decrease

(x -component) in the DM which is modulated by a slow oscillation with a period of about 40 fs caused by the initial nuclear wavepacket motion around the S_2 minimum. The second feature is an extremely fast oscillation which is especially dominant in the range of 10–45 fs. With the help of the ΔDM components (**Figure 6B**) these fast oscillations can be attributed to the coherent electron dynamics. Close to the pulse maximum a pronounced destructive interference appears around 35 fs which coincides with the slight backtransfer of the population (**Figure 3**). The Fourier transforms (**Figure 6C**) of the two ΔDM signals clearly reveal that both components share the same main frequencies at 6.18 eV. These frequencies agree very well with the excitation frequency of 6.12 eV. A table of all observed frequencies with an intensity larger than 0.1 can be found in



Supplementary Table 1. If we now compare the time evolution of the electric field of the pulse with the evolution of $y\text{-}\Delta DM$ (Figure 6D) this good agreement is confirmed and furthermore a maximum phase shift of about 0.5π between the field and the coherent part of the induced dipole moment can be recognized as expected [62, 63]. That means there is a briefly delayed response of the electron dynamics to the laser pulse. Also the beginning of the destructive interference of the electron wavefunctions at 33 fs is visible. In a final step of the analysis we have used a time-windowed Fourier transform of the $y\text{-}\Delta DM$ signal to determine the time at which the observed frequencies occur. In Figure 7 the result of the time-windowed Fourier transform is shown applying a Gaussian window function with a width of 120 data points corresponding to a time of 2.9 fs.

In the spectrogram only frequencies in an energy window between 5.5 and 7 eV are visible. During the simulation these frequencies are occurring twice, once between 10 and 45 fs with the maximum being located between 25 and 35 fs, and a second time much weaker from 60 fs onward. The first one is directly induced by the laser pulse and the starting point of this signal matches with the beginning of the population transfer into S_2 state. The second occurrence takes place at the end of the excitation pulse. Until then parts of the wavepacket traveled back to the FC area and are again resonant with the excitation pulse. This enables backtransfer from the S_2 state to the ground state creating again non-zero nuclear overlap terms in Equation (10) and thus coherent electron dynamics. As described in the theory section instead of using the total coupled electron density it is also possible to perform the calculations in the 1e-2o picture (see Equation 14). Besides small deviations, the results in the 1e-2o picture are quite similar and can be found in the **Supplementary Material**. A complete summary of all



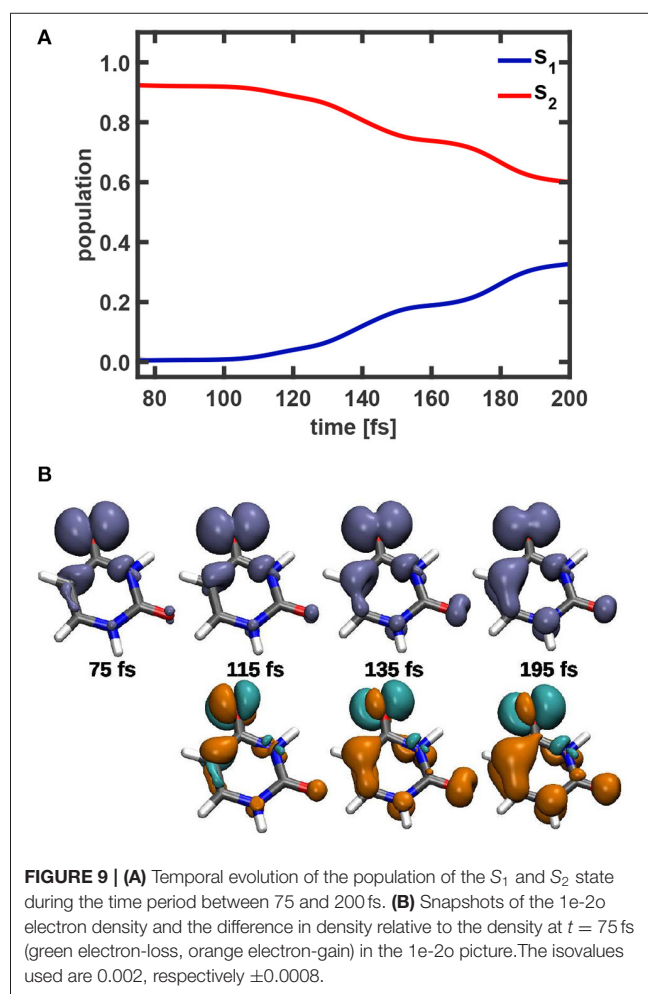
performed analyses of the coupled electron density can be found in **Supplementary Section IIIA**. In summary, the laser pulse builds up electronic coherence in the molecule. The subsequent nuclear movement leads to decoherence within 10 fs, but about 40 fs later a weak reappearance of the signal due to laser coupling is observed.

3.2. Conical Intersection Induced Dynamics

Since the coupled dynamics of the excitation process is well-described in the 1e-2o picture, we also performed the simulation for the conical intersection induced dynamics in this picture. The two active orbitals which are required to describe the NEMol-dynamics according to Equation (14) are shown in Figure 8 at the FC point. In this simplified picture the CoIn dynamics is characterized by the transfer of one electron from a non-bonding orbital into a bonding π orbital.

The population dynamics in the time window from 75 to 200 fs and snapshots of the coupled electron density in the 1e-2o picture are depicted in Figure 9. The corresponding snapshots obtained with the full electron density are shown in **Supplementary Figure 11**. A slow but steady decay of the S_2 population indicating two shallow steps (from 110 to 160 fs and from 170 to 200 fs) is visible. This rather continuous relaxation process is due to the delocalized nature of the nuclear wavepacket. In the 1e-2o picture the variation in the temporal evolution of the electron density is clearly visible (top row Figure 9B). For illustration also the difference in density with respect to the one at $t = 75$ fs is depicted. The snapshots reveal a transition from an exclusive non-bonding character at 75 fs to a mixed non-bonding and π character at 195 fs. Over the observed time the majority of the density is located at the upper oxygen atom, but the two left carbon atoms gain more and more density and a π -bond is formed.

For further analysis the temporal evolution of the induced dipole moment calculated with and without the coherent part of the electron density included was determined. The resulting DM components, the ΔDM of the x - and y -components and their Fourier transforms are shown in Figure 10. In addition the time-windowed Fourier transform of the $y\text{-}\Delta DM$ signal is depicted there, applying a Gaussian window function with a width of 2.9 fs. As for the excitation dynamics, the z -component of the induced dipole moment does not play a major role and is neglected also in the discussion of the CoIn induced dynamics.



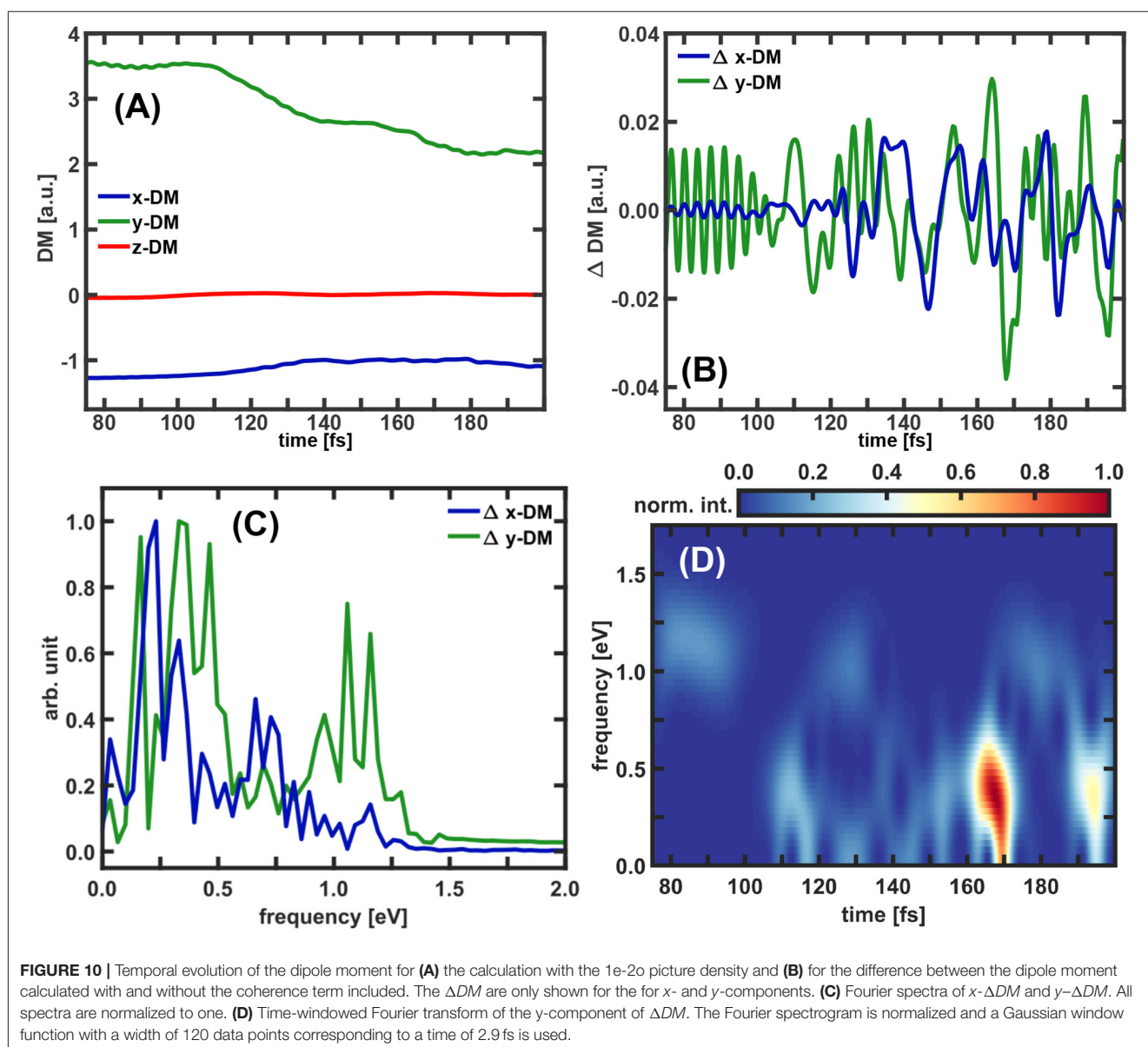
In the overall picture the x -component exhibits a slow and rather small increase, only the y -component shows significant changes and decreases step-wise analogously to the population in S_2 . Since the electron density moves mainly along the y -coordinate (see **Figure 9B**), it is logical that this component changes most. Superimposed weak and fast oscillations can be recognized for the y -DM signal and to some extent also for the x -DM signal. As in the previous analysis of the laser induced dynamics these oscillations can be assigned to the coherent electron dynamics. Using the ΔDM components (see **Figure 10B**), intervals with fast oscillations and with slow oscillations can be identified. For the y -component the fast ones appear in the range from 75 to 100 fs, around 120 and 180 fs while the slow ones have larger amplitudes and appear from 100 to 120 fs, 130 to 170 fs, and after 180 fs. Correspondingly two prominent frequency bands occur in the Fourier transforms (**Figure 10C**) of these two ΔDM signals. For the y -component, e.g., the stronger band is centered in a range from 0.25 to 0.75 eV and a weaker band is located between 0.9 and 1.25 eV. A table of all observed frequencies with an intensity larger than 0.1 can be found in **Supplementary Table 3**. Again, as final step of the analysis

we performed a time-windowed Fourier transform of the y - ΔDM signal using a Gaussian window function with a width of 2.9 fs. Compared to the case of the laser induced ΔDM (see **Figure 7**) the spectrogram (**Figure 10D**) shows significantly more structured signals. We observe two main peaks in an energy range from 0 to 0.75 eV at 170 and 195 fs and additionally many weaker signals in the same energy region, as well as for higher frequencies (1.0–1.25 eV). The frequencies appearing at early times (75–100 fs) originate from the first parts of the nuclear wavepacket reaching the coupling region but not actually the CoIn seam. This explains the higher energy reflecting the actual energy gap ΔE . Later at 100 fs also lower frequencies appear as the wavepacket now hits the CoIn seam and the energy gap between the states closes. From now on parts of the moving nuclear wavepacket can be found close to the CoIn or in its environment. The intense signals at 170 and 195 fs correlate with the efficient transitions through the CoIn (see **Figure 9A**). The same simulations were also performed to obtain the total coupled electron density according to Equation (12). Comparing the results of the full and the 1e-2o density, the same frequencies and pattern are observed in the electron dynamics. However, the intensities for the higher frequencies are dominant for full density. The results for the full density can be found in the **Supplementary Material**. A complete summary of all performed analyses of the total coupled electron density can be found in **Supplementary Section IIIB**.

In summary, two observations can be made from our NEMol simulation of the conical intersection induced dynamics. The first one is, that the CoIn induces coherent electron dynamics which slows down the closer the system approaches the CoIn. This is expected since CoIn's equalize the time scales of the electron and nuclear dynamics [16, 17]. The second aspect is the longevity of the observed coherence. Due to the delocalized character of the nuclear wavepacket parts of it induce almost continuously coherence in the vicinity of the CoIn leading to a long lived observable signal. This is in good agreement with recently published simulations [52] of TRUECARs signals (transient redistribution of ultrafast electronic coherences in attosecond Raman signals) of the uracil S_2/S_1 CoIn. There, the long lived signal of coherence is also observed and the time-resolved vibronic frequency maps are in the same energy region.

4. CONCLUSION

In this paper, we applied our ansatz for the calculation of the coupled electron and nuclear dynamics in molecular systems (NEMol) [28–32] to the nucleobase uracil. We use the recently formulated extended version [32] operating on the NEMol-grid. As the interplay between nuclear and electron dynamics plays a crucial role in excitation processes as well as during non-adiabatic transitions both situations were studied. The NEMol ansatz treats the nuclear and the electron dynamics both quantum-mechanically. The electronic wavefunctions are propagated in the eigenstate bases and coupled to the nuclear dynamics simulated on coupled potential energy surfaces.



With a simple approximation it was possible to simplify the description of the excitation and relaxation processes by expressing the total electron density in the one-electron-two-orbital (1e-2o) picture [32]. In this work, both, the total coupled electron density and the simplified 1e-2o picture, were applied.

The NEMol simulations were used to study the photo-excitation and the CoIn mediated relaxation in uracil. By the choice of ultrashort light pulses these two processes are temporally and spatially separated and can be treated separately. During the excitation one electron is promoted from a bonding π orbital into an anti-bonding π^* orbital. This general change is clearly visible in the NEMol dynamics but it also enables us

to analyze the excitation process in greater depth. As a possible observable in an experiment we choose to focus on the induced dipole moment. Studying its temporal evolution, fast oscillations are observed which could be directly attributed to the coherent electron dynamics. Their frequencies are close to the central frequency of the excitation pulse. The coherent dynamics is induced by the laser pulse and subsequent nuclear movement leads to decoherence. A partial reappearance is induced at the end of the laser pulse when the S_2 wavepacket has reentered the FC area. The good agreement between the results obtained with the total electron density and that of the 1e-2o picture supports that the simplified 1e-2o picture can be sufficient to describe the coupled electron dynamics. This 1e-2o picture was

used to monitor the coupled electron dynamics induced by the S_2/S_1 conical intersection. The electronic coherence is induced by parts of the rather delocalized nuclear wavepacket and its recurrences at the CoIn and thus can be observed for long times. The frequencies in the induced dipole moment are now rather small, as expected since at the CoIn's the electron dynamics slows down [16–18]. A distinct modulation of these frequencies is observed in the time-windowed Fourier transform reflecting the movement of the nuclear wavepacket around the CoIn seam. Both the longevity and the modulation of the coherence by the nuclear motion is in good agreement with the recent simulation of the TRUECARs signal of the uracil S_2/S_1 CoIn [52]. Here, we demonstrated the capability of the NEMol ansatz to describe the coupled nuclear and electron dynamics in a complex molecular system like uracil. We were able to investigate the electronic coherence that is built up by the laser excitation and modulated by the subsequent nuclear motion. The following relaxation via a conical intersection induces again electronic coherence in the system, which is also treated within the NEMol approach. The verified 1e-2o picture will allow to simulate even larger system.

DATA AVAILABILITY STATEMENT

The raw data supporting the conclusions of this article are available from the corresponding author upon reasonable request.

REFERENCES

1. Khorana HG. Rhodopsin, photoreceptor of the rod cell—an emerging pattern for structure and function. *J Biol Chem.* (1992) 267:1–4. doi: 10.1016/S0021-9258(18)48444-X
2. Send R, Sundholm D. Stairway to the conical intersection: a computational study of the retinal isomerization. *J Phys Chem A.* (2007) 111:8766–73. doi: 10.1021/jp073908l
3. Polli D, Altoè P, Weingart O, Spillane KM, Manzoni C, Brida D, et al. Conical intersection dynamics of the primary photoisomerization event in vision. *Nature.* (2010) 467:440–3. doi: 10.1038/nature09346
4. Webber AN, Lubitz W. P700: the primary electron donor of photosystem I. *Biochim Biophys Acta.* (2001) 1507:61–79. doi: 10.1016/S0005-2728(01)00198-0
5. Mirkovic T, Ostroumov EE, Anna JM, van Grondelle R, Govindjee, Scholes GD. Light absorption and energy transfer in the antenna complexes of photosynthetic organisms. *Chem Rev.* (2017) 117:249–93. doi: 10.1021/acs.chemrev.6b00002
6. Loll B, Kern J, Saenger W, Zouni A, Biesiadka J. Towards complete cofactor arrangement in the 3.0 angstrom resolution structure of photosystem II. *Nature.* (2005) 438:1040–4. doi: 10.1038/nature04224
7. Scholes GD, Fleming GR, Olaya-Castro A, van Grondelle R. Lessons from nature about solar light harvesting. *Nat Chem.* (2011) 3:763–74. doi: 10.1038/nchem.1145
8. Collings AF, Critchley C. *Artificial Photosynthesis: From Basic Biology to Industrial Application.* London: Wiley (2005). doi: 10.1002/3527606742
9. Andrea Rozzi C, Maria Falke S, Spallanzani N, Rubio A, Molinari E, Brida D, et al. Quantum coherence controls the charge separation in a prototypical artificial light-harvesting system. *Nat Commun.* (2013) 4:1602. doi: 10.1038/ncomm.s2603
10. Roncali J, Leriche P, Blanchard P. Molecular materials for organic photovoltaics: small is beautiful. *Adv Mater.* (2014) 26:3821–38. doi: 10.1002/adma.201305999
11. Mazzio KA, Luscombe CK. The future of organic photovoltaics. *Chem Soc Rev.* (2015) 44:78–90. doi: 10.1039/C4CS00227J
12. Pelzer KM, Darling SB. Charge generation in organic photovoltaics: a review of theory and computation. *Mol Syst Des Eng.* (2016) 1:10–24. doi: 10.1039/C6ME00005C
13. Ismail AA, Bahnemann DW. Photochemical splitting of water for hydrogen production by photocatalysis: a review. *Solar Energy Mater Solar Cells.* (2014) 128:85–101. doi: 10.1016/j.solmat.2014.04.037
14. Wenderich K, Mul G. Methods, mechanism, and applications of photodeposition in photocatalysis: a review. *Chem Rev.* (2016) 116:14587–619. doi: 10.1021/acs.chemrev.6b00327
15. Nelson TR, White AJ, Bjorgaard JA, Sifain AE, Zhang Y, Nebgen B, et al. Non-adiabatic excited-state molecular dynamics: theory and applications for modeling photophysics in extended molecular materials. *Chem Rev.* (2020) 120:2215–87. doi: 10.1021/acs.chemrev.9b00447
16. Yarkony DR. Diabolical conical intersections. *Rev Mod Phys.* (1996) 68:985–1013. doi: 10.1103/RevModPhys.68.985
17. Baer M. Introduction to the theory of electronic non-adiabatic coupling terms in molecular systems. *Phys Rep.* (2002) 358:75–142. doi: 10.1016/S0370-1573(01)00052-7
18. Domcke W, Yarkony D, Köppel H. *Conical Intersections: Electronic Structure, Dynamics and Spectroscopy.* Vol. 15. Singapore: World Scientific (2004). doi: 10.1142/5406
19. Runge E, Gross EKH. Density-functional theory for time-dependent systems. *Phys Rev Lett.* (1984) 52:997–1000. doi: 10.1103/PhysRevLett.52.997
20. Klamroth T. Laser-driven electron transfer through metal-insulator-metal contacts: time-dependent configuration interaction singles calculations for a Jellium model. *Phys Rev B.* (2003) 68:245421. doi: 10.1103/PhysRevB.68.245421

AUTHOR CONTRIBUTIONS

TS, MK, and RV-R initiated the project. LB performed the calculations. LB, TS, and RV-R analyzed and interpreted the results. All authors contributed to the final version of the manuscript.

ACKNOWLEDGMENTS

The authors gratefully acknowledge the support by the German Research Foundation via VI 144/9-1 and KL-1439/11-1 and the center of excellence Munich Centre of Advanced Photonics (MAP).

SUPPLEMENTARY MATERIAL

The Supplementary Material for this article can be found online at: <https://www.frontiersin.org/articles/10.3389/fphy.2021.674573/full#supplementary-material>

See the **Supplementary Material** for the details of the wavepacket simulation setup and additional figures and tables for the analyses of the NEMol-dynamics. Animations of the coupled electron density in the 1e-2o picture and the ones using the full density for dynamics induced by the excitation pulse and the CoIn are also shown in the **Supplementary Material**.

Supplementary Data Sheet 1 | Movie electron dynamics at CoIn.

Supplementary Data Sheet 2 | Movie of electron dynamics during excitation.

21. Rohringer N, Gordon A, Santra R. Configuration-interaction-based time-dependent orbital approach for *ab initio* treatment of electronic dynamics in a strong optical laser field. *Phys Rev A*. (2006) 74:043420. doi: 10.1103/PhysRevA.74.043420
22. Skeidsvoll AS, Balbi A, Koch H. Time-dependent coupled-cluster theory for ultrafast transient-absorption spectroscopy. *Phys Rev A*. (2020) 102:023115. doi: 10.1103/PhysRevA.102.023115
23. Vila FD, Rehr JJ, Kas JJ, Kowalski K, Peng B. Real-time coupled-cluster approach for the cumulant Green's function. *J Chem Theory Comput*. (2020) 16:6983–92. doi: 10.1021/acs.jctc.0c00639
24. Ojanperä A, Havu V, Lehtovaara L, Puska M. Nonadiabatic Ehrenfest molecular dynamics within the projector augmented-wave method. *J Chem Phys*. (2012) 136:144103. doi: 10.1063/1.3700800
25. Alonso JL, Castro A, Echenique P, Rubio A. In: Marques MAL, Maitra NT, Nogueira FMS, Gross EKV, Rubio A, editors. On the combination of TDDFT with molecular dynamics: new developments. In: *Fundamentals of Time-Dependent Density Functional Theory*. Berlin; Heidelberg: Springer Berlin Heidelberg (2012). p. 301–15. doi: 10.1007/978-3-642-23518-4_15
26. Takatsuka K. Theory of molecular nonadiabatic electron dynamics in condensed phases. *J Chem Phys*. (2017) 147:174102. doi: 10.1063/1.4993240
27. Takatsuka K. Nuclear wavepackets along quantum paths in nonadiabatic electron wavepacket dynamics. *Chem Phys*. (2018) 515:52–9. doi: 10.1016/j.chemphys.2018.07.006
28. Geppert D, von den Hoff P, de Vivie-Riedle R. Electron dynamics in molecules: a new combination of nuclear quantum dynamics and electronic structure theory. *J Phys B Atomic Mol Opt Phys*. (2008) 41:074006. doi: 10.1088/0953-4075/41/7/074006
29. von den Hoff P, Znakovskaya I, Kling MF, de Vivie-Riedle R. Attosecond control of the dissociative ionization via electron localization: a comparison between D2 and CO. *Chem Phys*. (2009) 366:139–47. doi: 10.1016/j.chemphys.2009.09.021
30. Znakovskaya I, von den Hoff P, Zherebtsov S, Wirth A, Herrwerth O, Vrakking MJJ, et al. Attosecond control of electron dynamics in carbon monoxide. *Phys Rev Lett*. (2009) 103:103002. doi: 10.1103/PhysRevLett.103.103002
31. Kling MF, von den Hoff P, Znakovskaya I, de Vivie-Riedle R. (Sub-)femtosecond control of molecular reactions via tailoring the electric field of light. *Phys Chem Chem Phys*. (2013) 15:9448–67. doi: 10.1039/c3cp50591j
32. Schnappinger T, de Vivie-Riedle R. Coupled nuclear and electron dynamics in the vicinity of a conical intersection. *J Chem Phys*. (2021) 154:134306. doi: 10.1063/5.0041365
33. Cederbaum LS. Born–Oppenheimer approximation and beyond for time-dependent electronic processes. *J Chem Phys*. (2008) 128:124101. doi: 10.1063/1.2895043
34. Abedi A, Maitra NT, Gross EKV. Exact factorization of the time-dependent electron-nuclear wave function. *Phys Rev Lett*. (2010) 105:123002. doi: 10.1103/PhysRevLett.105.123002
35. Abedi A, Maitra NT, Gross EKV. Correlated electron-nuclear dynamics: exact factorization of the molecular wavefunction. *J Chem Phys*. (2012) 137:22A530. doi: 10.1063/1.4745836
36. Chiang YC, Klaiman S, Otto F, Cederbaum LS. The exact wavefunction factorization of a vibronic coupling system. *J Chem Phys*. (2014) 140:054104. doi: 10.1063/1.4863315
37. Middleton CT, de La Harpe K, Su C, Law YK, Crespo-Hernández CE, Kohler B. DNA excited-state dynamics: from single bases to the double helix. *Annu Rev Phys Chem*. (2009) 60:217–39. doi: 10.1146/annurev.physchem.59.032607.093719
38. Barbatti M, Aquino AJA, Lischka H. The UV absorption of nucleobases: semi-classical *ab initio* spectra simulations. *Phys Chem Chem Phys*. (2010) 12:4959–67. doi: 10.1039/b924956g
39. Esposito L, Banyasz A, Douki T, Perron M, Markovitsi D, Improta R. Effect of C5-methylation of cytosine on the photoreactivity of DNA: a joint experimental and computational study of TCG trinucleotides. *J Am Chem Soc*. (2014) 136:10838–41. doi: 10.1021/ja5040478
40. Tommasi S, Denissenko MF, Pfeifer GP. Sunlight induces pyrimidine dimers preferentially at 5-methylcytosine bases. *Cancer Res*. (1997) 57:4727–30.
41. Pfeifer GP, You YH, Besaratinia A. Mutations induced by ultraviolet light. *Mutat Res Fundam Mol Mech Mutagen*. (2005) 571:19–31. doi: 10.1016/j.mrfmmm.2004.06.057
42. de Gruijl FR. Skin cancer and solar UV radiation. *Eur J Cancer*. (1999) 35:2003–9. doi: 10.1016/S0959-8049(99)00283-X
43. He YG, Wu CY, Kong W. Decay pathways of thymine and methyl-substituted uracil and thymine in the gas phase. *J Phys Chem A*. (2003) 107:5145–8. doi: 10.1021/jp034733s
44. Kang H, Lee KT, Jung B, Ko YJ, Kim SK. Intrinsic lifetimes of the excited state of DNA and RNA bases. *J Am Chem Soc*. (2002) 124:12958–9. doi: 10.1021/ja027627x
45. Crespo-Hernandez CE, Cohen B, Hare PM, Kohler B. Ultrafast excited-state dynamics in nucleic acids. *Chem Rev*. (2004) 104:1977–2019. doi: 10.1021/cr0206770
46. Ullrich S, Schultz T, Zgierski MZ, Stolow A. Electronic relaxation dynamics in DNA and RNA bases studied by time-resolved photoelectron spectroscopy. *Phys Chem Chem Phys*. (2004) 6:2796–801. doi: 10.1039/b316324e
47. Keefer D, Thallmair S, Matsika S, de Vivie-Riedle R. Controlling photorelaxation in uracil with shaped laser pulses: a theoretical assessment. *J Am Chem Soc*. (2017) 139:5061–6. doi: 10.1021/jacs.6b12033
48. Reiter S, Keefer D, de Vivie-Riedle R. RNA environment is responsible for decreased photostability of uracil. *J Am Chem Soc*. (2018) 140:8714–20. doi: 10.1021/jacs.8b02962
49. Hudock HR, Levine BG, Thompson AL, Satzger H, Townsend D, Gador N, et al. *Ab initio* molecular dynamics and time-resolved photoelectron spectroscopy of electronically excited uracil and thymine. *J Phys Chem A*. (2007) 111:8500–8. doi: 10.1021/jp0723665
50. Richter M, Mai S, Marquetand P, Leticia Gonzalez L. Ultrafast intersystem crossing dynamics in uracil unravelled by *ab initio* molecular dynamics. *Phys Chem Chem Phys*. (2014) 16:24423–36. doi: 10.1039/C4CP04158E
51. Fingerhut BP, Dorfman KE, Mukamel SJ. Probing the conical intersection dynamics of the RNA base uracil by UV-pump stimulated-Raman-probe signals; *ab initio* simulations. *J Chem Theory Comput*. (2014) 10:1172–88. doi: 10.1021/ct401012u
52. Keefer D, Schnappinger T, de Vivie-Riedle R, Mukamel S. Visualizing conical intersection passages via vibronic coherence maps generated by stimulated ultrafast X-ray Raman signals. *Proc Natl Acad Sci USA*. (2020) 117:24069–75. doi: 10.1073/pnas.2015988117
53. Vacher M, Mendive-Tapia D, Bearpark MJ, Robb MA. Electron dynamics upon ionization: control of the timescale through chemical substitution and effect of nuclear motion. *J Chem Phys*. (2015) 142:094105. doi: 10.1063/1.4913515
54. Jenkins AJ, Vacher M, Twidale RM, Bearpark MJ, Robb MA. Charge migration in polycyclic norbornadiene cations: winning the race against decoherence. *J Chem Phys*. (2016) 145:164103. doi: 10.1063/1.4965436
55. Arnold C, Vendrell O, Santra R. Electronic decoherence following photoionization: full quantum-dynamical treatment of the influence of nuclear motion. *Phys Rev A*. (2017) 95:033425. doi: 10.1103/PhysRevA.95.033425
56. von den Hoff P, Siemering R, Kowalewski M, de Vivie-Riedle R. Electron dynamics and its control in molecules: from diatomics to larger molecular systems. *IEEE J Select Top Quantum Electron*. (2012) 18:119–29. doi: 10.1109/JSTQE.2011.2107893
57. Nikodem A, Levine RD, Remacle F. Quantum nuclear dynamics pumped and probed by ultrafast polarization controlled steering of a coherent electronic state in LiH. *J Phys Chem A*. (2016) 120:3343–52. doi: 10.1021/acs.jpca.6b00140
58. Jia D, Manz J, Yang Y. Timing the recoherences of attosecond electronic charge migration by quantum control of femtosecond nuclear dynamics: a case study for HCCI+. *J Chem Phys*. (2019) 151:244306. doi: 10.1063/1.5134665
59. Schüppel F, Schnappinger T, Bäumli L, de Vivie-Riedle R. Waveform control of molecular dynamics close to a conical intersection. *J Chem Phys*. (2020) 153:224307. doi: 10.1063/5.0031398
60. Bhattacharjee A, Leone SR. Ultrafast X-ray transient absorption spectroscopy of gas-phase photochemical reactions: a new universal probe of photoinduced molecular dynamics. *Acc Chem Res*. (2018) 51:3203–11. doi: 10.1021/acs.accounts.8b00462

61. Zinchenko KS, Ardana-Lamas F, Seidu I, Neville SP, van der Veen J, Lanfaloni VU, et al. Sub-7-femtosecond conical-intersection dynamics probed at the carbon K-edge. *Science*. (2021) 371:489–94. doi: 10.1126/science.abf1656
62. Bayer T, Braun H, Sarpe C, Siemering R, von den Hoff P, de Vivie-Riedle R, et al. Charge oscillation controlled molecular excitation. *Phys Rev Lett*. (2013) 110:123003. doi: 10.1103/PhysRevLett.110.123003
63. Braun H, Bayer T, Sarpe C, Siemering R, de Vivie-Riedle R, Baumert T, et al. Coupled electron-nuclear wavepacket dynamics in potassium dimers. *J Phys B Atomic Mol Opt Phys*. (2014) 47:124015. doi: 10.1088/0953-4075/47/12/124015

Conflict of Interest: The authors declare that the research was conducted in the absence of any commercial or financial relationships that could be construed as a potential conflict of interest.

Copyright © 2021 Bäumli, Schnappinger, Kling and de Vivie-Riedle. This is an open-access article distributed under the terms of the Creative Commons Attribution License (CC BY). The use, distribution or reproduction in other forums is permitted, provided the original author(s) and the copyright owner(s) are credited and that the original publication in this journal is cited, in accordance with accepted academic practice. No use, distribution or reproduction is permitted which does not comply with these terms.

3.3 Coupled Nuclear and Electron Dynamics in NO₂

The second system that is used to test the potential of NEMol in combination with the grid extension and the 1e-2o approximation is the small symmetric molecule NO₂. Probably even more than in uracil, the photochemical properties of NO₂ are well studied both in experiment [274–281] and in theory [223–226, 282–290]. After excitation into the first excited state, a CoIn enables an ultrafast non-adiabatic transition back to the ground state within less than 100 fs. Again, the coherent electron dynamics induced by the passage through the CoIn region is monitored with the help of NEMol. However, the situation in NO₂ is different from the uracil case since the nuclear wave packet is much more localized and the studied coupling region in NO₂ is determined by a single CoIn with a well-defined GP and not a complex seam of multiple CoIns. The symmetric and quite decent structure of the coupling region, together with the quite high transition dipole moment between the involved states offer in principle a good possibility to control the dynamics at the CoIn with the help of a few-cycle IR pulse. As shown in chapter 2.2 the variation of the CEP of such a pulse can control the population dynamics. Previous theoretical works [223–226] have already shown that this type of control works for NO₂ but these studies focused mainly on the population dynamics and the evolution of the nuclear wave packet influenced by the laser pulse.

With the help of NEMol it is possible to observe the impact of the laser pulse on the coherent electron dynamics and compare it with the field-free situation. For this detailed analyses of the nuclear and electron dynamics it is necessary to link the electronic density which is represented in the laboratory frame with the nuclear wave packet which is calculated in an internal coordinate space. The connection between these two coordinate systems and their inherent symmetry is visualized in Figure 3.4. The two dimensional internal coordinate space is defined by the bending angle α and the asymmetric stretching coordinate b , for the definition of b see bottom left of Figure 3.4. The molecule is orientated in such a way that the molecular plane is equivalent to the yz -plane and the center of mass defines the origin of the laboratory frame. For this orientation the molecule is mirror symmetric with respect to xy -plane at the FC point and for all relevant critical structures (left side dotted black line Figure 3.4). Each violation of this symmetry makes a distinction between the right side and the left side of the molecule possible. The same mirror plane is found in the internal coordinate space for the coordinate b being equal to zero. This mirror plane is shown in white on the right of Figure 3.4 with help of the ground state PES. If the nuclear wave packet is not symmetric with respect to this plane a distinction between left (negative b value) and right (positive b value) can be made.

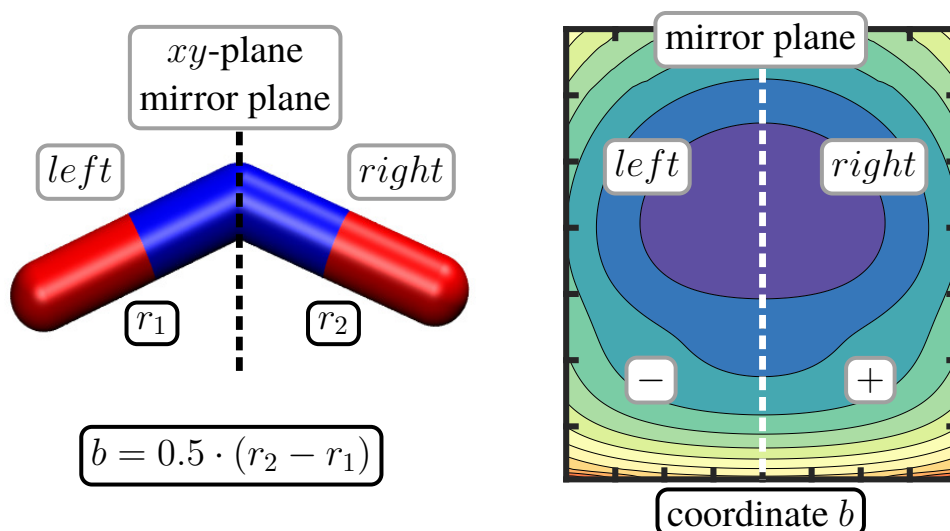


Figure 3.4: Connection between the molecular orientation in the laboratory frame (left) and the two dimensional internal coordinate space (right) used for the simulation of the coupled nuclear and electron dynamics in NO₂. The geometry shown on the left corresponds to the FC point and the ground state PES is used on the right side.

In the article “Coupled Nuclear and Electron Dynamics in the Vicinity of a Conical Intersection” published by the Journal of Chemical Physics [291] the question of how a few-cycle IR pulse can influence and control the dynamics in NO₂ has been extended. The reaction of the electron dynamics on the variation of the CEP is monitored and in addition the control of the nuclear dynamics is also rigorously analyzed once again. The key findings of the article are:

- The coupled nuclear and electron dynamics of NO₂ in the field-free case is analyzed using the temporal evolution of the induced dipole moment in the 1e-2o approximation. The signal of coherent electron dynamics appears each time the nuclear wave packet passes the CoIn but it is not strong and only short lived. The observed frequencies of the coherent electron dynamics cover a range up to 2.3 eV which originates from the nuclear overlap term as well as from the electronic phase term. The nuclear wave packet and the coupled electron density are symmetric with respect to the mirror-plane shown in Figure 3.4. Due to this symmetric behavior the electronic coherence is weak and short lived, which is expected since the individual contributions cancel out [292].
- The few-cycle IR pulse is applied to influence the first passage (10 fs) through the CoIn, since here the largest electronic coherence in the field-free case is observed. The pulse generates an asymmetric movement of the nuclear and electronic wave packets with respect to mirror planes. The symmetry breaking of the nuclear motion and the change of the population dynamics lead to a significant increase of electronic coherence. This enhanced build-up of the coherent electron dynamics by the laser pulse is clearly visible the induced dipole moment.
- To characterize and to quantify the effect of the CEP control scheme on the nuclear dynamics two objectives are used. The first one is the CEP efficiency $\Gamma(t)$ defined in equation 2.11 in section 2.2. It can be used to determine the CEP dependency of the population. The second objective is the CEP-dependent asymmetry parameter $AN(t, \phi)$ quantifying the CEP induced asymmetry in the nuclear motion with respect to the coordinate b , i.e. the mirror plane (for definition see Figure 3.4).

$$AN(t, \phi) = \frac{P_{D0}^R(t, \phi) - P_{D0}^L(t, \phi)}{P_{D0}(t, \phi)}. \quad (3.19)$$

It provides a distinction between left and right within the molecular plane (yz -plane) and allows to quantify the CEP dependency of the nuclear motion. Similar to $\Gamma(t)$ a maximum asymmetry $AN_{max}(t)$ is calculated as:

$$AN_{max}(t) = \max(AN(t, \phi)) + \min(AN(t, \phi')). \quad (3.20)$$

Applying the two objectives, two different responses of the nuclear dynamics on the CEP variation are observed. The asymmetry parameter $AN(t, \phi)$ shows a 2π periodicity which is typical for an interference process (see section 2.2). For the population itself the CEP dependence shows a π periodicity, arising from the temporal asymmetry of the few-cycle pulse [230, 293].

- For the analysis of the coherent electron dynamics, comparable objectives are defined. To monitor the induced asymmetry of the 1e-2o-density $\rho(r, t, \phi)$ the CEP dependent asymmetry parameter $AE(t, \phi)$ is calculated.

$$AE(t, \phi) = \frac{N^R(t, \phi) - N^L(t, \phi')}{N^R(t, \phi) + N^L(t, \phi')}. \quad (3.21)$$

with the probabilities $N^L(t, \phi)$ and $N^R(t, \phi)$ to find the electron on the left or the right side of the molecule (for definition see Figure 3.4). The maximum asymmetry of the electron density $AE_{max}(t)$ is calculated as follows:

$$AE_{max}(t) = \max(AE(t, \phi)) + \min(AE(t, \phi')). \quad (3.22)$$

At its temporal maximum the electron dynamics shows the highest CEP dependence and thus the highest controllability. As further objectives, the induced dipole moment in the y and the z direction are used. For both quantities the maximum CEP dependence $\gamma_y(t)$ and $\gamma_z(t)$ are evaluated as

the difference of its maximum and the minimum value for each time step. When analyzing the asymmetry parameter $AE(t, \phi)$ or the z component of the dipole moment, the CEP dependency shows a 2π periodicity like the nuclear asymmetry parameter $AN_{max}(t)$. The y component of the induced dipole moment reveals a π periodicity similar to the CEP dependent population.

- The effect of the few-cycle IR pulse lives considerably longer than the pulse in all investigated quantities. Depending on the chosen observable a π or 2π periodicity can be found, indicating two separate mechanisms which are present in the nuclear as well as in the electron dynamics. The periodicities indicate that one is based on interference and the other one induced by the waveform of the pulse itself. In summary, the CEP scheme offers the possibility to control both the nuclear and the electron motion near a CoIn.
- This work demonstrates that the NEMol ansatz is able to describe the coupled nuclear and electron dynamics in molecular systems like NO₂ where the dynamics in the excited state is dominated by fast changing wave packet interference effects. Furthermore, it is possible to directly investigate the influence of the CEP scheme on the coherent electron dynamics.

The article “Coupled Nuclear and Electron Dynamics in the Vicinity of a Conical Intersection” is reprinted from *Journal of Chemical Physics* **154** (2021), 2134306 with permission from AIP Publishing. The supporting information of this article is available under <https://aip.scitation.org/doi/full/10.1063/5.0041365>.

Coupled nuclear and electron dynamics in the vicinity of a conical intersection

Cite as: J. Chem. Phys. 154, 134306 (2021); doi: 10.1063/5.0041365

Submitted: 22 December 2020 • Accepted: 11 March 2021 •

Published Online: 5 April 2021



View Online



Export Citation



CrossMark

Thomas Schnappinger and Regina de Vivie-Riedle^{a)}

AFFILIATIONS

Department of Chemistry, LMU Munich, Germany, D-81377 Munich, Germany

Note: This paper is part of the JCP Special Topic on Quantum Dynamics with *Ab Initio* Potentials.

^{a)} Author to whom correspondence should be addressed: Regina.de_Vivie@cup.uni-muenchen.de

ABSTRACT

Ultrafast optical techniques allow us to study ultrafast molecular dynamics involving both nuclear and electronic motion. To support interpretation, theoretical approaches are needed that can describe both the nuclear and electron dynamics. Hence, we revisit and expand our ansatz for the coupled description of the nuclear and electron dynamics in molecular systems (NEMol). In this purely quantum mechanical ansatz, the quantum-dynamical description of the nuclear motion is combined with the calculation of the electron dynamics in the eigenfunction basis. The NEMol ansatz is applied to simulate the coupled dynamics of the molecule NO₂ in the vicinity of a conical intersection (CoIn) with a special focus on the coherent electron dynamics induced by the non-adiabatic coupling. Furthermore, we aim to control the dynamics of the system when passing the CoIn. The control scheme relies on the carrier envelope phase of a few-cycle IR pulse. The laser pulse influences both the movement of the nuclei and the electrons during the population transfer through the CoIn.

Published under license by AIP Publishing. <https://doi.org/10.1063/5.0041365>

I. INTRODUCTION

The continuous development of attosecond laser pulses enables spectroscopic techniques, which allow for the time resolved investigations of ultrafast photo-initiated processes in atoms, molecules, and solids. Nowadays, it is possible to study electronic correlation and ultrafast molecular dynamics through pump-probe experiments.^{1–7} Within these experiments, attosecond, broadband pulses are used to generate electron wavepackets in highly excited states of molecules, leading to the discovery of effects such as electron localization in diatomic molecules^{3,8} and, later, of purely electronic charge migration in biologically relevant molecules.^{5–7} To explain and interpret the observations of these experiments, theoretical approaches are needed that can describe the dynamics of electrons in molecules. Most approaches use time-dependent analogs of well-established quantum-chemical methods such as time-dependent Hartree-Fock theory (TD-HF)⁹ or time-dependent density-functional theory (TD-DFT).¹⁰ Furthermore, time-dependent post-Hartree-Fock methods such as time-dependent configuration-interaction (TD-CI),^{11,12} time-dependent coupled-cluster (TD-CC),^{13,14} and multi-configuration time-dependent Hartree-Fock¹⁵ are available for the correlated description of electron dynamics in molecular systems. In other

theoretical approaches, the electronic wavefunction is propagated directly in time with the help of Green's function¹⁶ or in the basis of molecular orbitals.¹⁷ All these theories focus on the evolution of the electronic subsystem driven by electronic correlation^{18,19} and predict long-lived coherences. The neglect of the nuclear motion is justified by the assumption that the dynamics of the electrons is much faster than that of the heavier nuclei. This results in charge migration, an oscillatory motion of electron density with frequencies defined by the energy gaps among the states populated with the initial laser pulse. If the states of the superposition are close together, the electron dynamics becomes slow, and therefore, the nuclear motion can no longer be neglected. However, as shown in numerous theoretical works,^{8,20–25} nuclear motion, in general, causes decoherence in molecular systems and should not be neglected in any cases. This decoherence causes the electronic wavepackets to exist only for short time scales.²⁴ For small systems such as H₂⁺ or D₂⁺, a full quantum treatment of the coupled electron and nuclear dynamics is possible.²⁶ Beyond these three particle problems, there are computationally very demanding methods available based on a multi-configurational ansatz²⁷ or on the coupled description of nuclear and electronic flux.^{28,29} Further techniques are based on the coupled propagation of the nuclear and electronic wavefunctions on a single time-dependent potential energy surface.^{30–33} However, for

larger molecular systems, the main techniques used are mixed quantum classical representations.^{34–37} For example, the electron dynamics is described using TD-DFT and the nuclear motion is considered using an Ehrenfest approach.^{34,35} However, these methods do not reflect the quantum nature of the nuclei, which becomes important for ultrashort pulse excitation and non-adiabatic transitions.

In this paper, we want to revisit and expand an ansatz for the coupled description of the nuclear and electron dynamics in molecular systems^{8,38,39} (shortened NEMol) developed in our group. It is based on electronic structure calculations and nuclear quantum dynamics. In its initial formulation, the electronic wavefunctions are represented as Slater determinants and propagated in the eigenstate basis. The coupling of the nuclear motion to the electron motion is incorporated explicitly through the nuclear wavepacket motion as well as through a coherence term with contributions from the nuclear and electronic wavefunctions. Compared to similar approaches,^{30–33} the feedback of the electron motion to the nuclear dynamics is less directly introduced by simulating the nuclear dynamics on coupled potential energy surfaces (PES's). The central equation of the original NEMol ansatz^{8,38,39} relates the dynamics of the coupled one-electron density to the temporal evolution of the expected value of the nuclear positions. In the first part of this work, we want to generalize the NEMol ansatz by extending beyond this single geometry approximation. Therefore, we introduce the NEMol-grid in order to represent the electron dynamics at multiple points on the grid used for the nuclear wavepacket propagation. In the limit, the NEMol-grid is equal to the grid representing the nuclear wavepacket, but in practice, we choose a coarser one. By means of a simple approximation, it is possible to obtain a condensed representation of time-dependent electron density in the one-electron-two-orbital (1e-2o) picture.

In the second part, we want to explore the potential of our NEMol ansatz. For this purpose, we consider a situation that can generate coherent electron dynamics in excited states of molecules even without a laser pulse present. Such a scenario occurs in the vicinity of a conical intersection (CoIn).^{40–44} For this ubiquitous but nevertheless extraordinary points in a molecular system, the adiabatic separation between nuclear and electronic motion breaks down^{40,45,46} and the electronic states involved become degenerate. Beside the creation of funnels for radiationless electronic transitions, a coherent electron wavepacket is created whose dynamics approaches the time scale of the nuclear dynamics. All these properties of CoIn's are determined by the shape and size of the non-adiabatic coupling elements (NAC's) and the topography of the vicinity. As a realistic molecular system that provides such a situation, we have chosen the NO₂ molecule. After excitation into the first excited state, a CoIn enables an ultrafast non-adiabatic transition back to the ground state within less than 100 fs. This fast relaxation and the photophysics of NO₂, in general, have been widely explored both theoretically^{47–59} and experimentally.^{56,60–67} Beside the free relaxation of NO₂, we also studied the influence on the coupled electron dynamics when applying a few-cycle IR laser pulse in the vicinity of the CoIn. The variation of the carrier envelope phase ϕ (CEP) of such a few-cycle pulse offers the possibility to steer electrons and nuclei.^{56,57,59,64,68–76} Similar to previous studies,^{56,57,59,64} we apply this CEP-control-scheme to NO₂ and evaluate the CEP-dependence of the resulting coupled nuclear and electron dynamics.

II. COUPLED NUCLEAR AND ELECTRON DYNAMICS (NEMol)

In the original NEMol ansatz,^{8,38,39} the coupled one-electron density $\rho(r, t; \langle R \rangle(t))$ is defined according to Eq. (1). For convenience, the detailed derivation of this equation can be found in the Appendix adapted to the current notation

$$\rho(r, t; \langle R \rangle(t)) = \sum_j A_{jj}(t) \rho_{jj}(r; \langle R \rangle(t)) + \sum_{k \neq j} 2\text{Re} \left\{ A_{jk}(t) \rho_{jk}(r; \langle R \rangle(t)) e^{-i\xi_{jk}(t)} \right\}, \quad (1)$$

with

$$\xi_{jk}(t) = \Delta E_{jk}(\langle R \rangle(t)) \Delta t + \xi_{jk}(t - \Delta t). \quad (2)$$

The first summation consists of the state specific electronic density $\rho_{jj}(r, t; \langle R \rangle(t))$ weighted with the corresponding time-dependent population $A_{jj}(t)$. The second summation defines the coherent contribution to the coupled electron density and consists of the time-dependent overlap $A_{jk}(t)$, the one-electron transition density $\rho_{jk}(r, t; \langle R \rangle(t))$, and its pure electronic phase defined by the energy difference ΔE_{jk} between the electronic states involved. All quantities related to the electronic wavefunction are calculated for one nuclear geometry per time step, which is defined by the time-dependent expected value of the position $\langle R \rangle(t)$ (for definition, see the Appendix). As long as we are focusing on situations with quite localized wavepackets and/or one-dimensional systems,^{8,38,39} this approximation works quite well. However, in order to treat higher dimensional systems and more complex processes, we want to generalize the NEMol ansatz in this work. To extend the ansatz, the integration over the full nuclear coordinate space is split up in segments to improve the resolution of the spatial dependence of the electronic phase term. For this purpose, a second grid, the NEMol-grid, is introduced. The resulting modified NEMol ansatz is described using an exemplary system with two nuclear coordinates c_1 and c_2 . The complete two-dimensional coordinate space is split up into $M \times L$ segments defined by their boundaries m_{\min} , m_{\max} and l_{\min} , l_{\max} . For each of these segments ml , the population terms $\alpha_{jj}^{ml}(t)$ and the overlap terms $\alpha_{jk}^{ml}(t)$ are calculated,

$$\alpha_{jk}^{ml}(t) = \int_{m_{\min}}^{m_{\max}} \int_{l_{\min}}^{l_{\max}} \chi_j^*(R, t) \chi_k(R, t) dc_1 dc_2. \quad (3)$$

The sum of these segment terms results in the corresponding total population and overlap,

$$\sum_{m=1}^M \sum_{l=1}^L \alpha_{jk}^{ml}(t) = \langle \chi_j(R, t) | \chi_k(R, t) \rangle_R = A_{jk}(t). \quad (4)$$

At the center R_{ml} of each segment, the state specific electronic densities, the one-electron transition densities, and the eigenenergies are determined, and with these values, the coupled one-electron density for each segment $\rho_{ml}(r, t; R_{ml})$ is calculated,

$$\rho_{ml}(r, t; R_{ml}) = \sum_j \alpha_{jj}^{ml}(t) \rho_{jj}(r; R_{ml}) + \sum_{k \neq j} 2\text{Re} \left\{ \alpha_{jk}^{ml}(t) \rho_{jk}(r; R_{ml}) e^{-i\xi_{jk}^{ml}(t)} \right\}, \quad (5)$$

with

$$\xi_{jk}^{ml}(t) = \Delta E_{jk}(R_{ml})\Delta t + \xi_{jk}^{ml}(t - \Delta t). \quad (6)$$

It should be noted that for each segment, the ΔE_{jk} values and the electron densities are no longer dependent on $\langle R \rangle(t)$. In contrast to the original NEMol ansatz, now many ΔE values are simultaneously contributing to the overall electron dynamics. They are addressed whenever the nuclear wavepacket is located there. To obtain the total coupled electron density, the individual contributions of each segment are summed up,

$$\rho(r, t; R) = \sum_{m=1}^M \sum_{l=1}^L \rho_{ml}(r, t; R_{ml}). \quad (7)$$

This total coupled electron density $\rho(r, t; R)$ describes the electron dynamics coupled to multiple grid points on which the nuclear wavepacket is represented.

A second aspect that we would like to introduce is a further simplification. For clarity reasons, it is here formulated in terms of the original NEMol ansatz. We now consider a system of two electronic states described by their electronic wavefunctions φ_1 and φ_2 . In the simplest case, the wavefunctions of both states are described by two Slater determinants, which only differ in the occupation of one spin orbital θ . Now, the coupled total electron density can be simplified by expressing the densities and transition densities using the spin orbitals,

$$\begin{aligned} \rho(r, t; \langle R \rangle(t)) &= \sum_{j=1}^{N-1} |\theta_j(r; \langle R \rangle(t))|^2 + \sum_{k=1}^2 A_{kk}(t) |\theta_k(r; \langle R \rangle(t))|^2 \\ &+ 2\text{Re} \left\{ A_{12}(t) \theta_1(r; \langle R \rangle(t)) \theta_2(r; \langle R \rangle(t)) e^{-i\xi_{12}(t)} \right\}. \end{aligned} \quad (8)$$

The summation at the beginning includes the densities of all equally occupied orbitals and is followed by the densities of the remaining two orbitals θ_1 and θ_2 weighted with the populations $A_{11}(t)$ and $A_{22}(t)$. The coherent part contains the product of the orbitals θ_1 and θ_2 . Within this simplification, it is now possible to neglect the contributions of the equally occupied orbitals in order to study the coupled electron dynamics in a one-electron-two-orbital (1e-2o) picture. Under the above mentioned approximation, this 1e-2o picture is a possibility to examine the coherent part of the electron dynamics in a very condensed way. This simplification can also be made in combination with the NEMol-gird.

III. NO₂ COUPLED DYNAMICS

We apply our extended NEMol approach to the non-adiabatic dynamics of NO₂. In this molecule, a CoIn [depicted in Fig. 1(b)] between the D_1 and the D_0 state enables radiationless relaxation. The ultrafast non-adiabatic transition takes less than 100 fs and has been widely explored both theoretically^{47–59} and experimentally.^{56,63–67} First, we analyze the relaxation itself, and next, we apply a few-cycle IR laser pulse to control the dynamics in the vicinity of the CoIn, similar to previous studies.^{56,57,59,64} With our NEMol ansatz, we can study its influence on the motion of the nuclei and the electrons.

The nuclear dynamics is performed on the two-dimensional adiabatic potential energy surfaces of the D_1 and the D_0 state shown in Fig. 1. The coordinates spanning the PES's are the gradient difference and derivative coupling vectors defining the branching space of

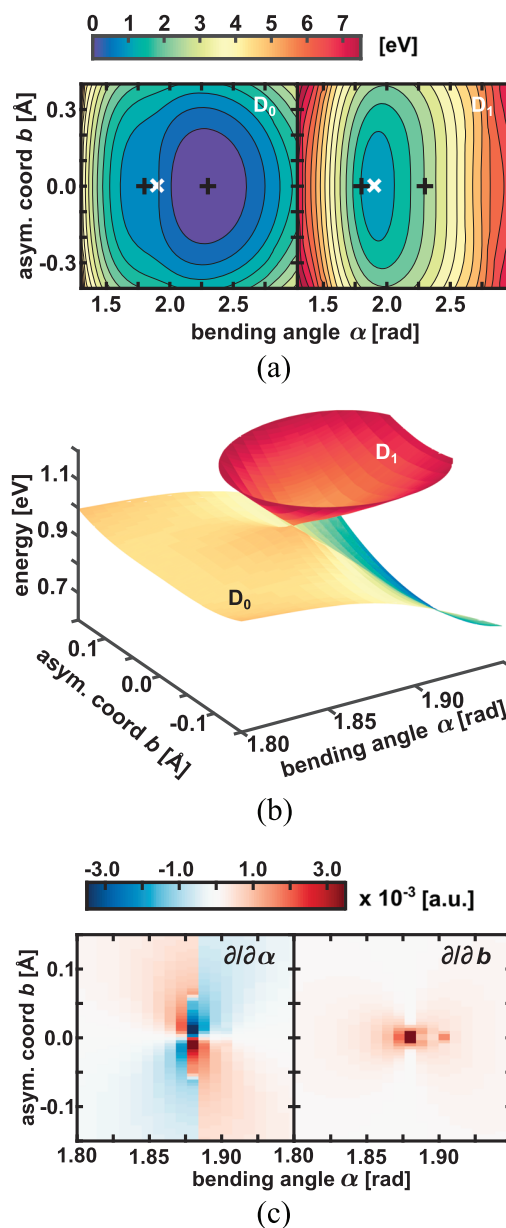


FIG. 1. (a) Adiabatic potential energy surfaces of the D_0 state (left) and the D_1 state (right) of NO₂. The CoIn is marked in white, and the positions of the relevant minima in the two-dimensional subspace are displayed in black. The two marked minima are only slightly higher in energy than the fully optimized minimum structures shown in the [supplementary material](#). (b) The vicinity of the D_1/D_0 -CoIn. (c) Non-adiabatic coupling elements between D_1 and D_0 at the CoIn: α -element (left) and b -element (right).

the D_1/D_0 -CoIn depicted in Fig. 1(b). These two vectors correspond to the bending angle α and the asymmetric stretching coordinate b , defined as half the difference between the two NO distances. The last internal degree of freedom, the symmetric stretch coordinate, is kept constant at the value of the optimized D_1/D_0 -CoIn (1.267 Å). As

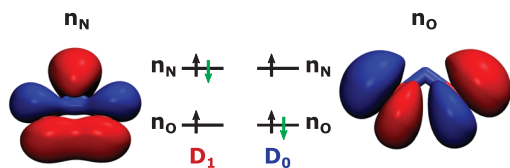


FIG. 2. Molecular orbital schematic with the active electron indicated in green and corresponding orbitals at the optimized CoIn. Orbitals are shown with an isovalue of 0.05.

shown by Richter *et al.*,⁵⁷ the population dynamics obtained within this two-dimensional coordinate space is in very good agreement with the full dimensional simulations performed by Arasaki *et al.*⁵⁶ We performed our dynamics simulations in the adiabatic representation, and the corresponding NAC's between D_1 and D_0 are shown in Fig. 1(c). It should be mentioned that in previous studies,^{56,57,59} the simulations were performed in the diabatic representation, and therefore, small deviations may occur due to the limitation of the grid spacing. Further information about the simulation setup can be found in Sec. II of the [supplementary material](#).

In order to calculate the coupled electron density according to Eq. (7), we define a NEMol-grid of 15×13 points that are equally distributed between 1.34 and 2.86 rad in the α -coordinate and between -0.33 and 0.33 Å in the b -coordinate. The necessary population- and overlap-terms are calculated for equal-spaced segments around these grid points. To cover the entire PES, the segments for the boundary grid points are larger. The transformation of the full wavepacket onto the NEMol-grid, the overlap terms, and the resulting coherence terms are visualized in Fig. S6 (free propagation)

and Fig. S10 (propagation with laser pulse) of the [supplementary material](#). The two active orbitals that are required to describe the NEMol-dynamics in the one-electron-two-orbital (1e-2o) picture are shown in Fig. 2 at the optimized CoIn. The non-binding orbital n_N with contributions at the nitrogen atom is associated with the D_1 state, and the non-binding orbital n_O located only at the oxygen atoms is attributed to the D_0 state. The energy difference ΔE between the D_0 and D_1 state for each grid point is shown in Fig. S4 of the [supplementary material](#).

A. Free dynamics of NO₂

To initiate the dynamics simulation in the D_1 state, we assumed a delta pulse excitation. The temporal evolution of the population of both states is shown in the upper panel of Fig. 3, and the dynamics of the nuclear wavepackets integrated over the α -coordinate and the b -coordinate is depicted in Fig. S5 for both surfaces. The nuclear wavepacket started in D_1 reaches the vicinity of the CoIn after ~ 7 fs for the first time. While passing the coupling region in the time interval from 7 to 15 fs, the population of the electronic ground state increases to over 60%. The part of the nuclear wavepacket remaining in the D_1 state reaches its turning point around 15 fs and then propagates backwards. This leads to a second passage through the CoIn area and an increase in the population of the D_0 state around 22 fs. The nuclear wavepacket evolving on the lower adiabatic surface re-encounters the CoIn region later at around 30 fs. During this third passage, a substantial part of the population is transferred back into the excited state. After 35 fs, the wavepacket is delocalized on both surfaces and the population is nearly equal in both states. Toward the end of the simulation at around 50 fs, a fourth passage occurs. The

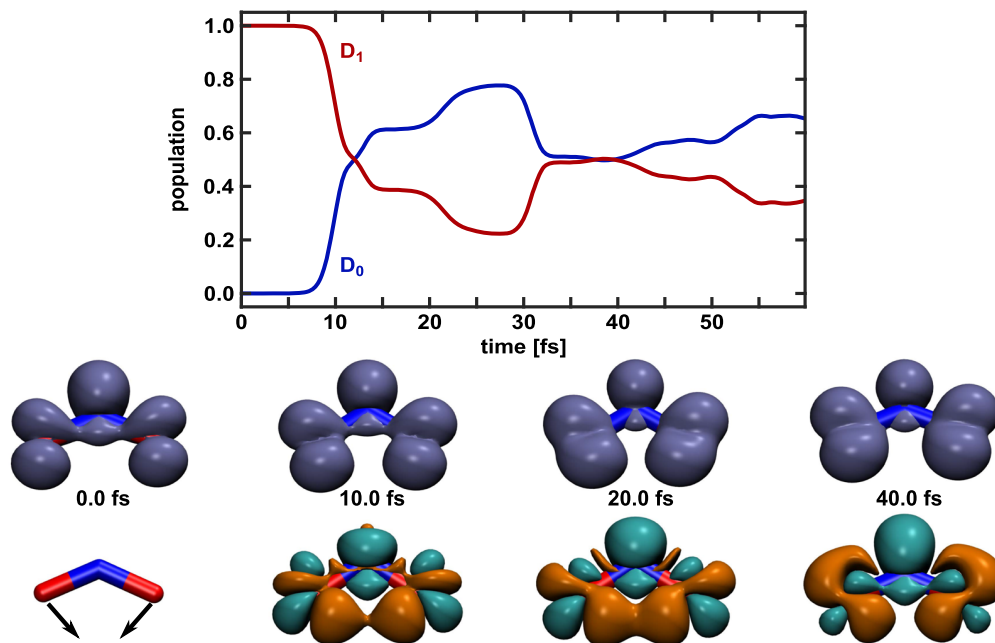


FIG. 3. Free dynamics of NO₂. Upper panel: Populations of the D_0 and D_1 states as a function of simulation time. Lower panel: Snapshots of the electron density in the 1e-2o picture and the difference in density relative to the initial density (green: electron-loss and orange: electron-gain). The isovalues used are 0.006 and ± 0.002 . The arrows on the left geometry (0.0 fs) indicate the movement of the nuclei. An animation of the electron density in the 1e-2o picture and the difference density can be found in the [supplementary material](#).

wavepacket remains symmetrical with respect to the b -coordinate for the whole simulation time. For the wavepacket on the lower PES [see right sight of Fig. S5(b) of the [supplementary material](#)], the formation of a nodal structure for $b = 0.0$ Å is clearly visible, which is a signature of destructive self-interference due to the geometric phase effect.^{45,46,77}

In the lower part of Fig. 3, snapshots of the electron density in the 1e-2o picture are shown. For a better visualization, also the difference in density with respect to $t = 0$ fs is depicted. The molecule is orientated in such a way that the molecular plane is equivalent to the yz -plane and the center of mass defines the origin of the laboratory frame. Therefore, the internal α -coordinate points to the same direction as the y -coordinate and the internal b -coordinate is associated with the z -coordinate. The orientation of the molecule is shown in the upper right corner of Fig. 4. In correspondence to the non-adiabatic transition from the D_1 state to the D_0 state, the main feature of the electron dynamics is the loss of density at the nitrogen atoms and the corresponding gain of density at the oxygen atoms. In addition, the change in the electron density attributed to the motion of the nuclei (Born–Oppenheimer part) is present. Due to the high symmetry of NO_2 , the electron density is mirror-symmetrical with respect to the xy -plane, which is equivalent to the symmetric behavior of the nuclear wavepacket with respect to the b -coordinate.

To analyze the electron dynamics, we calculated the dipole moment of the electron density within the 1e-2o picture. In the upper panel of Fig. 4, the temporal evolution of its three components is shown; for the molecular orientation, see the upper right corner of Fig. 4. To distinguish the Born–Oppenheimer part of the

dynamics from the coherent electron dynamics, the density was calculated once with the coherent part included and once without. For both quantities, the respective dipole moments were determined as well as their difference, hereinafter labeled as Δ 1e-2o, and are shown in the lower panel of Fig. 4. The active orbitals do not change along the x -coordinate, and thus, the 1e-2o- x -component of the dipole moment stays zero and is excluded from further discussions. The 1e-2o- y -component shows the largest values and the strongest changes over time. Its evolution follows the dynamics of the population. In the initial 20 fs, the first passage through the CoIn region occurs and, simultaneously, the value of the 1e-2o- y -component changes from 0.3 to -0.3 a.u. The zero crossing occurs at 10 fs. For later times, when dephasing and partial recurrence of the nuclear wavepackets become important, the y -component approaches zero at about 40 fs and becomes negative thereafter again. These main features disappear for the Δ 1e-2o- y -component (lower panel Fig. 4), and only fast oscillations with one order of magnitude smaller amplitudes are left. The largest amplitudes are observed around 10, 30, and 50 fs. These amplitudes coincide with the passages of the wavepacket through the CoIn region. The large difference between the 1e-2o and the Δ 1e-2o value means that the dynamics of the y -component is dominated by the nuclear motion. That is understandable since the y -coordinate is aligned along the main direction of dynamics (α -coordinate), which mediates the non-adiabatic transition. The temporal evolution of the 1e-2o- z -component is an order of magnitude smaller and almost identical to its Δ value. The dynamics of the z -component is not dominated by the nuclear motion but solely induced by the coherent electron dynamics. Therefore, we can use the y - and the z -component to distinguish between the two contributions of the coupled electron dynamics. As the Δ values of both components lie amplitude-wise in the same region and show a similar pattern, they are suitable to monitor the coherent electron dynamics in the system. Overall, the nuclear motion has a much larger impact on the dipole moment than the coherent electron dynamics.

By applying the Fourier transform to the temporal evolution of the dipole moments, the corresponding frequencies are determined. Beside the Δ 1e-2o- and 1e-2o-components, the dipole moment calculated with the full density was also used. The resulting spectra for the y - and the z -component for all three cases are shown in Fig. 5. The spectra are all normalized to one individually. The relative magnitude between all quantities can be estimated from Fig. 4. All frequencies with an intensity larger than 0.1 are listed in Tables S3 and S4 of the [supplementary material](#).

The Δ 1e-2o spectra (Fig. 5, blue), reflecting the coherent electron dynamics, cover the largest frequency range from 0.2 to 2.3 eV for both components, whereas the energy differences ΔE (0.0–1.0 eV, see Fig. S4) in the vicinity of the CoIn, which enter in the coherent part of the electronic wavepacket, are smaller. These discrepancies can be rationalized when taking a closer look at the coherence term [see Eq. (1)]. Two of the factors in the product contribute to the overall phase, the nuclear overlap and the electronic phase term containing the ΔE values. The phase of the overlap term relates to the difference in momentum of the nuclear wavepackets involved. In our test system NO_2 , the wavepacket on D_1 approaches the CoIn with a high momentum, larger than the ΔE gaps near the CoIn. In other words, the coherent dynamics of the electronic wavepacket is in the NO_2 case also significantly influenced by the phase-differences of the nuclear wavepackets moving on different

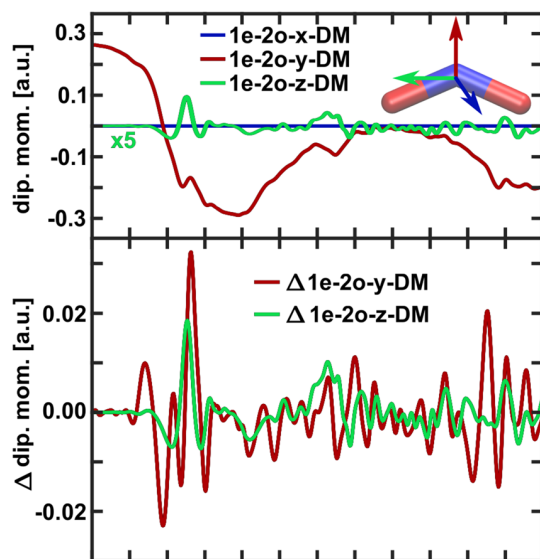


FIG. 4. Field-free temporal evolution of the dipole moment components based on the electron density in the 1e-2o picture. Upper panel: total value of all three components. The 1e-2o- z -component is enhanced by a factor of five. The orientation of the molecule is shown as inset in the upper right corner. Lower panel: Difference between the dipole moment components (Δ 1e-2o), one time calculated with the coherence term included and once without it. Differences only shown for the y - and z -components.

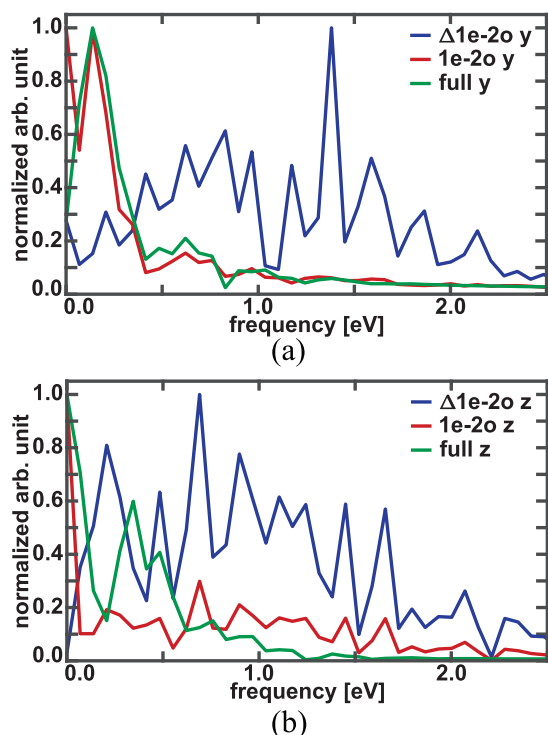


FIG. 5. The Fourier spectra of the y -component (a) and z -component (b) of the dipole moment obtained using the Δ 1e-2o-components (blue), the 1e-2o-components (red), and the components calculated with the full density (green). All spectra are normalized to one individually.

potentials. This correlation is illustrated in Fig. S7 of the [supplementary material](#) for two individual NEMol-grid points. The frequencies for the 1e-2o-components (Fig. 5, red) are dominated by the slower nuclear dynamics (Born–Oppenheimer part) giving rise

to the strong peaks below 0.5 eV. Simultaneously, high energy parts lose intensity. This effect is stronger for the y -component, whereas for the z -component, the initial pattern is still recognizable. This behavior is further increased for the full density (Fig. 5, green). For both components, some peaks appear in all three cases, especially in the energy range between 0.5 and 0.75 eV. They can be attributed to the coherent electron dynamics and may also be experimentally observable.

Further information can be gained by extracting the time when these frequencies occur. This allows us to connect them to a specific movement in the system. Therefore, we performed short-time Fourier transform spectra for the Δ 1e-2o- y and Δ 1e-2o- z components using a Gaussian windowing function with a width of 180 data points corresponding to a time of 18.14 fs. The resulting two spectrograms are shown in Fig. 6. The Δ 1e-2o- y spectrogram (left) shows two main pairs of signals around 10 fs (0.5–1.7 eV) and 50 fs (0.7–1.7 eV), which correspond to the first and the fourth passage of the wavepacket through the CoIn region. The signals are most pronounced at the first passage and significantly attenuated at the fourth passage. There are considerably weaker peaks observable at 25 and 30 fs, which can be attributed to the second and the third passage. In addition, the Δ 1e-2o- z spectrogram (right) shows two main signals. The first one appears around 10 fs (first passage through the CoIn) and covers a frequency range from 0.5 to 1.7 eV. The third passage around 30 fs can be attributed to the second signal, which extends over low-frequency components (0.1–1.0 eV) and has a lower intensity. Again, considerably weaker peaks can be found around 20–25 fs (second passage) and after 50 fs (fourth passage). Thus, each passage of the nuclear wavepacket through the CoIn region induces coherent electron dynamics, although not to the same extent for both components. The coherent dynamics is only short-lived for 5–7 fs, and the intensity of its signal decreases with time. The highest intensities are observed for the first transition when the localized initial nuclear wavepacket hits the CoIn. The subsequent dephasing and branching of the nuclear wavepacket blur the electronic coherence. In summary, we observe a short but recurring

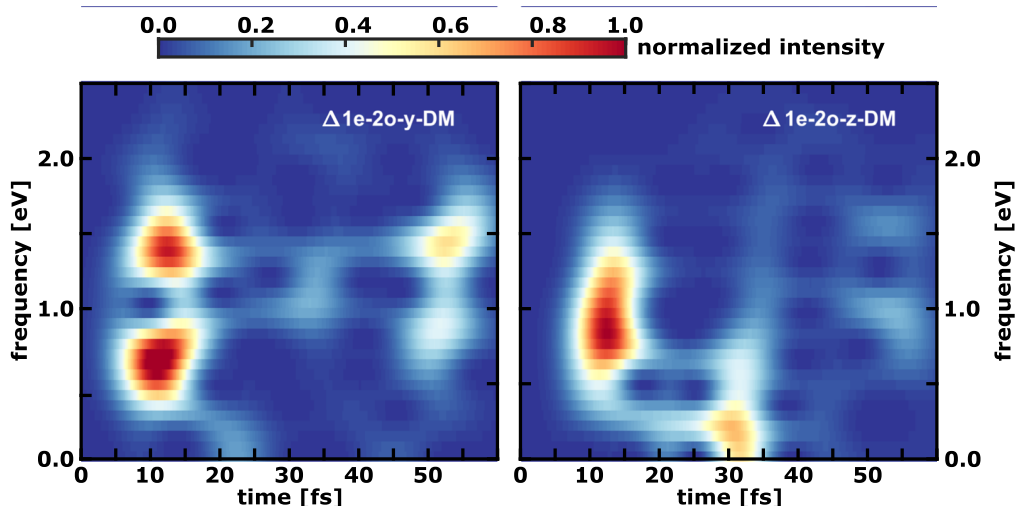


FIG. 6. Short-time Fourier transform of the Δ 1e-2o- y dipole moment component (left) and Δ 1e-2o- z dipole moment component (right). The Fourier spectrograms are normalized, and a Gaussian windowing function with a width of 180 data points corresponding to a time of 18.14 fs is used.

appearance of the coherent electron dynamics that is modulated by the nuclear wavepacket motion. In the following, we focus on the first passage (10 fs) for applying a few-cycle IR pulse to influence the coupled dynamics of NO₂ since here the largest electronic coherence in the field-free case exists.

B. Dynamics in the presence of a few-cycle IR pulse

Again, a delta pulse excitation is used to initiate the dynamics. With the appropriate time delay, a few-cycle IR laser pulse is applied to influence the first passage through the CoIn and thereby the subsequent coupled dynamics. The used few-cycle pulse has a Gaussian shape and is defined as

$$E(t) = E_{\max} \cdot e^{-2\left(\frac{t-t_0}{\sigma}\right)^2} \cdot \cos(\omega_0(t-t_0) + \phi),$$

with

$$\sigma = \frac{\text{FWHM}}{\sqrt{2\log(2)}}, \quad (9)$$

with the central frequency ω_0 , the time zero t_0 , the maximal field amplitude E_{\max} , the full width half maximum (FWHM), and the carrier envelope phase ϕ (CEP). The time zero t_0 of the pulse, defining the position of its maximum, was chosen to match the time window when the wavepacket is located near the CoIn ($t_0 = 10$ fs). For this time, the nuclear wavepacket is still very localized and the electronic coherence is maximal. The central frequency ω_0 is chosen to be resonant with the actual energy gap $\Delta E = 0.76$ eV between the electronic states. The remaining three pulse parameters, the field amplitude E_{\max} , the full width half maximum (FWHM), and the CEP

ϕ , are set to $E_{\max} = 0.103$ GV cm⁻¹ (which corresponds to a maximum intensity of 1.4×10^{13} W cm⁻²), FWHM = 8 fs, and $\phi = 0\pi$. In comparison with the pulse parameters used by Richter *et al.*,^{57,59} all values are quite similar. Only our intensity is lower to stay in the range where the influence of the CEP pulse is mainly determined by the interplay of the non-adiabatic transition and the light induced electronic coherence.⁷⁶ By this, we also ensure to stay below or at the threshold of ionization. The light-matter interaction is treated within the dipole approximation (for details, see Sec. I of the [supplementary material](#)). We assume that the electric component of the pulse is optimally aligned with the transition dipole moment. The absolute value of the TDM is used, which is shown in Fig. S3(a) of the [supplementary material](#). As stated by Richter *et al.*,⁵⁷ already a moderate molecular alignment distribution is sufficient to observe the effect of such a control pulse.

The evolution of the adiabatic populations influenced by the few-cycle IR-field is shown in the upper panel of Fig. 7. The related nuclear wavepacket dynamics on both surfaces integrated over the α -coordinate and the b -coordinate is depicted in Fig. S8 of the [supplementary material](#). During the first transition through the CoIn region (7–15 fs), a 50:50 population of both states is created. The interaction with the light pulse is reflected in the small wriggles around 10 fs. The subsequent dynamics is comparable to the field-free case up to 30 fs. Thereafter, no clear passage through the CoIn region is observable. Thus, the IR pulse induces a change in the nuclear dynamics, which persists beyond the pulse duration. As an important consequence, the nuclear motion becomes asymmetric with respect to the b -coordinate, and the nuclear wavepacket even loses its nodal structure [compare both Figs. S5(b) and S8(b) of the

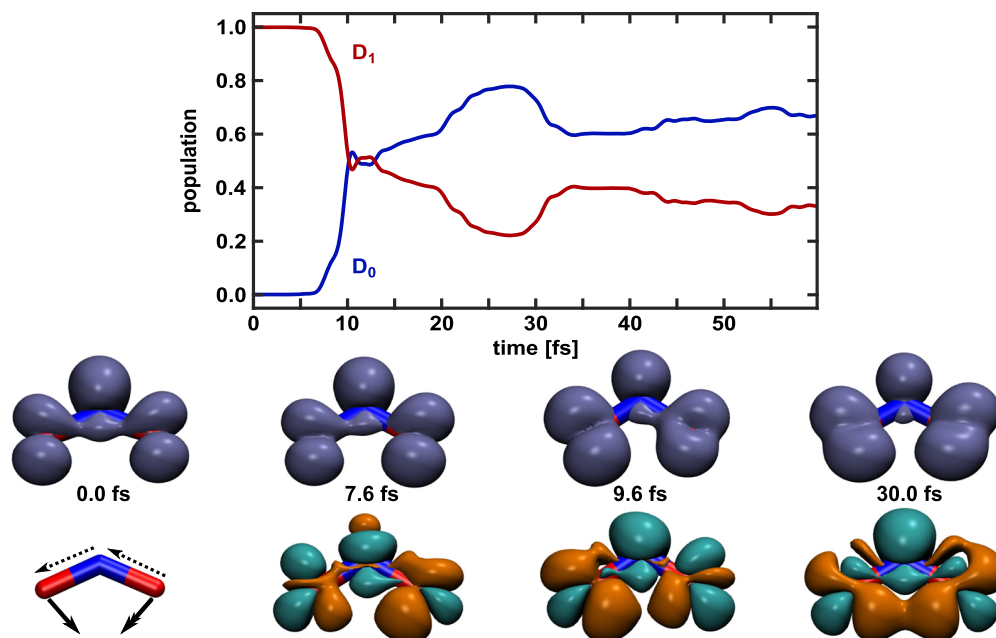


FIG. 7. Dynamics of NO₂ in the presence of a few-cycle IR laser pulse. Upper panel: Populations of the D_0 and D_1 states as a function of simulation time. Lower panel: Snapshots of the electron density in the 1e-2o picture and the density difference relative to the initial density (green: electron-loss and orange: electron-gain). The isovalues used are 0.006 and ± 0.002 . The arrows on the left geometry (0.0 fs) indicate the movement of the nuclei (main direction is shown as bold, and additional movement is shown as dotted arrows). An animation of the electron density in the 1e-2o picture and the difference density can be found in the [supplementary material](#).

supplementary material], which was also observed by Richter *et al.*⁵⁷ This asymmetry leads to the partly deviations from the CoIn region after 30 fs. On the lower panel of Fig. 7, snapshots of the electron density in the 1e-2o picture are shown. Again, the difference in density with respect to $t = 0$ fs is depicted. The main features in the dynamics are quite similar to the field-free case. However, like for the nuclear motion, the dynamics of the electron density becomes asymmetric with respect to the xy -plane, i.e., the b -coordinate. This asymmetry persists after the laser pulse is no longer active (for example, see the snapshots at 30.0 fs). The oscillation of the electron density from the right to the left oxygen is most prominently observable for the snapshots at 7.6 and 9.6 fs.

The oscillations of the electron density are again recorded by the three dipole moment components, shown in the upper panel of Fig. 8. The coherent part of electron dynamics is visualized by the Δ 1e-2o dipole moment components for the y - and z -coordinates in the lower panel. Again, the 1e-2o- x -component stays zero for the whole simulation time. As the few-cycle IR pulse induces the asymmetry mainly along the b -coordinate, the overall temporal evolution of the 1e-2o- y - and the Δ 1e-2o- y components is similar to the field-free case. The 1e-2o- z -component experiences the main changes. During the pulse, strong and fast oscillations are observed with an amplitude nearly thirty times larger than for the field-free case. The oscillations stay up to ten times larger after the pulse. The superimposed slow oscillation with a period of about 20 fs can be assigned to the asymmetry in the nuclear motion. It does not appear for the Δ 1e-2o- z component reflecting solely the coherent electron dynamics. By breaking the symmetry of the nuclear motion with the laser

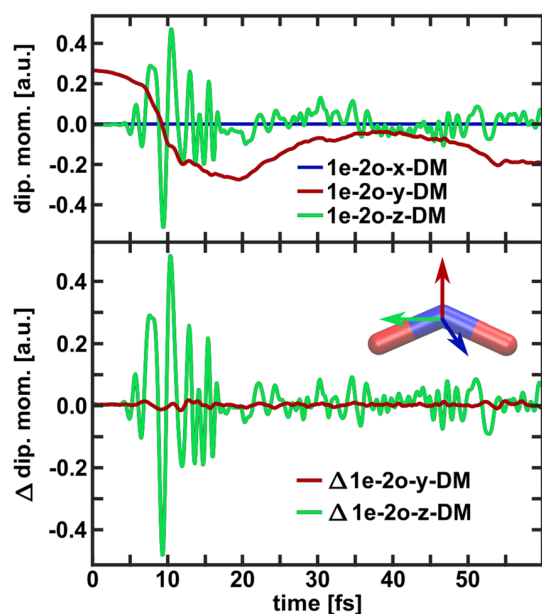


FIG. 8. Temporal evolution of the dipole moment components (DM component) based on the electron density in the 1e-2o picture in the presence of a few-cycle IR pulse. Upper panel: total value of all three components. The orientation of the molecule is shown as inset in the middle. Lower panel: Difference between the dipole moment components one time calculated with the coherence term included and once without it. Differences only shown for the y - and z -DM components.

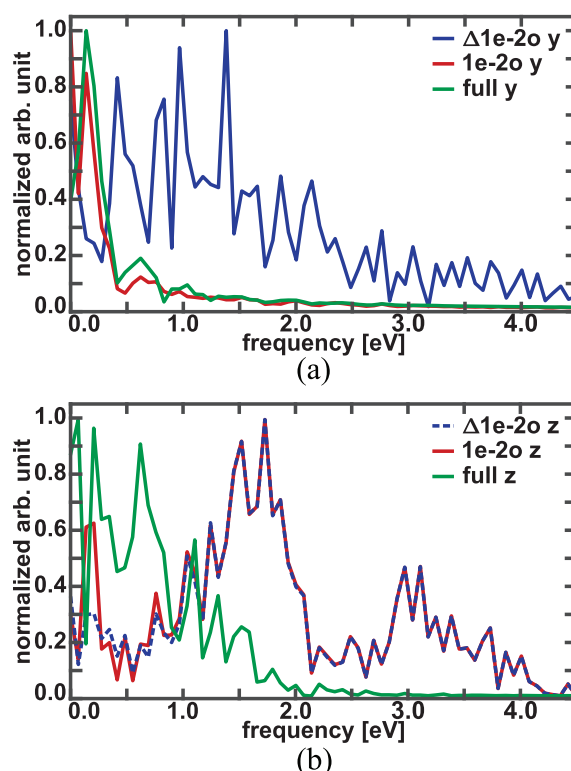


FIG. 9. The Fourier spectra of the y -component (a) and z -component (b) of the dipole moment in the presence of a CEP-pulse (0.0π) obtained using the Δ 1e-2o-components (blue), the 1e-2o-components (red), and the components calculated with the full density (green). All spectra are normalized to one individually.

pulse, the electronic coherence induced in the NO₂ molecule is significantly larger. Again, it is observable mainly in the z -component and b -coordinate. During the light pulse, it is now the coherent electron dynamics that is responsible for the largest changes in the dipole moment.

The corresponding frequencies for the Δ 1e-2o-components, the 1e-2o-components, and the dipole moment calculated with the full density are again determined by Fourier transform. Their spectra are shown in Fig. 9. All frequencies with an intensity larger than 0.1 are listed in Tables S5 and S6 of the supplementary material. In both Δ 1e-2o spectra, frequencies up to 4.0 eV appear, which are higher compared to the field-free case. As expected, the main peaks of the Δ 1e-2o- y spectra [Fig. 9(a), blue] are in the same energy region as in the field-free case and only the Δ 1e-2o z -spectrum [Fig. 9(b), blue dotted line] shows differences. The main peaks are shifted to higher energies by roughly 0.7 eV. The laser pulse injects energy (0.76 eV) into the system, which influences the momentum of the nuclear wavepacket and thereby the phase of the overlap term [Eq. (1)], which subsequently leads to higher frequencies observed in the coherent electron dynamics. The correlation between the phase of the overlap term, the electronic phase, and the laser pulse is illustrated in Fig. S11 of the supplementary material for two individual grid points. The frequencies for the y -component determined with the 1e-2o-density

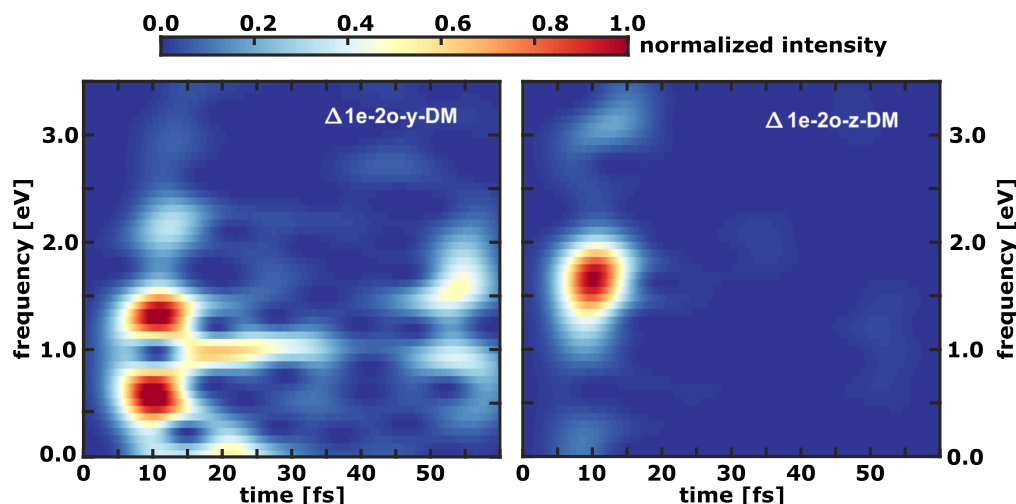


FIG. 10. Short-time Fourier transform of the Δ 1e-2o-y dipole moment component (left) and Δ 1e-2o-z dipole moment component (right) with a few-cycle IR pulse included in the simulation. The Fourier spectrograms are normalized, and a Gaussian windowing function with a width of 180 data points corresponding to a time of 18.14 fs is used.

[Fig. 9(a), red] and the full-density [Fig. 9(a), green] exhibit the same behavior as in the field-free case. The high energy parts significantly lose intensity since the slower nuclear dynamics (Born–Oppenheimer part) dominates this signal. The dominance of the oscillating dipole moment originating from the coherent electron dynamics shows up in the nearly identical spectra for 1e-2o-z [Fig. 9(b), red] and Δ 1e-2o-z [Fig. 9(b), blue]. For the z-spectra of the full-density [Fig. 9(b), green], the high energy parts lose some intensity but still more high energy contributions survive compared to the field-free case.

The results of the short-time Fourier transform for the Δ 1e-2o-y and the Δ 1e-2o-z dipole moment component using a Gaussian windowing function with a width of 180 data points corresponding to a time of 18.14 fs are shown in Fig. 10. Both spectrograms show a dominant signal that is attributed to the first passage through the CoIn region. The observable electron dynamics is significantly strengthened by the simultaneous light pulse interaction. In the case of the Δ 1e-2o-y spectrogram (left), some new features between 10 and 30 fs appear. Due to the symmetry breaking of the nuclear motion by the laser pulse, signals with very low frequencies and an extended signal around 1.0 eV appear. For the more affected Δ 1e-2o-z component, only one dominant peak is observed. In summary, the presence of a few-cycle IR pulse modifies the coupled dynamics by breaking the symmetry of the nuclear motion and changing the temporal evolution of the population. Both factors lead to a significant increase in electronic coherence in the molecule especially along the z-coordinate (laboratory frame) and the b-coordinate (internal frame).

IV. WAVEFORM CONTROL OF MOLECULAR DYNAMICS

In the last part, we investigate the controllability of the nuclear and electron dynamics by the variation of the CEP ϕ of a few-cycle IR laser pulse. As shown in the literature,^{68,70–72,74–76} the CEP control

scheme offers the possibility to steer electrons and nuclei not only in the ionization process but also during the passage through a CoIn. The few-cycle IR pulse builds up a coherent electronic and nuclear wavepacket with a well-defined phase-relationship controllable by the CEP. In the vicinity of a CoIn, also the non-trivial geometric phase (Pancharatnam–Berry phase) is introduced.^{45,46,77,78} The interplay of both phase-terms lead to an interference process when the CoIn is passed. The interference (constructive or destructive) can be manipulated by the CEP.

A. Control of the nuclear dynamics

As a first step, we focus on the controllability of the nuclear dynamics. Therefore, we define control objectives that are directly accessible via the nuclear wavepacket and use the population $P_{D0}(t, \phi)$ of the D_0 ground state as reference

$$P_{D0}(t, \phi) = \langle \chi_{D0}(R, t, \phi) | \chi_{D0}(R, t, \phi) \rangle_R. \quad (10)$$

One objective is the CEP efficiency $\Gamma(t)$,⁷⁶ which is calculated as the difference of the maximum and the minimum population $P_{D0}(t, \phi)$ for each time step,

$$\Gamma(t) = \max(P_{D0}(t, \phi)) - \min(P_{D0}(t, \phi')). \quad (11)$$

For its maximum value, the population of the target state shows the highest CEP-dependence and consequently the highest degree of controllability with respect to the population transfer. The light pulse amplifies the coherent electron dynamics in the system by breaking the symmetry with respect to the asymmetric stretching coordinate b , as shown in Sec. III B. Therefore, the second objective is the CEP-dependent asymmetry parameter $AN(t, \phi)$, quantifying the CEP induced asymmetry in the nuclear motion with respect to the coordinate b ,

$$AN(t, \phi) = \frac{P_{D0}^R(t, \phi) - P_{D0}^L(t, \phi)}{P_{D0}(t, \phi)}, \quad (12)$$

where $P_{D0}^L(t, \phi)$ and $P_{D0}^R(t, \phi)$ are defined as follows:

$$P_{D0}^L(t, \phi) = \int_{\alpha_{\min}}^{\alpha_{\max}} d\alpha \int_{b_{\min}}^0 db \chi_{D0}^*(R, t, \phi) \chi_{D0}(R, t, \phi), \quad (13)$$

$$P_{D0}^R(t, \phi) = \int_{\alpha_{\min}}^{\alpha_{\max}} d\alpha \int_0^{b_{\max}} db \chi_{D0}^*(R, t, \phi) \chi_{D0}(R, t, \phi). \quad (14)$$

In the spirit of the efficiency $\Gamma(t)$, a maximal asymmetry $AN_{\max}(t)$ is calculated as

$$AN_{\max}(t) = \max(AN(t, \phi)) + \min(AN(t, \phi')). \quad (15)$$

For its maximum, the motion of the nuclear wavepacket shows the highest asymmetry and controllability. Its CEP dependence is illustrated in Fig. 11.

The temporal evolution of $\Gamma(t)$ and the CEP dependent population $P_{D0}(t, \phi)$ at three selected times are shown in Fig. 12. The CEP efficiency (blue line) reaches its global maximum (13%) nearly simultaneously with the peak intensity ($t_0 = 10$ fs) of the laser pulse (gray area). The increase in $\Gamma(t)$ is slightly delayed, and the subsequent decrease to 3% occurs in two steps. After the laser pulse, approximately at 15 fs, $\Gamma(t)$ has a finite oscillating value with a maximum of about 5% around 20 fs, which indicates the second passage through the CoIn region. The later passages through the CoIn region at 30 fs and after 40 fs can roughly be seen in the increase in $\Gamma(t)$. The deviation (violet curve) of the mean population (averaged over all CEPs) from the population in the field-free case is significant, especially during the IR pulse and after 30 fs. As discussed with respect to Fig. 7, the induced asymmetry leads to a partial missing of the CoIn region after 30 fs, which is almost independent of the CEP chosen. The CEP-dependence of the population $P_{D0}(t, \phi)$ [see Fig. 12(b)] is recorded for three selected times marked as vertical lines in 12(a). For better visualization, the mean difference is used here and, unless otherwise stated, in all following respective figures. The first line at 15 fs (green) matches the end of the laser pulse. The second (red line) and the third point (yellow line) correspond to the second and fourth passages through the CoIn region. For all three times, $P_{D0}(t, \phi)$ shows a sinusoidal oscillation with a periodicity of

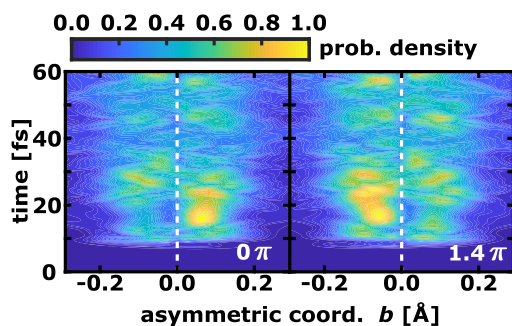


FIG. 11. Normalized nuclear probability density evolution in the presence of a few-cycle IR pulse with a CEP of 0.0π (left) and 1.4π (right) on the adiabatic D_0 -surface integrated over the α -coordinate. For the other probability densities, see Figs. S8 and S9 of the supplementary material.

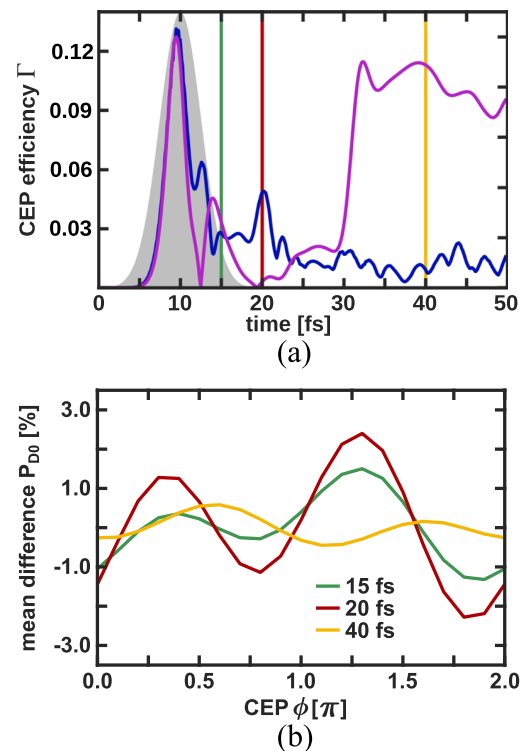


FIG. 12. (a) Temporal evolution of the CEP efficiency $\Gamma(t)$ (blue). The vertical colored lines indicate the points in time that are examined more closely. The violet curve indicates the deviation of the mean population (averaged over all CEPs) from the population in the field-free case. The envelope of the IR pulse is indicated in gray. (b) Mean difference of the CEP-dependent populations $P_{D0}(t, \phi)$ given in percentage for different times.

approximately π . For interference, a periodicity of 2π should emerge. Thus, the observed π dependence of the population is an indication that it is mostly due to the temporal asymmetry of the few-cycle laser pulse.^{69,76}

An analog analysis is performed for the asymmetry of the nuclear motion along the stretching coordinate b and shown in Fig. 13. The maximal asymmetry $AN_{\max}(t)$ shows its global maximum around 8 fs. As it is defined with respect to the population in D_0 alone, the values for the early times (in the beginning of the laser pulse) are overestimated compared to the actual population in the D_0 state. Nevertheless, we can deduce that $AN_{\max}(t)$ follows the envelope of the laser pulse. The subsequent peaks between 15 and 20 fs, at 30 fs, and between 42 and 48 fs correspond to the passages through the CoIn region. The decreasing height of the maxima reflects again the delocalization of the nuclear wavepacket with time. The CEP-dependence of the asymmetry of the nuclear motion [see Fig. 13(b)] $AN(t, \phi)$ is recorded for the same times as previously selected for the CEP-dependent populations $P_{D0}(t, \phi)$. It should be mentioned that the entire value of $AN(t, \phi)$ is shown here and not the mean difference. The asymmetry in the nuclear motion along the coordinate b shows a sinusoidal oscillation, now with a periodicity of 2π for all three times, which is typical for interference.

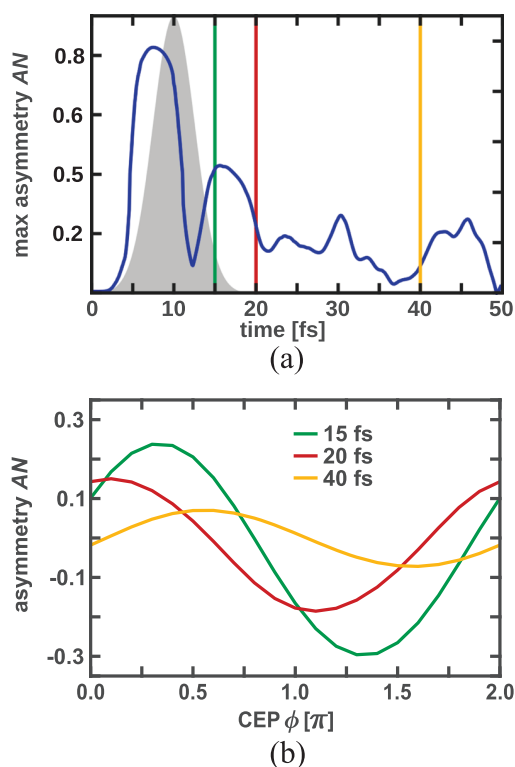


FIG. 13. (a) Temporal evolution of the maximal asymmetry of the nuclei $AN_{max}(t)$. The vertical colored lines indicate the points in time that are examined more closely. The envelope of the IR pulse is indicated in gray. (b) The CEP-dependent asymmetry parameter $AN(t, \phi)$ for different points in time.

This means that for the two quantities $P_{D0}(t, \phi)$ and $AN(t, \phi)$, we observe a different CEP-dependence. In other words, there are two different mechanisms active in the system, which can be projected out by using different observables.

In addition, we calculated the temporal evolution of $\Gamma(t)$ and $AN_{max}(t)$, as well as the CEP-dependence of $P_{D0}(t, \phi)$ and $AN(t, \phi)$ using the y -component and the z -component of the TDM. Since the results are quite similar, for the ones obtained with the absolute value of the TDM, the orientation of the molecule with respect to electric field of the pulse should not play a major role. For more details, see Sec. IV of the [supplementary material](#).

B. Control of the electron dynamics

As shown in Sec. III B, the laser pulse is creating a coherent electronic superposition in the vicinity of the CoIn. Therefore, we also examined the influence of the CEP variation on the electron density. The first control objective is the CEP-dependent asymmetry parameter $AE(t, \phi)$ of the 1e-2o-density $\rho(r, t, \phi)$,

$$AE(t, \phi) = \frac{N^R(t, \phi) - N^L(t, \phi')}{N^R(t, \phi) + N^L(t, \phi')}, \quad (16)$$

with the probabilities $N^L(t, \phi)$ and $N^R(t, \phi)$ to find the electron on the left or the right side of the molecule given by

$$N^L(t, \phi) = \int_{x_{min}}^{x_{max}} dx \int_{y_{min}}^{y_{max}} dy \int_{z_{min}}^0 dz \rho(r, t, \phi), \quad (17)$$

$$N^R(t, \phi) = \int_{x_{min}}^{x_{max}} dx \int_{y_{min}}^{y_{max}} dy \int_0^{z_{max}} dz \rho(r, t, \phi). \quad (18)$$

The maximal asymmetry of the electron density $AE_{max}(t)$ is calculated as follows:

$$AE_{max}(t) = \max(AE(t, \phi)) + \min(AE(t, \phi')). \quad (19)$$

For its maximum, the electron dynamics shows the highest CEP-dependence and thus the highest controllability. The temporal evolution of $AE_{max}(t)$ and the CEP-dependent asymmetry of the electron density $AE(t, \phi)$ at three selected times are shown in Fig. 14. The maximal asymmetry $AE_{max}(t)$ is highest during the laser pulse (gray area). It decreases within 8 fs and becomes smaller by a factor of ten. However, during this time period, two peaks at 12 and 15 fs can be recognized. Afterward, the maximal asymmetry oscillates between

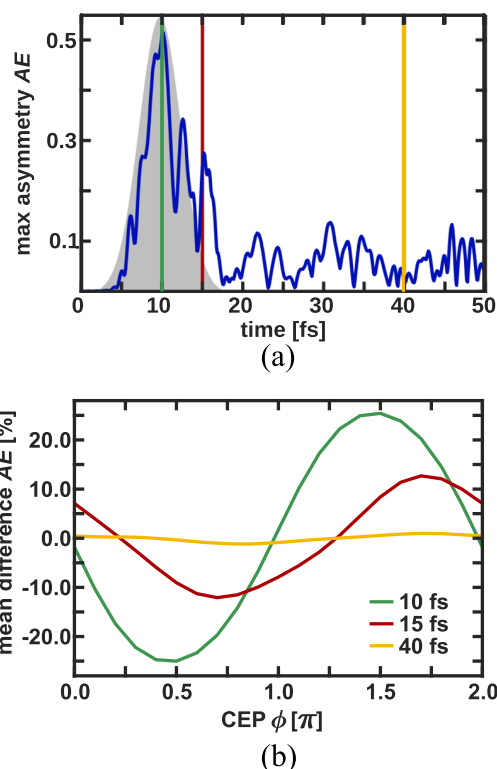


FIG. 14. (a) Temporal evolution of the maximal asymmetry of the active electron $AE_{max}(t)$. The vertical colored lines indicate the points in time that are examined more closely. The envelope of the IR pulse is indicated in gray. (b) Mean difference of the CEP-dependent asymmetry parameter of the active electron $AE(t, \phi)$ given in percentage for different times.

nearly zero and 0.125 until the end of the simulation time. Comparing the maximal asymmetry of the electron density $AE_{max}(t)$ with the one of the nuclei $[AN_{max}(t)]$, faster oscillations are observed. To further analyze the response of the electron density [see Fig. 14(b)], $AE(t, \phi)$ is recorded for three selected points in time marked as vertical lines in 14(a). The first line at 10 fs (green) corresponds to the main peak of $AE_{max}(t)$ and is taken at the maximum of the pulse. The second point (red line) is taken at 15 fs when the laser pulse is approximately over. The last point in time (yellow line) is at 40 fs. At all three times, $AE(t, \phi)$ shows a sinusoidal oscillation with a periodicity of approximately 2π and a decreasing amplitude with time. The asymmetry of the electron density thus has the same periodicity as the nuclear asymmetry $AN(t, \phi)$, which is as previously mentioned typical for an interference process.

As already discussed in Sec. III B, the response of the dipole moment to the applied laser field is an observable directly connected to the electron motion. In this case, the 1e-2o-y- and the 1e-2o-z-component are of interest. Their maximal CEP-dependence $\gamma_y(t)$ and $\gamma_z(t)$ are evaluated as the difference of the maximum and the minimum value of 1e-2o-y-DM(t, ϕ) and 1e-2o-z-DM(t, ϕ), respectively, for each time step. The maximal CEP-dependence $\gamma_y(t)$ is depicted as a function of time in Fig. 15(a) and its related component 1e-2o-y in Fig. 15(b) at three selected times.

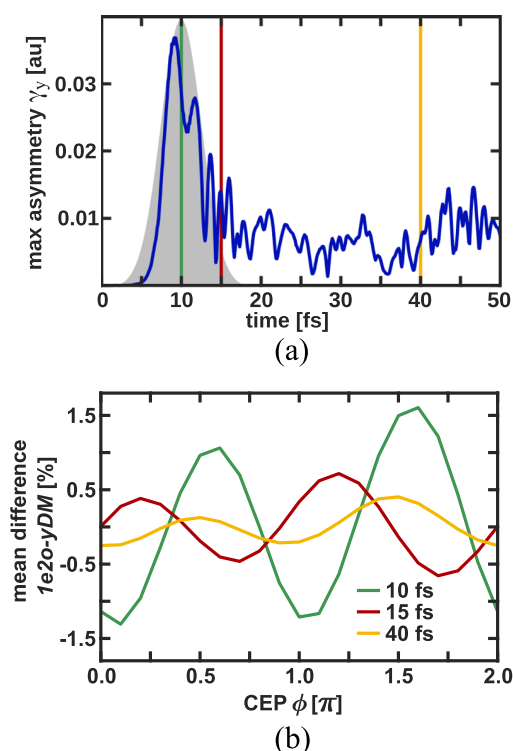


FIG. 15. (a) Temporal evolution of the maximal asymmetry $\gamma_y(t)$ of the 1e-2o-y-component of the dipole moment. The vertical colored lines indicate the points in time that are examined more closely. The envelope of the IR pulse is indicated in gray. (b) Mean difference of the CEP-dependent 1e-2o-y-component for different points in time.

The maximal CEP-dependence $\gamma_y(t)$ like all other objectives shows its maximum simultaneously with the maximum of the IR pulse. In this period, the shape of the $\gamma_y(t)$ curve is similar to the $\Gamma(t)$ curve [see Fig. 12(a)], only the decrease with decaying pulse intensity is even more asymmetric. After the pulse in the time window from 20 to 40 fs, the CEP-dependence oscillates. Again, the oscillations are significantly faster than for the nuclear objectives. The CEP-dependence of the 1e-2o-y-component is recorded in Fig. 15(b) for the same three selected times as for $AE(t, \phi)$. It shows a sinusoidal oscillation with a periodicity of approximately π and a decreasing amplitude with later times. Thus, the component shows the same periodicity as $\Gamma(t)$ even with the same phase.

The temporal evolution of the maximal CEP-dependence $\gamma_z(t)$ and its 1e-2o-z-component as a function of the CEP are shown in Fig. 16. The maximal CEP-dependence $\gamma_z(t)$ is significantly larger than $\gamma_y(t)$ in consistency with our finding in Sec. III B that the z-component reacts more strongly to the laser pulse. The overall shape of $\gamma_z(t)$ is quite similar to the temporal evolution of $AE_{max}(t)$ [see Fig. 14(a)], and the 1e-2o-z-component shows the same periodicity of 2π as $AE(t, \phi)$. The only difference is a phase shift of π .

In summary, two different responses on the CEP variation are present in the nuclear and electron dynamics. Both asymmetry parameters $AN(t, \phi)$ and $AE(t, \phi)$ as well as the 1e-2o-z-component of the dipole moment provide a distinction between left and right

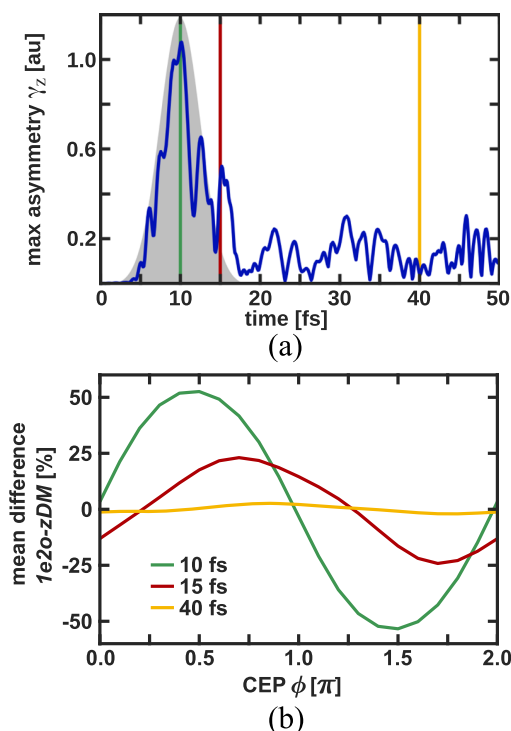


FIG. 16. (a) Temporal evolution of the maximal asymmetry $\gamma_z(t)$ of the 1e-2o-z-component of the dipole moment. The vertical colored lines indicate the points in time that are examined more closely. The envelope of the IR pulse is indicated in gray. (b) Mean difference of the CEP-dependent 1e-2o-z-component for different points in time.

within the molecular plane (yz -plane). The associated 2π periodicity is typical for an interference process. $\Gamma(t)$ and the $1e$ - $2o$ - y -component of the dipole moment are directly sensitive to the main direction of motion along the α -coordinate and the y -coordinate. The motion in this direction mediates the non-adiabatic transfer between the D_1 and D_0 states. For these cases, the CEP-dependence shows a π periodicity, arising from the temporal asymmetry of the few-cycle pulse itself.^{69,76} Both mechanisms are present for the nuclear as well as for the electron dynamics and can be detected depending on the chosen observable.

V. CONCLUSION

In this paper, we expand our ansatz for the description of the coupled nuclear and electron dynamics in molecular systems^{8,38,39} (NEMol). We applied our method to the photoinduced ultrafast dynamics in NO_2 , which is dominated by a CoIn. We observe the appearance of a coherent electronic wavepacket at each passage of the CoIn. The coherence is not strong and only short lived due to the high symmetry of the molecule, which cancels out the individual contributions.⁷⁹ Beside the field-free relaxation, we also studied the influence of a few-cycle IR laser pulse applied in the vicinity of the CoIn. The induced symmetry breaking significantly enhances the degree of coherence and its life time. Inspired by previous works,^{56,57,73,75,76} we varied the carrier envelope phase ϕ (CEP) of the IR pulse to control the movement of electrons and nuclei during the passage through the CoIn.

In the first part, we generalized our NEMol ansatz. The principle advantage of this ansatz is based on the combination of highly developed quantum-chemical methods with the accurate description of the nuclear quantum dynamics. In the original ansatz,^{8,38,39} an expression for the time-dependent electronic wavepacket is formulated, where the electronic part of the total wavefunction is propagated in the electronic eigenstate basis. Its dynamics is extracted from the nuclear wavepacket propagation on coupled potential energy surfaces by introducing the parametric dependence on the time-dependent expected value of position $\langle R \rangle(t)$. By extending the NEMol ansatz with a grid representation, it is possible to couple the electron dynamics to multiple grid points on which the nuclear wavepacket is represented. Through a simple approximation, we were able to condense the coupled dynamics of the one-electron excitation process in the density of one active electron ($1e$ - $2o$ -picture). In the second part, we compared the coupled nuclear and electron dynamics of NO_2 with and without an IR pulse present when the system reaches the CoIn for the first time. Using the NEMol ansatz, we characterized the coherent electron dynamics by analyzing the temporal evolution of the induced dipole moment. The observed frequencies of the coherent electron dynamics cover a range up to 2.3 eV. These high values originate from the nuclear overlap term and the electronic phase term. In NO_2 , the phase contribution of the nuclear overlap term is high and therefore provides a significant contribution to the electron dynamics. The applied few-cycle IR laser pulse generated an asymmetric movement of the nuclear and electronic wavepackets, which is vital for the controllability at the CoIn. The induced oscillating dipole reflects an enhanced buildup of the coherent electron dynamics by the laser pulse, which survives for several 10 fs. In the last part, the CEP of the IR pulse was varied to influence both the nuclear dynamics and

the electron dynamics. The CEP-dependent effect lives considerably longer than the pulse in all investigated observables. Depending on the chosen observable, a π or 2π periodicity can be found indicating two mechanisms, one based on an interference process (2π) and the other induced by the temporal asymmetry of the few-cycle pulse itself (π). Both periodicities are observed for the nuclear and the electron dynamics. In each case, they can be projected out by using different observables.

We demonstrated the potential of our NEMol ansatz to describe the coupled nuclear and electron dynamics in molecular systems beyond diatomics. In NO_2 , we followed the dynamics in the excited state dominated by fast changing wavepacket interference effects. The ansatz is expandable to simulate the induced coherent electron dynamics in the excitation process itself as well as the higher-dimensional molecular system as long as the underlying nuclear dynamics can be treated quantum mechanically. Two electron processes could be realized by using pair densities.

SUPPLEMENTARY MATERIAL

See the [supplementary material](#) for the details of the wavepacket simulation setup, the underlying quantum chemical data of NO_2 , and additional figures and tables for the NEMol-dynamics. A section contains the results for the CEP-control obtained with the y -component and the z -component of the TDM. Animations of the coupled electron density in the $1e$ - $2o$ picture for the free propagation and in the presence of a few-cycle IR laser pulse with a CEP of 0.0π and 1.4π are also added in the [supplementary material](#).

AUTHORS' CONTRIBUTIONS

T.S. performed all calculations. T.S. and R.d.V.-R. analyzed the results and contributed equally to the final version of the manuscript.

ACKNOWLEDGMENTS

The authors gratefully acknowledge the DFG Normalverfahren and the Munich Center of Advanced Photonics (MAP).

There are no conflicts to declare.

APPENDIX: THE ORIGINAL NEMol ANSATZ

The following detailed formulation of the NEMol ansatz^{8,38,39} is given here in the improved notation. The total molecular wavefunction $\Psi_{tot}(r, R, t)$ is setup as the sum over the electronic states, with $\chi(R, t)$ being the nuclear wavefunctions, $\varphi(r, t; R)$ being the electronic wavefunctions, R and r being the nuclear and electronic coordinates, respectively, and t being the time,

$$\Psi_{tot}(r, R, t) = \sum_i \chi_i(R, t) \cdot \varphi_i(r, t; R). \quad (\text{A1})$$

Applying the Born–Oppenheimer approximation, the uncoupled electronic wavefunctions φ_i are hereby parametrically depending on the nuclear coordinates R and define a multi-dimensional vector φ_{tot} . The total nuclear wavefunction χ_{tot} also represents a multi-dimensional vector, spanned by the coupled wavefunctions χ_i . For

details on how the temporal evolution of the nuclear wavefunctions χ_i on coupled potential energy surfaces (PES's) is determined, see Sec. I of the [supplementary material](#). Multiplying $\Psi_{tot}(r, R, t)$ from the left with χ_{tot} and subsequently integrating over the nuclear coordinates results in an expression of the coupled total electronic wavefunction,^{8,38,39}

$$\Phi_{tot}(r, t; \langle R \rangle(t)) = \int \chi_{tot}^*(R, t) \cdot \Psi_{tot}(r, R, t) dR = \begin{pmatrix} \Phi_1(r, t; \langle R \rangle(t)) \\ \Phi_2(r, t; \langle R \rangle(t)) \\ \vdots \\ \Phi_j(r, t; \langle R \rangle(t)) \end{pmatrix}, \quad (A2)$$

with

$$\langle R \rangle(t) = \sum_i \langle \chi_i(R, t) | R | \chi_i(R, t) \rangle_R. \quad (A3)$$

The coupled total electronic wavefunction is parametrically depending on the time-dependent expected value of the position $\langle R \rangle(t)$. In other words, Φ_{tot} is evaluated at one single nuclear geometry, which changes with time. The individual components Φ_j are defined by the following equation:

$$\Phi_j(r, t; \langle R \rangle(t)) = A_{ji}(t) \cdot \varphi_j(r, t; \langle R \rangle(t)) + \sum_{k \neq j} A_{jk}(t) \cdot \varphi_k(r, t; \langle R \rangle(t)), \quad (A4)$$

with

$$A_{jk}(t) = \langle \chi_j(R, t) | \chi_k(R, t) \rangle_R. \quad (A5)$$

The first part depends on the population A_{ji} of the respective state j , while all others summands include the nuclear overlap term A_{jk} , which specifies the degree of coherence induced between the two states j and k . The population and coherence of the electronic states as well as the influence of all coupling terms are already determined by the nuclear quantum-dynamics simulation. If the coupling between the electronic states is weak, the nuclear wavefunctions propagate independently and the coherence term becomes zero. In this case, the coupled electronic wavefunctions Φ_j in Eq. (A4) become equivalent to the uncoupled electronic wavefunction φ_j . Standard quantum-chemical calculations at the $\langle R \rangle(t)$ structure yield the real-valued wavefunctions $\varphi_j(r; \langle R \rangle(t))$ of the relevant electronic states and their eigenenergies. The temporal evolution of $\varphi_j(r, t; \langle R \rangle(t))$ is determined by the deformation of the electronic structure induced by the nuclear motion (Born–Oppenheimer part) and an oscillation through phase space defined by a pure electronic phase,^{8,38,39}

$$\varphi_j(r, t; \langle R \rangle(t)) = \varphi_j(r; \langle R \rangle(t)) \cdot e^{-i\xi_j(t)}. \quad (A6)$$

The phase term $\xi_j(t)$ depends on the eigenenergies $E_j(\langle R \rangle(t))$ and has to be calculated recursively,

$$\xi_j(t) = E_j(\langle R \rangle(t))\Delta t + \xi_j(t - \Delta t). \quad (A7)$$

This recursive evaluation is necessary to retain the memory of the progressing electronic phase. Thereby, the propagation velocity of the phase in the complex plane changes smoothly in time while the nuclear wavepacket propagates. Using the coupled total electronic wavefunction $\Phi_{tot}(r, t; \langle R \rangle(t))$, the associated electron density

$\rho(r, t; \langle R \rangle(t))$ can be determined by multiplying $\Phi_{tot}(r, t; \langle R \rangle(t))$ from the left with φ_{tot} and subsequently integrating over $N - 1$ electronic coordinates (with N being the total number of electrons),

$$\rho(r, t; \langle R \rangle(t)) = \int \varphi_{tot}^* \cdot \Phi_{tot} dr_2 \dots dr_N = \sum_j A_{ji}(t) \rho_{ji}(r; \langle R \rangle(t)) + \sum_{k \neq j} 2\text{Re} \left\{ A_{jk}(t) \rho_{jk}(r; \langle R \rangle(t)) e^{-i\xi_{jk}(t)} \right\}, \quad (A8)$$

with

$$\xi_{jk}(t) = \Delta E_{jk}(\langle R \rangle(t))\Delta t + \xi_{jk}(t - \Delta t). \quad (A9)$$

The first summation consists of the state specific electronic density $\rho_{ji}(r, t; \langle R \rangle(t))$ weighted with the corresponding time-dependent population $A_{ji}(t)$. The dynamics of these contributions to the coupled electron density is determined by the temporal evolution of the nuclear wavepacket, i.e., its expected value of the position $\langle R \rangle(t)$. The second summation defines the coherent contribution to the coupled electron density and consists of the time-dependent overlap $A_{jk}(t)$, the one-electron transition density $\rho_{jk}(r, t; \langle R \rangle(t))$, and its pure electronic phase defined by the energy difference ΔE_{jk} between the involved electronic states.

DATA AVAILABILITY

The data that support the findings of this study are available from the corresponding author upon reasonable request.

REFERENCES

- M. Hentschel, R. Kienberger, C. Spielmann, G. A. Reider, N. Milosevic, T. Brabec, P. Corkum, U. Heinzmann, M. Drescher, and F. Krausz, "Attosecond metrology," *Nature* **414**, 509–513 (2001).
- E. Goulielmakis, V. S. Yakovlev, A. L. Cavalieri, M. Uiberacker, V. Pervak, A. Apolonski, R. Kienberger, U. Kleineberg, and F. Krausz, "Attosecond control and measurement: Lightwave electronics," *Science* **317**, 769–775 (2007).
- G. Sansone, F. Kelkensberg, J. F. Pérez-Torres, F. Morales, M. F. Kling, W. Siu, O. Ghafur, P. Johnsson, M. Swoboda, E. Benedetti, F. Ferrari, F. Lépine, J. L. Sanz-Vicario, S. Zharebtsov, I. Znakovskaya, A. L'Huillier, M. Y. Ivanov, M. Nisoli, F. Martín, and M. J. J. Vrakking, "Electron localization following attosecond molecular photoionization," *Nature* **465**, 763–766 (2010).
- P. M. Kraus, S. B. Zhang, A. Gijsbertsen, R. R. Lucchese, N. Rohringer, and H. J. Wörner, "High-harmonic probing of electronic coherence in dynamically aligned molecules," *Phys. Rev. Lett.* **111**, 243005 (2013).
- C. Andrea Rozzi, S. Maria Falke, N. Spallanzani, A. Rubio, E. Molinari, D. Brida, M. Maiuri, G. Cerullo, H. Schramm, J. Christoffers, and C. Lienau, "Quantum coherence controls the charge separation in a prototypical artificial light-harvesting system," *Nat. Commun.* **4**, 1602 (2013).
- E. Romero, R. Augulis, V. I. Novoderezhkin, M. Ferretti, J. Thieme, D. Zigmantas, and R. van Grondelle, "Quantum coherence in photosynthesis for efficient solar-energy conversion," *Nat. Phys.* **10**, 676–682 (2014).
- F. Calegari, D. Ayuso, A. Trabattini, L. Belshaw, S. De Camillis, S. Anumula, F. Frassetto, L. Poletto, A. Palacios, P. Decleva, J. B. Greenwood, F. Martín, and M. Nisoli, "Ultrafast electron dynamics in phenylalanine initiated by attosecond pulses," *Science* **346**, 336–339 (2014).
- P. von den Hoff, I. Znakovskaya, M. F. Kling, and R. de Vivie-Riedle, "Attosecond control of the dissociative ionization via electron localization: A comparison between D₂ and CO," *Chem. Phys.* **366**, 139–147 (2009).
- K. C. Kulander, "Time-dependent Hartree-Fock theory of multiphoton ionization: Helium," *Phys. Rev. A* **36**, 2726–2738 (1987).
- E. Runge and E. K. U. Gross, "Density-functional theory for time-dependent systems," *Phys. Rev. Lett.* **52**, 997–1000 (1984).

- ¹¹T. Klamroth, "Laser-driven electron transfer through metal-insulator-metal contacts: Time-dependent configuration interaction singles calculations for a jellium model," *Phys. Rev. B* **68**, 245421 (2003).
- ¹²N. Rohringer, A. Gordon, and R. Santra, "Configuration-interaction-based time-dependent orbital approach for *ab initio* treatment of electronic dynamics in a strong optical laser field," *Phys. Rev. A* **74**, 043420 (2006).
- ¹³A. S. Skedsvoll, A. Balbi, and H. Koch, "Time-dependent coupled-cluster theory for ultrafast transient-absorption spectroscopy," *Phys. Rev. A* **102**, 023115 (2020).
- ¹⁴F. D. Vila, J. J. Rehr, J. J. Kas, K. Kowalski, and B. Peng, "Real-time coupled-cluster approach for the cumulant Green's function," *J. Chem. Theory Comput.* **16**, 6983–6992 (2020).
- ¹⁵J. Zanghellini, M. Kitzler, T. Brabec, and A. Scrinzi, "Testing the multi-configuration time-dependent Hartree-Fock method," *J. Phys. B: At., Mol. Opt. Phys.* **37**, 763–773 (2004).
- ¹⁶A. I. Kuleff, J. Breidbach, and L. S. Cederbaum, "Multielectron wave-packet propagation: General theory and application," *J. Chem. Phys.* **123**, 044111 (2005).
- ¹⁷F. Remacle and R. D. Levine, "An electronic time scale in chemistry," *Proc. Natl. Acad. Sci. U. S. A.* **103**, 6793–6798 (2006).
- ¹⁸A. I. Kuleff and L. S. Cederbaum, "Charge migration in different conformers of glycine: The role of nuclear geometry," *Chem. Phys.* **338**, 320–328 (2007).
- ¹⁹N. V. Golubev and A. I. Kuleff, "Control of charge migration in molecules by ultrashort laser pulses," *Phys. Rev. A* **91**, 051401 (2015).
- ²⁰P. von den Hoff, S. Thallmair, M. Kowalewski, R. Siemering, and R. de Vivie-Riedle, "Optimal control theory – closing the gap between theory and experiment," *Phys. Chem. Chem. Phys.* **14**, 14460–14485 (2012).
- ²¹P. von den Hoff, R. Siemering, M. Kowalewski, and R. de Vivie-Riedle, "Electron dynamics and its control in molecules: From diatomics to larger molecular systems," *IEEE J. Sel. Top. Quantum Electron.* **18**, 119–129 (2012).
- ²²M. Vacher, D. Mendive-Tapia, M. J. Bearpark, and M. A. Robb, "Electron dynamics upon ionization: Control of the timescale through chemical substitution and effect of nuclear motion," *J. Chem. Phys.* **142**, 094105 (2015).
- ²³A. J. Jenkins, M. Vacher, R. M. Twidale, M. J. Bearpark, and M. A. Robb, "Charge migration in polycyclic norbornadiene cations: Winning the race against decoherence," *J. Chem. Phys.* **145**, 164103 (2016).
- ²⁴C. Arnold, O. Vendrell, and R. Santra, "Electronic decoherence following photoionization: Full quantum-dynamical treatment of the influence of nuclear motion," *Phys. Rev. A* **95**, 033425 (2017).
- ²⁵D. Jia, J. Manz, and Y. Yang, "Timing the recoherences of attosecond electronic charge migration by quantum control of femtosecond nuclear dynamics: A case study for HCCl^+ ," *J. Chem. Phys.* **151**, 244306 (2019).
- ²⁶A. D. Bandrauk, S. Chelkowski, and H. S. Nguyen, "Attosecond localization of electrons in molecules," *Int. J. Quantum Chem.* **100**, 834–844 (2004).
- ²⁷M. Nest, "The multi-configuration electron-nuclear dynamics method," *Chem. Phys. Lett.* **472**, 171–174 (2009).
- ²⁸V. Pohl and J. C. Tremblay, "Adiabatic electronic flux density: A Born-Oppenheimer broken-symmetry ansatz," *Phys. Rev. A* **93**, 012504 (2016).
- ²⁹R. Matsuzaki and K. Takatsuka, "Electronic and nuclear flux analysis on nonadiabatic electron transfer reaction: A view from single-configuration adiabatic Born-Huang representation," *J. Comput. Chem.* **40**, 148–163 (2019).
- ³⁰L. S. Cederbaum, "Born-Oppenheimer approximation and beyond for time-dependent electronic processes," *J. Chem. Phys.* **128**, 124101 (2008).
- ³¹A. Abedi, N. T. Maitra, and E. K. U. Gross, "Exact factorization of the time-dependent electron-nuclear wave function," *Phys. Rev. Lett.* **105**, 123002 (2010).
- ³²A. Abedi, N. T. Maitra, and E. K. U. Gross, "Correlated electron-nuclear dynamics: Exact factorization of the molecular wavefunction," *J. Chem. Phys.* **137**, 22A530 (2012).
- ³³Y.-C. Chiang, S. Klaiman, F. Otto, and L. S. Cederbaum, "The exact wavefunction factorization of a vibronic coupling system," *J. Chem. Phys.* **140**, 054104 (2014).
- ³⁴A. Ojanperä, V. Havu, L. Lehtovaara, and M. Puska, "Nonadiabatic Ehrenfest molecular dynamics within the projector augmented-wave method," *J. Chem. Phys.* **136**, 144103 (2012).
- ³⁵A. Alonso, J. L. Castro, P. Echenique, and A. Rubio, "On the combination of TDDFT with molecular dynamics: New developments," in *Fundamentals of Time-Dependent Density Functional Theory*, edited by M. A. Marques, N. T. Maitra, F. M. Nogueira, E. Gross, and A. Rubio (Springer Berlin Heidelberg, Berlin, Heidelberg, 2012), pp. 301–315.
- ³⁶K. Takatsuka, "Theory of molecular nonadiabatic electron dynamics in condensed phases," *J. Chem. Phys.* **147**, 174102 (2017).
- ³⁷K. Takatsuka, "Nuclear wavepackets along quantum paths in nonadiabatic electron wavepacket dynamics," *Chem. Phys.* **515**, 52–59 (2018).
- ³⁸D. Geppert, P. von den Hoff, and R. de Vivie-Riedle, "Electron dynamics in molecules: A new combination of nuclear quantum dynamics and electronic structure theory," *J. Phys. B: At., Mol. Opt. Phys.* **41**, 074006 (2008).
- ³⁹I. Znakovskaya, P. von den Hoff, S. Zherebtsov, A. Wirth, O. Herrwerth, M. J. J. Vrakking, R. de Vivie-Riedle, and M. F. Kling, "Attosecond control of electron dynamics in carbon monoxide," *Phys. Rev. Lett.* **103**, 103002 (2009).
- ⁴⁰W. Domcke, D. Yarkony, and H. Köppel, *Conical Intersections: Electronic Structure, Dynamics and Spectroscopy* (World Scientific, Singapore, 2004), Vol. 15.
- ⁴¹M. Abe, Y. Ohtsuki, Y. Fujimura, Z. Lan, and W. Domcke, "Geometric phase effects in the coherent control of the branching ratio of photodissociation products of phenol," *J. Chem. Phys.* **124**, 224316 (2006).
- ⁴²D. Egorova, M. F. Gelin, M. Thoss, H. Wang, and W. Domcke, "Effects of intense femtosecond pumping on ultrafast electronic-vibrational dynamics in molecular systems with relaxation," *J. Chem. Phys.* **129**, 214303 (2008).
- ⁴³M. Kowalewski, K. Bennett, K. E. Dorfman, and S. Mukamel, "Catching conical intersections in the act: Monitoring transient electronic coherences by attosecond stimulated x-ray Raman signals," *Phys. Rev. Lett.* **115**, 193003 (2015).
- ⁴⁴D. Keefer, T. Schnappinger, R. de Vivie-Riedle, and S. Mukamel, "Visualizing conical intersection passages via vibronic coherence maps generated by stimulated ultrafast x-ray Raman signals," *Proc. Natl. Acad. Sci. U. S. A.* **117**, 24069–24075 (2020).
- ⁴⁵D. R. Yarkony, "Diabolical conical intersections," *Rev. Mod. Phys.* **68**, 985–1013 (1996).
- ⁴⁶M. Baer, "Introduction to the theory of electronic non-adiabatic coupling terms in molecular systems," *Phys. Rep.* **358**, 75–142 (2002).
- ⁴⁷E. Haller, H. Köppel, and L. S. Cederbaum, "The visible absorption spectrum of NO_2 : A three-mode nuclear dynamics investigation," *J. Mol. Spectrosc.* **111**, 377–397 (1985).
- ⁴⁸S. Mahapatra, H. Köppel, and L. S. Cederbaum, "Impact of nonadiabatic coupling between the conically intersecting \tilde{X}^2A_1 and \tilde{A}^2B_2 states of NO_2 on the negative ion photoelectron spectra of NO_2^- ," *J. Chem. Phys.* **110**, 5691–5701 (1999).
- ⁴⁹F. Santoro and C. Petrongolo, "Nonadiabatic wave packet dynamics of NO_2 on the $\tilde{X}^2A_1/\tilde{A}^2A'$ conical intersection," *J. Chem. Phys.* **110**, 4419–4427 (1999).
- ⁵⁰S. Mahapatra, H. Köppel, L. S. Cederbaum, P. Stampfuß, and W. Wenzel, "Nonadiabatic wave packet dynamics on the coupled X^2A_1/\tilde{A}^2B_2 electronic states of NO_2 based on new *ab initio* potential energy surfaces," *Chem. Phys.* **259**, 211–226 (2000).
- ⁵¹F. Santoro, C. Petrongolo, G. Granucci, and M. Persico, "Quantum and semi-classical dynamics of the Franck-Condon wave packet on the coupled potential surfaces of the X^2A_1/\tilde{A}^2A' conical intersection," *Chem. Phys.* **259**, 193–200 (2000).
- ⁵²V. Kurkal, P. Fleurat-Lessard, and R. Schinke, " NO_2 : Global potential energy surfaces of the ground (1^2A_1) and the first excited (1^2B_2) electronic states," *J. Chem. Phys.* **119**, 1489–1501 (2003).
- ⁵³M. Sanrey and M. Joyeux, "Quantum mechanical and quasiclassical investigations of the time domain nonadiabatic dynamics of NO_2 close to the bottom of the $X^2A_1-\tilde{A}^2B_2$ conical intersection," *J. Chem. Phys.* **125**, 014304 (2006).
- ⁵⁴Y. Arasaki and K. Takatsuka, "Quantum wavepacket dynamics for time-resolved photoelectron spectroscopy of the NO_2 conical intersection," *Chem. Phys.* **338**, 175–185 (2007).
- ⁵⁵R. Schinke, S. Y. Grebenshchikov, and H. Zhu, "The photodissociation of NO_2 in the second absorption band: *Ab initio* and quantum dynamics calculations," *Chem. Phys.* **346**, 99–114 (2008).
- ⁵⁶Y. Arasaki, K. Takatsuka, K. Wang, and V. McKoy, "Time-resolved photoelectron spectroscopy of wavepackets through a conical intersection in NO_2 ," *J. Chem. Phys.* **132**, 124307 (2010).

- ⁵⁷M. Richter, F. Bouakline, J. González-Vázquez, L. Martínez-Fernández, I. Corral, S. Patchkovskii, F. Morales, M. Ivanov, F. Martín, and O. Smirnova, "Sub-laser-cycle control of coupled electron–nuclear dynamics at a conical intersection," *New J. Phys.* **17**, 113023 (2015).
- ⁵⁸A. Tehlar, A. von Conta, Y. Arasaki, K. Takatsuka, and H. J. Wörner, "Ab initio calculation of femtosecond-time-resolved photoelectron spectra of NO₂ after excitation to the A-band," *J. Chem. Phys.* **149**, 034307 (2018).
- ⁵⁹M. Richter, J. González-Vázquez, Z. Mašín, D. S. Brambila, A. G. Harvey, F. Morales, and F. Martín, "Ultrafast imaging of laser-controlled non-adiabatic dynamics in NO₂ from time-resolved photoelectron emission," *Phys. Chem. Chem. Phys.* **21**, 10038–10051 (2019).
- ⁶⁰A. T. J. B. Eppink, B. J. Whitaker, E. Gloaguen, B. Soep, A. M. Coroiu, and D. H. Parker, "Dissociative multiphoton ionization of NO₂ studied by time-resolved imaging," *J. Chem. Phys.* **121**, 7776–7783 (2004).
- ⁶¹N. T. Form, B. J. Whitaker, L. Poisson, and B. Soep, "Time-resolved photoion and photoelectron imaging of NO₂," *Phys. Chem. Chem. Phys.* **8**, 2925–2932 (2006).
- ⁶²A. Vredenburg, W. G. Roeterdink, and M. H. M. Janssen, "Femtosecond time-resolved photoelectron-photoion coincidence imaging of multiphoton multichannel photodynamics in NO₂," *J. Chem. Phys.* **128**, 204311 (2008).
- ⁶³I. Wilkinson and B. J. Whitaker, "Some remarks on the photodynamics of NO₂," *Annu. Rep. Prog. Chem., Sect. C* **106**, 274–304 (2010).
- ⁶⁴Y. Arasaki, K. Wang, V. McKoy, and K. Takatsuka, "Monitoring the effect of a control pulse on a conical intersection by time-resolved photoelectron spectroscopy," *Phys. Chem. Chem. Phys.* **13**, 8681–8689 (2011).
- ⁶⁵H. J. Wörner, J. B. Bertrand, B. Fabre, J. Higuette, H. Ruf, A. Dubrouil, S. Patchkovskii, M. Spanner, Y. Mairesse, V. Blanchet, E. Mével, E. Constant, P. B. Corkum, and D. M. Villeneuve, "Conical intersection dynamics in NO₂ probed by homodyne high-harmonic spectroscopy," *Science* **334**, 208–212 (2011).
- ⁶⁶H. Ruf, C. Handschin, A. Ferré, N. Thiré, J. B. Bertrand, L. Bonnet, R. Cireasa, E. Constant, P. B. Corkum, D. Descamps, B. Fabre, P. Larregaray, E. Mével, S. Petit, B. Pons, D. Staedter, H. J. Wörner, D. M. Villeneuve, Y. Mairesse, P. Halvick, and V. Blanchet, "High-harmonic transient grating spectroscopy of NO₂ electronic relaxation," *J. Chem. Phys.* **137**, 224303 (2012).
- ⁶⁷P. M. Kraus, Y. Arasaki, J. B. Bertrand, S. Patchkovskii, P. B. Corkum, D. M. Villeneuve, K. Takatsuka, and H. J. Wörner, "Time-resolved high-harmonic spectroscopy of nonadiabatic dynamics in NO₂," *Phys. Rev. A* **85**, 043409 (2012).
- ⁶⁸K.-M. Weitzel, "Controlling the electrons provides means for controlling chemistry," *ChemPhysChem* **8**, 213–215 (2007).
- ⁶⁹V. Roudnev and B. D. Esry, "General theory of carrier-envelope phase effects," *Phys. Rev. Lett.* **99**, 220406 (2007).
- ⁷⁰M. F. Kling and M. J. J. Vrakking, "Attosecond electron dynamics," *Annu. Rev. Phys. Chem.* **59**, 463–492 (2008).
- ⁷¹I. Znakovskaya, P. von den Hoff, N. Schirmel, G. Urbasch, S. Zhrebtsov, B. Bergues, R. de Vivie-Riedle, K.-M. Weitzel, and M. F. Kling, "Waveform control of orientation-dependent ionization of DCl in few-cycle laser fields," *Phys. Chem. Chem. Phys.* **13**, 8653–8658 (2011).
- ⁷²I. Znakovskaya, P. von den Hoff, G. Marcus, S. Zhrebtsov, B. Bergues, X. Gu, Y. Deng, M. J. J. Vrakking, R. Kienberger, F. Krausz, R. de Vivie-Riedle, and M. F. Kling, "Subcycle controlled charge-directed reactivity with few-cycle midinfrared pulses," *Phys. Rev. Lett.* **108**, 063002 (2012).
- ⁷³M. F. Kling, P. von den Hoff, I. Znakovskaya, and R. de Vivie-Riedle, "(Sub-) femtosecond control of molecular reactions via tailoring the electric field of light," *Phys. Chem. Chem. Phys.* **15**, 9448–9467 (2013).
- ⁷⁴A. Alnaser, M. Kübel, R. Siemering, B. Bergues, N. G. Kling, K. Betsch, Y. Deng, J. Schmidt, Z. Alahmed, A. Azzeer, J. Ullrich, I. Ben-Itzhak, R. Moshhammer, U. Kleineberg, F. Krausz, R. de Vivie-Riedle, and M. Kling, "Subfemtosecond steering of hydrocarbon deprotonation through superposition of vibrational modes," *Nat. Commun.* **5**, 3800 (2014).
- ⁷⁵C. Arnold, O. Vendrell, R. Welsch, and R. Santra, "Control of nuclear dynamics through conical intersections and electronic coherences," *Phys. Rev. Lett.* **120**, 123001 (2018).
- ⁷⁶F. Schüppel, T. Schnappinger, L. Bäuml, and R. de Vivie-Riedle, "Waveform control of molecular dynamics close to a conical intersection," *J. Chem. Phys.* **153**, 224307 (2020).
- ⁷⁷M. V. Berry, "Quantal phase factors accompanying adiabatic changes," *Proc. R. Soc. London, Ser. A* **392**, 45–57 (1984).
- ⁷⁸H. C. Longuet-Higgins, U. Öpik, M. H. L. Pryce, and R. A. Sack, "Studies of the Jahn-Teller effect. II. The dynamical problem," *Proc. R. Soc. London, Ser. A* **244**, 1–16 (1958).
- ⁷⁹S. P. Neville, A. Stolow, and M. S. Schuurman, "The role of geometric phase in the formation of electronic coherences at conical intersections," *arXiv:2011.06728 [physics.chem-ph]* (2020).

SUMMARY AND OUTLOOK

The coupled electron and nuclear dynamics in molecules induced by light is the central subject of this work and theoretical studies were presented which focus on different aspects of this topic in more details. The aspect shown in the first chapter deals with relaxation processes after photoexcitation which are studied with help of semiclassical *ab initio* molecular dynamics simulations. These processes are characterized by the interplay of multiple electronic states with different spin symmetry and the coupling of nuclear and electronic motion. The second part of this work addresses the possibility of controlling the motion of both electrons and nuclei in the vicinity of CoIns. In the last chapter a method which allows the full-quantum description of the coupled nuclear and electron dynamics in molecules is introduced.

The deactivation processes after photoexcitation of thiophene and of small oligothiophenes up to three rings were investigated in the first part of this work. The presented studies [169, 173] give a consistent dynamic description of these three molecules taking into account IC and ISC. Compared to previous investigations based on static quantum chemical calculations [82, 132–137] or dynamics simulations [165–168] for only short time scales the presented studies result in a modified description of the relaxation processes. For thiophene the relaxation is still characterized by ring-opening via a carbon-sulfur bond cleavage. During this process ISC is already partly active and for the open-ring structures an extended region of quasidegeneracy between triplet and singlet states is formed. The molecule is trapped in these entropically favored open-ring structures for long timescales. The subsequent, slow ring closure is only observed in the ground state. For 2,2'-bithiophene and 2,2':5',2''-terthiophene the ring-opening pathway is still dominant even though the complexity is strongly increased. The bond cleavage occurs in combination with inter-ring rotation, which was predicted to play an important role in the relaxation [82]. Again the open-ring structures establish a complex equilibrium between singlet and triplet states trapping the molecule. The subsequent ring closure can take place either on the S_0 state or the T_1 state. The extension of the π -system going from the monomer to the trimer increases the period of time until the ring-opening occurs. In addition the ring-opening itself is getting less pronounced. Consequently the ISC is reduced for longer thiophene chains since it is mediated by the increasing SOCs during the carbon-sulfur bond elongation. However, one must keep in mind that all simulations were performed in gas phase. The presence of an environment, such as polymeric matrices or even a simple solvent, has an influence on the dynamics of oligothiophenes [168, 294–297]. Therefore, a logical next step is to perform non-adiabatic dynamics in oligothiophenes embedded in rigid polymeric matrices with the help of quantum mechanics/molecular mechanics (QM/MM) approaches [168, 298–302].

The second chapter demonstrates the control of the molecular dynamics at a CoIn with the help of a few-cycle IR pulse. Before the CoIn is reached by the molecular wave packet the incarceration with the laser pulse creates a coherent superposition between the two states forming the CoIn. Its composition is tunable by varying the CEP of the pulse. When this superposition passes through the CoIn region the interaction with the NACs and the associated GP leads to interference. By controlling this interference via the CEP the molecular dynamics can be controlled. In this work the CEP based control scheme was

applied to a two-dimensional analytic model system and the CoIn mediated relaxation after photoexcitation of the nucleobase uracil and the symmetric molecule NO_2 . The few-cycle IR pulse triggers two types of mechanisms in the studied systems which can be both active, vary in their strength, and even obstruct each other. The first one described above is based on an interference process and reflects the interaction of a laser-induced superposition with the CoIn. The second mechanism, also called field-only mechanism, is due to the few-cycle waveform of the laser pulse and shows no dependence on the shape and size of the NACs. The periodicity while varying the CEP observed in different observables, for example the population or the dipole moment, can be used to distinguish between the two mechanisms. The field-only mechanism causes a π periodicity and the interference process a 2π periodicity. The chosen laser parameters and the molecular properties around the CoIn determine which mechanism can occur and to what extent. This control scheme based on the CEP of few-cycle IR pulse even works for quite challenging boundary conditions as found in uracil and thus is a quite general concept.

The idea of controlling the coherent electron dynamics in a molecule directly leads to the topic of the third and last chapter: The simulation of the coupled nuclear and electron dynamics in a molecular system. Many approaches which simulate electron dynamics explicitly are modified versions of their well-known quantum chemical counterparts and neglect the influence of the nuclear motion [233–237] or treat it classically [244–247]. However, in the situations studied in this work, namely the control of molecular dynamics in the vicinity of CoIns with the help of ultrashort laser pulses, the nuclear motion and the quantum nature of the nuclei can not simply be neglected. The NEMol ansatz is one possibility to treat both the nuclear and electron dynamics in a molecular system quantum mechanically. As part of this work the concept of the NEMol-grid was developed and the 1e-2o approximation was introduced. NEMol in combination with these two new features is suitable to capture the coupled nuclear and electron dynamics in complex high dimensional molecular systems. To test the capabilities of NEMol the coherent electron dynamics induced by laser pulse excitation and the relaxation via CoIns was investigated for the nucleobase uracil and the symmetric molecule NO_2 . One of the main findings in both studies is that the electron dynamics even in molecular systems beyond diatomic reflect coherence, decoherence and reappearance due to nuclear motion. In addition NEMol was used to monitor the control of the coherent electron dynamics applying the CEP control scheme. In all examples shown in this work the underlying nuclear quantum dynamics simulations were performed on two dimensional PESs but in principle NEMol can also be used for higher-dimensional problems. This is possible if the underlying nuclear dynamics offers a description of the nuclear overlap, which is for example true for methods like *ab initio* multiple spawning (AIMS) [303, 304] or MCTDH [212, 213, 217]. Moving forward, the combination of NEMol with one of these methods should be able to simulate the coupled electron and nuclear dynamics for small organic molecules including all nuclear degrees of freedom. A second interesting extension of NEMol might be the inclusion of environmental effects in the nuclear dynamics in order to investigate their influence on the coherent electron dynamics. This could be done using a rather simple quantum dynamics/molecular dynamics approach [264, 305] for which the nuclear quantum dynamics is combined with an atomistic modeling of the solvent environment. The environment is sampled with classical molecular dynamics trajectories and snapshots of the surrounding enter the nuclear quantum dynamics via an additional static potential term in the Hamiltonian. To go beyond a static potential term a quantum-classical time-dependent self-consistent field method [205] can be used. The environmental effects onto the reactive system are captured by simultaneously propagating a quantum solute system coupled to a classical solvent system. This methodology in combination with NEMol would allow studying the influence of decoherence on the electron dynamics. Transient X-ray absorption spectroscopy [306–308] could provide a possible experimental access to the phenomena of coherent electron dynamics simulated with the NEMol, since this method allows to probe changes and fluctuations in the electron density with high temporal resolution.

As final remark a short résumé is drawn between the semiclassical and the full-quantum description of the coupled electron and nuclear dynamics. Both descriptions have their inherent strengths and depending on which system is studied and what questions are asked, the right one must be chosen. If the complete photorelaxation process of a molecule is to be investigated, naturally, the full-dimensional simulation of

the whole dynamics is desirable. Non-adiabatic semiclassical on-the-fly dynamics are well suited for this purpose and it can be accepted that CoIns and laser-interaction are described as a simple possibility for population transfer. However, if the question raised includes aspects such as coherence and decoherence, the manipulation of the phase or the explicit interaction of the molecule with light, the whole system, including the also the nuclei, must be treated quantum mechanically.

BIBLIOGRAPHY

- [1] A. N. Webber and W. Lubitz, "P700: The Primary Electron Donor of Photosystem I", *Biochimica et Biophysica Acta (BBA) - Bioenergetics* **1507**, 61 (2001).
- [2] B. Loll, J. Kern, W. Saenger, A. Zouni, and J. Biesiadka, "Towards Complete Cofactor Arrangement in the 3.0 Angstrom Resolution Structure of Photosystem II", *Nature* **438**, 1040 (2005).
- [3] G. D. Scholes, G. R. Fleming, A. Olaya-Castro, and R. van Grondelle, "Lessons from Nature about Solar Light Harvesting", *Nature Chemistry* **3**, 763 (2011).
- [4] T. Mirkovic, E. E. Ostroumov, J. M. Anna, R. van Grondelle, Govindjee, and G. D. Scholes, "Light Absorption and Energy Transfer in the Antenna Complexes of Photosynthetic Organisms", *Chemical Reviews* **117**, 249 (2017).
- [5] H. G. Khorana, "Rhodopsin, Photoreceptor of the Rod Cell - an Emerging Pattern for Structure and Function", *Journal of Biological Chemistry* **267**, 1 (1992).
- [6] R. Send and D. Sundholm, "Stairway to the Conical Intersection: A Computational Study of the Retinal Isomerization", *The Journal of Physical Chemistry A* **111**, 8766 (2007).
- [7] D. Polli, P. Altoè, O. Weingart, K. M. Spillane, C. Manzoni, D. Brida, G. Tomasello, G. Orlandi, P. Kukura, R. A. Mathies, M. Garavelli, and G. Cerullo, "Conical Intersection Dynamics of the Primary Photoisomerization Event in Vision", *Nature* **467**, 440 (2010).
- [8] N. A. Anderson, J. J. Shiang, and R. J. Sension, "Subpicosecond Ring Opening of 7-Dehydrocholesterol Studied by Ultrafast Spectroscopy", *The Journal of Physical Chemistry A* **103**, 10730 (1999).
- [9] G.-D. Zhu and W. H. Okamura, "Synthesis of Vitamin D (Calciferol)", *Chemical Reviews* **95**, 1877 (1995).
- [10] O. Engelsen, M. Brustad, L. Aksnes, and E. Lund, "Daily Duration of Vitamin D Synthesis in Human Skin with Relation to Latitude, Total Ozone, Altitude, Ground Cover, Aerosols and Cloud Thickness", *Photochemistry and Photobiology* **81**, 1287 (2005).
- [11] A. R. Webb, "Who, What, Where and When - Influences on Cutaneous Vitamin D Synthesis", *Progress in Biophysics and Molecular Biology* **92**, 17 (2006).
- [12] S. Tommasi, M. F. Denissenko, and G. P. Pfeifer, "Sunlight Induces Pyrimidine Dimers Preferentially at 5-Methylcytosine Bases", *Cancer Research* **57**, 4727 (1997).
- [13] F. R. de Gruijl, "Skin Cancer and Solar UV Radiation", *European Journal of Cancer* **35**, 2003 (1999).
- [14] C. E. Crespo-Hernández, B. Cohen, and B. Kohler, "Base Stacking Controls Excited-state Dynamics in A-T DNA", *Nature* **436**, 1141 (2005).
- [15] C. T. Middleton, K. de La Harpe, C. Su, Y. K. Law, C. E. Crespo-Hernández, and B. Kohler, "DNA Excited-State Dynamics: From Single Bases to the Double Helix", *Annual Review of Physical Chemistry* **60**, 217 (2009).
- [16] J. Cadet, S. Mouret, J.-L. Ravanat, and T. Douki, "Photoinduced Damage to Cellular DNA: Direct and Photosensitized Reactions", *Photochemistry and Photobiology* **88**, 1048 (2012).

- [17] W. J. Schreier, P. Gilch, and W. Zinth, “Early Events of DNA Photodamage”, *Annual Review of Physical Chemistry* **66**, 497 (2015).
 - [18] M. Barbatti, A. C. Borin, and S. Ullrich, eds., *Photoinduced Phenomena in Nucleic Acids I: Nucleobases in the Gas Phase and in Solvents* (Springer International Publishing, Basel, CH, 2015).
 - [19] R. Improta, F. Santoro, and L. Blancafort, “Quantum Mechanical Studies on the Photophysics and the Photochemistry of Nucleic Acids and Nucleobases”, *Chemical Reviews* **116**, 3540 (2016).
 - [20] A. F. Collings and C. Critchley, eds., *Artificial Photosynthesis: From Basic Biology to Industrial Application* (Wiley-VCH Verlag GmbH & Co. KGaA, Weinheim, DE, 2005).
 - [21] C. Andrea Rozzi, S. Maria Falke, N. Spallanzani, A. Rubio, E. Molinari, D. Brida, M. Maiuri, G. Cerullo, H. Schramm, J. Christoffers, and C. Lienau, “Quantum Coherence Controls the Charge Separation in a Prototypical Artificial Light-harvesting System”, *Nature Communications* **4**, 1602 (2013).
 - [22] J. Roncali, P. Leriche, and P. Blanchard, “Molecular Materials for Organic Photovoltaics: Small is Beautiful”, *Advanced Materials* **26**, 3821 (2014).
 - [23] K. A. Mazzio and C. K. Luscombe, “The Future of Organic Photovoltaics”, *Chemical Society Reviews* **44**, 78 (2015).
 - [24] K. M. Pelzer and S. B. Darling, “Charge Generation in Organic Photovoltaics: A Review of Theory and Computation”, *Molecular Systems Design & Engineering* **1**, 10 (2016).
 - [25] A. A. Ismail and D. W. Bahnemann, “Photochemical Splitting of Water for Hydrogen Production by Photocatalysis: A review”, *Solar Energy Materials and Solar Cells* **128**, 85 (2014).
 - [26] K. Wenderich and G. Mul, “Methods, Mechanism, and Applications of Photodeposition in Photocatalysis: A Review”, *Chemical Reviews* **116**, 14587 (2016).
 - [27] B. L. Feringa, R. A. van Delden, N. Koumura, and E. M. Geertsema, “Chiroptical Molecular Switches”, *Chemical Reviews* **100**, 1789 (2000).
 - [28] A. Nenov, T. Cordes, T. T. Herzog, W. Zinth, and R. de Vivie-Riedle, “Molecular Driving Forces for Z/E Isomerization Mediated by Heteroatoms: The Example Hemithioindigo”, *The Journal of Physical Chemistry A* **114**, 13016 (2010).
 - [29] B. Maerz, S. Wiedbrauk, S. Oesterling, E. Samoylova, A. Nenov, P. Mayer, R. de Vivie-Riedle, W. Zinth, and H. Dube, “Making Fast Photoswitches Faster-Using Hammett Analysis to Understand the Limit of Donor–Acceptor Approaches for Faster Hemithioindigo Photoswitches”, *Chemistry - A European Journal* **20**, 13984 (2014).
 - [30] S. Kassem, T. van Leeuwen, A. S. Lubbe, M. R. Wilson, B. L. Feringa, and D. A. Leigh, “Artificial Molecular Motors”, *Chemical Society Reviews* **46**, 2592 (2017).
 - [31] B. L. Feringa, “The Art of Building Small: From Molecular Switches to Motors (Nobel Lecture)”, *Angewandte Chemie International Edition* **56**, 11060 (2017).
 - [32] F. F. Graupner, T. T. Herzog, F. Rott, S. Oesterling, R. de Vivie-Riedle, T. Cordes, and W. Zinth, “Photoisomerization of Hemithioindigo Compounds: Combining Solvent- and Substituent-effects into an Advanced Reaction Model”, *Chemical Physics* **515**, 614 (2018).
 - [33] R. Wilcken, M. Schildhauer, F. Rott, L. A. Huber, M. Guentner, S. Thumser, K. Hoffmann, S. Oesterling, R. de Vivie-Riedle, E. Riedle, and H. Dube, “Complete Mechanism of Hemithioindigo Motor Rotation”, *Journal of the American Chemical Society* **140**, 5311 (2018).
 - [34] D. R. Yarkony, “Diabolical Conical Intersections”, *Reviews of Modern Physics* **68**, 985 (1996).
 - [35] M. Baer, “Introduction to the Theory of Electronic Non-Adiabatic Coupling Terms in Molecular Systems”, *Physics Reports* **358**, 75 (2002).
 - [36] W. Domcke, D. R. Yarkony, and H. Köppel, eds., *Conical Intersections: Electronic Structure, Dynamics and Spectroscopy* (WORLD SCIENTIFIC, Singapore, SG, 2004).
 - [37] G. A. Worth and L. S. Cederbaum, “BEYOND BORN-OPPENHEIMER: Molecular Dynamics Through a Conical Intersection”, *Annual Review of Physical Chemistry* **55**, 127 (2004).
-

-
- [38] S. Osella, “Artificial Photosynthesis: Is Computation Ready for the Challenge Ahead?”, *Nanomaterials* **11**, 10.3390/nano11020299 (2021).
- [39] D. Strickland and G. Mourou, “Compression of Amplified Chirped Optical Pulses”, *Optics Communications* **55**, 447 (1985).
- [40] G. Cerullo, M. Nisoli, and S. De Silvestri, “Generation of 11 fs Pulses Tunable Across the Visible by Optical Parametric Amplification”, *Applied Physics Letters* **71**, 3616 (1997).
- [41] E. Riedle, M. Beutter, S. Lochbrunner, J. Piel, S. Schenkl, S. Spörlein, and W. Zinth, “Generation of 10 to 50 fs Pulses Tunable Through all of the Visible and the NIR”, *Applied Physics B* **71**, 457 (2000).
- [42] M. Hentschel, R. Kienberger, C. Spielmann, G. A. Reider, N. Milosevic, T. Brabec, P. Corkum, U. Heinzmann, M. Drescher, and F. Krausz, “Attosecond Metrology”, *Nature* **414**, 509 (2001).
- [43] J. Itatani, F. Quéré, G. L. Yudin, M. Y. Ivanov, F. Krausz, and P. B. Corkum, “Attosecond Streak Camera”, *Physical Review Letters* **88**, 4 (2002).
- [44] A. Baltuška, T. Udem, M. Uiberacker, M. Hentschel, E. Goulielmakis, C. Gohle, R. Holzwarth, V. S. Yakovlev, A. Scrinzi, T. W. Hänsch, and F. Krausz, “Attosecond Control of Electronic Processes by Intense Light Fields”, *Nature* **421**, 611 (2003).
- [45] P. Baum, S. Lochbrunner, and E. Riedle, “Generation of Tunable 7-fs Ultraviolet Pulses: Achromatic Phase Matching and Chirp Management”, *Applied Physics B* **79**, 1027 (2004).
- [46] C. Manzoni, D. Polli, and G. Cerullo, “Two-color Pump-probe System Broadly Tunable over the Visible and the Near Infrared with Sub-30fs Temporal Resolution”, *Review of Scientific Instruments* **77**, 023103 (2006).
- [47] D. Polli, M. Antognazza, D. Brida, G. Lanzani, G. Cerullo, and S. De Silvestri, “Broadband Pump-probe Spectroscopy with Sub-10-fs Resolution for Probing Ultrafast Internal Conversion and Coherent Phonons in Carotenoids”, *Chemical Physics* **350**, 45 (2008).
- [48] E. Goulielmakis, Z. H. Loh, A. Wirth, R. Santra, N. Rohringer, V. S. Yakovlev, S. Zherebtsov, T. Pfeifer, A. M. Azzeer, M. F. Kling, S. R. Leone, and F. Krausz, “Real-time Observation of Valence Electron Motion”, *Nature* **466**, 739 (2010).
- [49] N. Krebs, I. Pugliesi, and E. Riedle, “Pulse Compression of Ultrashort UV Pulses by Self-Phase Modulation in Bulk Material”, *Applied Sciences* **3**, 153 (2013).
- [50] A. R. Attar, A. Bhattacharjee, C. D. Pemmaraju, K. Schnorr, K. D. Closser, D. Prendergast, and S. R. Leone, “Femtosecond X-ray Spectroscopy of an Electrocyclic Ring-opening Reaction”, *Science* **356**, 54 (2017).
- [51] Y. Pertot, C. Schmidt, M. Matthews, A. Chauvet, M. Huppert, V. Svoboda, A. von Conta, A. Tehlar, D. Baykusheva, J. P. Wolf, and H. J. Wörner, “Time-resolved X-ray Absorption Spectroscopy with a Water Window High-harmonic Source”, *Science* **355**, 264 (2017).
- [52] Y. Kobayashi, K. F. Chang, T. Zeng, D. M. Neumark, and S. R. Leone, “Direct Mapping of Curve-crossing Dynamics in IBr by Attosecond Transient Absorption Spectroscopy”, *Science* **364**, 79 (2019).
- [53] M. J. Rosker, M. Dantus, and A. H. Zewail, “Femtosecond Real-Time Probing of Reactions. I. The Technique”, *The Journal of Chemical Physics* **89**, 6113 (1988).
- [54] M. Dantus, M. J. Rosker, and A. H. Zewail, “Femtosecond Real-Time Probing of Reactions. II. The Dissociation Reaction of ICN”, *The Journal of Chemical Physics* **89**, 6128 (1988).
- [55] A. H. Zewail, “Laser Femtochemistry”, *Science* **242**, 1645 (1988).
- [56] A. H. Zewail, “Femtochemistry: Atomic-Scale Dynamics of the Chemical Bond”, *The Journal of Physical Chemistry A* **104**, 5660 (2000).
- [57] F. Calegari, D. Ayuso, A. Trabattoni, L. Belshaw, S. De Camillis, S. Anumula, F. Frassetto, L. Poletto, A. Palacios, P. Decleva, J. B. Greenwood, F. Martín, and M. Nisoli, “Ultrafast Electron Dynamics in Phenylalanine Initiated by Attosecond Pulses”, *Science* **346**, 336 (2014).
-

- [58] P. M. Kraus, B. Mignolet, D. Baykusheva, A. Rupenyan, L. Horný, E. F. Penka, G. Grassi, O. I. Tolstikhin, J. Schneider, F. Jensen, L. B. Madsen, A. D. Bandrauk, F. Remacle, and H. J. Wörner, “Measurement and Laser Control of Attosecond Charge Migration in Ionized Iodoacetylene”, *Science* **350**, 790 (2015).
 - [59] M. Nisoli, P. Decleva, F. Calegari, A. Palacios, and F. Martín, “Attosecond Electron Dynamics in Molecules”, *Chemical Reviews* **117**, 10760 (2017).
 - [60] P. von den Hoff, I. Znakovskaya, M. Kling, and R. de Vivie-Riedle, “Attosecond Control of the Dissociative Ionization via Electron Localization: A Comparison Between D₂ and CO”, *Chemical Physics* **366**, 139 (2009).
 - [61] G. Sansone, F. Kelkensberg, J. F. Pérez-Torres, F. Morales, M. F. Kling, W. Siu, O. Ghafur, P. Johnsson, M. Swoboda, E. Benedetti, F. Ferrari, F. Lépine, J. L. Sanz-Vicario, S. Zharebtsov, I. Znakovskaya, A. L’Huillier, M. Y. Ivanov, M. Nisoli, F. Martín, and M. J. J. Vrakking, “Electron Localization Following Attosecond Molecular Photoionization”, *Nature* **465**, 763 (2010).
 - [62] C. Andrea Rozzi, S. Maria Falke, N. Spallanzani, A. Rubio, E. Molinari, D. Brida, M. Maiuri, G. Cerullo, H. Schramm, J. Christoffers, and C. Lienau, “Quantum Coherence Controls the Charge Separation in a Prototypical Artificial Light-harvesting System”, *Nature Communications* **4**, 1602 (2013).
 - [63] E. Romero, R. Augulis, V. I. Novoderezhkin, M. Ferretti, J. Thieme, D. Zigmantas, and R. van Grondelle, “Quantum Coherence in Photosynthesis for Efficient Solar-energy Conversion”, *Nature Physics* **10**, 676 (2014).
 - [64] T. Brixner and G. Gerber, “Quantum Control of Gas-Phase and Liquid-Phase Femtochemistry”, *ChemPhysChem* **4**, 418 (2003).
 - [65] M. F. Kling, P. von den Hoff, I. Znakovskaya, and R. de Vivie-Riedle, “(Sub-)Femtosecond Control of Molecular Reactions via Tailoring the Electric Field of Light”, *Physical Chemistry Chemical Physics* **15**, 9448 (2013).
 - [66] S. Thallmair, D. Keefer, F. Rott, and R. de Vivie-Riedle, “Simulating the Control of Molecular Reactions via Modulated Light Fields: From Gas Phase to Solution”, *Journal of Physics B: Atomic, Molecular and Optical Physics* **50**, 082001 (2017).
 - [67] D. J. Tannor, R. Kosloff, and S. A. Rice, “Coherent Pulse Sequence Induced Control of Selectivity of Reactions: Exact Quantum Mechanical Calculations”, *The Journal of Chemical Physics* **85**, 5805 (1986).
 - [68] D. J. Tannor and S. A. Rice, “Control of Selectivity of Chemical Reaction via Control of Wave Packet Evolution”, *The Journal of Chemical Physics* **83**, 5013 (1985).
 - [69] R. S. Judson and H. Rabitz, “Teaching Lasers to Control Molecules”, *Physical Review Letters* **68**, 1500 (1992).
 - [70] W. S. Warren, H. Rabitz, and M. Dahleh, “Coherent Control of Quantum Dynamics: The Dream Is Alive”, *Science* **259**, 1581 (1993).
 - [71] R. F. Loring and S. Mukamel, “Selectivity in Coherent Transient Raman Measurements of Vibrational Dephasing in Liquids”, *The Journal of Chemical Physics* **83**, 2116 (1985).
 - [72] S. Mukamel, “Multidimensional Femtosecond Correlation Spectroscopies of Electronic and Vibrational Excitations”, *Annual Review of Physical Chemistry* **51**, 691 (2000).
 - [73] M. Mazzeo, D. Pisignano, L. Favaretto, G. Barbarella, R. Cingolani, and G. Gigli, “Bright Oligothiophene-based Light Emitting Diodes”, *Synthetic Metals* **139**, 671 (2003).
 - [74] T. A. Skotheim and J. R. Reynolds, eds., *Handbook of Conducting Polymers*, 3rd ed. (CRC Press, Boca Raton, FL, 2007).
 - [75] I. F. Perepichka and D. F. Perepichka, eds., *Handbook of Thiophene-Based Materials: Applications in Organic Electronics and Photonics* (John Wiley & Sons Ltd, Chichester, UK, 2007).
-

-
- [76] N. J. Turro, V. Ramamurthy, and J. Scaiano, eds., *Modern Molecular Photochemistry*, 1st ed. (University Science Books, Mill Valley, CA, 2010).
- [77] F. Zhang, D. Wu, Y. Xu, and X. Feng, "Thiophene-based Conjugated Oligomers for Organic Solar Cells", *Journal of Materials Chemistry* **21**, 17590 (2011).
- [78] G. Turkoglu, M. E. Cinar, and T. Ozturk, "Thiophene-Based Organic Semiconductors", in *Sulfur Chemistry*, edited by X. Jiang (Springer International Publishing, Basel, CH, 2019), pp. 79–123.
- [79] D. Chi, S. Qu, Z. Wang, and J. Wang, "High Efficiency P3HT:PCBM Solar Cells with an Inserted PCBM Layer", *Journal of Materials Chemistry C* **2**, 4383 (2014).
- [80] M. Huix-Rotllant, H. Tamura, and I. Burghardt, "Concurrent Effects of Delocalization and Internal Conversion Tune Charge Separation at Regioregular Polythiophene-Fullerene Heterojunctions", *Journal of Physical Chemistry Letters* **6**, 1702 (2015).
- [81] S. L. Mousavi, F. Jamali-Sheini, M. Sabaeian, and R. Yousefi, "Enhanced Solar Cell Performance of P3HT:PCBM by SnS Nanoparticles", *Solar Energy* **199**, 872 (2020).
- [82] P. Kölle, T. Schnappinger, and R. de Vivie-Riedle, "Deactivation Pathways of Thiophene and Oligothiophenes: Internal Conversion Versus Intersystem Crossing", *Physical Chemistry Chemical Physics* **18**, 7903 (2016).
- [83] M. Richter, P. Marquetand, J. González-Vázquez, I. Sola, and L. González, "SHARC: *Ab Initio* Molecular Dynamics with Surface Hopping in the Adiabatic Representation Including Arbitrary Couplings", *Journal of Chemical Theory and Computation* **7**, 1253 (2011).
- [84] S. Mai, P. Marquetand, and L. González, "A General Method to Describe Intersystem Crossing Dynamics in Trajectory Surface Hopping", *International Journal of Quantum Chemistry* **115**, 1215 (2015).
- [85] S. Mai, P. Marquetand, and L. González, "Nonadiabatic Dynamics: The SHARC Approach", *WIREs Computational Molecular Science* **8**, e1370 (2018).
- [86] S. Mai, M. Richter, M. Heindl, M. F. S. J. Menger, A. Atkins, M. Ruckebauer, F. Plasser, L. M. Ibele, S. Kropf, M. Oppel, P. Marquetand, and L. González, *SHARC2.1: Surface Hopping Including Arbitrary Couplings - Program Package for Non-Adiabatic Dynamics*, sharc-md.org, 2019.
- [87] J. C. Tully, "Molecular Dynamics with Electronic Transitions", *The Journal of Chemical Physics* **93**, 1061 (1990).
- [88] M. Born and R. Oppenheimer, "Zur Quantentheorie der Molekeln", *Annalen der Physik* **389**, 457 (1927).
- [89] H. C. Longuet-Higgins, U. Öpik, M. H. L. Pryce, and R. A. Sack, "Studies of the Jahn-Teller Effect. II. The Dynamical Problem", *Proceedings of the Royal Society of London. Series A. Mathematical and Physical Sciences* **244**, 1 (1958).
- [90] M. V. Berry, "Quantal Phase Factors Accompanying Adiabatic Changes", *Proceedings of the Royal Society of London. A. Mathematical and Physical Sciences* **392**, 45 (1984).
- [91] A. F. Izmaylov, J. Li, and L. Joubert-Doriol, "Diabatic Definition of Geometric Phase Effects", *Journal of Chemical Theory and Computation* **12**, 5278 (2016).
- [92] I. G. Ryabinkin, L. Joubert-Doriol, and A. F. Izmaylov, "Geometric Phase Effects in Nonadiabatic Dynamics near Conical Intersections", *Accounts of Chemical Research* **50**, 1785 (2017).
- [93] J. Schön and H. Köppel, "Geometric Phase Effects and Wave Packet Dynamics on Intersecting Potential Energy Surfaces", *The Journal of Chemical Physics* **103**, 9292 (1995).
- [94] C. Xie, J. Ma, X. Zhu, D. R. Yarkony, D. Xie, and H. Guo, "Nonadiabatic Tunneling in Photodissociation of Phenol", *Journal of the American Chemical Society* **138**, 7828 (2016).
- [95] A. J. Jenkins, M. Vacher, R. M. Twidale, M. J. Bearpark, and M. A. Robb, "Charge Migration in Polycyclic Norbornadiene Cations: Winning the Race Against Decoherence", *The Journal of Chemical Physics* **145**, 164103 (2016).
-

- [96] M. Vacher, D. Mendive-Tapia, M. J. Bearpark, and M. A. Robb, “Electron Dynamics Upon Ionization: Control of the Timescale Through Chemical Substitution and Effect of Nuclear Motion”, *The Journal of Chemical Physics* **142**, 094105 (2015).
 - [97] C. Arnold, O. Vendrell, and R. Santra, “Electronic Decoherence Following Photoionization: Full Quantum-dynamical Treatment of the Influence of Nuclear Motion”, *Physical Review A: Atomic, Molecular, and Optical Physics* **95**, 033425 (2017).
 - [98] D. Jia, J. Manz, and Y. Yang, “Timing the Recoherences of Attosecond Electronic Charge Migration by Quantum Control of Femtosecond Nuclear Dynamics: A Case Study for HCCI^+ ”, *The Journal of Chemical Physics* **151**, 244306 (2019).
 - [99] P. von den Hoff, R. Siemering, M. Kowalewski, and R. de Vivie-Riedle, “Electron Dynamics and Its Control in Molecules: From Diatomics to Larger Molecular Systems”, *IEEE Journal of Selected Topics in Quantum Electronics* **18**, 119 (2012).
 - [100] D. Geppert, P. von den Hoff, and R. de Vivie-Riedle, “Electron Dynamics in Molecules: A New Combination of Nuclear Quantum Dynamics and Electronic Structure Theory”, *Journal of Physics B: Atomic, Molecular and Optical Physics* **41**, 074006 (2008).
 - [101] I. Znakovskaya, P. von den Hoff, S. Zharebtsov, A. Wirth, O. Herrwerth, M. J. J. Vrakking, R. de Vivie-Riedle, and M. F. Kling, “Attosecond Control of Electron Dynamics in Carbon Monoxide”, *Physical Review Letters* **103**, 103002 (2009).
 - [102] T. Bayer, H. Braun, C. Sarpe, R. Siemering, P. von den Hoff, R. de Vivie-Riedle, T. Baumert, and M. Wollenhaupt, “Charge Oscillation Controlled Molecular Excitation”, *Physical Review Letters* **110**, 123003 (2013).
 - [103] H. Braun, T. Bayer, C. Sarpe, R. Siemering, R. de Vivie-Riedle, T. Baumert, and M. Wollenhaupt, “Coupled Electron-nuclear Wavepacket Dynamics in Potassium Dimers”, *Journal of Physics B: Atomic, Molecular and Optical Physics* **47**, 124015 (2014).
 - [104] W. Lewis Nobles and C. DeWitt Blanton, “Thiophene Compounds of Biological Interest”, *Journal of Pharmaceutical Sciences* **53**, 115 (1964).
 - [105] J. Swanston, “Thiophene”, in *Ullmann’s Encyclopedia of Industrial Chemistry* (American Cancer Society, 2006).
 - [106] R. S. Keri, K. Chand, S. Budagumpi, S. B. Somappa, S. A. Patil, and B. M. Nagaraja, “An Overview of Benzo[*b*]thiophene-based Medicinal Chemistry”, *European Journal of Medicinal Chemistry* **138**, 1002 (2017).
 - [107] O. A. Kraevaya, A. S. Peregudov, N. E. Fedorova, R. R. Klimova, I. A. Godovikov, D. V. Mishchenko, A. F. Shestakov, D. Schols, A. A. Kushch, and P. A. Troshin, “Thiophene-based Water-soluble Fullerene Derivatives as Highly Potent Antiherpetic Pharmaceuticals”, *Organic & Biomolecular Chemistry* **18**, 8702 (2020).
 - [108] W. Yu, P. J. Donohoo-Vallett, J. Zhou, and A. E. Bragg, “Ultrafast Photo-induced Nuclear Relaxation of a Conformationally Disordered Conjugated Polymer Probed with Transient Absorption and Femtosecond Stimulated Raman Spectroscopies”, *Journal of Chemical Physics* **141**, 044201 (2014).
 - [109] C. Wang, M. Angelella, S. J. Doyle, L. A. Lytwak, P. J. Rossky, B. J. Holliday, and M. J. Tauber, “Resonance Raman Spectroscopy of the T_1 Triplet Excited State of Oligothiophenes”, *Journal of Physical Chemistry Letters* **6**, 3521 (2015).
 - [110] A. K. Thomas, H. A. Brown, B. D. Datko, J. A. Garcia-Galvez, and J. K. Grey, “Interchain Charge-Transfer States Mediate Triplet Formation in Purified Conjugated Polymer Aggregates”, *Journal of Physical Chemistry C* **120**, 23230 (2016).
 - [111] R. S. Becker, J. Seixas de Melo, A. L. Maçanita, and F. Elisei, “Comprehensive Evaluation of the Absorption, Photophysical, Energy Transfer, Structural, and Theoretical Properties of α -Oligothiophenes with One to Seven Rings”, *Journal of Physical Chemistry* **100**, 18683 (1996).
-

-
- [112] G. Gigli, O. Inganäs, M. Anni, M. De Vittorio, R. Cingolani, G. Barbarella, and L. Favaretto, "Multicolor Oligothiophene-based Light-emitting Diodes", *Applied Physics Letters* **78**, 1493 (2001).
- [113] T. Chen, B. Zhang, Z. Liu, L. Duan, G. Dong, Y. Feng, X. Luo, and D. Cui, "Synthesis and Properties of a Thiophene-substituted Diaza[7]helicene for Application as a Blue Emitter in Organic Light-emitting Diodes", *Tetrahedron Letters* **58**, 531 (2017).
- [114] S. Jang, K. H. Lee, J. Y. Lee, and Y. Lee, "Dibenzo[*b,d*]furan and Dibenzo[*b,d*]thiophene Molecular Dimers as Hole Blocking Materials for High-efficiency and Long-lived Blue Phosphorescent Organic Light-emitting Diodes", *Journal of Materials Chemistry C* **7**, 9599 (2019).
- [115] Z. Gao, F. Zhang, L. Gao, X. Tian, W. Qu, T. Yang, J. Li, K. Guo, and Y. Miao, "An A-D-A Type of Thiophene derivative with Morphology-determining Luminescent Performance: Synthesis and Application in a Light Emitting Device", *Journal of Luminescence* **219**, 116919 (2020).
- [116] B. L. Rupert, W. J. Mitchell, A. J. Ferguson, M. E. Köse, W. L. Rance, G. Rumbles, D. S. Ginley, S. E. Shaheen, and N. Kopidakis, "Low-bandgap Thiophene Dendrimers for Improved Light Harvesting", *Journal of Materials Chemistry* **19**, 5311 (2009).
- [117] P. M. Beaujuge and J. M. J. Fréchet, "Molecular Design and Ordering Effects in π -Functional Materials for Transistor and Solar Cell Applications", *Journal of the American Chemical Society* **133**, 20009 (2011).
- [118] H. Hu, K. Jiang, G. Yang, J. Liu, Z. Li, H. Lin, Y. Liu, J. Zhao, J. Zhang, F. Huang, Y. Qu, W. Ma, and H. Yan, "Terthiophene-Based D-A Polymer with an Asymmetric Arrangement of Alkyl Chains That Enables Efficient Polymer Solar Cells", *Journal of the American Chemical Society* **137**, 14149 (2015).
- [119] W. Yan, D. Jiang, Q. Liu, Q. Kang, and F. Zhou, "Solar Cells Constructed with Polythiophene Thin Films Grown along Tethered Thiophene-Dye Conjugates via Photoelectrochemical Polymerization", *ACS Applied Materials & Interfaces* **11**, 18755 (2019).
- [120] J. Munshi, T. Chien, W. Chen, and G. Balasubramanian, "Elasto-morphology of P3HT:PCBM Bulk Heterojunction Organic Solar Cells", *Soft Matter* **16**, 6743 (2020).
- [121] D. Lu, G. Lv, Z. Xu, Y. Dong, X. Ji, and Y. Liu, "Thiophene-Based Two-Dimensional Dion-Jacobson Perovskite Solar Cells with over 15% Efficiency", *Journal of the American Chemical Society* **142**, 11114 (2020).
- [122] J. Wu, G. Li, J. Fang, X. Guo, L. Zhu, B. Guo, Y. Wang, G. Zhang, L. Arunagiri, F. Liu, H. Yan, M. Zhang, and Y. Li, "Random Terpolymer Based on Thiophene-thiazolothiazole Unit Enabling Efficient Non-fullerene Organic Solar Cells", *Nature Communications* **11**, 4612 (2020).
- [123] M. Irie, T. Fukaminato, K. Matsuda, and S. Kobatake, "Photochromism of Diarylethene Molecules and Crystals: Memories, Switches, and Actuators", *Chemical Reviews* **114**, 12174 (2014).
- [124] G. Barbarella, M. Zambianchi, A. Ventola, E. Fabiano, F. Della Sala, G. Gigli, M. Anni, A. Bolognesi, L. Polito, M. Naldi, and M. Capobianco, "Bright oligothiophene N-Succinimidyl Esters for Efficient Fluorescent Labeling of Proteins and Oligonucleotides", *Bioconjugate Chemistry* **17**, 58 (2006).
- [125] H.-A. Ho, A. Najari, and M. Leclerc, "Optical Detection of DNA and Proteins with Cationic Polythiophenes", *Accounts of Chemical Research* **41**, 168 (2008).
- [126] M. Zambianchi, F. D. Maria, A. Cazzato, G. Gigli, M. Piacenza, F. D. Sala, and G. Barbarella, "Microwave-Assisted Synthesis of Thiophene Fluorophores, Labeling and Multilabeling of Monoclonal Antibodies, and Long Lasting Staining of Fixed Cells", *Journal of the American Chemical Society* **131**, 10892 (2009).
- [127] D. Musib, L. R. Devi, M. K. Raza, S. B. Chanu, and M. Roy, "A New Thiophene-based Aggregation-induced Emission Chemosensor for Selective Detection of Zn^{2+} Ions and Its Turn Off", *Chemistry Letters* **49**, 473 (2020).
-

- [128] A. Bhaskar, G. Ramakrishna, K. Hagedorn, O. Varnavski, E. Mena-Osteritz, P. Bäuerle, and T. Goodson, "Enhancement of Two-Photon Absorption Cross-Section in Macrocyclic Thiophenes with Cavities in the Nanometer Regime", *Journal of Physical Chemistry B* **111**, 946 (2007).
 - [129] H. Zhou, F. Zhou, S. Tang, P. Wu, Y. Chen, Y. Tu, J. Wu, and Y. Tian, "Two-Photon Absorption Dyes with Thiophene as π Electron Bridge: Synthesis, Photophysical Properties and Optical Data Storage", *Dyes and Pigments* **92**, 633 (2012).
 - [130] H. T. Turan, Y. Eken, M. Marazzi, M. Pastore, V. Aviyente, and A. Monari, "Assessing One- and Two-Photon Optical Properties of Boron Containing Arenes", *Journal of Physical Chemistry C* **120**, 17916 (2016).
 - [131] X. Mu, X. Wang, J. Quan, and M. Sun, "Photoinduced Charge Transfer in Donor-Bridge-Acceptor in One- and Two-Photon Absorption: Sequential and Superexchange Mechanisms", *The Journal of Physical Chemistry C* **124**, 4968 (2020).
 - [132] S. Millefiori, A. Alparone, and A. Millefiori, "Conformational Properties of Thiophene Oligomers", *Journal of Heterocyclic Chemistry* **37**, 847 (2000).
 - [133] M. Rubio, M. Merchán, R. Pou-Amérigo, and E. Ortí, "The Low-Lying Excited States of 2,2'-Bithiophene: A Theoretical Analysis", *ChemPhysChem* **4**, 1308 (2003).
 - [134] M. Rubio, M. Merchán, and E. Ortí, "A Theoretical Study on the Low-Lying Excited States of 2,2':5',2''-Terthiophene and 2,2':5',2'':5'',2'''-Quaterthiophene", *ChemPhysChem* **6**, 1357 (2005).
 - [135] F. Liu, P. Zuo, L. Meng, and S. J. Zheng, "On the Optical Properties of Thiophene Oligomers: Configuration Interaction Study on their Ground (S_0) and First Singlet Excited (S_1) States", *Journal of Molecular Structure: THEOCHEM* **726**, 161 (2005).
 - [136] S. Salzmann, M. Kleinschmidt, J. Tatchen, R. Weinkauf, and C. M. Marian, "Excited States of Thiophene: Ring Opening as Deactivation Mechanism", *Physical Chemistry Chemical Physics* **10**, 380 (2008).
 - [137] M. Stenrup, "Theoretical Study of the Radiationless Deactivation Mechanisms of Photo-excited Thiophene", *Chemical Physics* **397**, 18 (2012).
 - [138] S. Siegert, F. Vogeler, C. M. Marian, and R. Weinkauf, "Throwing Light on Dark States of α -oligothiophenes of Chain Lengths 2 to 6: Radical Anion Photoelectron Spectroscopy and Excited-state Theory", *Physical Chemistry Chemical Physics* **13**, 10350 (2011).
 - [139] A. Hofmann and R. de Vivie-Riedle, "Quantum Dynamics of Photoexcited Cyclohexadiene Introducing Reactive Coordinates", *The Journal of Chemical Physics* **112**, 5054 (2000).
 - [140] M. Araújo, B. Lasorne, A. L. Magalhães, M. J. Bearpark, and M. A. Robb, "Controlling Product Selection in the Photodissociation of Formaldehyde: Direct Quantum Dynamics from the S_1 Barrier", *The Journal of Physical Chemistry A* **114**, 12016 (2010).
 - [141] S. Thallmair, M. Kowalewski, J. P. P. Zauleck, M. K. Roos, and R. de Vivie-Riedle, "Quantum Dynamics of a Photochemical Bond Cleavage Influenced by the Solvent Environment: A Dynamic Continuum Approach", *The Journal of Physical Chemistry Letters* **5**, 3480 (2014).
 - [142] D. Keefer, S. Thallmair, S. Matsika, and R. de Vivie-Riedle, "Controlling Photorelaxation in Uracil with Shaped Laser Pulses: A Theoretical Assessment", *Journal of the American Chemical Society* **139**, 5061 (2017).
 - [143] S. Hammes-Schiffer and J. C. Tully, "Proton Transfer in Solution: Molecular Dynamics with Quantum Transitions", *The Journal of Chemical Physics* **101**, 4657 (1994).
 - [144] G. Granucci, M. Persico, and A. Zocante, "Including Quantum Decoherence in Surface Hopping", *The Journal of Chemical Physics* **133**, 134111 (2010).
 - [145] H. M. Jaeger, S. Fischer, and O. V. Prezhdo, "Decoherence-induced Surface Hopping", *The Journal of Chemical Physics* **137**, 22A545 (2012).
 - [146] J. E. Subotnik, A. Jain, B. Landry, A. Petit, W. Ouyang, and N. Bellonzi, "Understanding the Surface Hopping View of Electronic Transitions and Decoherence", *Annual Review of Physical Chemistry* **67**, 387 (2016).
-

-
- [147] M. Barbatti, “Nonadiabatic Dynamics with Trajectory Surface Hopping Method”, *WIREs Computational Molecular Science* **1**, 620 (2011).
- [148] E. Fabiano, T. Keal, and W. Thiel, “Implementation of Surface Hopping Molecular Dynamics Using Semiempirical Methods”, *Chemical Physics* **349**, 334 (2008).
- [149] A. W. Jasper, S. N. Stechmann, and D. G. Truhlar, “Fewest-switches with Time Uncertainty: A Modified Trajectory Surface-hopping Algorithm with Better Accuracy for Classically Forbidden Electronic Transitions”, *The Journal of Chemical Physics* **116**, 5424 (2002).
- [150] R. Crespo-Otero and M. Barbatti, “Recent Advances and Perspectives on Nonadiabatic Mixed Quantum-Classical Dynamics”, *Chemical Reviews* **118**, 7026 (2018).
- [151] D. Townsend, B. J. Sussman, and A. Stolow, “A Stark Future for Quantum Control”, *The Journal of Physical Chemistry A* **115**, 357 (2011).
- [152] J. J. Bajo, J. González-Vázquez, I. R. Sola, J. Santamaria, M. Richter, P. Marquetand, and L. González, “Mixed Quantum-Classical Dynamics in the Adiabatic Representation to Simulate Molecules Driven by Strong Laser Pulses”, *The Journal of Physical Chemistry A* **116**, 2800 (2012).
- [153] W. Pauli, “Zur Quantenmechanik des Magnetischen Elektrons”, *Zeitschrift für Physik* **43**, 601 (1927).
- [154] C. M. Marian, “Spin-Orbit Coupling and Intersystem Crossing in Molecules”, *WIREs Computational Molecular Science* **2**, 187 (2012).
- [155] B. A. Heß, C. M. Marian, U. Wahlgren, and O. Gropen, “A Mean-field Spin-Orbit Method Applicable to Correlated Wavefunctions”, *Chemical Physics Letters* **251**, 365 (1996).
- [156] F. Neese, “Efficient and Accurate Approximations to the Molecular Spin-Orbit Coupling Operator and Their Use in Molecular g-tensor Calculations”, *The Journal of Chemical Physics* **122**, 034107 (2005).
- [157] J. E. Subotnik, W. Ouyang, and B. R. Landry, “Can We Derive Tully’s Surface-hopping Algorithm from the Semiclassical Quantum Liouville Equation? Almost, But Only with Decoherence”, *The Journal of Chemical Physics* **139**, 214107 (2013).
- [158] R. Kapral, “Surface Hopping from the Perspective of Quantum-Classical Liouville Dynamics”, *Chemical Physics* **481**, 77 (2016).
- [159] A. Abedi, F. Agostini, Y. Suzuki, and E. K. U. Gross, “Dynamical Steps that Bridge Piecewise Adiabatic Shapes in the Exact Time-Dependent Potential Energy Surface”, *Physical Review Letters* **110**, 263001 (2013).
- [160] T. Fiedlschuster, J. Handt, E. K. U. Gross, and R. Schmidt, “Surface Hopping in Laser-driven Molecular Dynamics”, *Physical Review A* **95**, 063424 (2017).
- [161] S. Patchkovskii, “*Ab Initio* Investigation of Potential Energy Curves of the 23 Electronic States of IBr Correlating to Neutral ^2P Atoms”, *Physical Chemistry Chemical Physics* **8**, 926 (2006).
- [162] V. Vallet, L. Maron, C. Teichtel, and J.-P. Flament, “A Two-step Uncontracted Determinantal Effective Hamiltonian-based SO-CI Method”, *The Journal of Chemical Physics* **113**, 1391 (2000).
- [163] F. Wang and T. Ziegler, “A Simplified Relativistic Time-Dependent Density-functional Theory Formalism for the Calculations of Excitation Energies Including Spin-Orbit Coupling Effect”, *The Journal of Chemical Physics* **123**, 154102 (2005).
- [164] S. Mai, T. Müller, F. Plasser, P. Marquetand, H. Lischka, and L. González, “Perturbational Treatment of Spin-Orbit Coupling for Generally Applicable High-level Multi-reference Methods”, *The Journal of Chemical Physics* **141**, 074105 (2014).
- [165] G. Cui and W. Fang, “*Ab Initio* Trajectory Surface-Hopping Study on Ultrafast Deactivation Process of Thiophene”, *The Journal of Physical Chemistry A* **115**, 11544 (2011).
- [166] D. Fazzi, M. Barbatti, and W. Thiel, “Modeling Ultrafast Exciton Deactivation in Oligothiophenes via Nonadiabatic Dynamics”, *Physical Chemistry Chemical Physics* **17**, 7787 (2015).
-

- [167] A. Prlj, B. F. E. Curchod, and C. Corminboeuf, “Excited State Dynamics of Thiophene and Bithiophene: New Insights into Theoretically Challenging Systems”, *Physical Chemistry Chemical Physics* **17**, 14719 (2015).
 - [168] M. Pederzoli and J. Pittner, “A new Approach to Molecular Dynamics with Non-Adiabatic and Spin-Orbit Effects with Applications to QM/MM Simulations of Thiophene and Selenophene”, *The Journal of Chemical Physics* **146**, 114101 (2017).
 - [169] T. Schnappinger, P. Kölle, M. Marazzi, A. Monari, L. González, and R. de Vivie-Riedle, “*Ab Initio* Molecular Dynamics of Thiophene: The Interplay of Internal Conversion and Intersystem Crossing”, *Physical Chemistry Chemical Physics* **19**, 25662 (2017).
 - [170] R. Weinkauf, L. Lehr, E. W. Schlag, S. Salzmann, and C. M. Marian, “Ultrafast Dynamics in Thiophene Investigated by Femtosecond Pump Probe Photoelectron Spectroscopy and Theory”, *Physical Chemistry Chemical Physics* **10**, 393 (2008).
 - [171] B. G. Levine, C. Ko, J. Quenneville, and T. J. Martínez, “Conical Intersections and Double Excitations in Time-Dependent Density Functional Theory”, *Molecular Physics* **104**, 1039 (2006).
 - [172] B. G. Levine, J. D. Coe, and T. J. Martínez, “Optimizing Conical Intersections without Derivative Coupling Vectors: Application to Multistate Multireference Second-Order Perturbation Theory (MS-CASPT2)”, *The Journal of Physical Chemistry B* **112**, 405 (2008).
 - [173] T. Schnappinger, M. Marazzi, S. Mai, A. Monari, L. González, and R. de Vivie-Riedle, “Intersystem Crossing as a Key Component of the Nonadiabatic Relaxation Dynamics of Bithiophene and Terthiophene”, *Journal of Chemical Theory and Computation* **14**, 4530 (2018).
 - [174] S. Rentsch, J. P. Yang, W. Paa, E. Birckner, J. Schiedt, and R. Weinkauf, “Size dependence of triplet and singlet states of α -oligothiophenes”, *Physical Chemistry Chemical Physics* **1**, 1707 (1999).
 - [175] K. C. Woo, D. H. Kang, and S. K. Kim, “Real-Time Observation of Nonadiabatic Bifurcation Dynamics at a Conical Intersection”, *Journal of the American Chemical Society* **139**, 17152 (2017).
 - [176] A. Hofmann and R. de Vivie-Riedle, “Adiabatic Approach for Ultrafast Quantum Dynamics Mediated by Simultaneously Active Conical Intersections”, *Chemical Physics Letters* **346**, 299 (2001).
 - [177] H. Rabitz, R. de Vivie-Riedle, M. Motzkus, and K. Kompa, “Whither the Future of Controlling Quantum Phenomena?”, *Science* **288**, 824 (2000).
 - [178] T. Baumert, T. Brixner, V. Seyfried, M. Strehle, and G. Gerber, “Femtosecond Pulse Shaping by an Evolutionary Algorithm with Feedback”, *Applied Physics B* **65**, 779 (1997).
 - [179] M. A. Dugan, J. X. Tull, and W. S. Warren, “High-resolution Acousto-optic Shaping of Unamplified and Amplified Femtosecond Laser Pulses”, *Journal of the Optical Society of America B: Optical Physics* **14**, 2348 (1997).
 - [180] F. Krausz and M. Ivanov, “Attosecond Physics”, *Reviews of Modern Physics* **81**, 163 (2009).
 - [181] U. Gaubatz, P. Rudecki, M. Becker, S. Schiemann, M. Külz, and K. Bergmann, “Population Switching between Vibrational Levels in Molecular Beams”, *Chemical Physics Letters* **149**, 463 (1988).
 - [182] U. Gaubatz, P. Rudecki, S. Schiemann, and K. Bergmann, “Population Transfer between Molecular Vibrational Levels by Stimulated Raman Scattering with Partially Overlapping Laser Fields. A New Concept and Experimental Results”, *The Journal of Chemical Physics* **92**, 5363 (1990).
 - [183] E. D. Potter, J. L. Herek, S. Pedersen, Q. Liu, and A. H. Zewail, “Femtosecond Laser Control of a Chemical Reaction”, *Nature* **355**, 66 (1992).
 - [184] R. Mitrić, M. Hartmann, J. Pittner, and V. Bonačić-Koutecký, “New Strategy for Optimal Control of Femtosecond Pump-Dump Processes”, *The Journal of Physical Chemistry A* **106**, 10477 (2002).
 - [185] D. Geppert, A. Hofmann, and R. de Vivie-Riedle, “Control of a Collision Complex via a Conical Intersection”, *The Journal of Chemical Physics* **119**, 5901 (2003).
-

-
- [186] J. L. Herek, W. Wohlleben, R. J. Cogdell, D. Zeidler, and M. Motzkus, “Quantum Control of Energy Flow in Light Harvesting”, *Nature* **417**, 533 (2002).
- [187] M. Abe, Y. Ohtsuki, Y. Fujimura, and W. Domcke, “Optimal Control of Ultrafast Cis-trans Photoisomerization of Retinal in Rhodopsin via a Conical Intersection”, *The Journal of Chemical Physics* **123**, 144508 (2005).
- [188] D. Keefer and R. de Vivie-Riedle, “Theoretical Quantum Control of Fluctuating Molecular Energy Levels in Complex Chemical Environments”, *Advanced Quantum Technologies* **2**, 1800099 (2019).
- [189] P. Brumer and M. Shapiro, “Control of Unimolecular Reactions Using Coherent Light”, *Chemical Physics Letters* **126**, 541 (1986).
- [190] M. Shapiro, J. W. Hepburn, and P. Brumer, “Simplified Laser Control of Unimolecular Reactions: Simultaneous (ω_1 , ω_3) Excitation”, *Chemical Physics Letters* **149**, 451 (1988).
- [191] K. Hoki, L. González, and Y. Fujimura, “Control of Molecular Handedness using Pump-dump Laser Pulses”, *The Journal of Chemical Physics* **116**, 2433 (2002).
- [192] B. Wolter, M. G. Pullen, A.-T. Le, M. Baudisch, K. Doblhoff-Dier, A. Senftleben, M. Hemmer, C. D. Schröter, J. Ullrich, T. Pfeifer, R. Moshhammer, S. Gräfe, O. Vendrell, C. D. Lin, and J. Biegert, “Ultrafast Electron Diffraction Imaging of Bond Breaking in Di-ionized Acetylene”, *Science* **354**, 308 (2016).
- [193] N. Moiseyev, M. Šindelka, and L. S. Cederbaum, “Laser-induced Conical Intersections in Molecular Optical Lattices”, *Journal of Physics B: Atomic, Molecular and Optical Physics* **41**, 221001 (2008).
- [194] G. J. Halász, M. Šindelka, N. Moiseyev, L. S. Cederbaum, and Á. Vibók, “Light-Induced Conical Intersections: Topological Phase, Wave Packet Dynamics, and Molecular Alignment”, *The Journal of Physical Chemistry A* **116**, 2636 (2012).
- [195] A. Natan, M. R. Ware, V. S. Prabhudesai, U. Lev, B. D. Bruner, O. Heber, and P. H. Bucksbaum, “Observation of Quantum Interferences via Light-Induced Conical Intersections in Diatomic Molecules”, *Physical Review Letters* **116**, 143004 (2016).
- [196] S. Felicetti, J. Fregoni, T. Schnappinger, S. Reiter, R. de Vivie-Riedle, and J. Feist, “Photoprotecting Uracil by Coupling with Lossy Nanocavities”, *The Journal of Physical Chemistry Letters* **11**, 8810 (2020).
- [197] E. Davidsson and M. Kowalewski, “Simulating Photodissociation Reactions in Bad Cavities with the Lindblad Equation”, *The Journal of Chemical Physics* **153**, 234304 (2020).
- [198] M. Gudem and M. Kowalewski, “Controlling the Photostability of Pyrrole with Optical Nanocavities”, *The Journal of Physical Chemistry A* **125**, 1142 (2021).
- [199] A. Hoffmann, “Ultraschnelle Molekulare Quantendynamik durch Konische Durchschneidungen”, PhD thesis (Max-Planck-Institut für Quantenoptik, 2001).
- [200] W. Domcke and G. Stock, “Theory of Ultrafast Nonadiabatic Excited-State Processes and their Spectroscopic Detection in Real Time”, in *Advances in Chemical Physics* (John Wiley & Sons, Ltd, 2007), pp. 1–169.
- [201] D. Kosloff and R. Kosloff, “A Fourier Method Solution for the Time Dependent Schrödinger Equation as a Tool in Molecular Dynamics”, *Journal of Computational Physics* **52**, 35 (1983).
- [202] H. Tal-Ezer and R. Kosloff, “An Accurate and Efficient Scheme for Propagating the Time Dependent Schrödinger Equation”, *The Journal of Chemical Physics* **81**, 3967 (1984).
- [203] R. Kosloff, “Time-Dependent Quantum-Mechanical Methods for Molecular Dynamics”, *The Journal of Physical Chemistry* **92**, 2087 (1988).
- [204] J. P. P. Zauleck, S. Thallmair, M. Loipersberger, and R. de Vivie-Riedle, “Two New Methods to Generate Internal Coordinates for Molecular Wave Packet Dynamics in Reduced Dimensions”, *Journal of Chemical Theory and Computation* **12**, 5698 (2016).
-

- [205] J. P. P. Zauleck and R. de Vivie-Riedle, “Constructing Grids for Molecular Quantum Dynamics Using an Autoencoder”, *Journal of Chemical Theory and Computation* **14**, 55 (2018).
 - [206] S. Reiter, T. Schnappinger, and R. de Vivie-Riedle, “Using an Autoencoder for Dimensionality Reduction in Quantum Dynamics”, in *Artificial Neural Networks and Machine Learning - ICANN 2019: Workshop and Special Sessions*, edited by I. V. Tetko, V. Kůrková, P. Karpov, and F. Theis (2019), pp. 783–787.
 - [207] B. Podolsky, “Quantum-Mechanically Correct Form of Hamiltonian Function for Conservative Systems”, *Physical Review* **32**, 812 (1928).
 - [208] E. B. Wilson Jr., J. C. Decius, and P. C. Cross, *Molecular Vibrations: The Theory of Infrared and Raman Vibrational Spectra* (Dover Publications, New York, NY, 1955).
 - [209] L. Schaad and J. Hu, “The Schrödinger Equation in Generalized Coordinates”, *Journal of Molecular Structure: THEOCHEM* **185**, 203 (1989).
 - [210] M. K. H. Roos, “Photoinitiated Processes in Functionally Diverse Organic Molecules Elucidated by Theoretical Methods”, PhD thesis (Ludwig-Maximilians-Universität München, 2018).
 - [211] S. Reiter, D. Keefer, and R. de Vivie-Riedle, “Exact Quantum Dynamics (Wave Packets) in Reduced Dimensionality”, in *Quantum Chemistry and Dynamics of Excited States* (John Wiley & Sons, Ltd, 2020) Chap. 11, pp. 355–381.
 - [212] H.-D. Meyer, U. Manthe, and L. S. Cederbaum, “The Multi-configurational Time-dependent Hartree Approach”, *Chemical Physics Letters* **165**, 73 (1990).
 - [213] M. Bonfanti, G. A. Worth, and I. Burghardt, “Multi-Configuration Time-dependent Hartree Methods: From Quantum to Semiclassical and Quantum-Classical”, in *Quantum Chemistry and Dynamics of Excited States* (John Wiley & Sons, Ltd, 2020) Chap. 12, pp. 383–411.
 - [214] G. A. Worth, H.-D. Meyer, and L. S. Cederbaum, “Relaxation of a System with a Conical Intersection Coupled to a Bath: A Benchmark 24-dimensional Wave Packet Study Treating the Environment Explicitly”, *The Journal of Chemical Physics* **109**, 3518 (1998).
 - [215] A. Raab, G. A. Worth, H.-D. Meyer, and L. S. Cederbaum, “Molecular Dynamics of Pyrazine after Excitation to the S₂ Electronic State Using a Realistic 24-mode Model Hamiltonian”, *The Journal of Chemical Physics* **110**, 936 (1999).
 - [216] A. Lehr, S. Gómez, M. A. Parkes, and G. A. Worth, “The Role of Vibronic Coupling in the Electronic Spectroscopy of Maleimide: A Multi-mode and Multi-state Quantum Dynamics Study”, *Physical Chemistry Chemical Physics* **22**, 25272 (2020).
 - [217] H.-D. Meyer, “Studying Molecular Quantum Dynamics with the Multiconfiguration Time-dependent Hartree Method”, *WIREs Computational Molecular Science* **2**, 351 (2012).
 - [218] A. Baltuška, T. Udem, M. Uiberacker, M. Hentschel, E. Goulielmakis, C. Gohle, R. Holzwarth, V. S. Yakovlev, A. Scrinzi, T. W. Hänsch, and F. Krausz, “Attosecond Control of Electronic Processes by Intense Light Fields”, *Nature* **421**, 611 (2003).
 - [219] A. S. Alnaser, M. Kübel, R. Siemering, B. Bergues, N. G. Kling, K. J. Betsch, Y. Deng, J. Schmidt, Z. A. Alahmed, A. M. Azzeer, J. Ullrich, I. Ben-Itzhak, R. Moshhammer, U. Kleineberg, F. Krausz, R. de Vivie-Riedle, and M. F. Kling, “Subfemtosecond Steering of Hydrocarbon Deprotonation through Superposition of Vibrational Modes”, *Nature Communications* **5**, 3800 (2014).
 - [220] C. Liekhus-Schmaltz, G. A. McCracken, A. Kaldun, J. P. Cryan, and P. H. Bucksbaum, “Coherent Control Using Kinetic Energy and the Geometric Phase of a Conical Intersection”, *The Journal of Chemical Physics* **145**, 144304 (2016).
 - [221] M. Kübel, R. Siemering, C. Burger, N. G. Kling, H. Li, A. S. Alnaser, B. Bergues, S. Zhrebtssov, A. M. Azzeer, I. Ben-Itzhak, R. Moshhammer, R. de Vivie-Riedle, and M. F. Kling, “Steering Proton Migration in Hydrocarbons Using Intense Few-Cycle Laser Fields”, *Physical Review Letters* **116**, 193001 (2016).
 - [222] C. Arnold, O. Vendrell, R. Welsch, and R. Santra, “Control of Nuclear Dynamics Through Conical Intersections and Electronic Coherences”, *Physical Review Letters* **120**, 123001 (2018).
-

-
- [223] M. Richter, F. Bouakline, J. González-Vázquez, L. Martínez-Fernández, I. Corral, S. Patchkovskii, F. Morales, M. Ivanov, F. Martín, and O. Smirnova, “Sub-laser-cycle Control of Coupled Electron-Nuclear Dynamics at a Conical Intersection”, *New Journal of Physics* **17**, 113023 (2015).
- [224] M. Richter, J. González-Vázquez, Z. Mašín, D. S. Brambila, A. G. Harvey, F. Morales, and F. Martín, “Ultrafast Imaging of Laser-controlled Non-adiabatic Dynamics in NO₂ from Time-resolved Photoelectron Emission”, *Physical Chemistry Chemical Physics* **21**, 10038 (2019).
- [225] Y. Arasaki and K. Takatsuka, “Optical Conversion of Conical Intersection to Avoided Crossing”, *Physical Chemistry Chemical Physics* **12**, 1239 (2010).
- [226] Y. Arasaki, K. Takatsuka, K. Wang, and V. McKoy, “Time-Resolved photoelectron spectroscopy of wavepackets through a conical intersection in NO₂”, *The Journal of Chemical Physics* **132**, 124307 (2010).
- [227] E. Wells, C. E. Rallis, M. Zohrabi, R. Siemering, B. Jochim, P. R. Andrews, U. Ablikim, B. Gaire, S. De, K. D. Carnes, B. Bergues, R. de Vivie-Riedle, M. F. Kling, and I. Ben-Itzhak, “Adaptive Strong-field Control of Chemical Dynamics Guided by Three-dimensional Momentum Imaging”, *Nature Communications* **4**, 2895 (2013).
- [228] P. T. von den Hoff, “Gekoppelte Kern- und Elektronendynamik: Molekulare Systeme und deren Kontrolle durch die Bewegung der Elektronen”, PhD thesis (Ludwig-Maximilians-Universität München, 2011).
- [229] P. v. d. Hoff, S. Thallmair, M. Kowalewski, R. Siemering, and R. d. Vivie-Riedle, “Optimal Control Theory - Closing the Gap Between Theory and Experiment”, *Physical Chemistry Chemical Physics* **14**, 14460 (2012).
- [230] F. Schüppel, T. Schnappinger, L. Bäuml, and R. de Vivie-Riedle, “Waveform control of molecular dynamics close to a conical intersection”, *The Journal of Chemical Physics* **153**, 224307 (2020).
- [231] D. Keefer and S. Mukamel, “Selective Enhancement of Spectroscopic Features by Quantum Optimal Control”, *Physical Review Letters* **126**, 163202 (2021).
- [232] K. C. Kulander, “Time-Dependent Hartree-Fock Theory of Multiphoton Ionization: Helium”, *Physical Review A: Atomic, Molecular, and Optical Physics* **36**, 2726 (1987).
- [233] E. Runge and E. K. U. Gross, “Density-Functional Theory for Time-Dependent Systems”, *Physical Review Letters* **52**, 997 (1984).
- [234] T. Klamroth, “Laser-driven Electron Transfer Through Metal-insulator-metal Contacts: Time-Dependent Configuration Interaction Singles Calculations for a Jellium Model”, *Physical Review B: Condensed Matter* **68**, 245421 (2003).
- [235] N. Rohringer, A. Gordon, and R. Santra, “Configuration-interaction-based Time-Dependent Orbital Approach for *Ab Initio* Treatment of Electronic Dynamics in a Strong Optical Laser Field”, *Physical Review A: Atomic, Molecular, and Optical Physics* **74**, 043420 (2006).
- [236] A. S. Skeidsvoll, A. Balbi, and H. Koch, “Time-Dependent Coupled-cluster Theory for Ultrafast Transient-absorption Spectroscopy”, *Physical Review A: Atomic, Molecular, and Optical Physics* **102**, 023115 (2020).
- [237] F. D. Vila, J. J. Rehr, J. J. Kas, K. Kowalski, and B. Peng, “Real-Time Coupled-Cluster Approach for the Cumulant Green’s Function”, *Journal of Chemical Theory and Computation* **16**, 6983 (2020).
- [238] P. Ehrenfest, “Bemerkung über die Angenäherte Gültigkeit der Klassischen Mechanik Innerhalb der Quantenmechanik”, *Zeitschrift für Physik* **45**, 455 (1927).
- [239] A. McLachlan, “A Variational Solution of the Time-Dependent Schrodinger Equation”, *Molecular Physics* **8**, 39 (1964).
- [240] G. D. Billing, “The Semiclassical Coupled States Method”, *The Journal of Chemical Physics* **65**, 1 (1976).
-

- [241] H.-D. Meyer and W. H. Miller, “A Classical Analog for Electronic Degrees of Freedom in Nonadiabatic Collision Processes”, *The Journal of Chemical Physics* **70**, 3214 (1979).
 - [242] S.-I. Sawada, A. Nitzan, and H. Metiu, “Mean-trajectory Approximation for Charge- and Energy-transfer Processes at Surfaces”, *Physical Review B: Condensed Matter* **32**, 851 (1985).
 - [243] G. D. Billing, ed., *The Quantum Classical Theory* (Oxford University Press, Oxford, U. K., 2003).
 - [244] A. Ojanperä, V. Havu, L. Lehtovaara, and M. Puska, “Nonadiabatic Ehrenfest Molecular Dynamics Within the Projector Augmented-wave Method”, *The Journal of Chemical Physics* **136**, 144103 (2012).
 - [245] J. L. Alonso, A. Castro, P. Echenique, and A. Rubio, “On the Combination of TDDFT with Molecular Dynamics: New Developments”, in *Fundamentals of Time-Dependent Density Functional Theory*, edited by M. A. Marques, N. T. Maitra, F. M. Nogueira, E. Gross, and A. Rubio (Springer Berlin Heidelberg, Berlin, Heidelberg, 2012), pp. 301–315.
 - [246] K. Takatsuka, “Theory of Molecular Non-adiabatic Electron Dynamics in Condensed Phases”, *The Journal of Chemical Physics* **147**, 174102 (2017).
 - [247] K. Takatsuka, “Nuclear wavepackets along quantum paths in nonadiabatic electron wavepacket dynamics”, *Chemical Physics* **515**, 52 (2018).
 - [248] P. V. Parandekar and J. C. Tully, “Detailed Balance in Ehrenfest Mixed Quantum-Classical Dynamics”, *Journal of Chemical Theory and Computation* **2**, 229 (2006).
 - [249] D. V. Shalashilin, “Quantum Mechanics with the Basis Set Guided by Ehrenfest Trajectories: Theory and Application to Spin-boson Model”, *The Journal of Chemical Physics* **130**, 244101 (2009).
 - [250] D. V. Shalashilin, “Multiconfigurational Ehrenfest Approach to Quantum Coherent Dynamics in Large Molecular Systems”, *Faraday Discussions* **153**, 105 (2011).
 - [251] A. D. Bandrauk, S. Chelkowski, and H. S. Nguyen, “Attosecond Localization of Electrons in Molecules”, *International Journal of Quantum Chemistry* **100**, 834 (2004).
 - [252] M. Nest, “The Multi-configuration Electron-nuclear Dynamics Method”, *Chemical Physics Letters* **472**, 171 (2009).
 - [253] V. Pohl and J. C. Tremblay, “Adiabatic Electronic Flux Density: A Born-Oppenheimer Broken-symmetry Ansatz”, *Physical Review A: Atomic, Molecular, and Optical Physics* **93**, 012504 (2016).
 - [254] R. Matsuzaki and K. Takatsuka, “Electronic and Nuclear Flux Analysis on Nonadiabatic Electron Transfer Reaction: A View from Single-configuration Adiabatic Born-Huang Representation”, *Journal of Computational Chemistry* **40**, 148 (2019).
 - [255] L. S. Cederbaum, “Born-Oppenheimer Approximation and beyond for Time-Dependent Electronic Processes”, *The Journal of Chemical Physics* **128**, 124101 (2008).
 - [256] A. Abedi, N. T. Maitra, and E. K. U. Gross, “Exact Factorization of the Time-Dependent Electron-Nuclear Wave Function”, *Physical Review Letters* **105**, 123002 (2010).
 - [257] A. Abedi, N. T. Maitra, and E. K. U. Gross, “Correlated Electron-nuclear Dynamics: Exact Factorization of the Molecular Wavefunction”, *The Journal of Chemical Physics* **137**, 22A530 (2012).
 - [258] Y.-C. Chiang, S. Klaiman, F. Otto, and L. S. Cederbaum, “The Exact Wavefunction Factorization of a Vibronic Coupling System”, *The Journal of Chemical Physics* **140**, 054104 (2014).
 - [259] F. Agostini and E. K. U. Gross, “Exact Factorization of the Electron-Nuclear Wave Function: Theory and Applications”, in *Quantum Chemistry and Dynamics of Excited States* (John Wiley & Sons, Ltd, 2020) Chap. 17, pp. 531–562.
 - [260] H. R. Hudock, B. G. Levine, A. L. Thompson, H. Satzger, D. Townsend, N. Gador, S. Ullrich, A. Stolow, and T. J. Martinez, “*Ab Initio* Molecular Dynamics and Time-resolved Photoelectron Spectroscopy of Electronically Excited Uracil and Thymine”, *Journal of Physical Chemistry A* **111**, 8500 (2007).
-

-
- [261] M. Barbatti, A. J. A. Aquino, and H. Lischka, "The UV Absorption of Nucleobases: Semi-classical *Ab Initio* Spectra Simulations", *Physical Chemistry Chemical Physics* **12**, 4959 (2010).
- [262] M. Richter, S. Mai, P. Marquetand, and L. Leticia González, "Ultrafast Intersystem Crossing Dynamics in Uracil Unravelling by *Ab Initio* Molecular Dynamics", *Physical Chemistry Chemical Physics* **16**, 24423 (2014).
- [263] B. P. Fingerhut, K. E. Dorfman, and S. J. Mukamel, "Probing the Conical Intersection Dynamics of the RNA Base Uracil by UV-Pump Stimulated-Raman-Probe Signals; *Ab Initio* Simulations", *Journal of Chemical Theory and Computation* **10**, 1172 (2014).
- [264] S. Reiter, D. Keefer, and R. de Vivie-Riedle, "RNA environment is responsible for decreased photostability of uracil", *Journal of the American Chemical Society* **140**, 8714 (2018).
- [265] D. Keefer, T. Schnappinger, R. de Vivie-Riedle, and S. Mukamel, "Visualizing Conical Intersection Passages via Vibronic Coherence Maps Generated by Stimulated Ultrafast X-ray Raman Signals", *Proceedings of the National Academy of Sciences* **117**, 24069 (2020).
- [266] H. Kang, K. T. Lee, B. Jung, Y. J. Ko, and S. K. Kim, "Intrinsic Lifetimes of the Excited State of DNA and RNA Bases", *Journal of the American Chemical Society* **124**, 12958 (2002).
- [267] Y. G. He, C. Y. Wu, and W. Kong, "Decay Pathways of Thymine and Methyl-substituted Uracil and Thymine in the Gas Phase", *Journal of Physical Chemistry A* **107**, 5145 (2003).
- [268] C. E. Crespo-Hernández, B. Cohen, P. M. Hare, and B. Kohler, "Ultrafast Excited-state Dynamics in Nucleic Acids", *Chemical Reviews* **104**, 1977 (2004).
- [269] L. Esposito, A. Banyasz, T. Douki, M. Perron, D. Markovitsi, and R. Improta, "Effect of C5-Methylation of Cytosine on the Photoreactivity of DNA: A Joint Experimental and Computational Study of TCG Trinucleotides", *Journal of the American Chemical Society* **136**, 10838 (2014).
- [270] G. P. Pfeifer, Y. H. You, and A. Besaratinia, "Mutations Induced by Ultraviolet Light", *Mutation Research - Fundamental and Molecular Mechanisms of Mutagenesis* **571**, 19 (2005).
- [271] P. M. Hare, C. E. Crespo-Hernández, and B. Kohler, "Solvent-Dependent Photophysics of 1-Cyclohexyluracil: Ultrafast Branching in the Initial Bright State Leads Nonradiatively to the Electronic Ground State and a Long-Lived $1n\pi^*$ State", *The Journal of Physical Chemistry B* **110**, 18641 (2006).
- [272] L. Bäuml, T. Schnappinger, M. F. Kling, and R. de Vivie-Riedle, "Photo-Induced Coupled Nuclear and Electron Dynamics in the Nucleobase Uracil", *Frontiers in Physics* **9**, 246 (2021).
- [273] A. Nikodem, R. D. Levine, and F. Remacle, "Quantum Nuclear Dynamics Pumped and Probed by Ultrafast Polarization Controlled Steering of a Coherent Electronic State in LiH", *The Journal of Physical Chemistry A* **120**, 3343 (2016).
- [274] A. T. J. B. Eppink, B. J. Whitaker, E. Gloaguen, B. Soep, A. M. Coroiu, and D. H. Parker, "Dissociative Multiphoton Ionization of NO₂ Studied by Time-resolved Imaging", *The Journal of Chemical Physics* **121**, 7776 (2004).
- [275] A. Vredenborg, W. G. Roeterdink, and M. H. M. Janssen, "Femtosecond Time-resolved Photoelectron-photoion Coincidence Imaging of Multiphoton Multichannel Photodynamics in NO₂", *The Journal of Chemical Physics* **128**, 204311 (2008).
- [276] I. Wilkinson and B. J. Whitaker, "Some remarks on the photodynamics of NO₂", *Annual Reports on the Progress of Chemistry, Section C: Physical Chemistry* **106**, 274 (2010).
- [277] H. J. Wörner, J. B. Bertrand, B. Fabre, J. Higuier, H. Ruf, A. Dubrouil, S. Patchkovskii, M. Spanner, Y. Mairesse, V. Blanchet, E. Mével, E. Constant, P. B. Corkum, and D. M. Villeneuve, "Conical Intersection Dynamics in NO₂ Probed by Homodyne High-Harmonic Spectroscopy", *Science* **334**, 208 (2011).
-

- [278] H. Ruf, C. Handschin, A. Ferré, N. Thiré, J. B. Bertrand, L. Bonnet, R. Cireasa, E. Constant, P. B. Corkum, D. Descamps, B. Fabre, P. Larregaray, E. Mével, S. Petit, B. Pons, D. Staedter, H. J. Wörner, D. M. Villeneuve, Y. Mairesse, P. Halvick, and V. Blanchet, “High-harmonic Transient Grating Spectroscopy of NO₂ Electronic Relaxation”, *The Journal of Chemical Physics* **137**, 224303 (2012).
 - [279] P. M. Kraus, Y. Arasaki, J. B. Bertrand, S. Patchkovskii, P. B. Corkum, D. M. Villeneuve, K. Takatsuka, and H. J. Wörner, “Time-resolved High-harmonic Spectroscopy of Nonadiabatic Dynamics in NO₂”, *Physical Review A* **85**, 043409 (2012).
 - [280] R. Forbes, A. E. Boguslavskiy, I. Wilkinson, J. G. Underwood, and A. Stolow, “Excited State Wavepacket Dynamics in NO₂ Probed by Strong-field Ionization”, *The Journal of Chemical Physics* **147**, 054305 (2017).
 - [281] X. Ding, R. Forbes, M. Kübel, K. F. Lee, M. Spanner, A. Y. Naumov, D. M. Villeneuve, A. Stolow, P. B. Corkum, and A. Staudte, “Threshold Photodissociation Dynamics of NO₂ Studied by Time-Resolved Cold Target Recoil Ion Momentum Spectroscopy”, *The Journal of Chemical Physics* **151**, 174301 (2019).
 - [282] E. Haller, H. Köppel, and L. S. Cederbaum, “The Visible Absorption Spectrum of NO₂: A Three-mode Nuclear Dynamics Investigation”, *Journal of Molecular Spectroscopy* **111**, 377 (1985).
 - [283] S. Mahapatra, H. Köppel, and L. S. Cederbaum, “Impact of Nonadiabatic Coupling between the Conically Intersecting X²A₁ and A²B₂ States of NO₂ on the Negative Ion Photoelectron Spectra of NO₂”, *The Journal of Chemical Physics* **110**, 5691 (1999).
 - [284] F. Santoro and C. Petrongolo, “Nonadiabatic Wave Packet Dynamics of NO₂ on the X²A₁/A²A₂ Conical Intersection”, *The Journal of Chemical Physics* **110**, 4419 (1999).
 - [285] S. Mahapatra, H. Köppel, L. S. Cederbaum, P. Stampfuß, and W. Wenzel, “Nonadiabatic Wave Packet Dynamics on the Coupled X²A₁/A²A₂ Electronic States of NO₂ Based on new *Ab Initio* Potential Energy Surfaces”, *Chemical Physics* **259**, 211 (2000).
 - [286] F. Santoro, C. Petrongolo, G. Granucci, and M. Persico, “Quantum and Semiclassical Dynamics of the Franck-Condon Wave Packet on the Coupled Potential Surfaces of the X²A₁/A²A₂ Conical Intersection”, *Chemical Physics* **259**, 193 (2000).
 - [287] V. Kurkal, P. Fleurat-Lessard, and R. Schinke, “NO₂: Global Potential Energy Surfaces of the Ground ²A₁) and the First Excited ²B₂ Electronic States”, *The Journal of Chemical Physics* **119**, 1489 (2003).
 - [288] M. Sanrey and M. Joyeux, “Quantum Mechanical and Quasiclassical Investigations of the Time Domain Nonadiabatic Dynamics of NO₂ Close to the Bottom of the X²A₁-A²B₂ Conical Intersection”, *The Journal of Chemical Physics* **125**, 014304 (2006).
 - [289] Y. Arasaki and K. Takatsuka, “Quantum Wavepacket Dynamics for Time-Resolved Photoelectron Spectroscopy of the NO₂ Conical Intersection”, *Chemical Physics* **338**, 175 (2007).
 - [290] R. Schinke, S. Y. Grebenshchikov, and H. Zhu, “The Photodissociation of NO₂ in the Second Absorption Band: *Ab Initio* and Quantum Dynamics Calculations”, *Chemical Physics* **346**, 99 (2008).
 - [291] T. Schnappinger and R. de Vivie-Riedle, “Coupled Nuclear and Electron Dynamics in the Vicinity of a Conical Intersection”, *The Journal of Chemical Physics* **154**, 134306 (2021).
 - [292] S. P. Neville, A. Stolow, and M. S. Schuurman, *The Role of Geometric Phase in the Formation of Electronic Coherences at Conical Intersections*, 2020.
 - [293] V. Roudnev and B. D. Esry, “General Theory of Carrier-Envelope Phase Effects”, *Physical Review Letters* **99**, 220406 (2007).
 - [294] T. Ito, T. Shimomura, and T. Miura, “Simulation Study of the Effect of the Side-Chain Structure on the Initial Nucleation Process of Polythiophene Derivatives”, *The Journal of Physical Chemistry B* **121**, 1108 (2017).
-

-
- [295] G. J. Hedley, F. Steiner, J. Vogelsang, and J. M. Lupton, “Determining the True Optical Gap in a High-Performance Organic Photovoltaic Polymer Using Single-Molecule Spectroscopy”, *The Journal of Physical Chemistry Letters* **8**, 3494 (2017).
- [296] M. Polkehn, H. Tamura, and I. Burghardt, “Impact of Charge-transfer Excitons in Regioregular Polythiophene on the Charge Separation at Polythiophene-fullerene Heterojunctions”, *Journal of Physics B: Atomic, Molecular and Optical Physics* **51**, 014003 (2017).
- [297] N. E. Jackson, “Coarse-Graining Organic Semiconductors: The Path to Multiscale Design”, *The Journal of Physical Chemistry B* **125**, 485 (2021).
- [298] H. Lin and D. G. Truhlar, “QM/MM: What Have We Learned, Where Are We, and Where Do We Go From Here?”, *Theoretical Chemistry Accounts* **117**, 185 (2006).
- [299] E. Brunk and U. Rothlisberger, “Mixed Quantum Mechanical/Molecular Mechanical Molecular Dynamics Simulations of Biological Systems in Ground and Electronically Excited States”, *Chemical Reviews* **115**, 6217 (2015).
- [300] G. Del Frate, F. Bellina, G. Mancini, G. Marianetti, P. Minei, A. Pucci, and V. Barone, “Tuning of Dye Optical Properties by Environmental Effects: A QM/MM and Experimental Study”, *Physical Chemistry Chemical Physics* **18**, 9724 (2016).
- [301] X.-Y. Liu, Y.-G. Fang, B.-B. Xie, W.-H. Fang, and G. Cui, “QM/MM Nonadiabatic Dynamics Simulations on Photoinduced Wolff Rearrangements of 1,2,3-thiadiazole”, *The Journal of Chemical Physics* **146**, 224302 (2017).
- [302] J. R. Gołkebiowski, J. R. Kermode, P. D. Haynes, and A. A. Mostofi, “Atomistic QM/MM Simulations of the Strength of Covalent Interfaces in Carbon Nanotube-Polymer Composites”, *Physical Chemistry Chemical Physics* **22**, 12007 (2020).
- [303] M. Ben-Nun, J. Quenneville, and T. J. Martínez, “*Ab Initio* Multiple Spawning: Photochemistry from First Principles Quantum Molecular Dynamics”, *The Journal of Physical Chemistry A* **104**, 5161 (2000).
- [304] B. F. E. Curchod, “Full and *Ab Initio* Multiple Spawning”, in *Quantum Chemistry and Dynamics of Excited States* (John Wiley & Sons, Ltd, 2020) Chap. 14, pp. 435–467.
- [305] S. Thallmair, J. P. P. Zauleck, and R. de Vivie-Riedle, “Quantum Dynamics in an Explicit Solvent Environment: A Photochemical Bond Cleavage Treated with a Combined QD/MD Approach”, *Journal of Chemical Theory and Computation* **11**, 1987 (2015).
- [306] A. Bhattacharjee and S. R. Leone, “Ultrafast X-ray Transient Absorption Spectroscopy of Gas-Phase Photochemical Reactions: A New Universal Probe of Photoinduced Molecular Dynamics”, *Accounts of Chemical Research* **51**, 3203 (2018).
- [307] K. S. Zinchenko, F. Ardana-Lamas, I. Seidu, S. P. Neville, J. van der Veen, V. U. Lanfaloni, M. S. Schuurman, and H. J. Wörner, “Sub-7-Femtosecond Conical-Intersection Dynamics Probed at the Carbon K-Edge”, *Science* **371**, 489 (2021).
- [308] D. Jadoun, M. Gudem, and M. Kowalewski, “Capturing Fingerprints of Conical Intersection: Complementary Information of Non-Adiabatic Dynamics from Linear X-Ray Probes”, *Structural Dynamics* **8**, 034101 (2021).
-

LIST OF ABBREVIATIONS

1e-2o	one-electron-two-orbital
BO	Born-Oppenheimer
CASPT2	complete active space perturbation theory to the second order
CASSCF	complete active space self-consistent field
CEP	carrier-envelope phase
CoIn	conical intersection
DFM	dynamic Fourier method
FC	Franck-Condon
GP	geometric phase
IC	internal conversion
IR	infrared
ISC	intersystem crossing
LR-TDDFT	linear-response time-dependent density functional theory
MCH	molecular Coulomb Hamiltonian
MCTDH	multi-configuration time-dependent Hartree
NAC	non-adiabatic coupling
NEMol	coupled nuclear and electron dynamics in molecular systems
OCT	optimal control theory
PES	potential energy surface
SH	surface hopping
SHARC	surface hopping including arbitrary couplings
SOC	spin-orbit coupling
TDSE	time-dependent Schrödinger equation
TISE	time-independent Schrödinger equation

DANKSAGUNG

I don't know half of you half as well as I
should like; and I like less than half of you
half as well as you deserve.

*The Lord of the Rings:
The Fellowship of the Ring*
J.R.R. Tolkien

Da das obige Zitat wohl für diesen Anlass nicht als Abschluss ausreicht, möchte ich mich im Folgenden bei denjenigen bedanken, die über die vergangenen Jahre hinweg in der einen oder anderen Weise zu dieser Doktorarbeit beigetragen haben.

Zuallerst gilt mein Dank meiner Doktormutter Frau Prof. Dr. Regina de Vivie-Riedle, die mich in ihre Arbeitsgruppe aufgenommen und mich in den letzten Jahren umfassend unterstützt hat. Insbesondere ihr menschliches Engagement, die wissenschaftlichen Freiräume, zahlreichen Diskussionen und Denkanstöße haben einen wesentlichen Teil zu dieser Arbeit beigetragen. Zudem möchte ich mich bei ihr für das entgegengebrachte Vertrauen, sowie für die Möglichkeit meine Ergebnisse auf zahlreichen Konferenzen zu präsentieren, bedanken.

Des Weiteren möchte ich mich bei allen Kooperationspartnern, besonders bei den Arbeitsgruppen von Frau Prof. Dr. Leticia González und von Herrn Prof. Dr. Matthias Kling für die gute, spannende und interessante Zusammenarbeit bedanken. Außerdem danke ich Herrn Prof. Dr. Matthias Kling für die Zweitkorrektur meiner Dissertation.

Dem Max Weber-Programm des Freistaats Bayern danke ich für die finanzielle und ideelle Förderung meines Studiums.

Ein großer Dank geht auch an alle ehemaligen und momentanen Kollegen im Arbeitskreis: Thali, Patrick, Robert, Sven, Julius, Matthias, Daniel, Flo, Franzi, Martin, Sebastian, Eva, Lena und Ferdinand. Das freundschaftliche Miteinander, die Hilfsbereitschaft und die konstruktiven Diskussionen hatten großen Anteil am Gelingen dieser Doktorarbeit. Nicht zu vergessen an dieser Stelle sind auch die Praktikanten, die ich mitbetreuen durfte: Lena Bäuml, Zekai Xiao, David Girardier, Ferdinand Kiss und Mikhail Belozertsev.

Ein besonderes Danke geht an Annette, Laurens und Sebastian für die viele Arbeit, die sie sich mit dem Korrekturlesen des Manuskripts gemacht haben.

Zuletzt möchte ich mich bei meiner Mutter bedanken, die mich immer gefördert und begleitet und mir das Studium ermöglicht hat.